

## **UC Merced**

### **UC Merced Electronic Theses and Dissertations**

#### **Title**

Smart Big Data in Precision Agricultural Applications: Acquisition, Advanced Analytics, and Plant Physiology-informed Machine Learning

#### **Permalink**

<https://escholarship.org/uc/item/1qc1k2sw>

#### **Author**

Niu, Haoyu

#### **Publication Date**

2022

Peer reviewed|Thesis/dissertation

UNIVERSITY OF CALIFORNIA, MERCED

**Smart Big Data in Precision Agricultural Applications: Acquisition,  
Advanced Analytics, and Plant Physiology-informed Machine Learning**

A dissertation submitted in partial satisfaction of the  
requirements for the degree  
Doctor of Philosophy

in

Electrical Engineering and Computer Science

by

Haoyu Niu

Committee in charge:

Professor YangQuan Chen, Chair

Professor Mukesh Singhal

Professor Wan Du

Dr. Andreas Westphal

Dr. Dong Wang

2022

Copyright  
Haoyu Niu, 2022  
All rights reserved.

The dissertation of Haoyu Niu is approved, and it is acceptable in quality and form for publication on microfilm and electronically:

---

(Professor Mukesh Singhal)

---

(Professor Wan Du)

---

(Dr. Andreas Westphal)

---

(Dr. Dong Wang)

---

(Professor YangQuan Chen, Chair)

University of California, Merced

2022

To my parents, Xiufang & Jianxun Niu.

## TABLE OF CONTENTS

	Signature Page . . . . .	iii
	List of Figures . . . . .	xii
	List of Tables . . . . .	xxii
	Acknowledgements . . . . .	xxvi
	Acronyms . . . . .	xxviii
	Vita and Publications . . . . .	xxxii
	Abstract . . . . .	xxxiv
<b>I</b>	<b>Why Big Data Is Not Smart Yet?</b>	<b>1</b>
Chapter 1	Introduction . . . . .	2
	1.1 Motivation . . . . .	2
	1.1.1 What Is Smart Big Data in Precision Agriculture?	4
	1.1.2 Plant Physiology-informed Machine Learning: A New Frontier . . . . .	5
	1.1.3 Big Data Acquisition and Advanced Analytics . .	7
	1.2 Dissertation Objectives and Methods . . . . .	8
	1.3 Dissertation Contributions . . . . .	10
	1.4 Dissertation Outlines . . . . .	10
Chapter 2	Why Do Big Data and Machine Learning Entail the Fractional Dynamics? . . . . .	13
	2.1 Fractional Calculus (FC) and Fractional-order Thinking (FOT) . . . . .	13
	2.2 Complexity and Inverse Power Laws (IPLs) . . . . .	15
	2.3 Heavy-tailed Distributions . . . . .	18
	2.3.1 The Lévy Distribution . . . . .	18
	2.3.2 The Mittag–Leffler PDF . . . . .	19
	2.3.3 The Weibull Distribution . . . . .	20
	2.3.4 The Cauchy Distribution . . . . .	20
	2.3.5 The Pareto Distribution . . . . .	20
	2.3.6 The $\alpha$ -stable Distribution . . . . .	21
	2.3.7 Mixture Distributions . . . . .	21
	2.4 Big Data, Variability and FC . . . . .	22
	2.4.1 The Hurst Parameter, fGn, and fBm . . . . .	24

2.4.2	Fractional Lower-order Moments (FLOMs) . . . . .	25
2.4.3	Fractional Autoregressive Integrated Moving Average (FARIMA) and Gegenbauer Autoregressive Moving Average (GARMA) . . . . .	26
2.4.4	Continuous Time Random Walk (CTRW) . . . . .	27
2.4.5	Unmanned Aerial Vehicles (UAVs) and Precision Agriculture . . . . .	27
2.5	Optimal Machine Learning and Optimal Randomness . . . . .	28
2.5.1	Derivative-free Methods . . . . .	30
2.5.2	Gradient-based Methods . . . . .	31
2.6	What Can the Control Community Offer to ML? . . . . .	34
2.7	Case Study: Optimal Randomness for Stochastic Configuration Network (SCN) with Heavy-tailed Distributions . . . . .	41
2.7.1	Introduction . . . . .	41
2.7.2	SCN with Heavy-tailed PDFs . . . . .	44
2.7.3	A Regression Model and Parameter Tuning . . . . .	44
2.7.4	MNIST Handwritten Digit Classification . . . . .	48
2.8	Conclusion and Future Research . . . . .	49

## II Smart Big Data Acquisition Platforms 52

Chapter 3	Small Unmanned Aerial Vehicles and Remote Sensing Payloads	53
3.1	The UAV Platform . . . . .	53
3.2	Lightweight Sensors . . . . .	55
3.2.1	The RGB Camera . . . . .	55
3.2.2	The Multispectral Camera . . . . .	56
3.2.3	The Short Wave Infrared Camera . . . . .	56
3.2.4	The Thermal Camera . . . . .	57
3.3	UAV Image Acquisition and Processing . . . . .	59
3.3.1	The Flight Mission Design . . . . .	59
3.3.2	UAV Image Processing . . . . .	60
3.4	Challenges and Opportunities . . . . .	62
3.4.1	UAVs . . . . .	62
3.4.2	UAV Path Planning and Image Processing . . . . .	62
3.4.3	Pre-flight Path Planning . . . . .	63
3.4.4	Multispectral Image Calibration . . . . .	63
3.4.5	Thermal Camera Calibration and Image Processing . . . . .	65
3.4.6	Images Stitching and Orthomosaic Image Generation . . . . .	67
3.5	Case Study I: A UAV Resolution and Waveband Aware Path Planning for Onion Irrigation Treatment Inference . . . . .	67
3.5.1	Introduction . . . . .	67

	3.5.2	Material and Methods . . . . .	69
	3.5.3	Results and Discussion . . . . .	73
	3.5.4	Conclusions . . . . .	77
	3.6	Case Study II: A Detailed Study on Accuracy of Uncooled Thermal Camera by Exploring the Data Collection Workflow . . . . .	77
	3.6.1	Introduction . . . . .	77
	3.6.2	Material and Methods . . . . .	79
	3.6.3	Results and Discussion . . . . .	81
	3.6.4	Conclusions and Future Work . . . . .	87
	3.7	Case Study III: High Spatial-resolution Has Little Impact on NDVI Mean Value of UAV-based Individual Tree-level Mapping: Evidence from 9 Field Tests and Implications . . . . .	90
	3.7.1	Introduction . . . . .	90
	3.7.2	Material and Methods . . . . .	92
	3.7.3	Results and Discussion . . . . .	93
	3.7.4	Conclusions and Future Work . . . . .	100
	3.8	Conclusion and Future Research . . . . .	101
Chapter 4		The Edge-AI Sensors and Internet of Living Things (IoLT) . . . . .	103
	4.1	Introduction . . . . .	103
	4.2	Proximate Sensors . . . . .	104
	4.2.1	The Spectrometer . . . . .	104
	4.2.2	A Pocket-sized Spectrometer . . . . .	106
	4.2.3	A Microwave Radio Frequency 3D Sensor . . . . .	106
	4.3	Case Study: Onion Irrigation Treatment Inference Using A Low-cost Edge-AI Sensor . . . . .	108
	4.3.1	Introduction . . . . .	108
	4.3.2	Material and Methods . . . . .	110
	4.3.3	Results and Discussion . . . . .	114
	4.3.4	Conclusions and Future Work . . . . .	117
	4.4	Conclusion and Future Research . . . . .	118
Chapter 5		The Unmanned Ground Vehicles (UGVs) for Precision Agriculture . . . . .	119
	5.1	Introduction . . . . .	119
	5.2	The UGV as A Data Acquisition Platform . . . . .	121
	5.2.1	Fundamental Research Questions for UGVs . . . . .	122
	5.2.2	Low Barriers to Entry . . . . .	123
	5.2.3	Cognitive Algorithms by Deep Learning . . . . .	125
	5.2.4	The Swarming Mechanism of UGVs . . . . .	126
	5.3	Case Study: Build A UGV platform for Agricultural Research from A Low-cost Toy Vehicle . . . . .	127

5.3.1	Introduction . . . . .	127
5.4	Conclusions and Future Research . . . . .	128

### **III Advanced Big Data Analytics, Plant Physiology-informed Machine Learning, and Fractional-order Thinking 130**

Chapter 6	A Low-cost Proximate Sensing Method for Early Detection of Nematodes in Walnut Using Machine Learning Algorithms . .	131
6.1	Introduction . . . . .	131
6.2	Material and Methods . . . . .	134
6.2.1	Study Area . . . . .	134
6.2.2	Reflectance Measurements with A Radio Frequency Sensor . . . . .	134
6.2.3	Groundtruth Data Collection and Processing . . .	136
6.2.4	Scikit-learn Classification Algorithms . . . . .	137
6.2.5	Deep Neural Networks (DNNs) and TensorFlow .	138
6.3	Results and Discussion . . . . .	139
6.3.1	Data Visualization (Project 45, 2019) . . . . .	139
6.3.2	Performance of Classifiers (Project 45, 2019) . . .	139
6.3.3	Performance of Classifiers (Project 45, 2020) . . .	145
6.4	Conclusions and Future Research . . . . .	151
Chapter 7	Evapotranspiration Estimation with Small UAVs . . . . .	152
7.1	Introduction . . . . .	152
7.2	ET Estimation Methods with UAVs: A Literature Review	157
7.2.1	One Source Energy Balance (OSEB) . . . . .	157
7.2.2	High Resolution Mapping of ET (HRMET) . . . .	159
7.2.3	Machine Learning (ML) and Artificial Neural Networks (ANN) . . . . .	160
7.2.4	Two Source Energy Balance (TSEB) Models . . .	161
7.2.5	Dual-Temperature-Difference (DTD) Model . . .	162
7.2.6	Surface Energy Balance Algorithm for Land (SEBAL) . . . . .	163
7.2.7	Mapping Evapotranspiration at High Resolution with Internalized Calibration (METRIC) . . . . .	164
7.3	Existing ET Estimation Methods with UAVs: Results and Discussion . . . . .	167
7.3.1	OSEB and TSEB Models . . . . .	167
7.3.2	HARMET Model . . . . .	168
7.3.3	Machine Learning and Neural Networks . . . . .	169
7.3.4	TSEB and DTD Models . . . . .	169
7.3.5	TSEB and DATTUTDUT Models . . . . .	171

	7.3.6	The SEBAL Model . . . . .	172
	7.3.7	METRIC and METRIC-HR Models . . . . .	174
	7.4	Estimating Actual Crop Evapotranspiration Using the Stochastic Configuration Networks and UAV-based Crop Coefficients . . . . .	176
	7.4.1	Introduction . . . . .	176
	7.4.2	Material and Methods . . . . .	178
	7.4.3	Results and Discussion . . . . .	180
	7.4.4	Conclusions . . . . .	187
	7.5	Reliable Tree-level Evapotranspiration Estimation of Pomegranate Trees Using Lysimeter and UAV Multispectral Imagery . . . . .	188
	7.5.1	Introduction . . . . .	188
	7.5.2	Material and Methods . . . . .	189
	7.5.3	Results and Discussion . . . . .	192
	7.5.4	Conclusions . . . . .	194
	7.6	Conclusion and Future Research . . . . .	196
Chapter 8		Individual Tree-level Water Status Inference Using High-resolution UAV Thermal Imagery and Complexity-informed Machine Learning . . . . .	199
	8.1	Introduction . . . . .	199
	8.2	Material and Methods . . . . .	202
	8.2.1	Experimental Site and Irrigation Management . . . . .	202
	8.2.2	Ground Truth: Infrared Canopy and Air Temperature . . . . .	203
	8.2.3	The Thermal Infrared Remote Sensing Data . . . . .	203
	8.2.4	The Complexity-informed Machine Learning (CIML) . . . . .	205
	8.2.5	The Principle of Tail Matching . . . . .	206
	8.2.6	Machine Learning Classification Algorithms . . . . .	207
	8.2.7	Image Preprocessing for the CNN Model . . . . .	207
	8.3	Results and Discussion . . . . .	208
	8.3.1	Comparison of Canopy Temperature Per Tree Based on Ground Truth and UAV Thermal Imagery . . . . .	208
	8.3.2	The Relationship Between $\Delta T$ and Irrigation Treatment . . . . .	210
	8.3.3	The Classification Performance of CIML on Irrigation Treatment Levels . . . . .	210
	8.3.4	The Performance of the CNN Model . . . . .	215
	8.4	Conclusion and Future Research . . . . .	218
Chapter 9		Scale-aware Pomegranate Yield Prediction Using UAV Imagery and Machine Learning . . . . .	219
	9.1	Introduction . . . . .	220

9.2	Material and Methods . . . . .	222
9.2.1	Experimental Field and Ground Data Collection . . . . .	222
9.2.2	UAV Platform and Imagery Data Acquisition . . . . .	222
9.2.3	UAV Image Feature Extraction . . . . .	224
9.2.4	The Machine Learning Methods . . . . .	226
9.3	Results and Discussion . . . . .	226
9.3.1	The Pomegranate Yield Performance in 2019 . . . . .	226
9.3.2	The Correlation between the Image Features and Pomegranate Yield . . . . .	227
9.3.3	The ML Algorithm Performance on Yield Estimation . . . . .	228
9.4	Conclusion and Future Research . . . . .	230

## **IV Towards Smart Big Data in Precision Agriculture 234**

Chapter 10	Intelligent Bugs Mapping and Wiping (iBMW): An Affordable Robot-driven Robot for Farmers . . . . .	235
10.1	Introduction . . . . .	235
10.2	Existing Solutions . . . . .	237
10.3	iBMW Innovation . . . . .	238
10.3.1	Cognitive of Pest Population Mapping and Wiping . . . . .	240
10.3.2	iBMW with TurtleBot 3 as “Brain” . . . . .	241
10.3.3	Real-time Vision Processing . . . . .	241
10.3.4	Optimal Path Planning Enabled by iBMW . . . . .	243
10.3.5	Ethical, Cultural and Legal Matters . . . . .	244
10.4	Measuring Success . . . . .	245
10.4.1	NOW Population Temporal and Spatial Distribution . . . . .	245
10.4.2	The Amount of Pesticide Being Used . . . . .	245
10.4.3	The Target Trees Almond Yield . . . . .	246
10.5	Conclusions and Future Research . . . . .	246
Chapter 11	A Non-invasive Stem Water Potential Monitoring Method Using Proximate Sensor and Machine Learning Algorithms . . . . .	248
11.1	Introduction . . . . .	248
11.2	Material and Methods . . . . .	249
11.2.1	Walnut Study Area . . . . .	249
11.2.2	Reflectance Measurements with A Radio Frequency Sensor . . . . .	250
11.2.3	Data Collection and Processing . . . . .	250
11.2.4	Scikit-learn Classification Algorithms . . . . .	251
11.3	Results and Discussion . . . . .	252

	11.4 Conclusion and Future Work . . . . .	254
Chapter 12	A Low-cost Soil Moisture Monitoring Method by Using Wal- abot and Machine Learning Algorithms . . . . .	256
	12.1 Introduction . . . . .	256
	12.2 Material and Methods . . . . .	258
	12.2.1 Study Site . . . . .	258
	12.2.2 The Proximate Sensor . . . . .	258
	12.2.3 The Experiment Setup . . . . .	258
	12.2.4 Data Collection and Processing . . . . .	259
	12.3 Results and Discussion . . . . .	261
	12.3.1 The Linear Discriminant Analysis Performance . .	261
	12.3.2 The Principal Component Analysis Performance .	265
	12.4 Conclusion and Future Research . . . . .	266
Chapter 13	Conclusions and Future Research . . . . .	268
	13.1 Concluding Remarks . . . . .	268
	13.2 Future Research Towards Smart Big Data in Precision Agricultural Applications . . . . .	269
Bibliography	. . . . .	271

## LIST OF FIGURES

Figure 1.1:	The ML can be classified as supervised, unsupervised, semi-supervised, and Reinforcement Learning (RL) based on whether or not human supervision is included. According to whether or not the ML algorithms can learn incrementally on the fly, they can be classified into online and batch learning. Based on whether or not the ML algorithms detect the training data patterns and create a predictive model, the ML can be classified into instance-based and model-based learning. . . . .	6
Figure 1.2:	The outline of the dissertation. . . . .	12
Figure 2.1:	Inverse power law (complexity “bow tie”): On the left are the systems of interest that are thought to be complex. In the center panel, an aspect of the empirical data is characterized by an inverse power law (IPL). The right panel lists the potential properties associated with systems with data that have been processed and yield an IPL property. See text for more details.	16
Figure 2.2:	Complex signals: Here, the signal generated by a complex system is depicted. Exemplars of the systems are given as the potential properties arising from the systems’ complexity. . . .	17
Figure 2.3:	Normalized difference vegetation index (NDVI) mapping of pomegranate trees. . . . .	28
Figure 2.4:	Data analysis in nature. . . . .	29
Figure 2.5:	The 2-D Alpine function for derivative-free methods. . . . .	31
Figure 2.6:	Sample paths analysis. Wei <i>et al.</i> investigated the optimal randomness in a swarm-based search. Four heavy-tailed PDFs were used for sample path analysis. The long steps, referring to the jump length, frequently happened for all distributions, which showed strong heavy-tailed performance. . . . .	32
Figure 2.7:	Gradient descent and its variants. . . . .	34
Figure 2.8:	The integrator model (embedded in $G(z)$ ). The integrator in the forward loop eliminates the tracking steady-state error for a constant reference signal (internal model principle (IMP)). . .	35
Figure 2.9:	Training loss ( <b>left</b> ); test accuracy ( <b>right</b> ). It is obvious that for different zeros and poles, the performance of the algorithms is different. One finds that both the $b = -0.25$ and $b = -0.5$ cases perform better than does the stochastic gradient descent (SGD) momentum. Additionally, both $b = 0.25$ and $b = 0.5$ perform worse. It is also shown that an additional zero can improve the performance, if adjusted carefully. (Courtesy of Professor Yuquan Chen) . . . . .	38

Figure 2.10: Training loss ( <b>left</b> ); test accuracy ( <b>right</b> ). (Courtesy of Professor Yuquan Chen) . . . . .	40
Figure 2.11: Performance of SCN, SCN-Lévy, SCN-Weibull, SCN-Cauchy and SCN-Mixture. The parameter L is the hidden node number. . . . .	47
Figure 2.12: The handwritten digit dataset example. . . . .	48
Figure 2.13: Classification performance of SCNs. . . . .	50
Figure 2.14: Timeline of FC (courtesy of Professor Igor Podlubny). . . . .	51
Figure 3.1: (a) The QuestUAV 200 UAV. (b) The MK Okto XL 6S12. (c) The DJI S1000. (d) The eBee Classic. (e) The Hover. . . . .	54
Figure 3.2: The Survey 2 sensors and the reflectance calibration ground target package. . . . .	55
Figure 3.3: The Rededge M is a commonly used multispectral camera. The Rededge M has five bands, which are Blue, Green, Red, Near-infrared, and Red edge. It has a spectral resolution of $1280 \times 960$ pixel, with a $46^\circ$ field of view. . . . .	56
Figure 3.4: The SWIR 640 P-Series, which is a shortwave infrared camera, has also been commonly used for agricultural research. The spectral band is from $0.9 \mu m$ to $1.7 \mu m$ . The accuracy for the SWIR camera is $\pm 1^\circ C$ . It has a resolution of $640 \times 512$ pixels. . . . .	57
Figure 3.5: The thermal camera has a resolution of $640 \times 480$ pixels. The spectral band is from $7 \mu m$ to $14 \mu m$ . The dimension of the thermal camera is $34 \text{ mm} \times 30 \text{ mm} \times 34 \text{ mm}$ . The accuracy is designed to be $\pm 2^\circ C$ . . . . .	58
Figure 3.6: The user interface of Mission Planner. The example of flight mission was for nematode data collection using UAV for Project 30 at UC Kearny Center. See Chapter 6 for more details. . . . .	59
Figure 3.7: Agisoft Metashape image processing workflow: (a) Align Photos. (b) Build Mesh. (c) Generate orthomosaick. . . . .	61
Figure 3.8: The UAV image reflectance calibration. (a) A color panel. (b) The MAPIR target calibration board. (c) The Rededge M calibration board. . . . .	64
Figure 3.9: Onion test site. The field study was conducted at the USDA-ARS, San Joaquin Valley Agricultural Sciences Center ( $36.59^\circ N$ , $119.51^\circ W$ ), Palier, California, 93648, USA. Since 2016, an onion test field has been set up for research of biomass soil amendments and deficit irrigation. . . . .	70
Figure 3.10: RGB image for the onion field. . . . .	71
Figure 3.11: NIR image for the onion field. . . . .	72
Figure 3.12: 36 plots of onion. Every image was converted into 2048 dimension vector for data processing. The data was distributed as 67% for training and 33% for testing. . . . .	74

Figure 3.13: This research was conducted in a field near MESA Lab in Atwater, California, USA (37.37°N, 120.57°W). There were five different materials being used, water, dry soil, wet soil, leaves and white panels. . . . .	80
Figure 3.14: Calibration's effect experiment. . . . .	80
Figure 3.15: View angle experiment. . . . .	86
Figure 3.16: The effect of stitching experiment. . . . .	89
Figure 3.17: The pomegranate study site at USDA. The pomegranate was planted in 2010 with a 5 m spacing between rows and 2.75 m within-row tree spacing in a 1.3 ha field. There are two large weighing lysimeters located in the center of the field, marked in red boxes. . . . .	92
Figure 3.18: The mean NDVI values of each sampling tree at 60 m, 90 m, and 120 m on May 8 <sup>th</sup> , 2019. The <i>x</i> -axis was the identification number (ID) for sampling trees, 82 in total. The <i>y</i> -axis was the mean NDVI value for each tree canopy. . . . .	94
Figure 3.19: The mean NDVI values of each sampling tree at 60 m, 90 m, and 120 m on Sep 19 <sup>th</sup> , 2019. The <i>x</i> -axis was the identification number (ID) for sampling trees, 82 in total. The <i>y</i> -axis was the mean NDVI value for each tree canopy. . . . .	95
Figure 3.20: The mean NDVI values of each sampling tree at 60 m, 90 m, and 120 m on Oct 3 <sup>rd</sup> , 2019. The <i>x</i> -axis was the identification number (ID) for sampling trees, 82 in total. The <i>y</i> -axis was the mean NDVI value for each tree canopy. . . . .	95
Figure 3.21: The individual tree-level mean NDVI correlation between 120 m and 90 m on Oct 3 <sup>rd</sup> , 2019. The <i>x</i> -axis was the mean NDVI values for sampling trees at 120 m flight height. The <i>y</i> -axis was the mean NDVI values for sampling trees at 90 m flight height. . . . .	96
Figure 3.22: The NDVI distribution of two individual lysimeter trees at 60 m, 90 m and 120 m on May 8 <sup>th</sup> , 2019. . . . .	97
Figure 3.23: The NDVI distribution of two individual lysimeter trees at 60 m, 90 m and 120 m on Sep 19 <sup>th</sup> , 2019. . . . .	98
Figure 3.24: The NDVI distribution of two individual lysimeter trees at 60 m, 90 m and 120 m on Oct 3 <sup>rd</sup> , 2019. . . . .	99
Figure 4.1: The spectrometer EPP2000-VIS-50. The StellarNet EPP2000 Spectrometers are miniature fiber optic instruments for ultra-violet (UV), visible (VIS), and near-infrared (NIR) measurements in 190 - 1700 nm ranges. . . . .	105

Figure 4.2:	A light and small near-infrared spectrometer, Scio. The low power consumption and zero warm up time make it highly responsive and extremely efficient, which allows it to perform hundreds of samplings from a small rechargeable battery. The Scio spectrometer works in NIR at wavelengths of 700 - 1100 <i>nm</i> . It can also be integrated into smart phone as an Edge-AI device. .	106
Figure 4.3:	A radio frequency 3D sensor, Walabot Developer (Front and back view). The frequency range was 3.3 - 10 GHz for the US/FCC model and 6.3 - 8 GHz for the EU/CE mode. The average transmitted energy of both models was below 41dBm/MHz and did not constitute health concerns for the user, nor did it impact the tested tissues. . . . .	108
Figure 4.4:	The principle of Walabot. The sensor uses an antenna array to send radio frequency to the area in front of it, e.g. walnut leaves, and then captures the returning signals (reflectance or response). The citation signals are produced, and the reflectance is then recorded by the radio frequency integrated circuits (RFIC).	109
Figure 4.5:	The measurement signal of the radio frequencies reflectance of the walnut leaves using Walabot. The research hypothesis is that the reflectance of walnut leaves will be significantly different towards root-lesion nematode infection levels. The spectral curve obtained from the leaves of walnut trees infected with nematodes could show the characteristic pattern of walnut under nematode stress. For more details of this research work, please refer to Chapter 6. . . . .	109
Figure 4.6:	The onion field (image taken by the “Hover” UAV platform). The study field was in the USDA-ARS, San Joaquin Valley Agricultural Sciences Center (36.59°N, 119.51°W), Parlier, California. Since 2016, an onion test field had been set up for research of biomass soil amendments and deficit irrigation. There were three irrigation treatment levels, High, Medium and Low. . . .	111
Figure 4.7:	The NIR reflectance measurement of Scio using a smartphone.	112
Figure 4.8:	The reflectance measurement of EPP2000-VIS-50. Each onion sampling was measured three times to reduce the likelihood of errors or anomalous results. . . . .	113
Figure 4.9:	Classifier Comparison (PCA dimension reduction) . . . . .	115
Figure 4.10:	Classifier Comparison (LDA dimension reduction) . . . . .	117
Figure 5.1:	The toy vehicle. . . . .	127
Figure 5.2:	The UGV platform. . . . .	128

Figure 6.1:	The study was conducted in an experimental walnut orchard at the Kearney Agricultural Research and Extension Center, 9240 S Riverbend Ave, Parlier, CA, 93648, USA (36.595°N, 119.508°W). There were three replications to detect the nematode infection levels, Project 30 (a, b), Project 45, and Project Smith. . . . .	135
Figure 6.2:	The Linear Discriminant Analysis (LDA) was used for data visualization, which learned the most critical axes between the classes. The axes were then used to define hyperplane to project the high-dimensional training data into two dimensions, which gained important insight by visually detecting patterns. The $x$ -axis and $y$ -axis had no scale because of hyperplane projection. The nematode infection levels were successfully clustered into four levels. The color bar values 1, 2, 3, and 4 represented the four nematode infection levels from 1 to 4 (low to high) (Table 6.2). . . . .	140
Figure 6.3:	The Linear Discriminant Analysis (LDA) was used for three-dimensional data visualization. The $x$ -axis and $y$ -axis had no scale because of hyperplane projection. The nematode infection levels were successfully clustered into four levels. The clusters' color was related to Fig. 6.2. . . . .	141
Figure 6.4:	A comparison of six classifiers in Scikit-learn on nematode testing dataset (Project 45, 2019). A confusion matrix was a summary of prediction results on a classification problem. The "True label" meant the ground truth of nematode infestation levels. The "Predicted label" identified the nematode infestation levels predicted by the trained model. . . . .	143
Figure 6.5:	There were $k$ models (in this case, $k = 100$ ). The best accuracy could be as high as 0.9 (marked as a red dot). The lowest accuracy was around 0.58 when the training instances could not represent the nematode infection levels dataset very well. The mean accuracy was 0.82 for the DNN classifier model. . . .	144
Figure 6.6:	A comparison of six classifiers in Scikit-learn on nematode testing dataset (Project 45, 2020). Table 6.8 showed the details of the test process of the $k$ -nearest neighbors method. . . . .	148
Figure 6.7:	The test performance of DNN for Project 45, 2020. There were 100 models and the best accuracy could be as high as 0.88 (marked as a red dot). The lowest accuracy was around 0.4 when the training instances could not represent the nematode infection levels dataset very well. The mean accuracy was 0.7 for the DNN classifier model. . . . .	150

Figure 7.1:	Pomegranate test site. The pomegranate was planted in 2010 with a 5 m spacing between rows and 2.75 m within-row tree spacing in a 1.3 ha field. There were two large weighing lysimeters, which were 2 m × 4 m by 3 m deep. The lysimeters had a resolution of 0.1 mm of water loss, which were located in the center of the field, marked in red boxes. . . . .	178
Figure 7.2:	Seasonal $K_c$ and NDVI at the pomegranate field in 2019. The values of $K_c$ were derived using equation (7.25). The $ET_c$ was recorded by the weighing lysimeter in the center of the pomegranate field. The $ET_o$ was calculated by the CIMIS near the pomegranate field. The NDVI was derived by image processing tools in MATLAB. . . . .	181
Figure 7.3:	Linear regression model for $K_c$ and NDVI. A strong correlation was shown between the $K_c$ and NDVI during the growing season in 2019. . . . .	182
Figure 7.4:	DeepSCNs training model. Since the dataset of $K_c$ and NDVI was not large, in this study, DeepSCNs was used for building the regression model between $K_c$ and NDVI. Four out of seven days of data were used for training the DeepSCNs regression model. All the data points were fitted very well in the trained model. . . . .	183
Figure 7.5:	The SCNs model evaluation performance. Three days of data were used to evaluate the trained model. The value of $R^2$ was 0.995. The value of RMSE was 0.046. Both of them showed good performance for estimating $K_c$ by using NDVI. The variations of $K_c$ were well explained by using the NDVI from UAV images. . . . .	185
Figure 7.6:	NDVI (top) and $K_c$ (bottom) maps of the pomegranate using UAVs. (Sept. 19 <sup>th</sup> , 2019) . . . . .	186
Figure 7.7:	Spatial and tree-by-tree view of ET distribution. . . . .	187
Figure 7.8:	The Pomegranate study site. Field studies were conducted in an experimental pomegranate ( <i>Punica granatum L.</i> , cv ‘Wonderful’) field at the USDA-ARS, San Joaquin Valley Agricultural Sciences Center (36.59°N, 119.51°W), Parlier, California, 93648, USA. The pomegranate field was randomly designed into 16 equal blocks, with four replications, to test four irrigation levels. The irrigation volumes are 35%, 50%, 75%, and 100% of $ET_c$ , which was measured by the weighing lysimeter in the field. There were five sampling trees in each block, 80 sampling trees in total, marked with red labels. . . . .	190

Figure 7.9:	Seasonal $K_c$ and NDVI for the tree in lysimeter. The sampling data started on May 8 <sup>th</sup> and ended on Oct 29 <sup>th</sup> . The linear relationship had an intercept of 0.6114 and a slope of 1.6493. It also had a high correlation coefficient of 0.8865, indicating a significant correlation between the $K_c$ and NDVI at the individual-tree level during the growing season in 2019. . . .	193
Figure 7.10:	The $K_c$ and $ET_c$ maps of May 8 <sup>th</sup> , 2019. . . . .	195
Figure 7.11:	100% ET irrigation sampling trees vs lysimeter tree. To validate the linear regression model on individual-tree-level ET estimation, the author compared the 20 sampling trees with the lysimeter daily $ET_c$ for the UAV flight dates (almost the whole growing season). The trends of the daily $ET_c$ for the 20 sampling trees (100% irrigation ) and the lysimeter tree were shown. Each ‘Serie’ meant an individual tree in the field. . . . .	196
Figure 7.12:	The boxplot of 100% ET sampling trees vs lysimeter tree. Compared with the lysimeter tree, the linear regression model estimated tree-level ET with an $R^2$ and mean absolute error (MAE) of 0.9143 and 0.39 mm/day, respectively. . . . .	197
Figure 8.1:	The pomegranate field at the USDA-ARS (36.594°N, 119.512°W). The weighing lysimeter is located in the center of the pomegranate field, marked as a red box. The blue marks are where the 14 IRT sensors were installed. . . . .	203
Figure 8.2:	The IRT sensor was installed 4.5 m above the soil surface, with a FOV of 20°. A quadcopter was used as the low-cost UAV platform (less than \$1000) to collect high-resolution thermal images at the height of 60 m. . . . .	204
Figure 8.3:	(A) All of the UAV thermal images were stitched together to generate the orthomosaick images in Metashape (Agisoft LLC, Russian); (B) To obtain the individual tree canopy images of the 250 sampling trees, the author used the SVM for classifying the tree canopy. (C) Histogram was generated for each tree canopy to check the variability of each tree canopy temperature.	205
Figure 8.4:	25 images were randomly selected from the training set and the class name for each image was displayed below. All the images were resized into $32 \times 32 \times 3$ in order to input into the CNN model. . . . .	208
Figure 8.5:	The correlation between the canopy temperature per tree measured by the IRT sensors and UAV thermal camera. The coefficient of determination ( $R^2$ ) was 0.8668, which indicated that the difference between the ground truth and UAV thermal camera was acceptable. The method was reliable for monitoring tree-level canopy temperature. . . . .	209

Figure 8.6:	The $\Delta T$ was significantly higher in the 35% irrigation treatment than the 100% irrigation treatment on different days. The values of $\Delta T$ decreased as the irrigation increased. This finding emphasized the importance of irrigation on the tree canopy temperature response. . . . .	211
Figure 8.7:	The summary of prediction results using histogram information on the tree-level irrigation treatment inference. “True label” meant the ground truth of $ET_c$ based irrigation treatment levels. “Predicted label” identified the irrigation treatment levels predicted by the trained model. . . . .	212
Figure 8.8:	The test performance for the histogram dataset. The t-distributed stochastic neighbor embedding (TSNE) method was used for data visualization, which learned the most critical axes between the classes. The axes were then used to define the hyperplane to project the high-dimensional training data into two dimensions, which gained important insight by visually detecting patterns. The $x$ -axis and $y$ -axis had no scale because of hyperplane projection. The irrigation treatment levels were successfully clustered into low-level (blue) and high-level (green). . . . .	214
Figure 8.9:	The performance of the CNN model, training and validation accuracy curves. . . . .	215
Figure 8.10:	The summary of prediction results on the irrigation treatment classification problem. “True label” meant the ground truth of $ET_c$ based irrigation treatment levels. “Predicted label” identified the irrigation treatment levels predicted by the trained CNN model. To simplify the visualization, low irrigation (30% and 50% ET) were labeled as “0”; high irrigation (75% and 100% ET) were labeled as “1”. . . . .	216
Figure 8.11:	To visualize the trained CNN model performance, the authors made predictions about some images in the test dataset. Correct prediction labels are blue and incorrect prediction labels are red. The number gives the percentage (out of 100) for the predicted label. . . . .	217
Figure 9.1:	The pomegranate field was randomly designed into 16 equal blocks, with four replications, to test four irrigation levels. The irrigation volumes were 35%, 50%, 75%, and 100% of $ET_c$ , which were measured by the weighing lysimeter in the field. . . . .	223
Figure 9.2:	There were five sampling trees in each block, 80 sampling trees in total, marked with red labels. . . . .	223

Figure 9.3:	The pomegranate yield performance at the individual tree level in 2019. For the 35% irrigation treatment, the total fruit weight per tree was 23.92 kg, which produced the lowest yield. For the 50% irrigation treatment, the total fruit weight per tree was 27.63 kg. For 75% and 100% irrigation treatment, the total fruit weight per tree was 29.84 kg and 34.85 kg, respectively. . . . .	227
Figure 9.4:	The correlation between the vegetation index and yield. . . . .	229
Figure 9.5:	The “Decision Trees” method training process. The “Decision Trees” usually uses a white box model, which means the explanation for the condition is easily explained by Boolean logic if a given situation is observable in a model. As shown here, the “Decision Trees” ML model started at the root node, if the NDVI <sub>re</sub> value were less than 0.334, the prediction process would move to the leaf child node. In this case, the model would predict that the input was a low-yield pomegranate tree. A node’s gini attribute measures its impurity: a node is “pure (gini = 0)” if all the training instances it applies are from the same class.	231
Figure 9.6:	The comparison of the eight different ML classifiers on individual tree level yield prediction. “True label” meant the ground truth of the yield. “Predicted label” identified the individual tree yield predicted by the trained model. The value 0 meant the low yield; value 1 meant the high yield. . . . .	232
Figure 10.1:	The iBMW workflow. The iBMW is an intelligent robot which can recognize and classify the NOW by using deep learning neural networks. By using swarming mechanism, several iBMWs can scout in orchard together to realize pest population mapping in a large scale. Based on the mapping analysis, the iBMWs can determine which areas are at the greatest risk and whether wiping treatment is needed. . . . .	239
Figure 10.2:	The concept of the iBMW. . . . .	240
Figure 10.3:	Road detection by Jetson TX2. . . . .	242
Figure 11.1:	This study was conducted in a walnut orchard at Merced, CA, 95340, USA (37.47°N, 120.45°W). There were three types of spacing treatment, 22’ × 22’, 26’ × 26’, and 30’ × 30’. The region of interest was marked with the red box. To determine the SWP of a walnut tree, midday SWP was measured by using a pressure chamber weekly from May to September 2018. . . . .	250

Figure 11.2: A comparison of six classifiers in Scikit-learn on SWP prediction. (a) “Decision Trees”; (b) “Nearest Neighbors”; (c) “Neural Net”; (d) “AdaBoost”; (e) “Random Forest”; (f) “Support Vector Machine”. “True label” meant the ground truth of SWP levels. “Predicted label” identified the SWP levels predicted by the trained model. . . . .	253
Figure 12.1: Walabot data collection. The experiment was conducted in the MESA Lab. The soil was sampled in an almond field near the lab and was divided into 3 cups. . . . .	259
Figure 12.2: LDA results for soil moisture measurement. There were five different soil moisture levels with different colors, “Dry,” “Wet1,” “Wet2,” “Wet3,” and “WetTotal”, which meant the soil sampling was saturated. LDA classifiers firstly reduced the original dimension to 2 components. Different colors meant different soil moisture levels and the axes of the figure were dimensionless. The LDA could classify the five different levels of soil moisture in different areas of the coordinate, so that the LDA could classify the soil moisture with an state-of-art performance. . . . .	264
Figure 12.3: PCA results for soil moisture measurement. “WetTotal” points were on the left and right sides of the image. The “Wet3” and “Wet2” data points did not drop in the same area. The reason might be that the PCA could not detect the features difference from the data. Similar to LDA, the PCA classifiers firstly reduced the original dimension to 2 components. Then, each classifier was tested against reduced dimensionality data with the component as 2. . . . .	267

## LIST OF TABLES

Table 2.1:	The 10 Vs of big data. . . . .	23
Table 2.2:	Variability in multiple research topics. . . . .	23
Table 2.3:	General second-order algorithm design. The parameter $\rho$ is the loop forward gain; see text for more details. . . . .	37
Table 2.4:	General third-order algorithm design, with parameters defined by Equation (2.39). . . . .	39
Table 2.5:	The continuous time fractional-order system. . . . .	40
Table 2.6:	SCNs with key parameters. . . . .	45
Table 2.7:	Performance comparison of SCN models on the regression problem. . . . .	47
Table 2.8:	Performance comparison between SCN, SCN-Lévy and SCN-Cauchy. . . . .	49
Table 3.1:	The specifications of “Hover”. The quadcopter is equipped with high efficient power system, including T-Motor MN3508 KV380 motor, 1552 folding propeller and Foxtech Multi-Pal 40A OPTP ESC, to ensure long flight time. . . . .	54
Table 3.2:	Orthomosaic images generation workflow in Agisoft Metashape. . . . .	61
Table 3.3:	Different resolutions accuracy for onion treatment inference. The best accuracy was 0.726, which showed up when the resolution was at 2.02 cm/pixel by using “Neural net” classifier. Compared with the other classifiers, the “Neural net” classifier performed the best in all resolution levels. . . . .	75
Table 3.4:	Bands configuration accuracy for onion treatment inference. The best accuracy was 0.840, which appeared when the RGB-NIR-TIR waveband images were used by “Gaussian process” classifier. Compared with the other classifiers, the “Gaussian process” classifier performed the best in all wavebands configuration. . . . .	76
Table 3.5:	The groundtruth. . . . .	83
Table 3.6:	The measurement from the non-calibrated camera. . . . .	84
Table 3.7:	The measurement from the calibrated camera. . . . .	85
Table 3.8:	The root mean square error. . . . .	85
Table 3.9:	The view angle experiment. . . . .	87
Table 3.10:	The stitching effect on the data. . . . .	88
Table 3.11:	The root mean square error. . . . .	89
Table 3.12:	The UAV flight schedule. The UAV flight height was 60 m, 90 m, and 120 m to acquire different high-resolution multispectral imagery. Data was collected successfully for three different days, 5-8-19, 9-19-19, and 10-3-19. . . . .	93

Table 3.13:	Entropy was used in the quantitative analysis and evaluation of image information, because it provided better comparison of the image details. Higher value of entropy meant more detailed information in the image. . . . .	100
Table 4.1:	The specifications of spectrometer EPP2000-VIS-50. . . . .	105
Table 4.2:	The specifications of spectrometer Scio. . . . .	107
Table 4.3:	Top 5 performing classifiers using PCA and MLP and their grid search parameters. . . . .	116
Table 5.1:	Specifications of several UGVs and the proposed Personal UGV. . . . .	123
Table 6.1:	Nematode numbers per gram of root in rootstock genotypes examined by Walabot measurements (Project 45, 2019). “RLN per gram of root” meant the root-lesion nematode number per gram of root extracted in laboratory procedures. . . . .	136
Table 6.2:	The classification of the nematode infestation levels (Project 45, 2019). . . . .	137
Table 6.3:	The performance of classification methods (Project 45, 2019). . . . .	142
Table 6.4:	The $k$ -nearest neighbors performance (Project 45, 2019). . . . .	144
Table 6.5:	The classification of the nematode infestation levels (Project 45, 2020). “RLN per gram of root” meant the root-lesion nematode number per gram of root that was extracted in laboratory procedures. . . . .	146
Table 6.6:	Nematode numbers per gram of root in rootstock genotypes examined by Walabot measurements (Project 45, 2020). “RLN per gram of root” meant the root-lesion nematode number per gram of root that was extracted in laboratory procedures. “ID” is a short form for “identity”. . . . .	147
Table 6.7:	The performance of classification methods (Project 45, 2020). . . . .	149
Table 6.8:	The $k$ -nearest neighbors performance (Project 45, 2020). . . . .	149
Table 7.1:	ET estimation using UAV platforms. . . . .	155
Table 7.2:	Multispectral and thermal infrared sensors on UAV platforms. . . . .	156
Table 7.3:	Comparisons of the different ET estimation methods. . . . .	158
Table 7.4:	Comparisons of the different ET estimation methods with UAVs. . . . .	167
Table 7.5:	The UAV flight schedule. The flight height was set up as 60 m. The overlapping of UAV images was set up as 80%, so that the UAV imagery of the pomegranate could be stitched together during image processing. The author flew the UAV bi-weekly over the pomegranate field at noon during the growing season in 2019. . . . .	180

Table 7.6:	DeepSCNs with properties. For example, the maximum times of random configuration $T_{max}$ was set as 100. The scale factor Lambdas in the activation function, which directly determined the range for the random parameters, was examined by performing different settings (0.5 - 200). The tolerance was set as 0.001.	184
Table 7.7:	Flight missions at the USDA in 2019. The UAV flight missions were configured by using the MissionPlanner (Ardupilot, USA). The flight altitude was set up as 60 m. The overlapping of UAV images was set up as 80% forward and 70% by the side.	191
Table 8.1:	The architecture of the CNN model.	209
Table 8.2:	The classification performance of CIML algorithms on irrigation treatment levels at individual tree level. All the methods showed a state-of-art performance, with an overall accuracy of 87%. The “Naive Bayes” had the highest accuracy of 0.90.	213
Table 8.3:	The CNN model performance.	216
Table 9.1:	UAV image features used in this study.	224
Table 9.2:	The “Decision Tree” performance on yield prediction. “NA” stands for “Not available”.	230
Table 9.3:	The performance of ML methods on yield prediction.	233
Table 11.1:	The stem water potential of walnut leaves. There were 16 sampling trees, which had unique ID numbers. For example, “20-4” meant the fourth tree on row 20. Each sampling tree was measured five times to reduce the likelihood of errors or anomalous results.	251
Table 11.2:	The SWP levels of walnut leaves. Based on the SWP range, the walnut trees were classified into three levels.	252
Table 11.3:	The performance of classification methods. The accuracy of the “Support Vector Machine” was 0.62. The “Random Forest” also had a low prediction accuracy of 0.60. The “AdaBoost,” “Nearest Neighbors,” and “Neural Network” had an accuracy of 0.60, 0.65, and 0.62, respectively.	254
Table 11.4:	The “Decision Trees” performance on SWP prediction. In the analysis as “Decision Tree” for the SWP Level 1, the trained model predicted the test data was in the range of Level 3. Therefore, the prediction accuracy (F1-score) of Level 1 was zero. The model successfully classified 22 out of 25 samplings in Level 2. For the Level 2, the model had performance with an F1-score of 0.92. For the Level 3, the model classified 9 out of 10 samplings. The overall prediction accuracy of the trained model was 0.78.	255

Table 12.1: Soil samplings. All the soil samplings were from the same spot in the almond field to make sure they are homogeneous. The soil was dried out to make sure all the 3 cups of soil were at the same lowest moisture level. The weights of three cups of dry soil were 632 grams, 630 grams, and 634 grams. 6 g or 8 g water was added in every cup each time (10 times in total) to increase the soil moisture until the soil moisture was saturated . . . . .	260
Table 12.2: The classifier accuracy. The best classifiers were “Nearest Neighbors,” “Gaussian Process,” “Decision Tree,” “Random Forest,” “Neural Net,” and “Naive Bayes” with an accuracy of 95%. The “QDA” was with 90% accuracy. The “Linear SVM” and “AdaBoost” were worst with 55% accuracy. . . . .	262
Table 12.3: The LDA Methods. Several LDA methods were used for soil moisture classification. . . . .	263
Table 12.4: The PCA Methods. . . . .	265

## ACKNOWLEDGEMENTS

I would like to express my deepest appreciation to my Ph.D. advisor, professor YangQuan Chen, who is an educationist and teacher in a research university for me. In the Tang dynasty, there was a Chinese scholar, poet, and government official called Han Yu (AD 768 - AD 824). In his “Discourse on Teachers”, Han discussed the importance and principles of learning from teachers, “In ancient times, those who wanted to learn surely had a teacher. A teacher is a person who propagates the Dao, imparts professional knowledge, and resolves doubts. Since no one is born omniscient, who can claim to have no doubt? Having doubt but neglect learning from a teacher, one’s doubt will never be resolved.” During my Ph.D. life at UC, Merced, there were always many doubts and challenges for my research and life. I am so lucky to meet with Dr. Chen, and he is always here to help resolve my doubts and challenges. His enthusiasm for research and optimistic attitude towards life always encourage me to learn new knowledge aggressively and explore the wonderful world.

I would like to extend my deepest gratitude to my dissertation committee members: Prof. Mukesh Singhal, Prof. Wan Du, Dr. Andreas Westphal, and Dr. Dong Wang. Their encouraging, critical, and constructive comments and suggestions increased the value of this dissertation. I am also extremely grateful to Dr. Bruce J. West, Prof. Reza Ehsani, Prof. Hede Ma, Prof. Adel Ghandakly, Prof. Ghang-Ho Lee, Prof. Kurtis Kredo II, Dr. Larry Wear, Marisol B. Gamboa, Dr. Brenden Peterson, Dr. Mikel Landajuela Larma, and Dr. Kari L. Arnold.

Many thanks to my lab colleagues Dr. Tiebiao Zhao, Dr. Guoxiang Zhang, Dr. Brandon Stark, Derek Hollenbeck, Jose Alcalá, Jairo Viola, Di An. Special thanks to Dr. Huifang Dou, Jin & Wayne Douglass, Cilla Jia, Jinghui Wang, Kaijun Qi, Dr. Feng Qi, Haiyang Wang, Dr. Mengjun Shu, Renjie Cui, Dr. Yuquan Chen, Dr. Lihong Guo, Dr. Tian Feng, Dr. Yanan Wang, Dr. Panpan Gu, Dr. Peng Wang, Dr. Zhenlong Wu, David Doll, Cameron At Zuber, Stella Zambrzuski, and Jennifer Bellig. Thanks go to the undergraduate researchers I have mentored and worked with: Dong Sen Yan, Emery Silberman, Andreas Anderson, Allan Murillo, Christopher Currier, Christopher Guzman, Daniel Perez-Zoghbi, Nicolas Limon,

Brendan Daddino, Julian Gionet-Gonzalez, Arturo Ramirez-Reyes, Christian Martin, Jaime Rivera, Kimberly Parra, Ryan Wong, Roberto Cordero, Jesus Coria, Kyle Chun, Merlin Appel, William Le, Levi Williams, Matthew Nor.

I deeply thank Jiamin Wei and my parents, Xiufang Niu and Jianxun Niu for their unconditional support, timely encouragement, and endless love.

## ACRONYMS

AI	Artificial Intelligence
ACF	Autocorrelation Function
ANN	Artificial Neural Network
API	Application Programming Interface
ARMA	Autoregressive and Moving Average
ARS	Agricultural Sciences Center
BRDF	Bidirectional Reflectance Distribution Function
CIMIS	California Irrigation Management Information System
CIML	Complexity-informed Machine Learning
CNNs	Convolutional Neural Networks
CRP	Calibrated Reflectance Panel
CS	Cuckoo Search
CTRW	Continuous Time Random Walk
dBm	Decibel Milliwatts
DEM	Digital Elevation Model
DLS	Downwelling Light Sensor
DN	Digital Number
DNNs	Deep Neural Networks
DOY	Day of Year
DTD	Dual Temperature Difference
EOM	Equation of Motion
ET	Evapotranspiration
fBm	fractional Brownian motion
fGn	fractional Gaussian noise
FARIMA	Fractional Autoregressive Integrated Moving Average
FC	Fractional Calculus
FCC	Federal Communications Commission
FIGARCH	Fractional Integral Generalized Autoregressive Conditional Heteroscedasticity
FLOMs	Fractional Lower-order Moments

FOCV	Fractional-order Calculus of Variation
FODA	Fractional-order Data Analysis
FOEL	Fractional-order Euler-Lagrange
FOT	Fractional-order Thinking
FOV	Field of View
GARMA	Gegenbauer Autoregressive Moving Average
GHz	Gigahertz
GPS	Global Positioning System
GPU	Graphics Processing Unit
HRMET	High Resolution Mapping of Evapotranspiration
ID	Identity
IPL	Inverse Power Law
IoT	Internet of Living Things
IR	Infrared
JPG	Joint Photographic Experts Group
LAI	Leaf Area Index
LDA	Linear Discriminant Analysis
LRD	Long Range Dependence
LTI	Linear Time-invariant
MAD	Modeling, Analysis, and Design
MAE	Mean Absolute Error
METRIC	Mapping Evapotranspiration with Internalized Calibration
ML	Machine Learning
MLL	Mittage-Leffler Law
MLP	Multi-layer Perceptron
NAGD	Nesterov Accelerated Gradient Descent
NDVI	Normalized Difference Vegetation Index
NIST	National Institute of Standards and Technology
NIR	Near Infrared
OSEB	One Source Energy Balance
PA	Precision Agriculture

PCA	Principal Component Analysis
PDF	Probability Distribution Function
POTM	Principle of Tail Matching
PPIML	Plant Physiology-informed Machine Learning
PSD	Power Spectral Density
PSO	Particle Swarm Optimization
QDA	Quadratic Discriminant Analysis
RFIC	Radio Frequency Integrated Circuits
RGB	Red, Green, and Blue
RL	Reinforcement Learning
RLN	Root Lesion Nematode
RMSE	Root Mean Square Error
ROS	Robotic Operation System
RSEB	Remote Sensing Energy Balance
SCN	Stochastic Configuration Network
SEBAL	Surface Energy Balance Algorithm for Land
SGD	Stochastic Gradient Descent
SPDA	Soil and Plant Development Analyzer
SRD	Short Range Dependence
SVM	Support Vector Machine
SWIR	Short-wave Infrared
TIR	Thermal Infrared
TSEB	Two-source Energy Balance
TSEB-PT	Priestley-Taylor TSEB
UAVs	Unmanned Aerial Vehicles
UGVs	Unmanned Ground Vehicles
US	United States
USDA	United States Department of Agriculture
UV	Ultraviolet
VIS	Visible
wGn	White Gaussian Noise

## VITA

2014	B.S. in Electrical Engineering and Automation, Hebei Agricultural University, China
2016	M.S. in Electrical and Computer Engineering, California State University, Chico, USA
2022	Ph.D. in Electrical Engineering and Computer Science, University of California, Merced, USA

## PUBLICATIONS

**Niu, Haoyu**, YangQuan Chen, and Bruce J. West., “Why do big data and machine learning entail the fractional dynamics?”, *Entropy*, 23.3 (2021): 297.

**Niu, Haoyu**, Jiamin Wei, and YangQuan Chen., “Optimal randomness for stochastic configuration network (SCN) with heavy-tailed distributions.”, *Entropy*, 23.1 (2021): 56.

**Niu, Haoyu**, Derek Hollenbeck, Tiebiao Zhao, Dong Wang, and YangQuan Chen., “Evapotranspiration estimation with small UAVs in precision agriculture.”, *Sensors*, 20.22 (2020): 6427.

**Niu, Haoyu**, YangQuan Chen., “High spatial-resolution has little impact on NDVI mean value of UAV-based individual tree-level mapping: Evidence from 9 field tests and implications.”, *Image and Signal Processing for Remote Sensing XXVII.*, Vol. 11862. SPIE, 2021.

**Niu, Haoyu**, Dong Wang, and YangQuan Chen., “Niu, Haoyu, et al. ”Reliable tree-level evapotranspiration estimation of pomegranate trees using lysimeter and UAV multispectral imagery.”, *IEEE Conference on Technologies for Sustainability (SusTech)*, IEEE, 2021.

**Niu, Haoyu**, Dong Wang, and YangQuan Chen., “Estimating crop coefficients using linear and deep stochastic configuration networks models and UAV-based Normalized Difference Vegetation Index (NDVI).”, *International Conference on Unmanned Aircraft Systems (ICUAS)*, IEEE, 2020.

**Niu, Haoyu**, Andreas, Westphal, and YangQuan Chen., “A low-cost proximate sensing method for early detection of nematodes in walnut using Walabot and scikit-learn classification algorithms.”, *Autonomous Air and Ground Sensing Systems for Agricultural Optimization and Phenotyping V.*, Vol. 11414. International Society for Optics and Photonics, 2020.

**Niu, Haoyu**, Dong Wang, and YangQuan Chen., “Estimating actual crop evapotranspiration using deep stochastic configuration networks model and UAV-based crop coefficients in a pomegranate orchard.”, *Autonomous Air and Ground Sensing Systems for Agricultural Optimization and Phenotyping V. Vol. 11414.*, International Society for Optics and Photonics, 2020.

**Niu, Haoyu**, Yanan Wang, Tiebiao Zhao, and YangQuan Chen., “A low-cost soil moisture monitoring method by using Walabot and machine learning algorithms.”, *IFAC-PapersOnLine*, 53.2, (2020): 15784-15789.

**Niu, Haoyu**, Tiebiao Zhao, Cameron Zuber, Jacqueline Vasquez-Mendoza, David Doll, Kari Arnold, and YangQuan Chen., “A low-cost stem water potential monitoring method using proximate sensor and scikit-learn classification algorithms.”, *ASABE Annual International Virtual Meeting*, American Society of Agricultural and Biological Engineers, 2020.

Wang, Peng, Junwei Tian, **Niu, Haoyu**, YangQuan Chen., “Smart Agricultural In-Field Service Robot: From Toy to Tool.”, *International Design Engineering Technical Conferences and Computers and Information in Engineering Conference*, Vol. 59292. American Society of Mechanical Engineers, 2019.

**Niu, Haoyu**, Yuquan Chen, and YangQuan Chen., “Fractional-order extreme learning machine with Mittag-Leffler distribution.”, *International Design Engineering Technical Conferences and Computers and Information in Engineering Conference.*, Vol. 59292. American Society of Mechanical Engineers, 2019.

Wang, Yanan, Junwei Tian, **Niu, Haoyu**, Peng Wang, Xiaozhong Liao, and Yangquan Chen., “Multi-Resolution Energy Strategy for Battery Management System of Unmanned Ground Vehicles in Agriculture.”, *International Design Engineering Technical Conferences and Computers and Information in Engineering Conference.*, Vol. 59292. American Society of Mechanical Engineers, 2019.

Tian, Junwei, **Niu, Haoyu**, Peng Wang, and YangQuan Chen., “Smart and autonomous farm field scouting service robot as an edge device under \$1000: Challenges and opportunities.”, *International Design Engineering Technical Conferences and Computers and Information in Engineering Conference.*, Vol. 59292. American Society of Mechanical Engineers, 2019.

Wang, Yanan, **Niu, Haoyu**, Tiebiao Zhao, Xiaozhong Liao, Lei Dong, and YangQuan Chen., “Contactless Li-Ion battery voltage detection by using walabot and machine learning.”, *International Design Engineering Technical Conferences and Computers and Information in Engineering Conference.*, Vol. 59292. American Society of Mechanical Engineers, 2019.

**Niu, Haoyu**, Tiebiao Zhao, YangQuan Chen., “Intelligent bugs mapping and wiping (iBMW): An affordable robot-driven robot for farmers”, *IEEE International Conference on Mechatronics and Automation (ICMA)*, IEEE, 2019.

**Niu, Haoyu**, Tiebiao Zhao, Dong Wang, YangQuan Chen., “A UAV resolution and waveband aware path planning for onion irrigation treatments inference.”, *International Conference on Unmanned Aircraft Systems (ICUAS)*, IEEE, 2019.

**Niu, Haoyu**, Tiebiao Zhao, Dong Wang, YangQuan Chen., “Estimating evapotranspiration with UAVs in agriculture: A review.”, *ASABE Annual International Meeting.*, American Society of Agricultural and Biological Engineers, 2019.

Tiebiao Zhao, **Niu, Haoyu**, Dong Wang, YangQuan Chen, and Bruce J. West., “Resolution Matters: A Case Study in Onion Crop Irrigation Inference Using Unmanned Aerial Vehicles.”, *ASA, CSSA, and CSA International Annual Meeting*, ASA-CSSA-SSSA, 2018.

Tiebiao Zhao, Alexander Koumis, **Niu, Haoyu**, Dong Wang, YangQuan Chen., “Onion irrigation treatment inference using a low-cost hyperspectral scanner.”, *Multispectral, Hyperspectral, and Ultraspectral Remote Sensing Technology, Techniques and Applications VII.*, Vol. 10780. International Society for Optics and Photonics, 2018.

Tiebiao Zhao, Yonghuan Yang, **Niu, Haoyu**, Dong Wang, YangQuan Chen., “Comparing U-Net convolutional network with mask R-CNN in the performances of pomegranate tree canopy segmentation.”, *Multispectral, Hyperspectral, and Ultraspectral Remote Sensing Technology, Techniques and Applications VII.*, Vol. 10780. International Society for Optics and Photonics, 2018.

Tiebiao Zhao, **Niu, Haoyu**, Andreas Anderson, YangQuan Chen, and Joshua Viers., “A detailed study on accuracy of uncooled thermal cameras by exploring the data collection workflow.”, *Autonomous Air and Ground Sensing Systems for Agricultural Optimization and Phenotyping III.*, Vol. 10664. International Society for Optics and Photonics, 2018.

Tiebiao Zhao, **Niu, Haoyu**, Erick de la Rosa, David Doll, Dong Wang, and YangQuan Chen., “Tree canopy differentiation using instance-aware semantic segmentation.”, *2018 ASABE Annual International Meeting.*, American Society of Agricultural and Biological Engineers, 2018.

## ABSTRACT OF THE DISSERTATION

### **Smart Big Data in Precision Agricultural Applications: Acquisition, Advanced Analytics, and Plant Physiology-informed Machine Learning**

by

Haoyu Niu

Doctor of Philosophy in Electrical Engineering and Computer Science

University of California Merced, 2022

Professor YangQuan Chen, Chair

Big data acquisition platforms, such as small unmanned aerial vehicles (UAVs), unmanned ground vehicles (UGVs), and proximate sensors for precision agriculture, especially for heterogeneous crops, such as vineyards and orchards, are gaining interest from both researchers and growers. For example, lightweight sensors mounted on UAVs, such as multispectral and thermal infrared cameras, can be used to collect high-resolution images. The higher temporal and spatial resolutions of the images, relatively low operational costs, and nearly real-time image acquisition make the UAVs an ideal platform for mapping and monitoring the variability of crops over large acreage. The data acquisition platforms and analytics can create big data and demand fractional-order thinking due to the “complexity” and, thus, variability inherent in the process. Much hope is placed on machine learning (ML). How can an ML model learn from big data efficiently (optimally) and make the big data “smart” is important in agricultural research. The key to the learning process is the plant physiology and optimization method. Designing an efficient optimization method poses three questions: 1.) What is the best way to optimize? 2.) What is the more optimal way to optimize? 3.) Can we demand “more optimal machine learning,” for example, deep learning with the minimum or smallest labeled data for agriculture? Therefore, in this dissertation, the author investigated the foundations of the plant physiology-informed machine learning

(PPIML) and the principle of tail matching (POTM) framework. He elucidated their role in modeling, analyzing, designing, and managing complex systems based on the big data in precision agriculture. Plant physiology entails the complexity of growth. The complex system has both deterministic and stochastic dynamic processes with external driving processes characterized and modeled using fractional calculus-based models, which will better inform the complexity-informed machine learning (CIML) algorithms. Data acquisition platforms, such as low-cost UAVs, UGVs, and edge-AI sensors, were designed and built to demonstrate their reliability and robustness for remote and proximate sensing in agricultural applications. Research results showed that the PPIML, POTM, CIML, and the data acquisition platforms were reliable, robust, and smart tools for precision agricultural research in varying situations, such as water stress detection, early detection of nematodes, yield estimation, and evapotranspiration (ET) estimation. The application of these tools has the potential to assist stakeholders in their crop management decisions.

## Part I

# Why Big Data Is Not Smart Yet?

# Chapter 1

## Introduction

### 1.1 Motivation

The term “big data” started showing up in the early 1990s. The world’s technological per capita capacity to store information has roughly doubled every 40 months since the 1980s [1]. Since 2012, there have been 2.5 exabytes ( $2.5 \times 2^{60}$  bytes) of data generated every day [2]. According to data report predictions, there will be 163 zettabytes of data by 2025 [3]. Firican proposed ten characteristics (properties) of big data to prepare for both the challenges and advantages of big data initiatives in [4].

- **Volume:** Best known characteristic of big data; more than 90 percent of the whole data were created in the past couple of years.
- **Velocity:** The speed at which data are being generated.
- **Variety:** Processing structured, unstructured and semi structured data.
- **Variability:** Inconsistent speed of data loading, multitude of data dimensions, and number of inconsistencies.
- **Veracity:** Confidence or trust in the data.
- **Validity:** Refers to how accurate and correct the data are.

- **Vulnerability:** Security concerns, data breaches.
- **Volatility:** Design policy for data currency, availability, and rapid retrieval of information when required.
- **Visualization:** Develop new tools considering the complex relationships between the above properties.
- **Value:** The most important of the 10 Vs; substantial value must be found.

With the development of big data technologies and high-performance computing, big data creates new opportunities for farmers and researchers to quantify, analyze and better understand data intensive processes in precision agriculture. Big data can provide us information on the weather, irrigation management, pest management, fertilizer requirements, and so on. This enables farmers to make better decisions, such as what kind of crops to grow for better profitability and when to harvest.

However, big data technology also faces challenges, which has been discussed and reviewed by many researchers [5, 6, 7]. For example, Zhang *et al.* pointed out three challenges faced by agricultural big data in [5], which were big data storage, big data analysis, and big data timeliness. The data storage could affect the efficiency of data analysis, they proposed to use timeliness as a measure standard based on the characteristics of agricultural big data. In [6], Gopal *et al.* proposed that how to obtain reliable data on farm management decision making both for current conditions and under scenarios of changing bio-physical and socioeconomic conditions was also one of the greatest challenges for big data applications in agriculture. Considering the complexity of agricultural datasets, multiple data models and algorithms are also needed at different procedures of big data processing. There are many challenges for traditional methods to extract meaningful information out of the big data [7], such as what is the optimal management zone for crops, and what is the optimal zone size for soil sampling to analyze the variability? The benefit of big data for precision agricultural applications remains elusive.

Therefore, the author proposes the concept of smart big data for agricultural applications by using plant physiology-informed machine learning (PPIML), in which variability analysis plays a key role. In this dissertation, **variability** is the most important characteristic being discussed for agricultural research. Variability refers to several properties of big data. First, it refers to the number of inconsistencies in the data, which need to be understood by using anomaly- and outlier-detection methods for any meaningful analytics to be performed. Second, variability can also refer to diversity [8, 9], resulting from disparate data types and sources, for example, healthy or unhealthy [10, 11]. Finally, variability can refer to multiple research topics [12].

### 1.1.1 What Is Smart Big Data in Precision Agriculture?

Big data technology, such as Internet of Things (IoT) and wireless sensors enables researchers to solve complex agricultural problems [13]. By applying the sensors in the field, farmers can track valuable data for farm management, such as soil moisture, wind speed, air temperature, humidity and so on. The amount of the data can be huge and challenging to process timely. How to make the big data “smarter” becomes necessary. Thus, the concept of smart big data analysis is proposed in this dissertation. Smart big data in agricultural applications is an interdisciplinary research topic that is related to the extraction of meaningful information from data of plant physiology, drawing techniques from a variety of fields, such as UAV image processing, deep learning, pattern recognition, high-performance computing, and statistics. The big data can then be filtered and becomes smart big data before being analyzed for insights, which leads to more efficient decision-making. Smart big data can be defined as big data that has been cleaned, filtered, and prepared for data analysis.

Recently, researchers are gaining interest of the smart big data in precision agricultural applications [14, 15, 16]. For example, Li and Niu proposed a design for smart agriculture using the big data and IoT in [17]. They optimized the data storage, data processing, and data mining procedures generated in the agricultural production process and used the  $k$ -means algorithm to study the data mining.

Based on the experimental results, the improved  $k$ -means clustering method had an average reduction of 0.23 second in total time and an average increase of 7.67% in the  $F$  metric value. In [18], Tseng *et al.* utilized the IoT devices to monitor the environmental factors on a farm. The experimental results demonstrated that farmers could gain a better understanding if a crop was appropriate for their farm by looking into factors such as temperature and soil moisture content. In [19], a big data analytic agricultural framework was developed to identify disease based on symptoms similarity and a solution was suggested based on the high similarity. Although their framework is crop and location specific, it has great potential to expand to more crops and areas in the future.

Researchers are exploring all kinds of methods to turn the collected big data into smart big data to gain better understanding of our agricultural system. The author believes that the smart big data will be a core component of big data applications in precision agriculture, which enables the stakeholders and researchers to identify patterns, make better decisions, and adapt to new environment. Smart big data will also lay the foundation of agricultural data analysis.

### **1.1.2 Plant Physiology-informed Machine Learning: A New Frontier**

Machine Learning (ML) is the science (and art) of programming computers so they can learn from data [20]. A more engineering-oriented definition was given by Tom Mitchell in 1997, “A computer program is said to learn from experience  $E$  with respect to some task  $T$  and some performance measure  $P$ , if its performance on  $T$ , as measured by  $P$ , improves with experience  $E$  [21].” In 2006, Hinton *et al.* trained a deep neural network (DNN) to recognize handwritten digits with an accuracy of more than 98% [22]. Since then, researchers are more and more interested in Deep Learning (DL), and this enthusiasm extends to many areas of ML, such as image processing [23, 24], natural language processing [25], and even precision agriculture [26, 27, 28].

Why do we need ML? In summary, ML algorithms can usually simplify a solution and perform better than traditional methods, which may require much

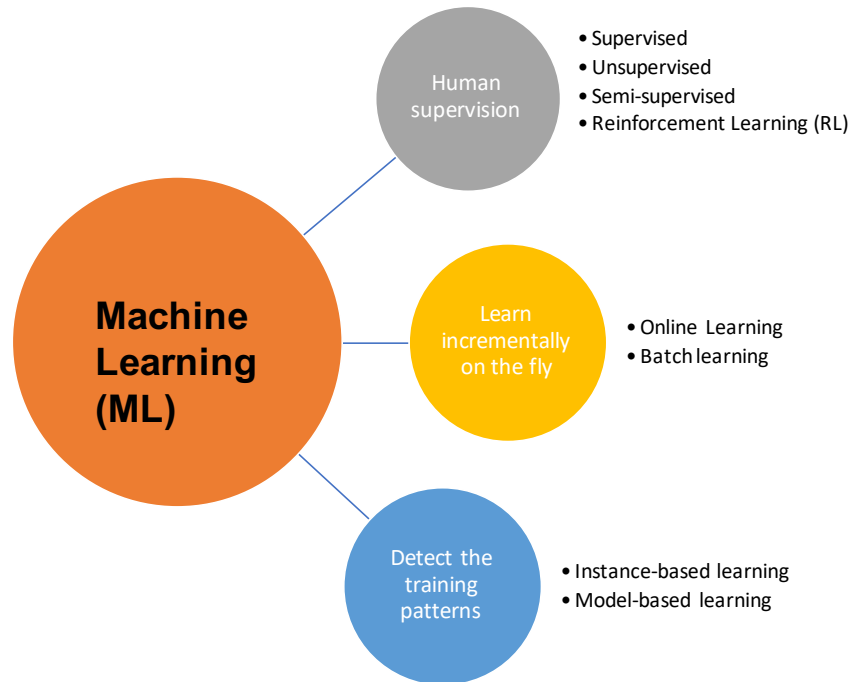


Figure 1.1: The ML can be classified as supervised, unsupervised, semi-supervised, and Reinforcement Learning (RL) based on whether or not human supervision is included. According to whether or not the ML algorithms can learn incrementally on the fly, they can be classified into online and batch learning. Based on whether or not the ML algorithms detect the training data patterns and create a predictive model, the ML can be classified into instance-based and model-based learning.

more hand-tuning rules. Furthermore, there may not exist a right solution for the complex phenomena by traditional methods. The ML techniques can help explain that kind of complexity and can adapt to new data better. The ML algorithms can obtain the variability about the complex problems and big data [12]. There are many different types and ways for ML algorithms classification (Fig. 1.1). ML can be classified as supervised, unsupervised, semi-supervised, and Reinforcement Learning (RL) based on whether human supervision is included. According to whether or not the ML algorithms can learn incrementally on the fly, they can be classified into online and batch learning. Based on whether or not the ML algorithms detect the training data patterns and create a predictive model, the ML can be classified into instance-based and model-based learning [20].

Considering the volume, diversity, and complexity of the agricultural dataset,

plant physiology-informed machine learning is proposed in this dissertation. The key of this concept is to extract meaningful agricultural information out of the big data to guide stakeholders and researchers to make better decisions for agriculture, in which the big data becomes “smart”. Instead of training the ML models directly, plant-physiology knowledge will be added into the training process, which helps explain the complexity and model performance. When complexity is under scrutiny, it is fair that we ask what it means? At what point do investigators begin identifying a system, network, or phenomenon as complex [29, 30]? It seems that a clear and unified definition of complexity is still unknown for us to answer the following questions:

1. How can we characterize complexity (More details in Chapter 2)?
2. What method should be used for the analysis of complexity in order to better understand real-world complex phenomena, such as the evapotranspiration of trees (See details in Chapter 7)?

There is agreement among a significant fraction of the scientific community that when the distribution of the data associated with the process of interest is IPL, the phenomenon is complex. In the book by West and Grigolini [31], there is a table listing a sample of the empirical power laws and IPLs uncovered in the past two centuries. For example, in scale-free networks, the degree distributions follow an IPL in connectivity [32, 33], in the processing of signals containing pink noise the power spectrum is IPL [34]. For other examples, such as the probability distribution function (PDF), the auto-correlation function (ACF) [35], allometry ( $Y = aX^b$ ) [36], anomalous relaxation (evolving over time) [37], anomalous diffusion (mean squared dissipation versus time) [38], self-similar, they can all be described by an IPL (See details in Chapter 2).

### 1.1.3 Big Data Acquisition and Advanced Analytics

Smart big data involves the use of artificial intelligence and machine learning to make big data acquisition and advanced analytics actionable, to transform big

data into insights, and to provide engagement capabilities for researchers and stakeholders. The smart big data acquisition and advanced analytics refer to the use of classification, conversion, extraction, and analysis methods to extract meaningful information from agricultural data. The acquisition and advanced analytics process generally contain the data preparation, the data analysis, and the result evaluation and explanation. Data preparation involves the agricultural data collection and integration using smart big data acquisition platforms, such as UAVs, Edge-AI sensors, and UGVs. Data analytics refers to examining the large dataset and extracting the useful information out of the raw dataset by using ML algorithms and tools, such as Pytorch, TensorFlow, and OpenCV, etc. Result evaluation and explanation involves the verification of patterns or characteristics produced by data analytics.

## 1.2 Dissertation Objectives and Methods

Considering that Smart Big Data is a new concept with great potential in precision agricultural applications, the main objective of this dissertation is developing a methodological framework for the plant physiology-informed machine learning supported by 1.) Smart big data acquisition platforms, such as UAV, Edge-AI sensors, and UGV, 2.) Advanced data analytics, such as fractional-order thinking, and artificial intelligence.

In order to accomplish the main objectives, the smart big data in precision agricultural applications will be grouped into the following specific parts:

1. Why Big Data Is Not Smart Now?
2. Smart Big Data Acquisition Platforms.
3. Advanced Big Data Analytics, Plant Physiology-informed Machine Learning, and Fractional-order Thinking.
4. Towards Smart Big Data in Precision Agriculture.

In the first part, the concept of smart big data is proposed and discussed in Chapter 1 to build the framework of smart big data applications for precision agriculture. The author discusses the importance of smart big data and investigates the correlation between the smart big data, machine learning, and fractional dynamics in Chapter 2.

In the second part, smart big data acquisition platforms are mainly discussed. A UAV platform for remote sensing data collection and a reliable image processing workflow are proposed. The challenges and opportunities for UAV image processing are also discussed in Chapter 3. In Chapter 4, the concept of IoLT is proposed and several proximate sensors are introduced. The potential of UGV platforms for agriculture is briefly discussed in Chapter 5.

For the third part, the author proposes the concept of plant physiology-informed machine learning and how to use advanced analytics and fractional-order thinking to make contributions. In Chapter 6, a non-invasive proximate sensing method for early detection of nematodes is proposed. Microwave reflectance from walnut leaves is analyzed using ML algorithms to classify the nematode infection levels in the walnut roots. In Chapter 7, reliable tree-level ET estimation methods are proposed using the UAV high-resolution imagery, ML algorithms and platforms, such as Python, MATLAB, Pytorch, and TensorFlow. In Chapter 8, individual tree-level water status inference is performed using the high-resolution UAV thermal imagery and complexity-informed machine learning. In Chapter 9, the author proposes a scale-aware pomegranate yield prediction method using UAV imagery and machine learning.

In the fourth part, the author discusses an intelligent bugs mapping and wiping robot for farmers in Chapter 10, which has great potential for pest management in the future. Then, the author proposes a non-invasive stem water potential monitoring method using proximate sensor and ML algorithms for a walnut orchard in Chapter 11 and a low-cost soil moisture monitoring method in Chapter 12. In the end, the author draws conclusive remarks and discusses the future research plan in Chapter 13.

## 1.3 Dissertation Contributions

The main contribution of the dissertation is to lay the foundation of the smart big data in precision agricultural applications. A framework is created to enable the plant physiology-informed machine learning using the smart big data acquisition platforms and advanced data analytics. Likewise, the following contributions can be obtained from this dissertation:

- A developing framework for plant physiology-informed machine learning adaptive to different kinds of trees and crops.
- A set of data acquisition platforms, advanced analytics for smart big data applications in precision agriculture.
- A non-invasive method for early detection of nematodes in walnut using Edge-AI sensors and PPIML.
- Proposed reliable tree-level ET estimation methods using UAV and remote sensing payloads.
- A concept of complexity-informed machine learning and its application for tree-level irrigation treatment inference.
- Scale-aware yield estimation method using UAV thermal image and plant physiology-informed ML algorithms.
- Proposed a UGV platform “iBMW” for pest management in agriculture.
- Investigated potential Edge-AI sensors for future agricultural research.

## 1.4 Dissertation Outlines

The dissertation is organized as follows (Fig. 1.2). In Part I, the author discusses the question “Why big data is not smart now?” and “Why do we need smart big data for precision agriculture?” (Chapter 1). The objectives, methods, and contributions of this dissertation are also listed in Chapter 1. In Chapter 2,

the author presents the correlation between the big data, machine learning, and the fractional dynamics. The author attempts to answer “Why do big data and machine learning entail the fractional dynamics?”

In Part II, the smart big data acquisition platforms are presented and their applications for precision agriculture are introduced. Chapter 3 presents the UAV platforms and the remote sensing payloads mounted on them. The UAV image acquisition workflow is described in details. Chapter 4 introduces the concept of IoLT and several Edge-AI sensors for agricultural applications. The potential of UGV platforms for agriculture is briefly discussed in Chapter 5.

In Part III, the main contribution of the author’s research work is discussed. Advanced big data analytics and fractional-order thinking are used for plant-informed machine learning. In Chapter 6, a low-cost proximate sensing method for early detection of nematodes in walnut orchard is presented. Evapotranspiration estimation with small UAVs is mainly discussed in Chapter 7. Reliable tree-level ET estimation methods are also proposed in this chapter. In Chapter 8, individual tree-level water status inference is performed using the high-resolution UAV thermal imagery and complexity-informed machine learning. In Chapter 9, the author proposes a scale-aware pomegranate yield prediction method using UAV imagery and machine learning.

In Part IV, the author discusses an intelligent bugs mapping and wiping robot for farmers in Chapter 10, which has great potential for pest management in the future. Then, the author proposes a non-invasive stem water potential monitoring method using proximate sensor and ML algorithms for a walnut orchard in Chapter 11 and a low-cost soil moisture monitoring method in Chapter 12. In the end, the author draws conclusive remarks and discusses the future research in Chapter 13.

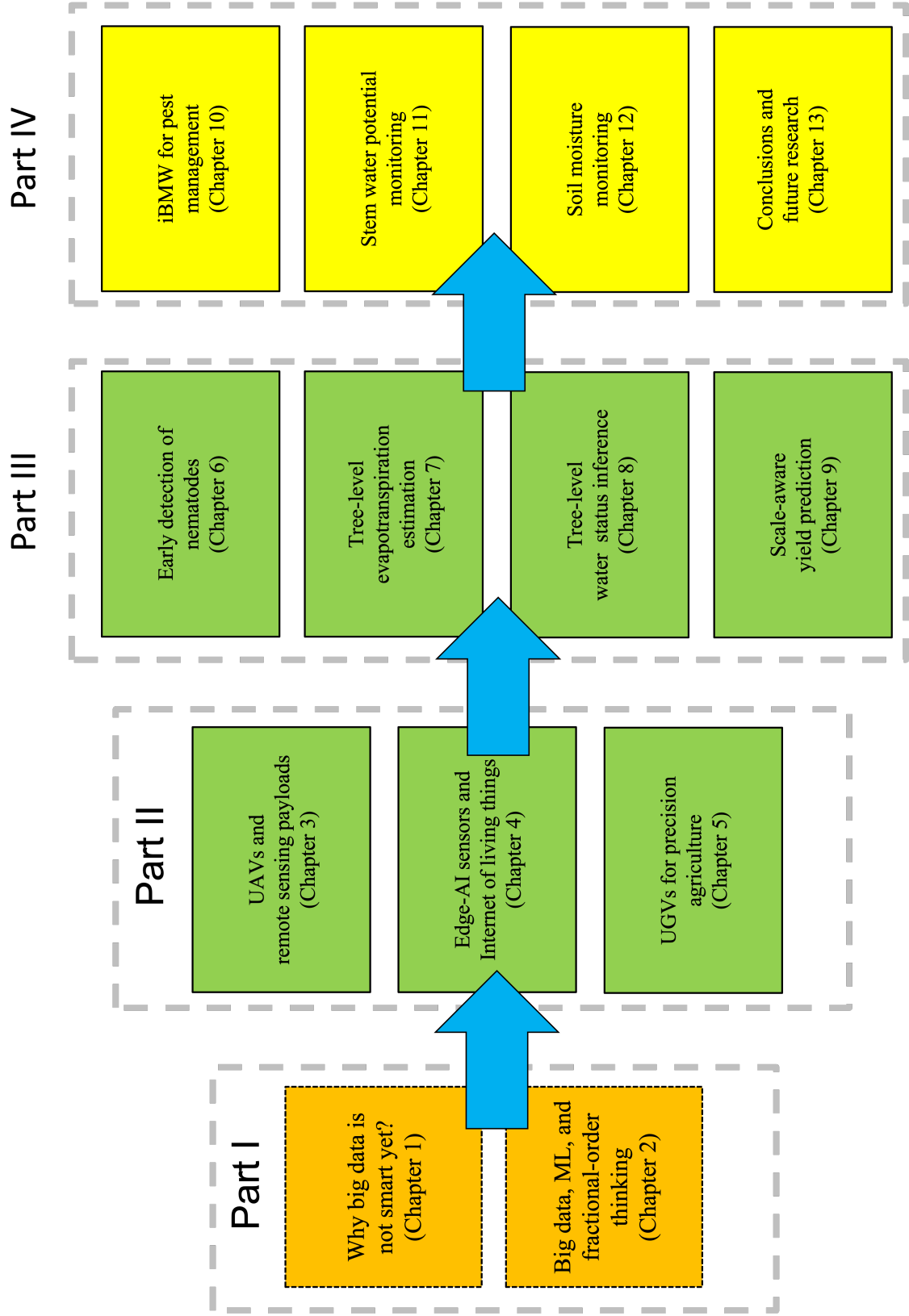


Figure 1.2: The outline of the dissertation.

## Chapter 2

# Why Do Big Data and Machine Learning Entail the Fractional Dynamics?

### 2.1 Fractional Calculus (FC) and Fractional-order Thinking (FOT)

Fractional calculus (FC) is the quantitative analysis of functions using non-integer-order integration and differentiation, where the order can be a real number, a complex number or even the function of a variable. The first recorded query regarding the meaning of a non-integer order differentiation appeared in a letter written in 1695 by Guillaume de l'Hôpital to Gottfried Wilhelm Leibniz, who at the same time as Isaac Newton, but independently of him, co-invented the infinitesimal calculus [39]. Numerous contributors have provided definitions for fractional derivatives and integrals since then [40], and the theory along with the applications of FC have been expanded greatly over the centuries [41, 42, 43]. In more recent decades, the concept of fractional dynamics has merged and gained followers in the statistical and chemical physics communities [44, 45, 46]. For example, optimal image processing has improved through the use of fractional-order differentiation and fractional-order partial differential equations as summarized in Chen *et al.*

[47, 48, 49]. Anomalous diffusion was described using fractional-diffusion equations in [50, 38], and Metzler *et al.* used fractional Langevin equations to model viscoelastic materials [51].

Recently, big data and machine learning (ML) are two of the hottest topics of applied scientific research, and they are closely related to each other. To better understand them, we also need fractional dynamics, as well as fractional-order thinking (FOT). Section 2.4 is devoted to the discussion of the relationships between big data, variability, and fractional dynamics, as well as to fractional-order data analytics (FODA) [52]. The topics touched on in this section include the Hurst parameter [53, 54], fractional Gaussian noise (fGn), fractional Brownian motion (fBm), the fractional autoregressive integrated moving average (FARIMA) [55], the formalism of continuous time random walk (CTRW) [56], unmanned aerial vehicles (UAVs) and precision agriculture (PA) [57]. In Section 2.5, how to learn efficiently (optimally) for ML algorithms is investigated. The key to developing an efficient learning process is the method of optimization. Thus, it is important to design an efficient or perhaps optimal optimization method. The derivative-free methods, and the gradient-based methods, such as the Nesterov accelerated gradient descent (NAGD) [58], are both discussed.

FOT is a way of thinking using FC. For example, there are non-integers between the integers; between logic 0 and logic 1, there is the fuzzy logic [59]; compared with integer-order splines, there are fractional-order splines [60]; between the high-order integer moments, there are non-integer-order moments, etc. FOT has been entailed by many research areas, for example, self-similar [61, 62], scale-free or scale-invariant, power-law, long-range-dependence (LRD) [63, 34], and  $1/f^\alpha$  noise [64, 65]. The terms porous media, particulate, granular, lossy, anomaly, disorder, soil, tissue, electrodes, biology [66], nano, network, transport, diffusion, and soft matters are also intimately related to FOT. However, in this section, the author mainly discusses **complexity and inverse power laws (IPL)**.

## 2.2 Complexity and Inverse Power Laws (IPLs)

When studying complexity, it is fair to ask, what does it mean to be complex? When do investigators begin identifying a system, network or phenomenon as complex [29, 30]? There is an agreement among a significant fraction of the scientific community that when the distribution of the data associated with the process of interest obeys an IPL, the phenomenon is complex; see Figure 2.1. On the left side of the figure, the complexity “bow tie” is the phenomenon of interest, thought to be a complex system [67, 68, 69, 70]. On the right side of the figure is the spectrum of system properties associated with IPL probability density functions (PDFs): the system has one or more of the properties of being scale-free, having a heavy tail, having a long-range dependence, and/or having a long memory [71, 72]. In the book by West and Grigolini [31], there is a table listing a sample of the empirical power laws and IPLs uncovered in the past two centuries. For example, in scale-free networks, the degree distributions follow an IPL in connectivity [32, 33]; in the processing of signals containing pink noise, the power spectrum follows an IPL [34]. For other examples, such as the probability density function (PDF), the autocorrelation function (ACF) [35], allometry ( $Y = aX^b$ ) [36], anomalous relaxation (evolving over time) [37], anomalous diffusion (mean squared dissipation versus time) [38], and self-similarity can all be described by the IPL “bow tie” depicted in Figure 2.1.

The power law is usually described as:

$$f(x) = ax^k, \quad (2.1)$$

when  $k$  is negative,  $f(x)$  is an IPL. One important characteristic of this power law is scale invariance [73] determined by:

$$f(cx) = a(cx)^k = c^k f(x) \propto f(x). \quad (2.2)$$

Note that when  $x$  is the time, the scaling depicts a property of the system dynamics. However, when the system is stochastic, the scaling is a property of the PDF (or correlation structure) and is a constraint on the collective properties of the system.

FC is entailed by complexity, since an observable phenomenon represented by a fractal function has integer-order derivatives that diverge. Consequently, for the

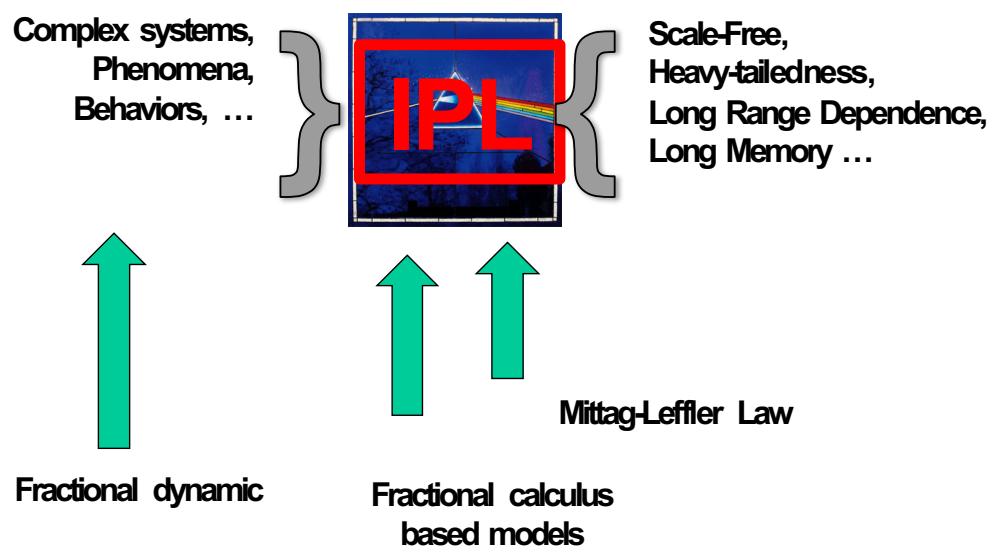


Figure 2.1: Inverse power law (complexity “bow tie”): On the left are the systems of interest that are thought to be complex. In the center panel, an aspect of the empirical data is characterized by an inverse power law (IPL). The right panel lists the potential properties associated with systems with data that have been processed and yield an IPL property. See text for more details.

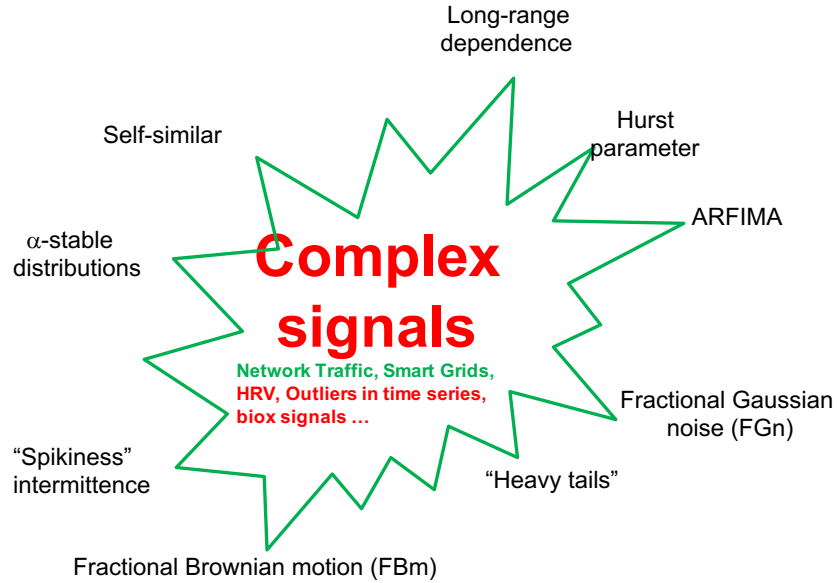


Figure 2.2: Complex signals: Here, the signal generated by a complex system is depicted. Exemplars of the systems are given as the potential properties arising from the systems' complexity.

complexity characterization and regulation, we ought to use the fractional dynamics point of view because the fractional derivative of a fractal function is finite. Thus, complex phenomena, no matter whether they are natural or carefully engineered, ought to be described by fractional dynamics. Phenomena in complex systems in many cases should be analyzed using FC-based models, where mathematically, the IPL is actually the “Mittag–Leffler law” (MLL), which asymptotically becomes an IPL (Figure 2.2), known as heavy-tail behavior.

When an IPL results from processing data, one should think about how the phenomena can be connected to the FC. In [74], Gorenflo *et al.* explained the role of the FC in generating stable PDFs by generalizing the diffusion equation to one of fractional order. For the Cauchy problem, they considered the space-fractional diffusion equation:

$$\frac{\partial u}{\partial t} = D(\alpha) \frac{\partial^\alpha u}{\partial |x|^\alpha}, \quad (2.3)$$

where  $-\infty < x < \infty$ ,  $t \geq 0$  with  $u(x, 0) = \delta(x)$ ,  $0 < \alpha \leq 2$ , and  $D(\alpha)$  is a suitable diffusion coefficient. The fractional derivative in the diffusion variable is of the Reisz–Feller form, defined by its Fourier transform to be  $|k|^\alpha$ . For the signalling

problem, they considered the so-called time-fractional diffusion equation [75]:

$$\frac{\partial^{2\beta} u}{\partial t^{2\beta}} = D(\beta) \frac{\partial^2 u}{\partial x^2}, \quad (2.4)$$

where  $x \geq 0$ ,  $t \geq 0$  with  $u(0, t) = \delta(t)$ ,  $0 < \beta < 1$ , and  $D(\beta)$  is a suitable diffusion coefficient. Equation (2.4) has also been investigated in [76, 77, 78]. Here, the Caputo fractional derivative in time is used.

There are rich forms in stochasticity [79], for example, heavytailedness, which corresponds to fractional-order master equations [80]. In Section 2.3, heavy-tailed distributions are discussed.

## 2.3 Heavy-tailed Distributions

In probability theory, heavy-tailed distributions are PDFs whose tails do not decay exponentially [81]. Consequently, they have more weight in their tails than does an exponential distribution. In many applications, it is the right tail of the distribution that is of interest, but a distribution may have a heavy left tail, or both tails may be heavy. Heavy-tailed distributions are widely used for modeling in different disciplines, such as finance [82], insurance [83], and medicine [84]. The distribution of a real-valued random variable  $X$  is said to have a heavy right tail if the tail probabilities  $P(X > x)$  decay more slowly than those of any exponential distribution:

$$\lim_{x \rightarrow \infty} \left( \frac{P(X > x)}{e^{-\lambda x}} \right) = \infty, \quad (2.5)$$

for every  $\lambda > 0$  [85]. For the heavy left tail, an analogous definition can be constructed [86]. Typically, there are three important subclasses of heavy-tailed distributions: fat-tailed, long-tailed and subexponential distributions.

### 2.3.1 The Lévy Distribution

A Lévy distribution, named after the French mathematician Paul Lévy, can be generated by a random walk whose steps have a probability of having a length determined by a heavy-tailed distribution [87]. As a fractional-order stochastic

process with heavy-tailed distributions, a Lévy distribution has better computational characteristics [88]. A Lévy distribution is stable and has a PDF that can be expressed analytically, although not always in closed form. The PDF of Lévy flight [89] is:

$$p(x, \mu, \gamma) = \begin{cases} \frac{\sqrt{\frac{\gamma}{2\pi}}}{e^{\frac{\gamma}{2(x-\mu)}(x-\mu)^{3/2}}}, & x > \mu, \\ 0, & x \leq \mu, \end{cases} \quad (2.6)$$

where  $\mu$  is the location parameter and  $\gamma$  is the scale parameter. In practice, the Lévy distribution is updated by

$$Lévy(\beta) = \frac{u}{|\nu|^{1/\beta}}, \quad (2.7)$$

where  $u$  and  $\nu$  are random numbers generated from a normal distribution with a mean of 0 and standard deviation of 1 [90]. The stability index  $\beta$  ranges from 0 to 2. Moreover, it is interesting to point out that the well-known Gaussian and Cauchy distributions are special cases of the Lévy PDF when the stability index is set to 2 and 1, respectively.

### 2.3.2 The Mittag–Leffler PDF

The Mittag–Leffler PDF for the time interval between events can be written as a mixture of exponentials with a known PDF for the exponential rates [91]:

$$E_{\theta}(-t^{\theta}) = \int_0^{\infty} \exp(-\mu t) g(\mu) d\mu, \quad (2.8)$$

with a weight for the rates given by:

$$g(\mu) = \frac{1}{\pi} \frac{\sin(\theta\pi)}{\mu^{1+\theta} + 2 \cos(\theta\pi)\mu + \mu^{1-\theta}}. \quad (2.9)$$

The most convenient expression for the random time interval was proposed by [92]:

$$\tau_{\theta} = -\gamma_t (\ln u \frac{\sin(\theta\pi)}{\tan(\theta\pi v)} - \cos(\theta\pi))^{1/\theta}, \quad (2.10)$$

where  $u, v \in (0,1)$  are independent uniform random numbers,  $\gamma_t$  is the scale parameter, and  $\tau_{\theta}$  is the Mittag–Leffler random number. In [93], Wei *et al.* used the Mittag–Leffler distribution for improving the Cuckoo Search algorithm, which showed an improved performance.

### 2.3.3 The Weibull Distribution

A random variable is described by a Weibull distribution if it has a PDF function  $F$ :

$$F(x) = e^{-(x/k)^{\lambda_w}}, \quad (2.11)$$

where  $k > 0$  is the scale parameter, and  $\lambda_w > 0$  is the shape parameter [94]. If the shape parameter is  $\lambda_w < 1$ , the Weibull distribution is determined to be heavy tailed.

### 2.3.4 The Cauchy Distribution

A random variable is described by a Cauchy PDF if its cumulative distribution is [95, 96]:

$$F(x) = \frac{1}{\pi} \arctan\left(\frac{2(x - \mu_c)}{\sigma}\right) + \frac{1}{2}, \quad (2.12)$$

where  $\mu_c$  is the location parameter and  $\sigma$  is the scale parameter. Cauchy distributions are examples of fat-tailed distributions, which have been empirically encountered in a variety of areas including physics, earth sciences, economics and political science [97]. Fat-tailed distributions include those whose tails decay like an IPL, which is a common point of reference in their use in the scientific literature [98]:

### 2.3.5 The Pareto Distribution

A random variable is said to be described by a Pareto PDF if its cumulative distribution function is

$$F(x) = \begin{cases} 1 - \left(\frac{b}{x}\right)^a, & x \geq b, \\ 0, & x < b, \end{cases} \quad (2.13)$$

where  $b > 0$  is the scale parameter and  $a > 0$  is the shape parameter (Pareto's index of inequality) [99].

### 2.3.6 The $\alpha$ -stable Distribution

A PDF is said to be stable if a linear combination of two independent random variables, each with the same distribution, has the same distribution for the conjoined variable. This PDF is also called the Lévy  $\alpha$ -stable distribution [100, 101]. Since the normal distribution, Cauchy distribution and Lévy distribution all have the above property, one can consider them to be special cases of stable distributions. Stable distributions have  $0 < \alpha \leq 2$ , with the upper bound corresponding to the normal distribution, and  $\alpha = 1$ , to the Cauchy distribution. The PDFs have undefined variances for  $\alpha < 2$ , and undefined means for  $\alpha \leq 1$ . Although their PDFs do not admit a closed-form formula in general, except in special cases, they decay with an IPL tail called the IPL index, which determines the behavior of the PDF. As the IPL index gets smaller, the PDF acquires a heavier tail.

### 2.3.7 Mixture Distributions

A mixture distribution is derived from a collection of other random variables. First, a random variable is selected by chance from the collection according to given probabilities of selection. Then, the value of the selected random variable is realized. The mixture PDFs are complicated in terms of simpler PDFs, which provide a good model for certain datasets. The different subsets of the data can exhibit different characteristics. Therefore, the mixed PDFs can effectively characterize the complex PDFs of certain real-world datasets. In [102], a robust stochastic configuration network (SCN) based on a mixture of Gaussian and Laplace PDFs was proposed. Thus, Gaussian and Laplace distributions are mentioned in this section for comparison purposes.

#### The Gaussian Distribution

A random variable  $X$  has a Gaussian distribution with the mean  $\mu_G$  and variance  $\sigma_G^2$  ( $-\infty < \mu_G < \infty$  and  $\sigma_G > 0$ ) if  $X$  has a continuous distribution for which the PDF is as follows [103]:

$$f(x|\mu_G, \sigma_G^2) = \frac{1}{(2\pi)^{1/2}\sigma_G} e^{-\frac{1}{2}\left(\frac{x-\mu_G}{\sigma_G}\right)^2}, \text{ for } -\infty < x < \infty. \quad (2.14)$$

## The Laplace Distribution

The PDF of the Laplace distribution can be written as follows [102]:

$$F(x|\mu_l, \eta) = \frac{1}{(2\eta^2)^{1/2}} e^{(-\frac{\sqrt{2}|x-\mu_l|}{\eta})}, \quad (2.15)$$

where  $\mu_l$  and  $\eta$  represent the location and scale parameters, respectively.

## 2.4 Big Data, Variability and FC

In Chapter 1, the author discussed the 10 characteristics (properties) of big data to prepare for both the challenges and advantages of big data initiatives (Table 2.1). In this chapter, variability is the most important characteristic being discussed. Variability can refer to multiple research topics (Table 2.2) [4].

Considering variability, Xunzi (312 BC–230 BC), who was a Confucian philosopher, made a useful observation: “Throughout a thousand acts and ten thousand changes, his way remains one and the same [104].” Therefore, we ask: what is the “one and the same” for big data? This is the **variability**, which refers to the behavior of the dynamic system. The ancient Greek philosopher Heraclitus (535 BC–475 BC) also realized the importance of variability, prompting him to say: “The only thing that is constant is change”; “It is in changing that we find purpose”; “Nothing endures but change”; “No man ever steps in the same river twice, for it is not the same river and he is not the same man.”

Heraclitus actually recognized the (fractional-order) dynamics of the river without modern scientific knowledge (in nature). After two thousand years, the integer-order calculus was invented by Sir Issac Newton and Gottfried Wilhelm Leibniz, whose main purpose was to quantify that change [105, 106]. From then, scientists started using integer-order calculus to depict dynamic systems, differential equations, modelling, etc. In the 1950s, Scott Blair, who first introduced the FC into rheology, pointed out that the integer-order dynamic view of change is only for our own “convenience” (a little bit selfish). In other words, denying fractional calculus is equivalent to denying the existence of non-integers between the integers!

Blair said: “We may express our concepts in Newtonian terms if we find this

Table 2.1: The 10 Vs of big data.

Characteristics	Description
1. Volume	Best known characteristic of big data; more than 90 percent of the whole data were created in the past couple of years.
2. Velocity	The speed at which data are being generated.
3. Variety	Processing structured, unstructured and semistructured data.
<b>4. Variability</b>	Inconsistent speed of data loading, multitude of data dimensions, and number of inconsistencies.
5. Veracity	Confidence or trust in the data.
6. Validity	Refers to how accurate and correct the data are.
7. Vulnerability	Security concerns, data breaches.
8. Volatility	Design policy for data currency, availability, and rapid retrieval of information when required.
9. Visualization	Develop new tools considering the complex relationships between the above properties.
10. Value	The most important of the 10 Vs; substantial value must be found.

Table 2.2: Variability in multiple research topics.

Topics	Description
1. Climate variability	Changes in the components of the climate system and their interactions.
2. Genetic variability	Measurements of the tendencies of individual genotypes between regions.
3. Heart rate variability	Physiological phenomenon where the time interval between heart beats varies.
4. Human variability	Measurements of the characteristics, physical or mental, of human beings.
5. Spatial variability	Measurements at different spatial points exhibit different values.
6. Statistical variability	A measure of dispersion in statistics.

convenient but, if we do so, we must realize that we have made a translation into a language which is foreign to the system which we are studying (1950) [107].”

Therefore, variability exists in big data. However, how do we realize the modeling, analysis and design (MAD) for the variability in big data within complex systems? We need fractional calculus! In other words, big data are at the nexus of complexity and FC. Metrics based on using the fractional-order signal processing techniques should be used for quantifying the generating dynamics of observed or perceived variability [52].

### 2.4.1 The Hurst Parameter, fGn, and fBm

The Hurst parameter or Hurst exponent ( $H$ ) was proposed for the analysis of the long-term memory of time series. It was originally developed to quantify the long-term storage capacity of reservoirs for the Nile river’s volatile rain and drought conditions more than a half century ago [53, 54]. To date, the Hurst parameter has also been used to measure the intensity of long range dependence (LRD) in time series [108], which requires accurate modeling and forecasting. The self-similarity and the estimation of the statistical parameters of LRD have commonly been investigated recently [109]. The Hurst parameter has also been used for characterizing the LRD process [108, 110]. A LRD time series is defined as a stationary process that has long-range correlations if its covariance function  $C(n)$  decays slowly as:

$$\lim_{n \rightarrow \infty} \frac{C(n)}{n^{-\alpha}} = c, \quad (2.16)$$

where  $0 < \alpha < 1$ , which relates to the Hurst parameter according to  $\alpha = 2 - 2H$  [111, 112]. The parameter  $c$  is a finite, positive constant. When the value of  $n$  is large,  $C(n)$  behaves as the IPL  $c/n^\alpha$  [113]. Another definition for an LRD process is that the weakly stationary time-series  $X(t)$  is said to be LRD if its power spectral density (PSD) follows:

$$f(\lambda) \sim C_f |\lambda|^{-\beta}, \quad (2.17)$$

as  $\lambda \rightarrow 0$ , for a given  $C_f > 0$  and a given real parameter  $\beta \in (0,1)$ , which corresponds to  $H = (1 + \beta)/2$  [114]. When  $0 < H < 0.5$ , it indicates that the

time intervals constitute a negatively correlated process. When  $0.5 < H < 1$ , it indicates that time intervals constitute a positively correlated process. When  $H = 0.5$ , it indicates that the process is uncorrelated.

Two of the most common LRD processes are fBm [115] and fGn [116]. The fBm process with  $H(0 < H < 1)$  is defined as:

$$B_H(t) = \frac{1}{\Gamma(H + 1/2)} \left\{ \int_{-\infty}^0 [(t-s)^{H-1/2} - (-s)^{H-1/2}] dW(s) + \int_0^t (t-s)^{H-1/2} dW(s) \right\}, \quad (2.18)$$

where  $W$  denotes a Wiener process defined on  $(-\infty, \infty)$  [117]. The fGn process is the increment sequences of the fBm process, defined as:

$$X_k = Y(k+1) - Y(k), \quad (2.19)$$

where  $Y(k)$  is a fBm process [118].

## 2.4.2 Fractional Lower-order Moments (FLOMs)

The FLOM is based on  $\alpha$ -stable PDFs. The PDFs of an  $\alpha$ -stable distribution decay in the tails more slowly than a Gaussian PDF does. Therefore, for sharp spikes or occasional bursts in signals, an  $\alpha$ -stable PDF can be used for characterizing signals more frequently than Gauss-distributed signals [119]. Thus, the FLOM plays an important role in impulsive processes [120], equivalent to the role played by the mean and variance in a Gaussian process. When  $0 < \alpha \leq 1$ , the  $\alpha$ -stable processes have no finite first- or higher-order moments; when  $1 < \alpha < 2$ , the  $\alpha$ -stable processes have a first-order moment and all the FLOMs with moments of fractional order that is less than 1. The correlation between the FC and FLOM was investigated in [121, 122]. For the Fourier-transform pair  $p(x)$  and  $\phi(\mu)$ , the latter is the characteristic function and is the Fourier transform of the PDF; a complex FLOM can have complex fractional lower orders [121, 122]. A FLOM-based fractional power spectrum includes a covariation spectrum and a fractional low-order covariance spectrum [123]. FLOM-based fractional power spectrum techniques have been successfully used in time-delay estimation [123].

### 2.4.3 Fractional Autoregressive Integrated Moving Average (FARIMA) and Gegenbauer Autoregressive Moving Average (GARMA)

A continuous-time linear time-invariant (LTI) system can be characterized using a linear difference equation, which is known as an autoregression and moving average (ARMA) model [124, 125]. The process  $X_t$  of ARMA( $p, q$ ) is defined as:

$$\Phi(B)X_t = \Theta(B)\epsilon_t, \quad (2.20)$$

where  $\epsilon_t$  is white Gaussian noise (wGn), and  $B$  is the backshift operator. However, the ARMA model can only describe a short-range dependence (SRD) property. Therefore, based on the Hurst parameter analysis, more suitable models, such as FARIMA [126, 127] and fractional integral generalized autoregressive conditional heteroscedasticity (FIGARCH) [128], were designed to more accurately analyze the LRD processes. The most important feature of these models is the long memory characteristic. The FARIMA and FIGARCH can capture both the short- and the long-memory nature of time series. For example, the FARIMA process  $X_t$  is usually defined as [129]:

$$\Phi(B)(1 - B)^d X_t = \Theta(B)\epsilon_t, \quad (2.21)$$

where  $d \in (-0.5, 0.5)$ , and  $(1 - B)^d$  is a fractional-order difference operator. The locally stationary long-memory FARIMA model has the same equation as that of Equation (2.21), except that  $d$  becomes  $d_t$ , which is a time-varying parameter [130]. The locally stationary long-memory FARIMA model captures the local self-similarity of the system.

The generalized locally stationary long-memory process FARIMA model was investigated in [130]. For example, a generalized FARIMA model, which is called the Gegenbauer autoregressive moving average (GARMA), was introduced in [131]. The GARMA model is defined as:

$$\Phi(B)(1 - 2uB + B^2)^d X_t = \Theta(B)\epsilon_t, \quad (2.22)$$

where  $u \in [-1, 1]$ , which is a parameter that can control the frequency at which the long memory occurs. The parameter  $d$  controls the rate of decay of the autocovariance function. The GARMA model can also be extended to the so-called “ $k$ -factor GARMA model,” which allows for long-memory behaviors to be associated with each of  $k$  frequencies (Gegenbauer frequencies) in the interval  $[0, 0.5]$  [132].

#### 2.4.4 Continuous Time Random Walk (CTRW)

The CTRW model was proposed by Montroll and Weiss as a generalization of diffusion process to describe the phenomenon of anomalous diffusion [56]. The basic idea is to calculate the PDF for the diffusion process by replacing the discrete steps with continuous time, along with a PDF for step lengths and a waiting-time PDF for the time intervals between steps. Montroll and Weiss applied random intervals between the successive steps in the walking process to account for local structure in the environment, such as traps [133]. The CTRW has been used for modeling multiple complex phenomena, such as chaotic dynamic networks [134]. The correlation between CTRW and diffusion equations with fractional time derivatives has also been established [135]. Meanwhile, time-space fractional diffusion equations can be treated as CTRWs with continuously distributed jumps or continuum approximations of CTRWs on lattices [136].

#### 2.4.5 Unmanned Aerial Vehicles (UAVs) and Precision Agriculture

As a new remote-sensing platform, researchers are gaining interest in the potential of small UAVs for precision agriculture [137, 138, 139, 140, 141, 142, 27, 28, 143, 144, 145], especially for heterogeneous crops, such as vineyards and orchards [146, 26]. Mounted on UAVs, lightweight sensors, such as RGB cameras, multispectral cameras and thermal infrared cameras, can be used to collect high-resolution images. The higher temporal and spatial resolutions of the images, relatively low operational costs, and nearly real-time image acquisition make the UAV an ideal platform for mapping and monitoring the variability of crops and



Figure 2.3: Normalized difference vegetation index (NDVI) mapping of pomegranate trees.

trees. UAVs can create big data and demand the FODA due to the “complexity” and, thus, variability inherent in the life process. For example, Figure 2.3 shows the normalized difference vegetation index (NDVI) mapping of a pomegranate orchard at the USDA-ARS experimental field (More details in Chapter 7). Under different irrigation levels, the individual trees can show strong variability during the analysis of water stress. Life is complex! Thus, it entails variability, which as discussed above, in turn, entails fractional dynamics. UAVs can then become “Tractor 2.0” for farmers in precision agriculture.

## 2.5 Optimal Machine Learning and Optimal Randomness

Most ML algorithms perform training by solving optimization problems that rely on first-order derivatives (*Jacobians*), which decide whether to increase or decrease weights. For huge speed boosts, faster optimizers are being used instead of the regular gradient descent optimizer. For example, the most popular boosters are

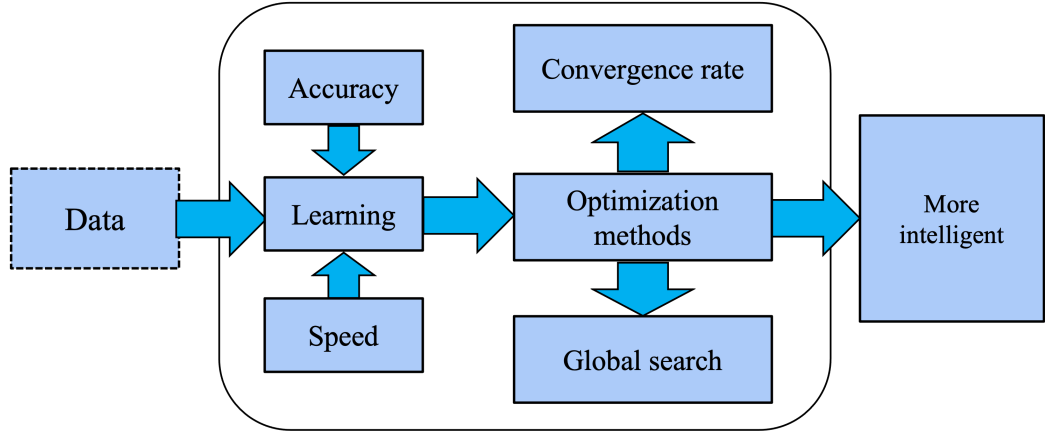


Figure 2.4: Data analysis in nature.

momentum optimization [147], Nesterov accelerated gradient [58], AdaGrad [148], RMSProp [149], and Adam optimization [150]. The second-order (*Hessian*) optimization methods usually find the solutions with faster rates of convergence but with higher computational costs. Therefore, the answer to the following question is important: 1.) What is a more optimal ML algorithm? 2.) What if the derivative is fractional order instead of integer order? In this section, we discuss some applications of fractional-order gradients to optimization methods in ML algorithms and investigate the accuracy and convergence rates.

As mentioned in the big data section, there is a huge amount of data in human society and nature. During the learning process of ML, we care not only about the speed, but also the accuracy of the data the machine is learning (Figure 2.4). The learning algorithm is important; otherwise, the data labeling and other labor costs will exhaust people beyond their abilities. When applying the artificial intelligence (AI) to an algorithm, a strong emphasis is on artificial, only followed weakly by intelligence. Therefore, the key to ML is what optimization methods are being applied. The convergence rate and global searching are two important parts of the optimization method.

**Reflection:** The ML is a hot research topic and will probably remain so into the near future. How a machine can learn efficiently (optimally) is always important. The key for the learning process is the optimization method. Thus, in de-

signing an efficient optimization method, it is necessary to answer the following three questions:

- What is the optimal way to optimize?
- What is the **more optimal** way to optimize?
- Can we demand “**more optimal machine learning,**” for example, deep learning with the minimum/smallest labeled data?

**Optimal randomness:** In the section of the Lévy PDF, the Lévy flight is the search strategy for food that the albatross has developed over millions of years of evolution. Admittedly, this is a slow optimization procedure [151]. From this perspective, we should call “Lévy distribution” an optimized or learned randomness used by albatrosses for food search. Therefore, we pose the question: “Can the search strategy be more optimal than Lévy flight?” The answer is yes if one adopts the FC [152]! Optimization is a very complex area of study. However, few studies have investigated using FC to obtain a better optimization strategy.

### 2.5.1 Derivative-free Methods

For derivative-free methods, there are single agent search and swarm-based search methods (Figure 2.5). Exploration is often achieved by randomness or random numbers in terms of some predefined PDFs. Exploitation uses local information such as gradients to search local regions more intensively, and such intensification can enhance the rate of convergence. Thus, a question was posed: what is the optimal randomness? Wei *et al.* investigated the optimal randomness in a swarm-based search [153]. Four heavy-tailed PDFs have been used for sample path analysis (Figure 2.6). Based on the experimental results, the randomness-enhanced cuckoo search (CS) algorithms [154, 93, 155] can identify the unknown specific parameters of a fractional-order system with better effectiveness and robustness. The randomness-enhanced CS algorithms can be considered as a promising tool for solving real-world complex optimization problems. The reason is that optimal randomness is applied with fractional-order noise during the exploration,

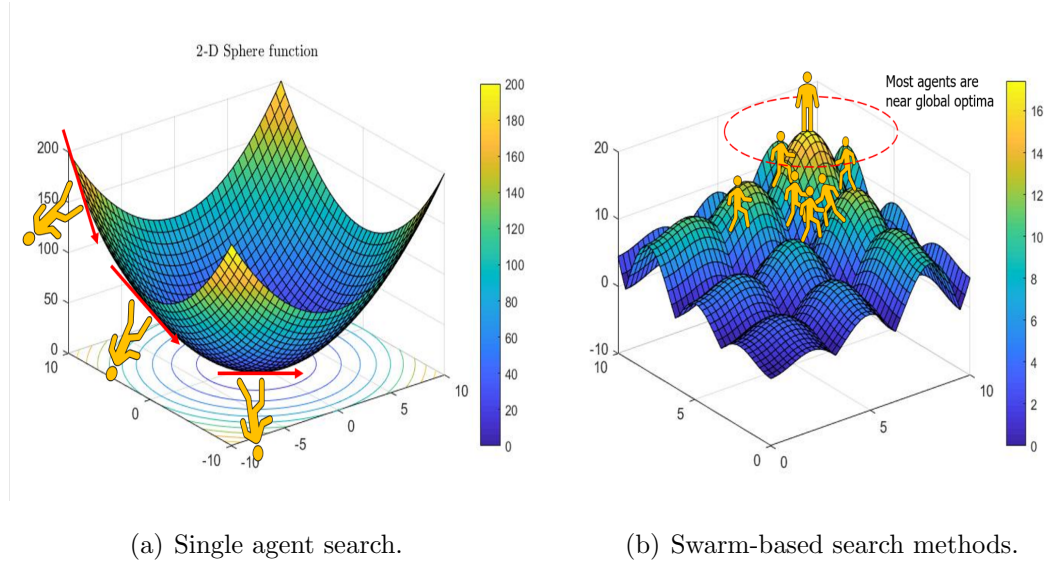
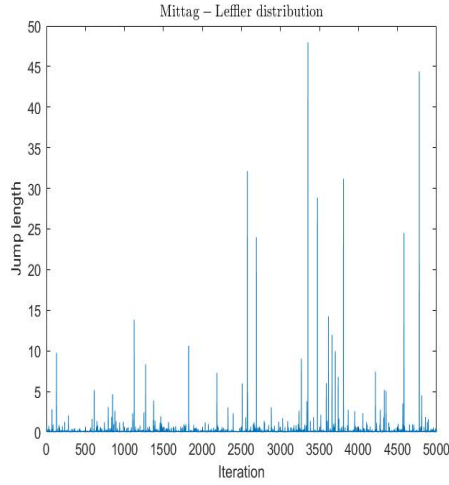


Figure 2.5: The 2-D Alpine function for derivative-free methods.

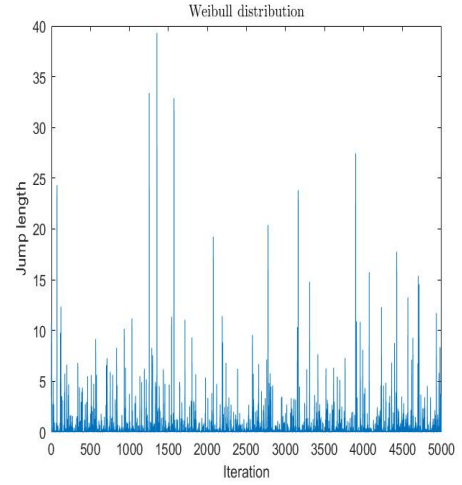
which is more optimal than the “optimized PSO”, CS. The fractional-order noise refers to the stable PDFs [74]. In other words, when we are discussing optimal randomness, we are discussing fractional calculus!

## 2.5.2 Gradient-based Methods

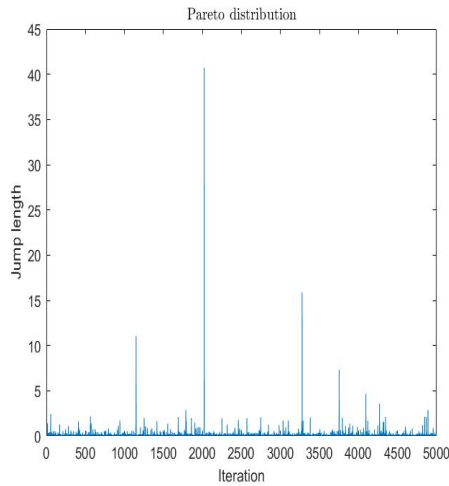
The gradient descent (GD) is a very common optimization algorithm, which can find the optimal solutions by iteratively tweaking parameters to minimize the cost function. The stochastic gradient descent (SGD) randomly selects times during the training process. Therefore, the cost function bounces up and down, decreasing on average, which is good for escape from local optima. Sometimes, noise is added into the GD method, and usually, such noise follows a Gaussian PDF in the literature. We ask, “Why not heavy-tailed PDFs”? The answer to this question can lead to interesting future research.



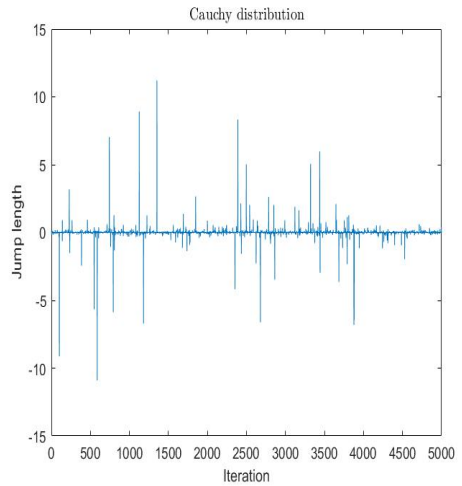
(a) Mittag-Leffler distribution.



(b) Weibull distribution.



(c) Pareto distribution.



(d) Cauchy distribution.

Figure 2.6: Sample paths analysis. Wei *et al.* investigated the optimal randomness in a swarm-based search. Four heavy-tailed PDFs were used for sample path analysis. The long steps, referring to the jump length, frequently happened for all distributions, which showed strong heavy-tailed performance.

### The Nesterov Accelerated Gradient Descent (NAGD)

There are many variants of GD analysis as suggested in Figure 2.7. One of the most popular methods is the NAGD [58]:

$$\begin{cases} y_{k+1} = ay_k - \mu \nabla f(x_k), \\ x_{k+1} = x_k + y_{k+1} + by_k, \end{cases} \quad (2.23)$$

where by setting  $b = -a/(1+a)$ , one can derive the NAGD. When  $b = 0$ , one can derive the momentum GD. The NAGD can also be formulated as:

$$\begin{cases} x_k = y_{k-1} - \mu \nabla f(y_{k-1}), \\ y_k = x_k + \frac{k-1}{k+2}(x_k - x_{k-1}). \end{cases} \quad (2.24)$$

Set  $t = k\sqrt{\mu}$ , and one can, in the continuous limit, derive the corresponding differential equation:

$$\ddot{X} + \frac{3}{t}\dot{X} + \nabla f(X) = 0. \quad (2.25)$$

The main idea of Jordan's work is to analyze the iteration algorithm in the continuous-time domain [156]. For differential equations, one can use the Lyapunov or variational method to analyze the properties; for example, the convergence rate is  $O(\frac{1}{t^2})$ . One can also use the variational method to derive the master differential equation for an optimization method, such as the least action principle [157], Hamilton's variational principle [158] and the quantum-mechanical path integral approach [159]. Wilson *et al.* built a Euler-Lagrange function to derive the following equation [156]:

$$\ddot{X}_t + 2\gamma\dot{X}_t + \frac{\gamma^2}{\mu}\nabla f(X_t) = 0. \quad (2.26)$$

which is in the same form as the master differential equation of NAGD.

Jordan's work revealed that one can transform an iterative (optimization) algorithm to its continuous-time limit case, which can simplify the analysis (Lyapunov methods). One can directly design a differential equation of motion (EOM) and then discretize it to derive an iterative algorithm (variational method). The key is to find a suitable Lyapunov functional to analyze the stability and convergent rate. The new exciting fact established by Jordan is that optimization algorithms

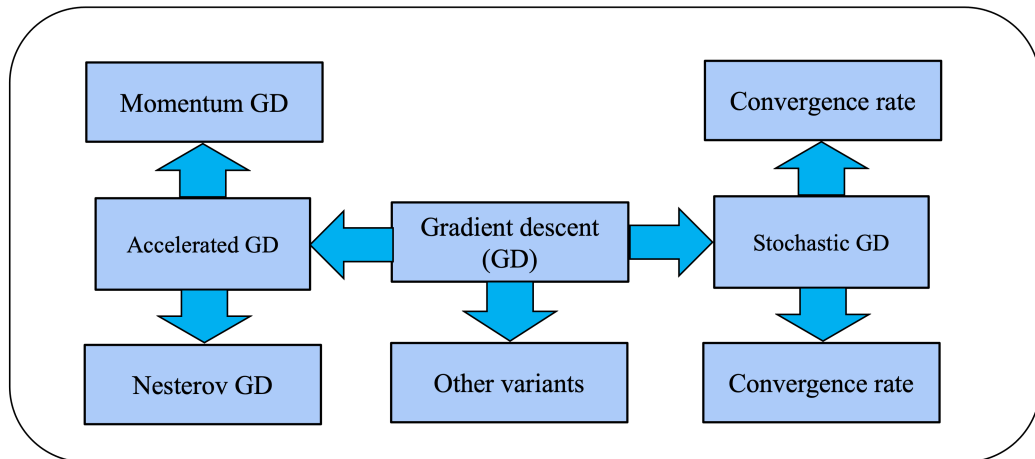


Figure 2.7: Gradient descent and its variants.

can be systematically synthesized using Lagrangian mechanics (Euler–Lagrange) through EOMs.

Thus, is there an optimal way to optimize using optimization algorithms stemming from Equation (2.26)? Obviously, why not an equation such as Equation (2.26) of fractional order? Considering the  $\dot{X}_t$  as  $X_t^{(\alpha)}$ , it will provide us with more research possibilities, such as the fractional-order calculus of variation (FOCV) and fractional-order Euler–Lagrange (FOEL) equation. For the SGD, optimal randomness using the fractional-order noises can also offer better than the best performance, similarly shown by Wei *et al.* [153].

## 2.6 What Can the Control Community Offer to ML?

In the IFAC 2020 World Congress Pre-conference Workshop, Eric Kerrigan proposed “The Three Musketeers” that the control community could contribute to ML [160]. These three were the internal model principle (IMP) [161], the Nu-Gap metric [162] and model discrimination [163]. Herein, we focused on the IMP. Kashima *et al.* transferred the convergence problem of numerical algorithms into a stability problem of a discrete-time system [164]. An *et al.* explained that the

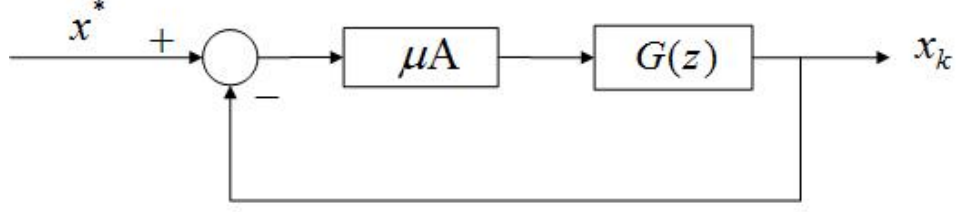


Figure 2.8: The integrator model (embedded in  $G(z)$ ). The integrator in the forward loop eliminates the tracking steady-state error for a constant reference signal (internal model principle (IMP)).

commonly used SGD-momentum algorithm in ML was a PI controller and designed a PID algorithm [165]. Motivated by [165] but differently from M. Jordan’s work, we proposed designing and analyzing the algorithms in the  $S$  or  $Z$  domain. Remember that GD is a first-order algorithm:

$$x_{k+1} = x_k - \mu \nabla f(x_k), \quad (2.27)$$

where  $\mu > 0$  is the step size (or learning rate). Using the  $Z$  transform, one can achieve:

$$X(z) = \frac{\mu}{z-1} [-\nabla f(x_k)]_z. \quad (2.28)$$

Approximate the gradient around the extreme point  $x^*$ , and one can obtain:

$$\nabla f(x_k) \approx A(x_k - x^*), \text{ with } A = \nabla^2 f(x^*). \quad (2.29)$$

For the plain GD in Figure 2.8, we have  $G(z) = 1/(z-1)$ , which is an integrator. For fractional-order GD (FOGD), the updating term of  $x_k$  in Equation (2.27) can be treated as a filtered gradient signal. In [166], Fan *et al.* shared similar thoughts: “Accelerating the convergence of the moment method for the Boltzmann equation using filters”. The integrator in the forward loop eliminates the tracking error for a constant reference signal according to the IMP. Similarly, the GD momentum (GDM) designed to accelerate the conventional GD, which is popularly used in ML, can be analyzed using Figure 2.8 by:

$$\begin{cases} y_{k+1} = \alpha y_k - \mu \nabla f(x_k), \\ x_{k+1} = x_k + y_{k+1}, \end{cases} \quad (2.30)$$

where  $y_k$  is the accumulation of the history gradient and  $\alpha \in (0, 1)$  is the rate of the moving average decay. Using the Z transform for the update rule, one can derive:

$$\begin{cases} zY(z) = \alpha Y(z) - \mu[\nabla f(x_k)]_z, \\ zX(z) = X(z) + zY(z). \end{cases} \quad (2.31)$$

Then, after some algebra, one obtains the following equation:

$$X(z) = \frac{\mu z}{(z-1)(z-\alpha)}[-\nabla f(x_k)]_z. \quad (2.32)$$

For the GD momentum, we have  $G(z) = \frac{z}{(z-1)(z-\alpha)}$  in Figure 2.8, with an integrator in the forward loop. The GD momentum is a second-order ( $G(z)$ ) algorithm with an additional pole at  $z = \alpha$  and one zero at  $z = 0$ . The “second-order” refers to the order of  $G(z)$ , which makes it different from the algorithm using the *Hessian* matrix information. Moreover, NAGD can be simplified as:

$$\begin{cases} y_{k+1} = x_k - \mu \nabla f(x_k), \\ x_{k+1} = (1 - \lambda)y_{k+1} + \lambda y_k, \end{cases} \quad (2.33)$$

where  $\mu$  is the step size and  $\lambda$  is a weighting coefficient. Using the Z transform for the update rule, one can derive:

$$\begin{cases} zY(z) = X(z) - \mu[\nabla f(x_k)]_z, \\ zX(z) = (1 - \lambda)zY(z) + \lambda Y(z). \end{cases} \quad (2.34)$$

Different from the GD momentum, and after some algebra, one obtains:

$$X(z) = \frac{-(1 - \lambda)z - \lambda}{(z-1)(z+\lambda)} \mu[\nabla f(x_k)]_z = \frac{z + \frac{\lambda}{1-\lambda}}{(z-1)(z+\lambda)} \mu(1 - \lambda)[- \nabla f(x_k)]_z. \quad (2.35)$$

For NAGD, we have  $G(z) = \frac{z + \frac{\lambda}{1-\lambda}}{(z-1)(z+\lambda)}$ , again, with an integrator in the forward loop (Figure 2.8). NAGD is a second-order algorithm with an additional pole at  $z = -\lambda$  and a zero at  $z = \frac{-\lambda}{1-\lambda}$ .

“Can  $G(z)$  be of higher order or fractional order”? Of course it can! As shown in Figure 2.8, a necessary condition for the stability of an algorithm is that all the poles of the closed-loop system are within the unit disc. If the Lipschitz continuous

Table 2.3: General second-order algorithm design. The parameter  $\rho$  is the loop forward gain; see text for more details.

$\rho$	0.4	0.8	1.2	1.6	2.0	2.4
a	-0.6	-0.2	0.2	0.6	1	1.4
b	1.5	0.25	-0.1667	-0.3750	-0.5	-0.5833

gradient constant  $L$  is given, one can replace  $A$  with  $L$ , and then, the condition is sufficient. For each  $G(z)$ , there is a corresponding iterative optimization algorithm.  $G(z)$  can be a third- or higher-order system. Apparently,  $G(z)$  can also be a fractional-order system. Considering a general second-order discrete system:

$$G(z) = \frac{z + b}{(z - 1)(z - a)}, \quad (2.36)$$

the corresponding iterative algorithm is Equation (2.23). As mentioned earlier, when setting  $b = -a/(1 + a)$ , one can derive the NAGD. When  $b = 0$ , one can derive the momentum GD. The iterative algorithm can be viewed as a state-space realization of the corresponding system. Thus, it may have many different realizations (all are equivalent). Since two parameters  $a$  and  $b$  are introduced for a general second-order algorithm design, we use the integral squared error (ISE) as the criterion to optimize the parameters. This is because for different target functions  $f(x)$ , the Lipschitz continuous gradient constant is different. Thus, the loop forward gain is defined as  $\rho := \mu A$ .

According to the experimental results (Table 2.3), interestingly, it is found that the optimal  $a$  and  $b$  satisfy  $b = -a/(1 + a)$ , which is the same design as NAGD. Other criteria such as the IAE and ITAE were used to find other optimal parameters, but the results are the same as for the ISE. Differently from for NAGD, the parameters were determined by search optimization rather than by mathematical design, which can be extended to more general cases. The algorithms were then tested using the MNIST dataset (Figure 2.9). It is obvious that for different zeros and poles, the performance of the algorithms is different. One finds that both the  $b = -0.25$  and  $b = -0.5$  cases perform better than does the SGD momentum. Additionally, both  $b = 0.25$  and  $b = 0.5$  perform worse. It is also shown that an additional zero can improve the performance, if adjusted properly. It is interesting

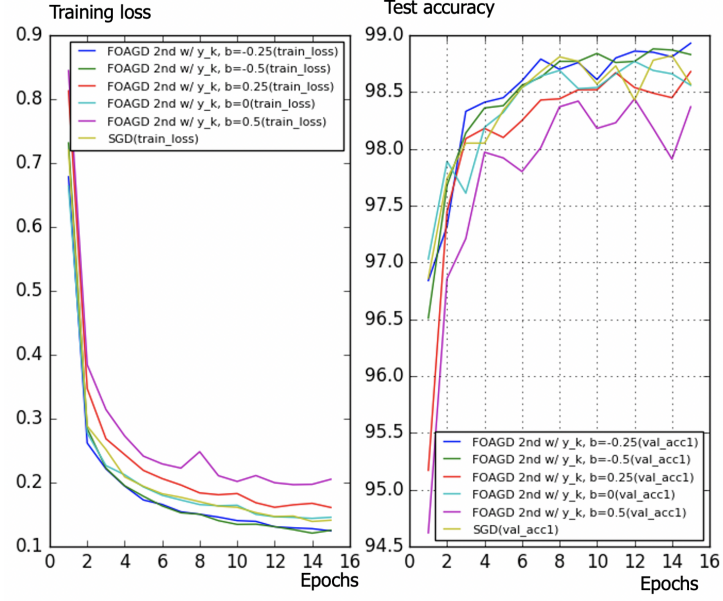


Figure 2.9: Training loss (**left**); test accuracy (**right**). It is obvious that for different zeros and poles, the performance of the algorithms is different. One finds that both the  $b = -0.25$  and  $b = -0.5$  cases perform better than does the stochastic gradient descent (SGD) momentum. Additionally, both  $b = 0.25$  and  $b = 0.5$  perform worse. It is also shown that an additional zero can improve the performance, if adjusted carefully. (Courtesy of Professor Yuquan Chen)

to observe that both the method and the Nesterov method give an optimal choice of the zero, which is closely related to the pole ( $b = -a/(1 + a)$ ).

Now, let us consider a general third-order discrete system:

$$G(z) = \frac{z^2 + cz + d}{(z - 1)(z^2 + az + b)}. \quad (2.37)$$

Set  $b = d = 0$ ; it will reduce to the second-order algorithm discussed above. Compared with the second-order case, the poles can now be complex numbers. More generally, a higher-order system can contain more internal models. If all the poles are real, then:

$$G(z) = \frac{1}{(z - 1)} \frac{(z - c)}{(z - a)} \frac{(z - d)}{(z - b)}, \quad (2.38)$$

Table 2.4: General third-order algorithm design, with parameters defined by Equation (2.39).

$\rho$	0.4	0.8	1.2	1.6	2.0	2.4
a	0.6439	0.5247	-0.4097	-0.5955	-1.0364	-1.4629
b	0.0263	0.0649	0.0419	-0.0398	0.0364	0.0880
c	1.5439	0.5747	-0.3763	-0.3705	-0.5364	-0.6462
d	0.0658	0.0812	0.0350	-0.0408	0.0182	0.0367

whose corresponding iterative optimization algorithm is

$$\begin{cases} y_{k+1} = y_k - \mu \nabla f(x_k), \\ z_{k+1} = az_k + y_{k+1} - cy_k, \\ x_{k+1} = bx_k + z_{k+1} - dz_k. \end{cases} \quad (2.39)$$

After some experiments (Table 2.4), it was found that since the ISE was used for tracking a step signal (it is quite simple), the optimal poles and zeros are the same as for the second-order case with a pole-zero cancellation. This is an interesting discovery. In this optimization result, all the poles and zeros are real, and the resulting performance is not very good, as expected. Compare this with the second-order case; the only difference is that in the latter, complex poles can possibly appear. Thus, the question arises: ‘‘How do complex poles play a role in the design?’’ The answer is obvious: by fractional calculus!

Inspired by M. Jordan’s idea in the frequency domain, a continuous time fractional-order system was designed:

$$G(s) = \frac{1}{s(s^\alpha + \beta)}, \quad (2.40)$$

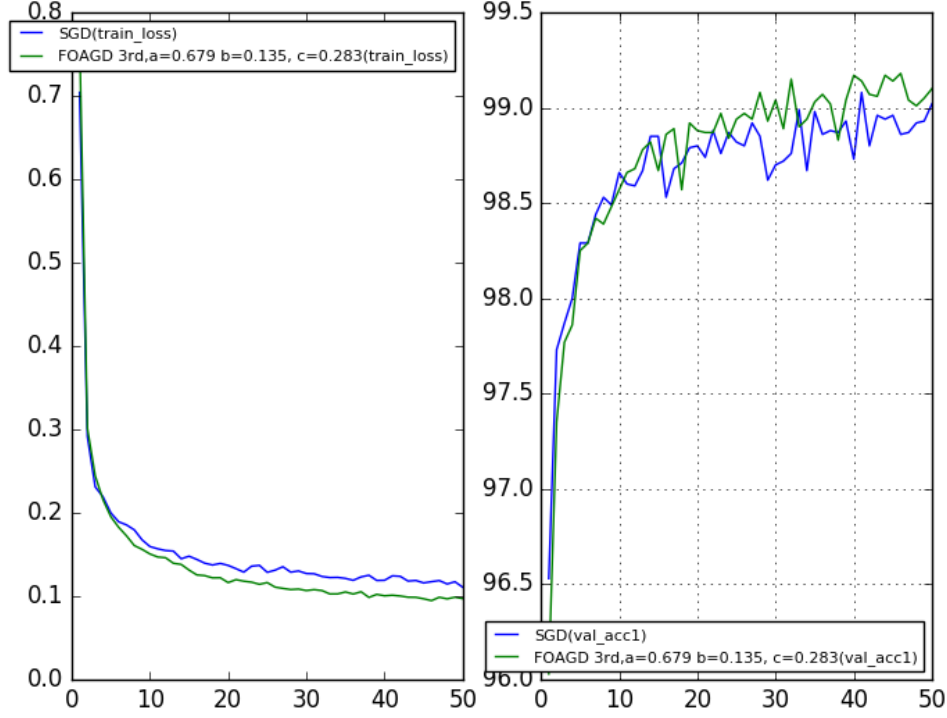
where  $\alpha \in (0, 2)$ ,  $\beta \in (0, 20]$  at first. It was then found that the optimal parameters were obtained by searching using the ISE criterion (Table 2.5).

Equation (2.40) encapsulates the continuous-time design, and one can use the numerical inverse Laplace transform (NILP) [167] and Matlab command `stmcb()` [168] to derive its discrete form. After the complex poles are included, one can have:

$$G(z) = \frac{(z + c)}{(z - 1)} \left( \frac{1}{z - a + jb} + \frac{1}{z - a - jb} \right), \quad (2.41)$$

Table 2.5: The continuous time fractional-order system.

$\rho$	0.3	0.5	0.7	0.9
$\alpha$	1.8494	1.6899	1.5319	1.2284
$\beta$	20	20	20	20

Figure 2.10: Training loss (**left**); test accuracy (**right**). (Courtesy of Professor Yuquan Chen)

whose corresponding iterative algorithm is:

$$\begin{cases} y_{k+1} = ay_k - bz_k - \mu \nabla f(x_k), \\ z_{k+1} = az_k + by_k, \\ x_{k+1} = x_k + y_{k+1} + cy_k. \end{cases} \quad (2.42)$$

Then, the algorithms were tested again using the MNIST dataset, and the results were compared with the SGD's. For the fractional order,  $\rho = 0.9$  was used,  $a = 0.6786$ ,  $b = 0.1354$ , and different values for zero  $c$  were used. When  $c = 0$ , the result was similar to that for the second-order SGD. When  $c$  was not equal

to 0, the result was similar to that for the second-order NAGD. For the SGD,  $\alpha$  was set to be 0.9, and the learning rate was 0.1 (Figure 2.10). Both  $c = 0$  and  $c = 0.283$  perform better than the SGD momentum; generally, with appropriate values of  $c$ , better performance can be achieved than in the second-order cases. The simulation results demonstrate that fractional calculus (complex poles) can potentially improve the performance, which is closely related to the learning rate.

In general, M. Jordan asked the question: “Is there an optimal way to optimize?” Our answer is a resounding yes, by limiting dynamics analysis and discretization and SGD with other randomness, such as Langevin motion. Herein, the question posed was: “Is there a more optimal way to optimize?” Again, the answer is yes, but it requires the fractional calculus to be used to optimize the randomness in SGD, random search and the IMP. There is more potential for further investigations along this line of ideas.

## 2.7 Case Study: Optimal Randomness for Stochastic Configuration Network (SCN) with Heavy-tailed Distributions

### 2.7.1 Introduction

The Stochastic Configuration Network (SCN) model is generated incrementally by using stochastic configuration (SC) algorithms [169]. Compared with the existing randomized learning algorithms for single-layer feed-forward neural networks (SLFNNs), the SCN can randomly assign the input weights ( $w$ ) and biases ( $b$ ) of the hidden nodes in a supervisory mechanism, which is selecting the random parameters with an inequality constraint and assigning the scope of the random parameters adaptively. It can ensure that the built randomized learner models have universal approximation property. Then, the output weights are analytically evaluated in either a constructive or selective manner [169]. In contrast with the known randomized learning algorithms, such as the Randomized Radial Basis Function (RBF) Networks [170] and the Random Vector Functional-link (RVFL)

[171], SCN can provide good generalization performance at a faster speed. Concretely, there are three types of SCN algorithms, which are SC-I, SC-II, and SC-III. SC-I algorithm uses a constructive scheme to evaluate the output weights only for the newly added hidden node [172]. All of the previously obtained output weights are kept the same. The SC-II algorithm recalculates part of the current output weights by analyzing a local least squares problem with user-defined shifting window size. The SC-III algorithm finds all the output weights together by solving a global least-squares problem.

SCN algorithms have been commonly studied and used in many areas, such as image data analytics [173, 28], prediction of component concentrations in sodium aluminate liquor [174], and etc. [175, 176]. For example, in [173], Li *et al.* developed a two-dimensional SCNs (2DSCNs) for image data modelling tasks. Experimental results on hand written digit classification and face recognition showed that the 2DSCNs have great potential for image data analytics. In [174], Wang *et al.* proposed a SCN-based model for measuring component concentrations in sodium aluminate liquor, which were usually acquired by titration analysis and suffered from larger time delays. From the results, the mechanism model showed the internal relationship. The improved performance can be achieved by using the SCN-based compensation model. In [102], Lu *et al.* proposed a novel robust SCN model based on a mixture of the Gaussian and Laplace distributions (MOGL-SCN) in the Bayesian framework. To improve the robustness of the SCN model, the random noise of the SCN model is assumed to follow a mixture of Gaussian distribution and Laplace distributions. Based on the research results, the proposed MOGL-SCN could construct prediction intervals with higher reliability and prediction accuracy.

Neural Networks (NNs) can learn from data to train feature-based predictive models. However, the learning process can be time-consuming and infeasible for applications with data streams. An optimal method is to randomly assign the weights of the NNs so that the task can become a linear least-squares problem. In [177], Wang *et al.* classified the NN models into three types. First, the feed-forward networks with random weights (RW-FNN) [178]. Second, recurrent NNs with ran-

dom weights [179]. Third, randomized kernel approximations [180]. According to [177], there are three benefits of the randomness: (1) Simplicity of implementation, (2) Faster learning and less human intervention, (3) Possibility of leveraging linear regression and classification algorithms. Randomness is used to define a feature map, which converts the data input into a high dimensional space where learning is more simpler. The resulting optimization problem becomes a standard linear least-squares, which is a simpler and scalable learning procedure.

For the original SCN algorithms, weights and biases are randomly generated in uniform distribution. Randomness plays a significant role in both exploration and exploitation. A good NNs architecture with randomly assigned weights can easily outperform a more deficient architecture with finely tuned weights [177]. Therefore, it is critical to discuss the optimal randomness for the weights and biases in SCN algorithms. In this study, the authors mainly discussed the impact of three different heavy-tailed distributions on the performance of the SCN algorithms, Lévy distribution, Cauchy distribution, and Weibull distribution [94]. Heavy-tailed distribution has shown optimal randomness for finding targets [181], which plays a significant role in exploration and exploitation [153]. It is important to point out that the proposed SCN models are very different from Lu *et al.* [102]. As mentioned earlier, Lu *et al.* assumed that the random noise of the SCN model following a mixture of Gaussian distribution and Laplace distributions. In this research study, the author randomly initialized the weights and biases with heavy-tailed distributions instead of uniform distribution. To compare with the mixture distributions, the author also used the mixture distributions for weight and bias generation. A more detailed comparison of the two heavy-tailed methods is shown in the following Results and Discussion section.

There are two objectives for this research: (1) Compare the performance of SCN algorithms with heavy-tailed distributions on a linear regression model [182]; (2) Evaluate the SCN algorithms performance on MNIST handwritten digit classification problem with heavy-tailed distributions.

### 2.7.2 SCN with Heavy-tailed PDFs

For the original SCN algorithms, weights and biases are randomly generated using a uniform PDF. Randomness plays a significant role in both exploration and exploitation. A good neural network architecture with randomly assigned weights can easily outperform a more deficient architecture with finely tuned weights [177]. Therefore, it is critical to discuss the optimal randomness for the weights and biases in SCN algorithms. Heavy-tailed PDFs have shown optimal randomness for finding targets [181, 183], which plays a significant role in exploration and exploitation [153]. Therefore, herein, heavy-tailed PDFs were used to randomly update the weights and biases in the hidden layers to determine if the SCN models display improved performance. Some of the key parameters of the SCN models are listed in Table 2.6. For example, the maximum times of random configuration  $T_{max}$  were set as 200. The scale factor lambda in the activation function, which directly determined the range for the random parameters, was examined by using different settings (0.5–200). The tolerance was set as 0.05. Most of the parameters for the SCN with heavy-tailed PDFs were kept the same with the original SCN algorithms for comparison purposes. For more details, please refer to [169].

### 2.7.3 A Regression Model and Parameter Tuning

The dataset of the regression model was generated by a real-valued function [182]:

$$f(x) = 0.2e^{-(10x-4)^2} + 0.5e^{-(80x-40)^2} + 0.3e^{-(80x-20)^2}, \quad (2.43)$$

where  $x \in [0, 1]$ . There were 1000 points randomly generated from the uniform distribution on the unit interval  $[0, 1]$  in the training dataset. The test set had 300 points generated from a regularly spaced grid on  $[0, 1]$ . The input and output attributes were normalized into  $[0, 1]$ , and all the results reported in this research represented averages over 1000 independent trials. The settings of the parameters were similar to the SCN in [169].

Heavy-tailed PDF algorithms have user-defined parameters, for example, the power-law index for SCN-Lévy, and location and scale parameters for SCN-Cauchy

Table 2.6: SCNs with key parameters.

Properties	Values
Name:	“Stochastic Configuration Networks”
version:	“1.0 beta”
L:	hidden node number
W:	input weight matrix
b:	hidden layer bias vector
Beta:	output weight vector
r:	regularization parameter
tol:	tolerance
Lambdas:	random weights range
$L_{max}$ :	maximum number of hidden neurons
$T_{max}$ :	maximum times of random configurations
nB:	number of node being added in one loop

and SCN-Weibull, respectively. Thus, to illustrate the effect of parameters on the optimization results and to offer reference values for the proposed SCN algorithms, parameter analysis was conducted, and corresponding experiments were performed. Based on the experimental results, for the SCN-Lévy algorithm, the most optimal power-law index is 1.1 for achieving the minimum number of hidden nodes. For the SCN-Weibull algorithm, the optimal location parameter  $\alpha$  and scale parameter  $\beta$  for the minimum number of hidden nodes are 1.9 and 0.2, respectively. For the SCN-Cauchy algorithm, the optimal location parameter  $\alpha$  and scale parameter  $\beta$  for the minimum number of hidden nodes are 0.9 and 0.1, respectively.

### **Performance Comparison among SCNs with Heavy-Tailed PDFs**

In Table 2.7, the performance of SCN, SCN-Lévy, SCN-Cauchy, SCN-Weibull and SCN-Mixture are shown, in which mean values are reported based on 1000 independent trials. Wang *et al.* used time cost to evaluate the SCN algorithms' performance [169]. In the present study, the author used the mean hidden node numbers to evaluate the performance. The number of hidden nodes was associated with modeling accuracy. Therefore, the analysis determined if an SCN with heavy-tailed PDFs used fewer hidden nodes to generate high performance, which would make the NNs less complex. According to the numerical results, the SCN-Cauchy used the lowest number of mean hidden nodes, 59, with a root mean squared error (RMSE) of 0.0057. The SCN-Weibull had a mean number of 63 hidden nodes, with an RMSE of 0.0037. The SCN-Mixture had a mean number of 70 hidden nodes, with an RMSE of 0.0020. The mean number of hidden nodes for SCN-Lévy was also 70. The original SCN model had a mean number of 75 hidden nodes. A more detailed training process is shown in Figure 2.11. With fewer hidden node numbers, the SCN models with heavy-tailed PDFs can be faster than the original SCN model. The neural network structure is also less complicated than the SCN. Our numerical results for the regression task demonstrate remarkable improvements in modeling performance compared with the current SCN model results.

Table 2.7: Performance comparison of SCN models on the regression problem.

Models	Mean hidden node number	RMSE
SCN	$75 \pm 5$	0.0025,
SCN-Lévy	$70 \pm 6$	0.0010,
SCN-Cauchy	$59 \pm 3$	0.0057,
SCN-Weibull	$63 \pm 4$	0.0037,
SCN-Mixture	$70 \pm 5$	0.0020.

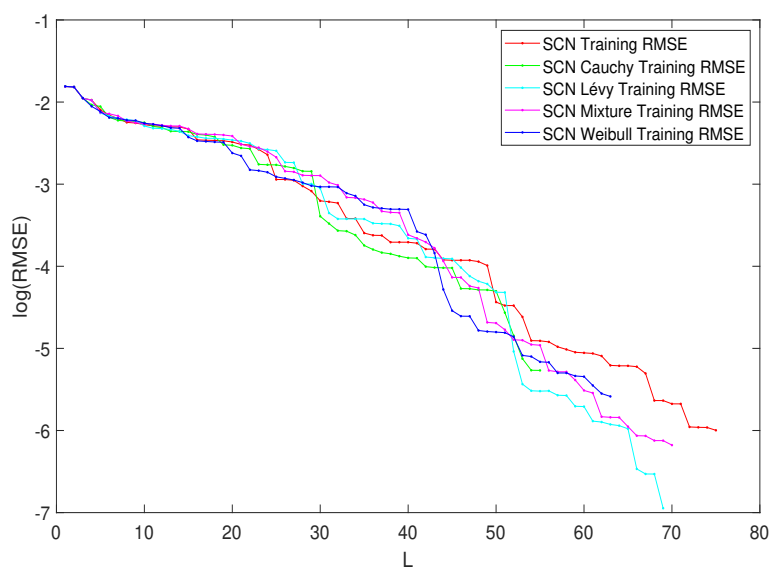


Figure 2.11: Performance of SCN, SCN-Lévy, SCN-Weibull, SCN-Cauchy and SCN-Mixture. The parameter L is the hidden node number.

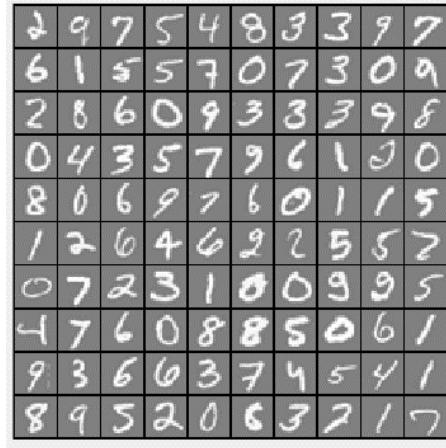


Figure 2.12: The handwritten digit dataset example.

#### 2.7.4 MNIST Handwritten Digit Classification

The handwritten digit dataset contains 4000 training examples and 1000 testing examples, a subset of the MNIST handwritten digit dataset. Each image is a  $20 \times 20$  pixel grayscale image of the digit (Figure 2.12). Each pixel is represented by a number indicating the grayscale intensity at that location. The  $20 \times 20$  grid of pixels is “unrolled” into a 400-dimensional vector. Similar to the parameter tuning for the regression model, parameter analysis was conducted to illustrate the impact of parameters on the optimization results and to offer reference values for the MNIST handwritten digit classification SCN algorithms. Corresponding experiments were performed. According to the experimental results, for the SCN-Lévy algorithm, the most optimal power law index is 1.6 for achieving the best RMSE performance. For the SCN-Cauchy algorithm, the optimal location parameter  $\alpha$  and scale parameter  $\beta$  for the lowest RMSE are 0.2 and 0.3, respectively.

#### Performance Comparison among SCNs on MNIST

The performance of the SCN, SCN-Lévy, SCN-Cauchy and SCN-Mixture are shown in Table 2.8. Based on the experimental results, the SCN-Cauchy, SCN-Lévy and SCN-Mixture have better performance in training and test accuracy, compared with the original SCN model. A detailed training process is shown in Figure 2.13.

Table 2.8: Performance comparison between SCN, SCN-Lévy and SCN-Cauchy.

Models	Training accuracy	Test accuracy
SCN	$94.0 \pm 1.9\%$	$91.2 \pm 6.2\%$ ,
SCN-Lévy	$94.9 \pm 0.8\%$	$91.7 \pm 4.5\%$ ,
SCN-Cauchy	$95.4 \pm 1.3\%$	$92.4 \pm 5.5\%$ .
SCN-Mixture	$94.7 \pm 1.1\%$	$91.5 \pm 5.3\%$ .

Within around 100 hidden nodes, the SCN models with heavy-tailed PDFs perform similarly to the original SCN model. When the number of the hidden nodes is greater than 100, the SCN models with heavy-tailed PDFs have lower RMSEs. Since more parameters for weights and biases are initialized in heavy-tailed PDFs, this may cause an SCN with heavy-tailed PDFs to converge to the optimal values at a faster speed. The experimental results for the MNIST handwritten classification problem demonstrate improvements in modeling performance. They also show that SCN models with heavy-tailed PDFs have a better search ability for achieving lower RMSEs.

## 2.8 Conclusion and Future Research

Big data and ML are two of the hottest topics of applied scientific research, and they are closely related to one another. To better understand them, in this chapter, we advocated fractional calculus (FC), as well as fractional-order thinking (FOT), for big data and ML analysis and applications. In Section 2.4, we discussed the relationships between big data, variability and FC, as well as why fractional-order data analytics (FODA) should be used and what it is. The topics included the Hurst parameter, fractional Gaussian noise (fGn), fractional Brownian motion (fBm), the fractional autoregressive integrated moving average (FARIMA), the formalism of continuous time random walk (CTRW), unmanned aerial vehicles (UAVs) and precision agriculture (PA).

In Section 2.5, how to learn efficiently (optimally) for ML algorithms was

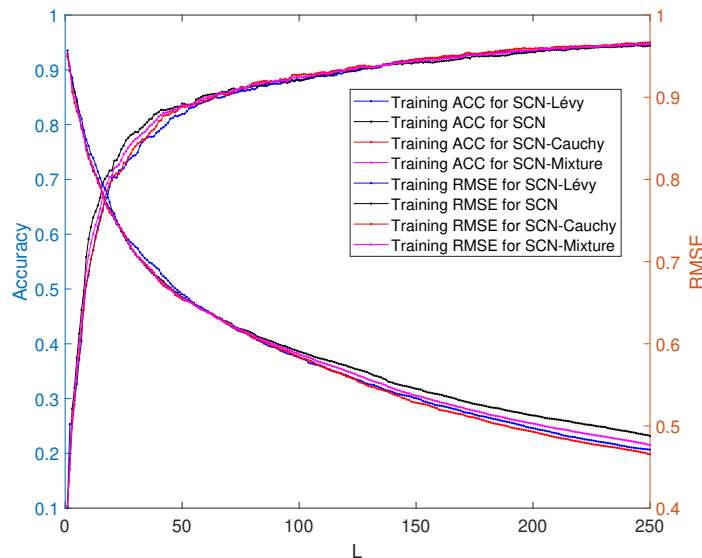


Figure 2.13: Classification performance of SCNs.

discussed. The key to developing an efficient learning process is the method of optimization. Thus, it is important to design an efficient optimization method. The derivative-free methods, as well as the gradient-based methods, such as the Nesterov accelerated gradient descent (NAGD), are discussed. Furthermore, it is shown to be possible, following the internal model principle (IMP), to design and analyze the ML algorithms in the  $S$  or  $Z$  transform domain in Section 2.6. FC is used in optimal randomness in the methods of stochastic gradient descent (SGD) and random search. Nonlocal models have commonly been used to describe physical systems and/or processes that cannot be accurately described by classical approaches [184]. For example, fractional nonlocal Maxwell's equations and the corresponding fractional wave equations were applied in [185] for fractional vector calculus [186]. The nonlocal differential operators [187], including nonlocal analogs of the gradient/Hessian, are the key of these nonlocal models, which could lead to very interesting research with FC in the near future.

Fractional dynamics is a response to the need for a more advanced characterization of our complex world to capture structure at very small or very large scales that had previously been smoothed over. If one wishes to obtain results

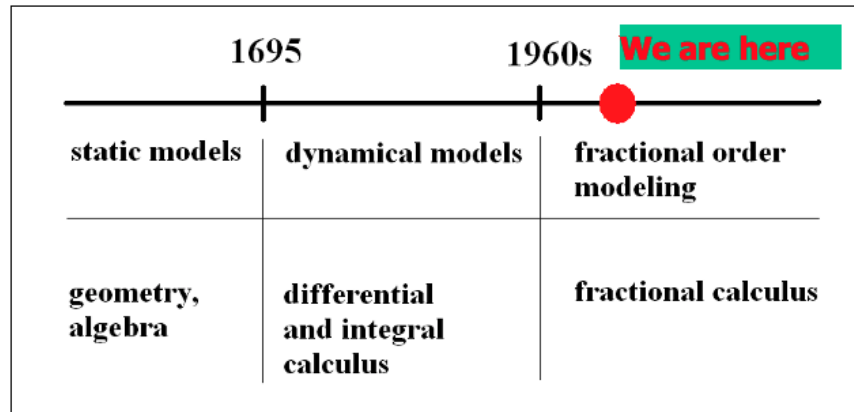


Figure 2.14: Timeline of FC (courtesy of Professor Igor Podlubny).

that are better than the best possible using integer-order calculus-based methods, or are “more optimal”, we advocate applying FOT and going fractional! In this era of big data, decision and control need FC, such as fractional-order signals, systems and controls. The future of ML should be physics-informed, scientific (cause–effect embedded or cause–effect discovery) and involving the use of FC, where the modeling is closer to nature. Laozi (unknown, around the 6<sup>th</sup> century to 4<sup>th</sup> century BC), the ancient Chinese philosopher, is said to have written a short book *Dao De Jing (Tao Te Ching)*, in which he observed: “The Tao that can be told is not the eternal Tao” [188]. People over thousands of years have shared different understandings of the meaning of the Tao. Our best understanding of the Tao is nature, whose rules of complexity can be explained in a non-normal way. Fractional dynamics, FC and heavytailedness may well be that non-normal way (Figure 2.14), at least for the not-too-distant future.

## Part II

# Smart Big Data Acquisition Platforms

# Chapter 3

## Small Unmanned Aerial Vehicles and Remote Sensing Payloads

### 3.1 The UAV Platform

Many kinds of UAVs are used for different research purposes, such as ET estimation. Some popular UAV platforms are shown in Fig. 3.1. Typically, there are two types of UAV platforms, fixed-wings and multirotors. Fixed-wings can usually fly longer with a larger payload. It can usually fly for about 2 hours, which is suitable for a large field. Multirotors can fly about 30 minutes with payload, which is suitable for short flight missions. Both of them have been used in agricultural research, such as [26, 23], which promises great potential in precision agriculture.

The author mainly used a quadcopter named “Hover” to collect aerial images, as shown in Fig. 3.1 (e). The “Hover” was equipped with a Pixhawk flight controller, GPS, telemetry antennas. It can fly over the field by waypoints mode (designed by using Mission Planner software). The lithium polymer battery of “Hover” has a capacity of 9500 mAh, which can support a 30-minute flight mission with cameras mounted on it. The specifications of the “Hover” are listed in Table 3.1 for reference. The “Hover” is equipped with high efficient power system, including T-Motor MN3508 KV380 motor, 1552 folding propeller, and Foxtech Multi-Pal 40A OPTP ESC, to ensure long flight time.

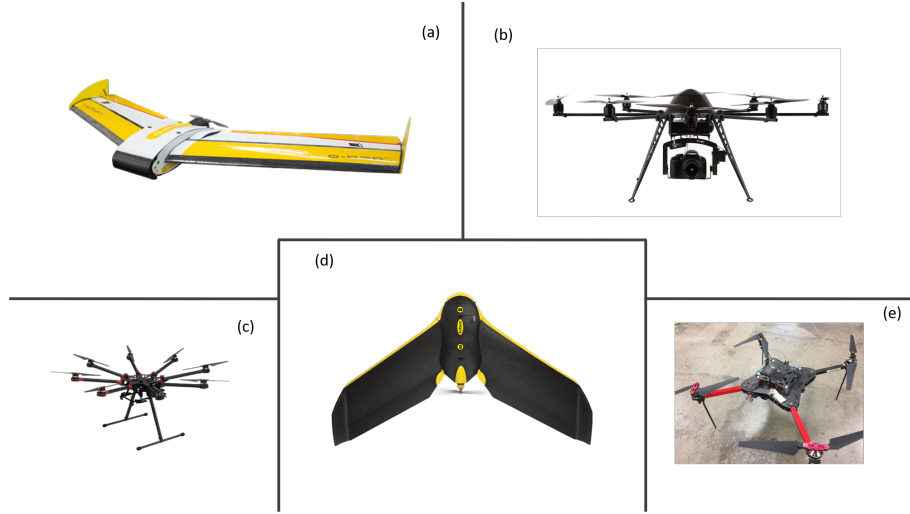


Figure 3.1: (a) The QuestUAV 200 UAV. (b) The MK Okto XL 6S12. (c) The DJI S1000. (d) The eBee Classic. (e) The Hover.

Table 3.1: The specifications of “Hover”. The quadcopter is equipped with high efficient power system, including T-Motor MN3508 KV380 motor, 1552 folding propeller and Foxtech Multi-Pal 40A OPTP ESC, to ensure long flight time.

<b>Specifications:</b>	
Wheelbase	610 mm,
Folding size	$285 \times 285 \times 175$ mm,
Propeller	Foxtech 1552 folding propeller,
Motor	T-Motor MN3508 KV380,
ESC	Foxtech Multi-Pal 40A OPTO ESC (Simonk Firmware),
Flight controller	Pixhawk cube orange standard set with Here 2 GNSS,
Operating temperature	$-20 \sim +50$ °C,
Suggested flight altitude	$< 1000$ m,
Max air speed	20 m/s.



Figure 3.2: The Survey 2 sensors and the reflectance calibration ground target package.

## 3.2 Lightweight Sensors

Mounted on UAVs, many light weight sensors can be used for collecting UAV imagery, such as RGB, multispectral, and thermal images, for agricultural research. In this section, the author listed the sensors that had been commonly used in most of his research work. The sensors being introduced here will be mentioned in the following chapters frequently. Therefore, the author introduced the sensors in this section in details.

### 3.2.1 The RGB Camera

The Survey 2 (MAPIR, San Diego, CA, USA)<sup>1</sup> camera has four bands, Blue, Green, Red, and Near-infrared (NIR), with a spectral resolution of  $4608 \times 3456$  pixels, and a spatial resolution of 1.01 cm/pixel (Fig. 3.2). The Survey 2 camera has a fast interval timer, 2 seconds for JPG mode, and 3 seconds for RAW + JPG mode. Faster interval timer will benefit the overlap design for UAV flight missions, such as reducing the flight time, and enabling higher overlapping.

<sup>1</sup>Mention of trade names or commercial products in this publication is solely for the purpose of providing specific information and does not imply recommendation or endorsement by the University of California. The University of California is equal opportunity providers and employers.



Figure 3.3: The Rededge M is a commonly used multispectral camera. The Rededge M has five bands, which are Blue, Green, Red, Near-infrared, and Red edge. It has a spectral resolution of  $1280 \times 960$  pixel, with a  $46^\circ$  field of view.

### 3.2.2 The Multispectral Camera

The Rededge M is a commonly used multispectral camera (Fig. 3.3). The Rededge M has five bands, which are Blue, Green, Red, Near-infrared, and Red edge. It has a spectral resolution of  $1280 \times 960$  pixel, with a  $46^\circ$  field of view. With a Downwelling Light Sensor (DLS), which is a 5-band light sensor that connects to the camera, the Rededge M can measure the ambient light during a flight mission for each of the five bands. Then, it can record the light information in the metadata of the images captured by the camera. After the camera calibration, the information detected by the DLS can be used to correct lighting changes during a flight, such as changes in cloud cover during a UAV flight.

### 3.2.3 The Short Wave Infrared Camera

The SWIR 640 P-Series (Infrared Cameras Inc, Beaumont, TX, USA.), which is a shortwave infrared camera, has also been commonly used for agricultural research



Figure 3.4: The SWIR 640 P-Series, which is a shortwave infrared camera, has also been commonly used for agricultural research. The spectral band is from  $0.9 \mu\text{m}$  to  $1.7 \mu\text{m}$ . The accuracy for the SWIR camera is  $\pm 1 \text{ }^\circ\text{C}$ . It has a resolution of  $640 \times 512$  pixels.

(Fig. 3.4). The spectral band is from  $0.9 \mu\text{m}$  to  $1.7 \mu\text{m}$ . The accuracy for the SWIR camera is  $\pm 1 \text{ }^\circ\text{C}$ . It has a resolution of  $640 \times 512$  pixels.

### 3.2.4 The Thermal Camera

The thermal camera ICI 9640 P (Infrared Cameras Inc, Beaumont, TX, USA.) has been used for collecting thermal images as reported in [189, 190, 191, 27]. The thermal camera has a resolution of  $640 \times 480$  pixels. The spectral band is from  $7 \mu\text{m}$  to  $14 \mu\text{m}$ . The dimension of the thermal camera is  $34 \text{ mm} \times 30 \text{ mm} \times 34 \text{ mm}$  (Fig. 3.5). The accuracy is designed to be  $\pm 2 \text{ }^\circ\text{C}$ . A Raspberry Pi Model B computer (Raspberry Pi Foundation, Cambridge, UK.) can be used to trigger the thermal camera during flight missions.



Figure 3.5: The thermal camera has a resolution of  $640 \times 480$  pixels. The spectral band is from  $7 \mu m$  to  $14 \mu m$ . The dimension of the thermal camera is  $34 \text{ mm} \times 30 \text{ mm} \times 34 \text{ mm}$ . The accuracy is designed to be  $\pm 2 \text{ }^\circ\text{C}$ .



Figure 3.6: The user interface of Mission Planner. The example of flight mission was for nematode data collection using UAV for Project 30 at UC Kearny Center. See Chapter 6 for more details.

## 3.3 UAV Image Acquisition and Processing

### 3.3.1 The Flight Mission Design

The author used the Mission Planner to program all flight missions (Fig. 3.6). The flight height was usually set up as 30, 60, 90, and 120 m based on research purpose. The overlapping of UAV imagery was set up as 80%, so that the UAV imagery of the crops or trees can be stitched together during image processing. A bi-weekly UAV flight schedule is suggested to collect sufficient data. If there is a UAV crash, unexpected weather conditions, hardware issues, or unknown reasons, data may not be collected successfully. If data is missed, people may have to wait for another year.

To minimize the shading effect on the images, the UAVs are usually flying at noon with clear sky conditions. Because each pixel in a UAV image is a percentage of the reflected light, pixel values need to be calibrated by using a known reflectance value. Therefore, the image of a calibration board needs to be taken before and after the flight missions, servicing as the reflectance reference. It is important to take pictures of the reference panel immediately before and after the

flight missions because the solar angle and light intensity can change [192], which causes inaccurate experiment results. UAV images usually have higher radiometric homogeneity than aircraft or satellite images because of the lower flight altitude [193]. However, there are also special UAVs image quality problems. For example, the camera position on the UAVs might be different for each flight mission, which can cause different spatial resolution or different viewing angles [193]. The low flight height of UAVs can also result in geometric distortion [193, 194]. Besides, lower flight height results in greater numbers of UAV images to keep effective overlapping, which makes image processing more time-consuming.

### 3.3.2 UAV Image Processing

After the flight missions, all of the aerial images were stitched together to generate the orthomosaick images (Table 3.2 and Fig. 3.7) in Metashape (Agisoft LLC, Russian). Preselection is recommended because it can speed up the processing of large datasets. Building the dense cloud can reconstruct a more accurate surface, which can improve the quality of the final orthomosaic. Higher quality usually can result in a more accurate surface, which means a greater number of points. However, higher quality is not recommended because of longer data processing time. Medium quality is sufficient for UAV image processing, especially for low variations field. Building Digital Elevation Model (DEM) allows generating an accurate surface, which can be used as a source for the orthomosaic generation. This will shorten the data processing time compared with Build Mesh operation because Build Mesh is usually used for a more complex surface. The source data for building DEM is the dense cloud. For the interpolation method, **Extrapolated** option is selected because it can generate a surface without gaps being extrapolated to the bound box sides. The default option for **Interpolation** is **Enabled**, which is not recommended because it will leave the valid elevation values only for fields that are seen from at least one aligned camera.

Table 3.2: Orthomosaic images generation workflow in Agisoft Metashape.

Step 1 : Align Photos	Step 2 : Build Mesh	Step 3 : Build Orthomosaick
Accuracy: Medium	Surface type: Height field (2.5D)	Type: Planar
Generic preselection: Yes	Source data: Sparse cloud	Projection plane: TOP XY
Key point limit: 40,000	Face count: Medium (30,000)	Rotation angle: 0
Tie point limit: 4,000	Interpolation: Enabled (default)	Surface: Mesh
Adaptive camera model fitting: No	Point classes: All	Blending mode: Mosaic (default)
	Calculate vertex colors: Yes	Enable hole filling: Yes
		Enable back-face culling: No

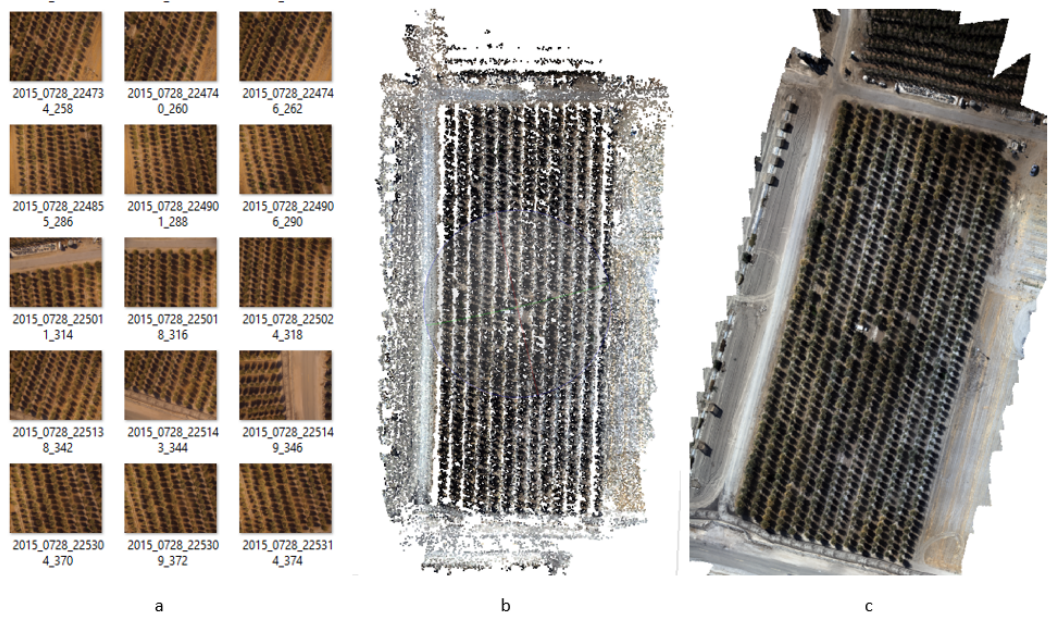


Figure 3.7: Agisoft Metashape image processing workflow: (a) Align Photos. (b) Build Mesh. (c) Generate orthomosaick.

## 3.4 Challenges and Opportunities

Compared with traditional remote sensing tools, such as satellite, the UAVs flight can be more flexible and frequent in the field. UAVs can fly at a lower altitude and can take higher spatial and temporal resolution images of crops [190]. As a low-cost scientific data collection platform, UAVs also make data acquisition relatively less expensive. While there are many advantages by using UAVs for agricultural research, there are still challenges for UAVs. These challenges are also commonly shown in different research work [195, 196, 197, 198, 199, 200, 201, 202, 203, 204, 205, 206].

### 3.4.1 UAVs

Although UAVs have shown great potential for precision agriculture, there are still many technical problems for UAVs, such as flight time, flight height control, path planning, stability in winds, and turbulence [207, 208]. For example, most UAVs can only fly around 30 minutes with payload, which is not enough for a large field. The power can also run low faster because of unexpected headwinds or other factors. Increasing the payload of UAVs will make the UAVs more capable. Flight height is another concern, in the United States, the maximum altitude for UAVs is limited to 120 m. The UAVs need to be in the sight of the operator, and a pilot license is also required. Consequently, it is necessary to have a flying team for UAVs. For a detailed discussion on technical limitations for UAVs, please refer to [209]. Fortunately, it is expected that with the development of UAV technology, new camera designs, lower costs, improved image processing techniques, and a greater number of experimental studies of UAV-based remote sensing for agriculture applications, UAVs will have better performance for agricultural research.

### 3.4.2 UAV Path Planning and Image Processing

Many researchers fly the UAVs in different height, using specialized equipment, controlling environments, and relying on data analysis expertise [210]. Is there any optimal point where the data can be the best representation of crops or trees? In

[210], Stark *et al.* built a conceptual framework for describing the optimality as a function of spatial, spectral, and temporal factors that represented the best solution. As researchers try to understand the potential of the UAVs, efficient workflow, image processing methods, and better software are still under developing [211, 212, 213, 214].

### 3.4.3 Pre-flight Path Planning

Being used as a remote sensing platform, UAVs also create new research problems, such as UAV image processing and flight path planning. Flight missions are usually designed by different kinds of software. The flight height is usually set up as 30 m, 60 m, and 120 m. For most flight missions in the reviewed papers, the overlap was usually set up between 75% to 85% to enable the images stitched together during image processing. The UAVs sensors are designed to take images at nearly 0 nadir angle.

Researchers usually fly UAVs biweekly to collect data. If there is a UAV crash, unexpected weather conditions, hardware issues, or unknown reasons, data may not be collected successfully. If data is missed, people may have to wait for another year. A bi-weekly UAV flight schedule is suggested to collect sufficient data.

### 3.4.4 Multispectral Image Calibration

To minimize the shading effect on the multispectral images, the UAVs are usually flying at noon with clear sky conditions. Because each pixel in a UAV image is a percentage of the reflected light, pixel values need to be calibrated by using a known reflectance value. Therefore, the image of a calibration board needs to be taken before and after the flight missions, servicing as the reflectance reference (Fig. 3.8).

It is important to take pictures of the reference panel immediately before and after the flight missions because the solar angle and light intensity can change [192], which causes inaccurate experiment results. The digital number of the images are converted to reflectance by [215]

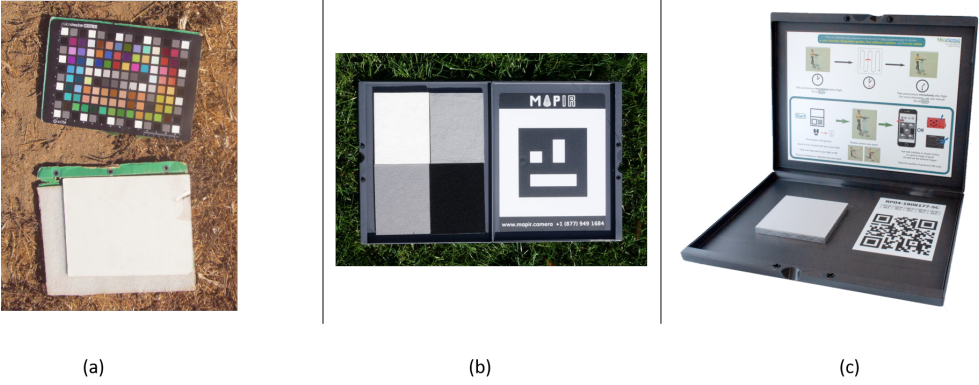


Figure 3.8: The UAV image reflectance calibration. (a) A color panel. (b) The MAPIR target calibration board. (c) The Rededge M calibration board.

$$\rho_\lambda = \frac{DN - DN_d}{DN_w - DN_d}, \tag{3.1}$$

where  $\rho_\lambda$  is the reflectance and  $DN$  is the digital number of the raw image,  $DN_d$  and  $DN_w$  are the dark reflectance point and white reflectance point in the color checker, respectively.

UAV images usually have higher radiometric homogeneity than aircraft or satellite images because of the lower flight altitude [193]. However, there are also special UAV image quality problems. For example, the camera position on the UAVs might be different for each flight mission, which can cause different spatial resolution or different viewing angles [193]. The low flight height of UAVs can also result in geometric distortion [193, 194]. Besides, lower flight height results in greater numbers of UAV images to keep effective overlapping, which makes image processing more time-consuming.

Although multispectral cameras have light sensors to calibrate light conditions, saturation issues can still be found in UAV images. As mentioned earlier, the Rededge M can measure the ambient light during a flight with a DLS and record the light information in the images. After the camera calibration, the information detected by the DLS can be used to correct lighting changes during a flight, which usually happens because the clouds cover the sun during a UAV flight. The clouds are believed to affect the saturation issues, even though sunshine is supposed to

correct reflectance for real-time conditions. Saturated values decrease the quality of the data. The retrieval of required indexes, such as NDVI and LAI, are important for the estimation of soil heat flux ( $G$ ) and sensible heat flux ( $H$ ).

Another critical issue with UAVs is the bidirectional reflectance distribution function (BRDF) effects. For many UAV application, the reflectance model for canopy measurements is simplified to assume a strict nadir (or straight down) viewing angle and a static illumination source [216, 217, 192]. However, this assumption does not consider the BRDF, which is a function of wavelength, observer azimuth, observer zenith, illumination azimuth, and illumination zenith [216]. In satellite images, the effect of BRDF is relatively uniform because the satellite covers a wide region in a single frame. However, this simplification is not valid for UAV platforms equipped with an imaging system with a wide field-of-view (FOV).

Further experiment should be based on multispectral measurements, and UAV image acquisition should be conducted to select those spectral bands which are most useful and sensitive for specific research purpose. Cameras should be designed only for those needed bands, which will lower the cost of the sensors. The availability of low-cost UAV platforms and specialized cameras will also make the UAV application on agriculture more competitive.

### 3.4.5 Thermal Camera Calibration and Image Processing

The thermal image from UAVs is becoming a useful source for agricultural research because of the higher temporal and spatial resolution compared with those obtained from the satellite. Thermal remote sensing images were first used in 1973 to estimate ET [218]. Temperature information is usually converted into land surface characteristics such as albedo, LAI, and surface emissivity. The TIR band is considered as the most critical variable for estimating the sensible heat flux and ground heat flux [196]. The cooled thermal cameras are usually more sensitive and accurate than uncooled thermal cameras [219]. However, cooled thermal cameras are very big, expensive, and energy-consuming [191]. Therefore, cooled thermal cameras can hardly be used on UAV platforms. In contrast, the uncooled thermal cameras are usually lighter [217], which are usually less than 200 grams, low power

consumption [220], and less expensive than cooled thermal cameras.

The uncooled thermal camera has many advantages, though, its microbolometer is not always sensitive and accurate [191]. Most thermal cameras are not always calibrated, which can only measure the relative temperature instead of the absolute values. In precision agriculture, it is necessary to measure the absolute temperature in many applications [217], such as crop monitoring [221], pest detection [222], and disease detection [223]. Unstable outdoor environmental factors can also cause serious measurement drift during flight missions. Post-processing like mosaicking might further lead to measurement errors. To solve these two fundamental problems, in [190], the authors conducted three experiments to research the best practice of thermal image collection using UAVs. To calibrate TIR images, in [206], Park *et al.* used the water body and rubber plates as cold and hot features. IR Flash Version 2 is usually used to process thermal UAV images for image format transformation.

The correlation between the measured IR temperature from calibration boards and the estimates by thermal cameras were found to be unacceptable sometimes. Without warming up the uncooled thermal camera, the temperature difference between the thermal camera and calibration board can be as high as  $\pm 10$  °C. For instance, the land surface temperature is the most important data for SEBAL and the estimation of surface energy fluxes; thus, its accuracy is the key for the agricultural research.

Many researchers also focus on thermal camera calibration issues. For example, Ribeiro *et al.* proposed a new calibration algorithm based on neural networks [191]. The calibration algorithms considered the thermal camera temperature and the digital response of the microbolometer as input data. Based on the calibration result, the accuracy increased from 3.55 °C to 1.37 °C. In [189], Torres-Rua *et al.* presented a vicarious calibration methodology (UAV-specific, time-specific, flight-specific, and sensor-specific) for thermal camera images traceable back to NIST-standards (National Institute of Standards and Technology) and current atmospheric correction methods.

For future research, uncooled thermal cameras can be used to evaluate with

other temperatures sensor information to acquire reliable thermal information, such as atmospherically corrected satellite images and temperature canopy sensors.

### **3.4.6 Images Stitching and Orthomosaic Image Generation**

After UAV images are collected, all of the aerial images need to be stitched together to generate the orthomosaic images. Some problems are identified when creating mosaics, such as fault lines, blurriness, and replicated features, especially with the thermal data. To overcome the thermal camera's effect, a higher overlap for the thermal camera can be a good choice. With an increase in the image overlap by 5%, most of the fuzziness and replicated problems were eliminated [201].

There are many types of software that can be used for image stitching, such as Pix4D (Pix4D, Prilly, Switzerland), Agisoft Metashape, RealityCapture, and DroneDeploy (DroneDeploy, San Francisco, CA, USA). For example, during the image stitching workflow using the Agisoft Metashape, there are several steps for image processing, which include aligning photos, optimize cameras, build mesh, build dense cloud, build digital elevation model (DEM), and generating orthomosaic.

## **3.5 Case Study I: A UAV Resolution and Waveband Aware Path Planning for Onion Irrigation Treatment Inference**

### **3.5.1 Introduction**

Over the past few years, unmanned aerial vehicles have been widely used as a remote sensing platform in agricultural applications, such as crop yield estimation [224], soil moisture monitoring, water stress estimation [146] and pest management [225]. Compared with traditional remote sensing tools, such as satellites, UAV flight time can be more flexible and more frequent in the field. UAVs also fly at lower altitude and can take higher resolution multispectral images or thermal

images of crops [190]. As a low-cost scientific data collection platform, UAVs also make data acquisition relatively less expensive. While there are many advantages by using UAVs for agricultural applications [224], there is still a lot of work for UAVs. Many researchers fly the UAVs in different standard, using specialized equipment, controlling environments and relying on data analysis expertise [210]. Is there any optimal point where the data can be the best representation of crops? In [210], Brandon *et al.* built a conceptual framework for describing the optimality as a function of spatial, spectral, and temporal factors which represented the best solution.

How to collect remote sensing data effectively can still be a big challenge. Many UAV tunable parameters can have significant impact on data quality and the data analysis, such as flight height, flight time, overlapping, and airspeed. In this section, flight height's effect on data analysis was discussed. It assumed that there must be an optimal point where the data analysis results from multispectral images or thermal images could greatly represent for, for example, the crops water stress status [146] or other crop characteristics. In this section, a resolution and waveband aware path planning was conducted in order to optimally collecting remote sensing aerial images with UAVs. Then, the flight mission design was tested in an onion field at USDA during the growing season in 2017.

Onion is one of the most widely produced vegetables all over the world. Onion also plays an important role in human diet and medical properties [226]. Therefore, onion is consumed among all nationalities and cultures [227]. Based on the data from Food and Agriculture Organization, onion production has been increasing continuously by 65 million tonne (1999 - 2009 period), in an area of 2.1 million hectare in 2009 [227]. California is the biggest onion producer in the United States, which is also the only state that can produce spring and summer-harvested onions in the US. 31% of the total onion in the US was produced in California in 2015 [228].

In the semi-arid and arid areas of California, onion production is highly dependent on irrigation. Water stress can happen in any onion growing stage and causes onion yield loss. Therefore, to optimize irrigation management, it is important

to have an optimal onion water stress monitoring method. Many research results have been published on using UAVs to detect water stress [229, 230, 231, 232, 192], which prove UAVs can be a reliable and effective remote sensing platform. In onion study area, multispectral cameras are mounted on the unmanned aerial vehicles for onions yield estimation, biomass monitoring [233], and disease detection [234]. However, to our best knowledge, nobody has studied the effect of UAV flight height on onion's multispectral image data analysis and irrigation treatment inference.

Therefore, in this section, the author mainly designed a UAV flight mission in order to optimally collecting onion remote sensing aerial images with UAVs. By using multispectral and thermal images collected by UAVs, the author was able to apply supervised learning methods to find the relationship between image features and onions irrigation treatments. The author also figured out how UAV flight height or resolution settings affected the accuracy of estimating onion irrigation treatment. Different spectral bands combination also had effect on onion irrigation treatment prediction.

### **3.5.2 Material and Methods**

#### **Onion Study Area**

As shown in Fig. 3.9, the field study was conducted at the USDA-ARS, San Joaquin Valley Agricultural Sciences Center (36.594 °N, 119.512 °W), Palier, California, 93648, USA. Since 2016, an onion test field had been set up for research of biomass soil amendments and deficit irrigation. There were three irrigation treatment levels and four soil amendments. Three irrigation levels were low, medium and high. The four soil amendments were biochar, check, biochar + compost, and biochar + compost + 1 bag of sulfur. There were also three replicate plots for each treatment combination.

#### **A UAV Platform and Sensors**

In this study, the author used a “Hover” (brand of the UAV) quadcopter as the UAV platform. The “Hover” was equipped with a Pixhawk flight controller,



Figure 3.9: Onion test site. The field study was conducted at the USDA-ARS, San Joaquin Valley Agricultural Sciences Center (36.59°N, 119.51°W), Palier, California, 93648, USA. Since 2016, an onion test field has been set up for research of biomass soil amendments and deficit irrigation.

GPS, telemetry antennas. It was able to fly over the onions field by waypoints mode (designed by using Mission Planner software). The lithium polymer battery had a capacity of 9500 mAh, which could support a 30-minute flight mission with cameras mounted on the UAV.

Multispectral images were collected by Survey 2 (MAPIR, USA) cameras with 4 bands, Blue, Green, Red (RGB) and Near-infrared (NIR). The MAPIR camera has a resolution of  $4608 \times 3456$  pixels, with a space resolution at 1.01 cm/pix. The Survey 2 cameras have a faster interval timer, 2 seconds for JPG mode and 3 seconds for RAW + JPG mode. Faster interval timer would benefit the overlap design for UAV flight missions, such as reducing the flight time, enabling higher overlapping.

The thermal camera ICI 9640 P-Series (ICI, USA) was applied for collecting thermal images of onions. The thermal camera has a resolution of  $640 \times 480$  pixels. The spectral band is from  $7 \mu\text{m}$  to  $14 \mu\text{m}$ . The dimensions of the thermal camera is  $34 \text{ mm} \times 30 \text{ mm} \times 34 \text{ mm}$ . The accuracy is supposed to be  $\pm 2 \text{ }^\circ\text{C}$ . A Raspberry Pi Model B computer was used to trigger the thermal cameras during



Figure 3.10: RGB image for the onion field.

the flight missions.

### UAV Images Collection and Pre-processing

Flight missions were programmed by using Mission Planner software. The flight height was setup as 10 m, 15 m, 30 m, and 60 m in order to compare the resolution's effect on onion irrigation treatment inference. For all the flight missions, the overlap was set up as 75% to make sure the images of onion can be stitched together during image pre-processing.

The author flew the UAV bi-weekly over the onions field at noon during the growing season in 2017. The images of a color panel were taken right before and after the flight missions, servicing as the reflectance reference. After the flight missions, all of the aerial images were stitched together to generate the orthomosaick images in PhotoScan (Agisoft LLC, Russian). An RGB image was shown in Fig. 3.10, and an NIR image was shown in Fig. 3.11. The process included aligning photos and building orthomosaick.

All of the thermal images were pre-processed by IR Flash (ICI, USA) in order to



Figure 3.11: NIR image for the onion field.

get .TIF thermal images. Then, thermal images were stitched together to generate the orthomosaick images in PhotoScan (Agisoft LLC, Russian). The process also included aligning photos and building orthomosaick.

### **The Principal Component Analysis**

For image processing, the author used two different machine learning methods, the Principal Component Analysis (PCA) and Linear Discriminant Analysis (LDA). Both of them could reduce the dataset dimensionality and increased the classification accuracy.

The PCA is a fast and flexible unsupervised method for data dimensionality reduction [235]. It can achieve linear projection to a lower-dimensional subspace by using singular value decomposition. The PCA can also maximize the variance of the projected data. Therefore, the PCA method is commonly used in exploratory data analysis and making predictive models.

## The Linear Discriminant Analysis

The Linear Discriminant Analysis (LDA) is a classifier with a linear decision boundary. It is generated by using Bayes' rule to fit class conditional densities to the data. It assumes that all classes share the same covariance matrix. After that, the LDA model can be used to reduce the dimensionality of the input data by projecting it to the most discriminative directions. Then, the output dimensionality is usually less than the number of classes; thus, the LDA is a very strong dimensionality reduction method [236].

### 3.5.3 Results and Discussion

To prepare the multispectral and thermal image data sets, the author firstly segmented 36 plots from the whole onion field in order to focus only on the area of interest, as shown in Fig. 3.12. Every image was converted into 2048 dimension vector for data processing by Python. The data was distributed as 67% for training and 33% for testing. Several classifiers in scikit-learn machine learning algorithms were used for onion irrigation treatment inference, such as, "Nearest Neighbors," "Linear SVM," "RBF SVM," "Gaussian Process," "Decision Tree," "Random Forest," "Neural Net," "AdaBoost," "Naive Bayes," and "QDA."

The accuracy was evaluated by scikit-learn's accuracy classification score function. This function computed the subset accuracy, in which the labels predicted for a sampling must exactly match the corresponding true labels. Estimators used this score method as the evaluation criterion for the classification problems. All scorer objects followed the convention that higher return values were better than lower return values.

The author mainly discussed two topics in this section, flight height or different resolution's effect on onion irrigation treatment estimation, and different wavebands combination on onion irrigation treatment prediction.



Figure 3.12: 36 plots of onion. Every image was converted into 2048 dimension vector for data processing. The data was distributed as 67% for training and 33% for testing.

### UAV Flight Height or Resolution's Effect

In this section, near-infrared images were used to analyze the flight height or image resolution's effect on data analysis. At 30 meters height, the MAPIR had a resolution as 1.01 cm/ pix. By image processing, the author set up 4 different resolutions, A, B, C, and D for onion images. Resolution A meant 0.55 cm/pix, resolution B meant 1.01 cm/pix, resolution C meant 2.02 cm/pix, and resolution D meant 4.04 cm/pix, as shown in Table 3.3.

From the Table 3.3, the author could figure out that the best accuracy was 0.726, which showed up when the resolution was at 2.02 cm/pixel by using "Neural net" classifier. Compared with the other classifiers, the "Neural net" classifier performed the best in all resolution levels. Based on most classifiers resolution analysis results in the Table 3.3, it turned out that when the author flew a UAV in the field, higher resolution did not mean better analysis results. The best resolution

Table 3.3: Different resolutions accuracy for onion treatment inference. The best accuracy was 0.726, which showed up when the resolution was at 2.02 cm/pixel by using “Neural net” classifier. Compared with the other classifiers, the “Neural net” classifier performed the best in all resolution levels.

Classifiers	A 0.55 cm/pix	B 1.01 cm/pix	C 2.02 cm/pix	D 4.04 cm/pix
“Nearest Neighbors”	0.625	0.608	0.593	0.608
“Linear SVM”	0.684	0.660	0.691	0.691
“RBF SVM”	0.375	0.365	0.347	0.323
“Gaussian Process”	0.653	0.674	0.708	0.642
“Decision Tree”	0.663	0.587	0.618	0.601
“Random Forest”	0.663	0.608	0.649	0.601
“Neural Net”	0.719	0.708	0.726	0.684
“AdaBoost”	0.649	0.590	0.653	0.639
“Naive Bayes”	0.600	0.604	0.618	0.538
“QDA”	0.708	0.694	0.694	0.642
“LDA”	0.691	0.684	0.691	0.677

did not promise the best estimation. Based on the accuracy trend of “Neural net” classifier, for example, it existed an optimal point near 2.02 cm/pixel resolution when “Neural net” was applied for onion irrigation estimation.

### Waveband Configuration’s Effect

In this section, remote sensing images were generated by using different wavebands configurations. There were red, green, blue (RGB), near-infrared (NIR), thermal (TIR), and NDVI (Normalized Difference Vegetation Index) being used in this section. As shown in Table 3.4, there were four combinations being used, RGB-NIR, All bands, RGB-NIR-TIR and TIR. Because RGB and NIR had a higher resolution (1.01 cm/pixel) than thermal images resolution (9 cm/pixel), the multispectral images were pre-processed in order to match the thermal images resolution.

From the Table 3.4, the author could figure out that the best accuracy was 0.840, which appeared when the RGB-NIR-TIR waveband images were used by

Table 3.4: Bands configuration accuracy for onion treatment inference. The best accuracy was 0.840, which appeared when the RGB-NIR-TIR waveband images were used by “Gaussian process” classifier. Compared with the other classifiers, the “Gaussian process” classifier performed the best in all wavebands configuration.

Classifiers	RGB-NIR	All	RGB-NIR-TIR	TIR
“Nearest Neighbors”	0.583	0.538	0.691	0.723
“Linear SVM”	0.569	0.590	0.774	0.743
“RBF SVM”	0.622	0.552	0.316	0.764
“Gaussian Process”	0.729	0.646	0.840	0.792
“Decision Tree”	0.615	0.569	0.715	0.719
“Random Forest”	0.590	0.615	0.646	0.750
“Neural Net”	0.625	0.618	0.826	0.785
“AdaBoost”	0.576	0.549	0.767	0.681
“Naive Bayes”	0.521	0.514	0.566	0.622
“QDA”	0.611	0.597	0.788	0.753
“LDA”	0.677	0.628	0.809	0.781

“Gaussian process” classifier. Compared with the other classifiers, the “Gaussian process” classifier performed the best in all wavebands configuration. Based on most classifiers resolution analysis results in the Table 3.4, it turned out that when we flew a UAV in the field, more wavebands information did not mean better analysis results. Knowing all the remote sensing data did not mean the best estimation. Based on the accuracy of “Gaussian process” classifier, it was meaningful to point out that TIR images itself could already get pretty good estimation results, as high as 0.792, which meant that we did not always need multispectral wavebands information for some coarse estimation research work. On the other side, adding RGB-NIR information did increase accuracy from 0.792 to 0.840, which was meaningful for precision agriculture applications.

### 3.5.4 Conclusions

In this study, a UAV resolution and waveband aware path planning was conducted in order to optimally collecting remote sensing aerial images with UAVs. Using multispectral and thermal images collected by UAVs, we were able to apply supervised learning methods to find the relationship between image features and onion irrigation treatments.

First, the author found out that the best accuracy for onion irrigation treatments was 0.726 , which showed up when the resolution was at 2.02 cm/pixel by using the “Neural net” classifier. The best resolution did not promise the best estimation. According to the accuracy trend of the “Neural net” classifier, it did exist an optimal point near 2.02 cm/pixel resolution when the “Neural net” was applied for onion irrigation estimation.

Second, this study also found out that different spectral bands combination also had effect on onion irrigation treatment prediction. Applying all the remote sensing data did not mean the best estimation. Based on the accuracy of the “Gaussian process” classifier, we figured out that TIR images itself could already get relatively good estimation results for onion irrigation estimation, as high as 0.792, which meant we do not always need multispectral bands information for it. On the other side, adding the RGB-NIR information did increase accuracy from 0.792 to 0.840, which was important for precision agriculture applications.

## 3.6 Case Study II: A Detailed Study on Accuracy of Uncooled Thermal Camera by Exploring the Data Collection Workflow

### 3.6.1 Introduction

Because the uncooled thermal camera is light [217], low power consumption [220] and less expensive than cooled thermal cameras, it has been widely used in many agricultural applications, such as plant disease detection [223], crop water

stress estimation [229, 192] and soil moisture detection [237]. Mounted on the UAVs, the uncooled thermal camera makes it possible for UAVs to collect high-resolution thermal images in precision agriculture (PA) [231]. Compared with traditional remote sensing method, such as satellites, the thermal camera and UAVs make the data collection more flexible and lower cost. The cooled thermal cameras are usually more sensitive and accurate than uncooled thermal cameras [219]. However, cooled thermal cameras are very big, expensive and energy consuming [191]. Thus, they can hardly be used on UAVs platform. In contrast, the uncooled thermal camera plays a more and more important role in remote sensing by UAV platforms.

The thermal camera has so many advantages, though, its micobolometer is not always sensitive and accurate [191]. Also, most thermal cameras are not always calibrated, which makes it can only measure the relative temperature instead of the accurate value. In precision agriculture, however, most time it is necessary to measure the accurate temperature in many applications [217], such as crop monitoring [221], pest detection [222] and disease detection [223]. We are using thermal camera more and more frequently without understanding its truth. Therefore, there is a highly strong demand to find a calibration method for the thermal camera in UAV applications.

Researchers have published many thermal camera calibration methods when the thermal camera was used in UAV platforms [238]. In [191], Ribeiro-Gomes *et al.* proposed a new calibration algorithm based on neural network [239]. It also improved the photogrammetry process by using Wallis Filter [240]. They increased the measurement accuracy from 3.55 °C to 1.37 °C. In [217], Berni *et al.* implemented an internal calibration for a thermal camera controlled by PC 104 embedded computer [241], which built a grid with resistive wires. When the wires were heated up, the thermal camera could detect the grid and calibrate the camera. In [242], they designed a lab calibration by using a calibration blackbody source (RAYBB400, Raytek, CA,USA). As mentioned above, researchers tried to solve the thermal camera calibration issues, though, the methods used in these papers were not quite appropriate in UAV platforms [231]. For example, the thermal

camera can have internal and external disturbance during the UAV flight. Internal disturbance can be caused by microbolometer [243]. For external disturbance, the wind can cool down the thermal cameras. The unstable outdoor environment can also cause serious measurement drift during flight missions. Not all of these factors were considered into the previous papers.

Therefore, in this section, the author mainly focused on the thermal camera calibration in UAV applications. The author tried to focus on the thermal camera itself. In agriculture applications, the thermal cameras were not always calibrated, researchers might use a thermal camera for several years without calibration. Therefore, it is very important to figure out how the calibration will affect the thermal camera's data collection. Also, when the UAVs are flying in the field, the thermal camera will capture images in different view of angles. In this section, the author also studied the effects of the thermal camera's view of angles on the temperature data. For the photogrammetry process, the software Agisoft PhotoScan is frequently used. Thermal images are stitched together into an orthomosaick picture. The author also figured out if the stitching had any effect on the data process. To our best knowledge, there was little study talking about these thermal camera calibration issues before.

### 3.6.2 Material and Methods

#### Study Site

This research was conducted in a field near MESA Lab in Atwater, California, USA (37.37°N, 120.57°W). There were five different materials being used, water, dry soil, wet soil, leaves and white panels. All materials were put in cups, as shown in Fig. 3.13.

#### The Thermal Image Collection

The thermal camera ICI 9640 P-Series (ICI, USA) was used to collect thermal images. The thermal camera has a resolution of  $640 \times 480$  pixels. The spectral band is from  $7 \mu\text{m}$  to  $14 \mu\text{m}$ . The dimensions of the thermal camera is  $34 \text{ mm} \times$



Figure 3.13: This research was conducted in a field near MESA Lab in Atwater, California, USA (37.37°N, 120.57°W). There were five different materials being used, water, dry soil, wet soil, leaves and white panels.



(a) Experiment field.

(b) Thermal picture by IR Flash.

Figure 3.14: Calibration's effect experiment.

30 mm  $\times$  34 mm. In these research experiments, the .TIF images were taken for further image processing by Agisoft PhotoScan. The camera was attached under the experiment platform, as shown in Fig. 3.14(a). The camera was triggered 10 times per second by the ICI Software's function Capture Series Images in ground station computer (Fig. 3.14(b)).

### Groundtruth Data Collection

The infrared radiometer Apogee MI-220 was used in the research experiments to collect thermal data as groundtruth value. The MI-220 has a 18° half-angle field

of view (FOV). The response time for the MI-220 is only 0.6 seconds. It can be used in many areas, such as tree canopy temperature measurement, water stress estimation, soil temperature measurement and so on.

### **3.6.3 Results and Discussion**

#### **Experiment Setup**

There were three different experiments in this section. In the first experiment, the author analyzed the calibration's effect on thermal cameras. Second, the author studied the thermal camera's angle effect on the temperature data. Third, the author analyzed stitching's effect on the orthomosaick pictures. The author prepared five different materials for all experiments to stimulate the situations one might meet in the field. As shown in Fig. 3.14, there were water, wet soil, fresh leaves, dry soil, and white paper panels. Thus, we could analyze the thermal camera's effect on different materials.

#### **Thermal Camera Warm Up Time**

A thermal camera needs to be at (or close to) thermal equilibrium in order to produce accurate data. When the camera is turned on, the electronics inside produce heat, and it takes a while for the camera body to heat up enough for the rate of heat loss at the surface to match the rate of heat being produced on the inside.

This poses a challenge to flying a thermal camera on a UAV: even if the camera has been given sufficient time to reach equilibrium on the ground, the airflow increases heat transport away from the camera, upsetting the equilibrium again, and requiring additional time to adjust. However, due to the limited flight time of UAVs, especially multicopters, this time may be longer than the available flight time itself. The recommended equalization time for the camera used in the experiments was about half an hour.

## Calibration Experiment

In this section, the author compared two thermal cameras' temperature data. One was a new thermal camera, which meant calibrated thermal camera. The other one was a used camera, which was not calibrated. To minimize the thermal camera's effect on the experimental results, the author used exactly the same model ICI 9640 P for the calibrated and non-calibrated thermal cameras. As shown in Fig. 3.14(a), the author put the two thermal cameras at the same height 69.5325 cm to our materials. Both of them captured the same materials at the same time. Apogee MI-220 was used to collect data as groundtruth. As seen in Fig. 3.14(b), all materials were labeled by IR Flash, so it could test exactly the same temperature at the selected areas.

According to the Table 3.5, Table 3.6, Table 3.7, and Table 3.8, the calibrated camera had better root mean square error (RMSE) than the non-calibrated camera. For the calibrated camera, the RMSEs for water, wet soil, dry soil and leaf were 1.61 °C, 1.92 °C, 2.89 °C and 1.47 °C. For the non-calibrated camera, the RMSEs were 3.07 °C, 3.00 °C, 4.09 °C and 2.83 °C. The result was obviously as expected that calibrated camera had better results than non-calibrated thermal camera. In this experiment, however, we tried to figure out if the data collected by thermal cameras was always consistent. If the thermal camera was not accurate, was the temperature value always above or below the groundtruth value? Unfortunately, the answer was no. It made thermal calibration more difficult to estimate and to deal with.

## The View Angle of Thermal Camera

In this experiment, the author tested the thermal cameras' view angle effect on temperature. In an unmanned aerial vehicle system, the thermal cameras are usually mounted on the UAVs and capturing images when the UAVs are flying over field. For example, in an almond orchard, the tree canopies can show up in different positions in thermal images. This may cause the canopy has different temperature in different view of angles. In this section, the author figured out if the view angles had any effect on the thermal images. The thermal picture has

Table 3.5: The groundtruth.

Time	Water (°C)	wet soil (°C)	dry soil (°C)	leaf (°C)
2:53	34.2	36.9	51.2	44.1
3:02	34.1	34.7	52.3	42.9
3:06	35.2	36.3	51.7	41.2
3:10	35.0	36.4	52.5	43.0
3:14	32.1	35.1	50.3	41.0
3:17	36.5	37.0	49.8	41.3
3:21	35.0	37.5	50.2	41.2
3:25	34.1	37.4	51.5	40.8
3:29	34.1	34.6	50.5	39.7
3:32	34.2	36.9	49.6	39.6
3:36	34.5	33.6	50.5	41.6
3:40	34.1	34.3	50.3	41.6
3:44	33.9	34.0	49.5	42.9
3:48	33.8	35.2	50.3	41.3
3:51	33.0	33.1	49.0	38.3

Table 3.6: The measurement from the non-calibrated camera.

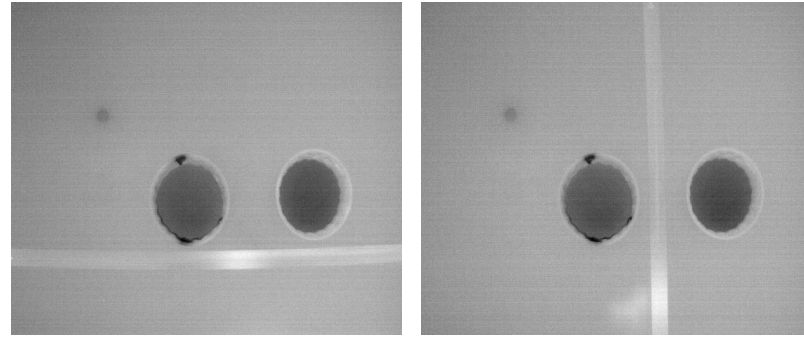
Time	Water (°C)	wet soil (°C)	dry soil (°C)	leaf (°C)
2:53	41.27	42.53	59.22	48.45
3:02	37.32	38.30	54.96	44.91
3:06	36.42	37.46	54.86	43.91
3:10	35.44	36.10	53.63	45.04
3:14	36.67	37.13	54.55	46.13
3:17	36.59	36.71	53.96	43.11
3:21	37.38	38.63	55.86	42.91
3:25	36.03	42.32	53.85	41.95
3:29	33.82	34.39	51.66	39.71
3:32	36.64	37.09	53.69	40.26
3:36	37.53	38.33	54.97	46.21
3:40	35.50	35.89	52.78	41.93
3:44	35.87	36.66	52.94	42.93
3:48	38.29	39.30	55.37	45.38
3:51	35.83	36.34	52.69	42.01

Table 3.7: The measurement from the calibrated camera.

Time	Water (°C)	wet soil (°C)	dry soil (°C)	leaf (°C)
2:53	34.38	35.99	53.21	41.95
3:02	36.03	37.38	54.28	43.50
3:06	34.42	35.88	52.85	40.23
3:10	35.22	36.21	53.31	42.24
3:14	35.83	37.01	54.00	44.33
3:17	35.73	36.53	53.47	41.03
3:21	34.96	36.03	53.45	40.20
3:25	36.12	37.41	54.60	41.38
3:29	35.39	36.49	53.44	37.89
3:32	35.53	36.63	53.11	40.07
3:36	35.39	36.72	53.46	42.63
3:40	35.46	36.74	53.26	43.60
3:44	36.22	37.47	53.52	44.36
3:48	34.60	36.03	51.91	39.75
3:51	35.00	36.06	52.28	39.06

Table 3.8: The root mean square error.

Materials	Calibrated camera (°C)	Non-calibrated camera (°C)
Water	1.61	3.07
Wet soil	1.92	3.00
Dry soil	2.89	4.09
Leaf	1.47	2.83



(a) Thermal picture by IR Flash, horizontal measurement. (b) Thermal picture by IR Flash, vertical measurement.

Figure 3.15: View angle experiment.

a pixel value of  $640 \times 480$ . The central point pixel value is  $320 \times 240$ . After we found the test point temperature, we also found the pixel value of the test point (Fig. 3.15). In the thermal picture, one pixel value represented 0.09525 cm. Then, we could calculate the horizontal distance between the camera center and the test point. As mentioned in the previous section, the camera's vertical distance to the test point was 69.5325 cm. Then, the accurate half view angle could be calculated in this experiment.

According to Table 3.9, there were 8 different half view angles,  $4.2^\circ$ ,  $4.6^\circ$ ,  $6.0^\circ$ ,  $8.3^\circ$ ,  $11.6^\circ$ ,  $12.7^\circ$ ,  $14.3^\circ$ , and  $16.7^\circ$ . The errors between the groundtruth and the collection data were less than  $0.5^\circ\text{C}$ . The root mean square error was much less than  $0.01^\circ\text{C}$ . The results showed that the the thermal camera's view angles had little effect on collecting data.

### The Effect of Stitching

After the thermal images were collected from thermal cameras, many researchers liked to process the data by Agisoft PhotoScan software. In this software, we could stitch all the pictures into one orthomosaick picture which represented the whole field, as shown in Fig. 3.16(b). In this experiment, it figured out if this Align Photos function had any effect on temperature data. As shown in Table 3.10, there were 28 samples in this experiment. They were divided into four groups, which

Table 3.9: The view angle experiment.

Half view angle(°)	Location in the picture	Point temperature(°C)	Groundtruth(°C)
4.2	363 × 275	12.41	12.40
4.6	372 × 269	12.52	12.40
6	354 × 311	11.79	12.40
8.3	352 × 344	12.28	12.40
11.6	342 × 391	12.38	12.40
12.7	337 × 406	12.11	12.40
14.3	336 × 428	11.90	12.40
16.7	329 × 462	12.26	12.40

were water, dry soil, wet soil and white paper panels. There were labels in each picture, so we could accurately find the same temperature point in the single image and the orthomosaick picture. To calculate the temperature, the author used the MATLAB 2017b to get the average temperature for a selected area.

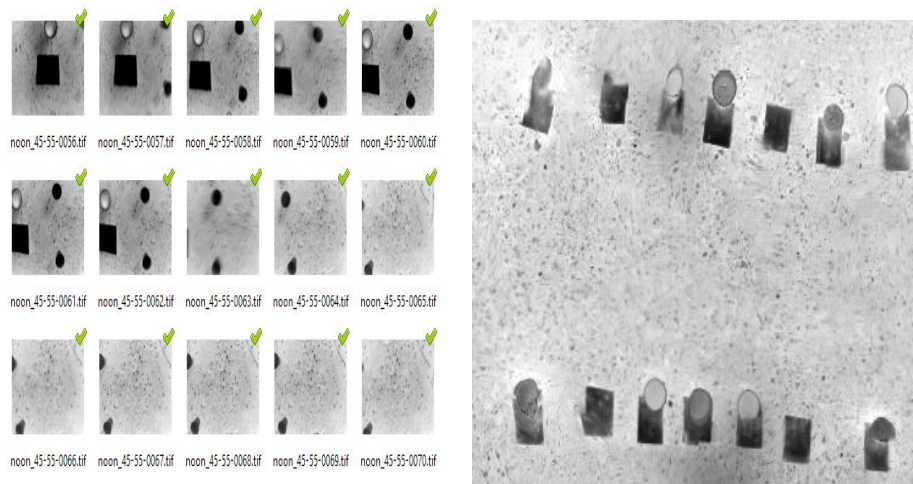
Based on the data in Table 3.10, the temperature errors between the single image and the orthomosaick were less than 1 °C. According to Table 3.11, for different materials, the root mean square errors were different. For example, the water in a single image had a root mean square error as 0.646 °C. In the orthomosaick picture, the value was 0.834 °C. The result showed that the Agisoft PhotoScan’s stitching process had little effect on the thermal data.

### 3.6.4 Conclusions and Future Work

In this section, it discussed three factors’ effect on the thermal camera calibration. They were fundamental and useful. First, calibrated thermal camera did have better results compared with the non-calibrated thermal camera. However, even the calibrated thermal camera’s data was not consistent. The thermal camera itself could be a reason. The uncooled thermal camera’ microrobolometer was not accurate and sensitive. Second, the thermal camera’s view angles had little effect on the temperature data. The thermal camera’s accuracy was  $\pm 1$  °C. The data errors in this section was less than 1 °C and the root mean square error was less than 0.01 °C. Third, after the photogrammetry process, the stitching did have a

Table 3.10: The stitching effect on the data.

Sample number	Materials	Groundtruth (°C)	Single image (°C)	Orthomosaick (°C)
1	water	17.4	17.74	18.2648
2	water	17.5	17.53	17.9962
3	water	17.4	17.75	18.1876
4	water	17.2	18.23	18.4245
5	water	17.2	16.35	16.5322
6	water	17.4	16.73	17.2438
7	water	16.8	17.47	17.9345
8	dry soil	15.8	15.72	16.6309
9	dry soil	14.4	13.93	14.5372
10	dry soil	14.2	13.53	13.3192
11	dry soil	14.7	14.61	14.8676
12	dry soil	15.4	15.45	15.6241
13	dry soil	14.8	15.51	15.6242
14	dry soil	14.5	15.26	15.3906
15	wet soil	14.8	14.84	15.8454
16	wet soil	13.9	14.38	15.7918
17	wet soil	14.8	14.06	14.9511
18	wet soil	14.1	15.37	14.3389
19	wet soil	14.9	14.89	15.7558
20	wet soil	14.6	14.24	14.8981
21	wet soil	14.3	14.77	15.2562
22	paper	13.6	12.67	13.9083
23	paper	13.8	12.42	12.9427
24	paper	14.5	14.02	15.2562
25	paper	12.8	11.55	13.9083
26	paper	12.4	11.75	12.9427
27	paper	13.9	11.13	12.1386
28	paper	12.4	11.36	11.8678



(a) The images taken by ICI thermal camera. (b) The thermal orthomosaick picture which represented the whole field.

Figure 3.16: The effect of stitching experiment.

Table 3.11: The root mean square error.

Materials	Single images ( $^{\circ}\text{C}$ )	Orthomosaick ( $^{\circ}\text{C}$ )
Water	0.646	0.834
Dry soil	0.503	0.658
Wet soil	0.626	0.963
White panel	0.912	0.949

little effect on the orthomosaick picture we got. The temperature in the orthomosaick was greater than the temperature in single image. This could be caused by the stitching process.

In the future, the author will keep working on the thermal camera calibration problem. A more accurate, real time and state-of-art thermal camera calibration method will be proposed in the future.

## 3.7 Case Study III: High Spatial-resolution Has Little Impact on NDVI Mean Value of UAV-based Individual Tree-level Mapping: Evidence from 9 Field Tests and Implications

### 3.7.1 Introduction

The normalized difference vegetation index (NDVI) has been used for many agriculture-related research topics, such as water stress detection [192, 232], crop yield assessment [224], and *ET* estimation [142, 28]. The NDVI is usually calculated by

$$NDVI = \frac{\rho_{nir} - \rho_r}{\rho_{nir} + \rho_r}, \quad (3.2)$$

where  $\rho_{nir}$  and  $\rho_r$  are the reflectances of the near-infrared and red wavebands, respectively. NDVI is a standardized method to measure healthy vegetation. When the NDVI is high, it indicates the vegetation has a higher level of photosynthesis.

To date, satellite-derived NDVI has been commonly used for crop coefficient values estimation [244, 245, 246]. For example, Trout *et al.* [247] and Zhang *et al.* [248] applied a remote sensing method using the NDVI to estimate canopy ground cover as a basis for generating crop coefficient ( $K_c$ ). Kamble *et al.* [244] used a simple linear regression model to establish a relationship between the NDVI and  $K_c$ . Although satellite imagery can obtain spatially distributed measurements, they cannot acquire high spatio-temporal resolution images for precision agriculture applications [249]. The timing of satellite overpass is not always synchronous

with research requirements, either.

With the development of new remote sensing technology, the unmanned aerial vehicles (UAVs) have been commonly used in agricultural applications, such as crop yield estimation [224], irrigation managements [24, 27], water stress estimation [146], and pest management [225, 250]. Compared with the satellite, the flight of UAVs can be more flexible and frequent in the field. The UAVs fly at a lower altitude and take higher resolution imagery of crops [190]. The UAVs also make data acquisition relatively less expensive. However, one may fly the UAV at different flight heights. What is the optimal UAV flight height for research can be an interesting topic. In previous paper [251], Awais *et al.* investigated the optimal timing and altitude for thermal imagery collection using UAV in an Anji tea plant experimental field. The results reported that the thermal imagery could provide the best correlation and accurate canopy temperature when the UAV flights were at 11 am and 60 m altitude. In previous article [27], the authors applied supervised learning methods to study the correlation between imagery features and onions irrigation treatments. Then, it figured out how UAV flight height or resolution settings affect the accuracy of onion irrigation treatment inference.

Studies of [27, 251] showed the importance of UAV flight height or spatial resolution's effect on data analysis. To date, few studies have investigated the association between NDVI and UAV flight height or spatial resolution at **individual tree level**. The **objective of this study** are: 1. Investigate how the UAV flight height or spatial resolution affects the mean NDVI for individual tree-level canopy. 2. Check the reliability of the multispectral sensor for different heights of UAV flight missions. The **major contribution of this section** are: 1. Publish a dataset on Dryad for a high-spatial-resolution UAV imagery research study. All the datasets will be available at DRYAD<sup>2</sup> for research purpose. 2. Point out the importance of variability analysis of individual tree-level research.

---

<sup>2</sup>All the datasets will be available at <https://doi.org/10.6071/M3JH4Q> for research purpose. Citation: Niu, Haoyu; Chen, YangQuan (2021), Rededge M pomegranate field 60m, 90m, 120m, Dryad, Dataset, <https://doi.org/10.6071/M3JH4Q>



Figure 3.17: The pomegranate study site at USDA. The pomegranate was planted in 2010 with a 5 m spacing between rows and 2.75 m within-row tree spacing in a 1.3 ha field. There are two large weighing lysimeters located in the center of the field, marked in red boxes.

### 3.7.2 Material and Methods

#### The Study Site

The flight missions were conducted in a pomegranate field (Fig. 3.17) at the USDA-ARS, San Joaquin Valley Agricultural Sciences Center (36.594 °N, 119.512 °W), Parlier, California, 93648, USA.

#### The UAV and the Multispectral Sensor

In this article, the UAV platform, named “Hover,” was adopted to conduct this exploratory study. The authors chose the Rededge M camera (MicaSense, Seattle, WA, USA) to obtain multispectral imagery. The multispectral sensor has five different bands, which are Blue (475 nm), Green (560 nm), Red (668 nm), Near-infrared (840 nm), and Red edge (717 nm). The Rededge M has a spectral resolution of 8.2 cm/pixel (per band) at 120 m (400 ft.) above ground level (AGL), with a 46° field of view.

Table 3.12: The UAV flight schedule. The UAV flight height was 60 m, 90 m, and 120 m to acquire different high-resolution multispectral imagery. Data was collected successfully for three different days, 5-8-19, 9-19-19, and 10-3-19.

Dates	Flight time	Flight height
May 8 <sup>th</sup> , 2019	12 - 1 pm	60 m, 90 m and 120 m,
Sep 19 <sup>th</sup> , 2019	12 - 1 pm	60 m, 90 m and 120 m,
Oct 3 <sup>rd</sup> , 2019	12 - 1 pm	60 m, 90 m and 120 m.

### Details of the UAV Imagery Dataset

The UAV flight height was 60 m, 90 m, and 120 m to acquire different high-resolution multispectral imagery. Data was collected successfully (Table 3.12) for three different days, 5-8-19, 9-19-19, and 10-3-19. All of the multispectral images were then processed to generate the orthomosaick images in Metashape (Agisoft LLC, Russian).

The source data for building DEM was the dense cloud. For the interpolation method, **Extrapolated** option was selected because it could generate a surface without gaps being extrapolated to the bound box sides. The default option for **Interpolation** was **Enabled**, which was not recommended because it would leave the valid elevation values only for fields seen from at least one aligned camera.

### 3.7.3 Results and Discussion

#### The Relationship Between NDVI and UAV Flight Height

The mean NDVI values of each sampling tree were shown in Fig. 3.18, Fig. 3.19, and Fig. 3.20. Theoretically, for each sampling tree, the mean NDVI value of the tree canopy should have the same value at 60m, 90m, and 120m. However, the values of NDVI could be very different from each other considering the weather conditions (Fig. 3.19), such as the cloud.

**Key observation:** In Fig. 3.19, the NDVI values were significantly different for trees from 1 to 20, and from 31 to 50. The reason was that for image segmentation,

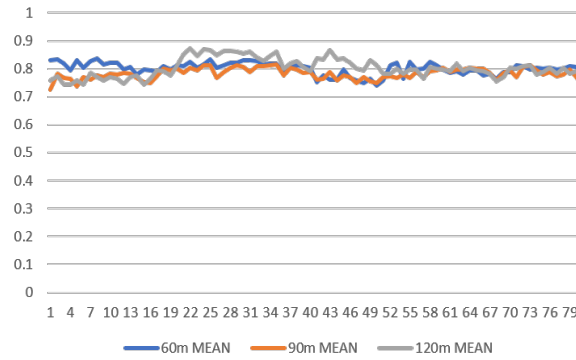


Figure 3.18: The mean NDVI values of each sampling tree at 60 m, 90 m, and 120 m on May 8<sup>th</sup>, 2019. The  $x$ -axis was the identification number (ID) for sampling trees, 82 in total. The  $y$ -axis was the mean NDVI value for each tree canopy.

more shades were included in the tree canopy. In Fig. 3.18 and Fig. 3.20, the data was more consistent for different UAV flight height. For example, in Fig. 3.21, the author compared the correlation of NDVI values between 90 m and 120 m. The result showed there was a strong correlation between them, with  $R^2 = 0.7$ .

### Individual Tree Canopy Segmentation Using Support Vector Machine (SVM)

To obtain the individual tree level NDVI values of the 82 sampling trees, the author used the SVM for classifying the tree canopy. Using the SVM classifier could map the input data vectors into a higher dimensional feature space. Then, the SVM optimally separated the data into different classes. Since the multispectral UAV imagery was large, the SVM classifier was adopted, which was less susceptible to noise, correlated bands, and unbalanced number or size of training sites within each class. All the sampling trees were successfully segmented using the SVM classifier.

**Key observation:** For simplicity, the author only created the NDVI distribution for the two trees in lysimeter (Fig. 3.22, Fig. 3.23 and Fig. 3.24). For example, in Fig. 3.22, the NDVI distributions for the two trees in the lysimeter were generated. The NDVI was for May 8<sup>th</sup>, and the UAV flight height was at 60

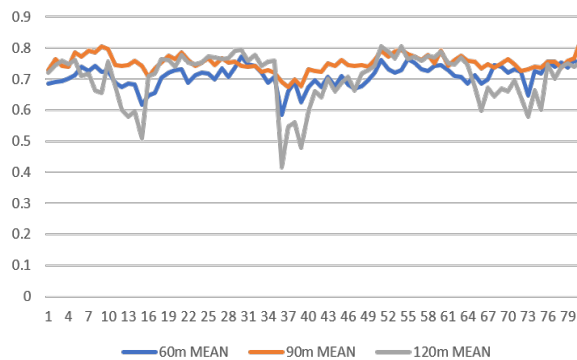


Figure 3.19: The mean NDVI values of each sampling tree at 60 m, 90 m, and 120 m on Sep 19<sup>th</sup>, 2019. The  $x$ -axis was the identification number (ID) for sampling trees, 82 in total. The  $y$ -axis was the mean NDVI value for each tree canopy.

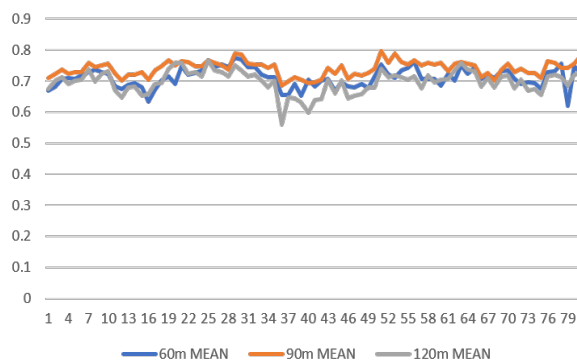


Figure 3.20: The mean NDVI values of each sampling tree at 60 m, 90 m, and 120 m on Oct 3<sup>rd</sup>, 2019. The  $x$ -axis was the identification number (ID) for sampling trees, 82 in total. The  $y$ -axis was the mean NDVI value for each tree canopy.

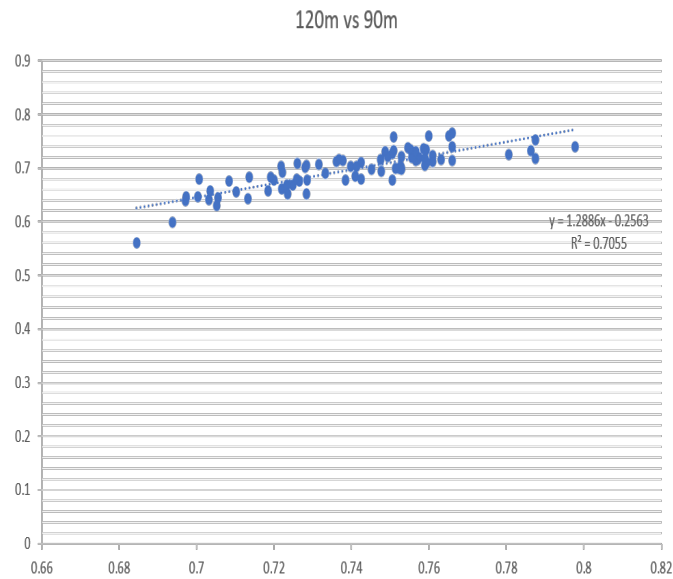
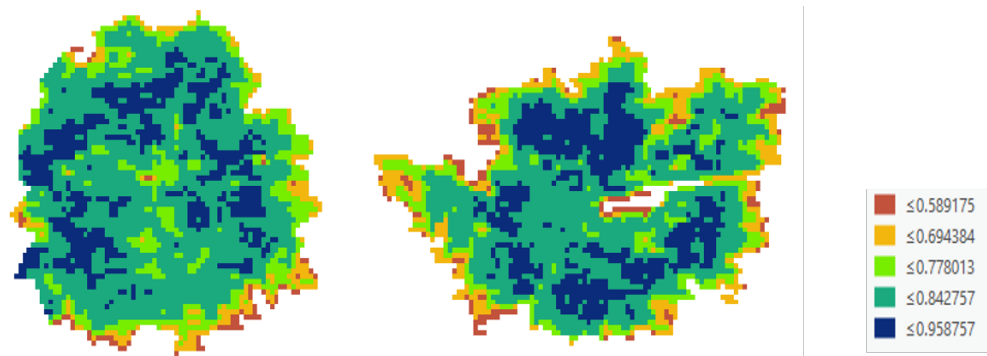


Figure 3.21: The individual tree-level mean NDVI correlation between 120 m and 90 m on Oct 3<sup>rd</sup>, 2019. The  $x$ -axis was the mean NDVI values for sampling trees at 120 m flight height. The  $y$ -axis was the mean NDVI values for sampling trees at 90 m flight height.

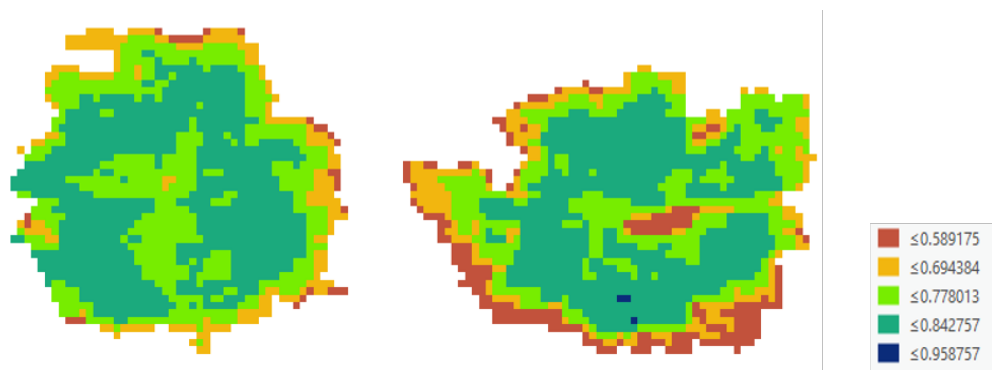
m, 90 m, and 120 m. The color bar meant the range of the NDVI values (from -1 to 1). Based on the above section, “The relationship between NDVI and UAV flight height”, there was no significant difference for mean NDVI value at individual tree level. However, as shown in Fig. 3.22, lower flight height (60 m) gave a higher spatial resolution image. The NDVI distribution inside the canopy was more precise than that in higher flight height. Therefore, what the average told us could be wrong. How to use this high-resolution benefit from UAV imagery can be discussed in the near future. Variability analysis may play an important role in individual tree-level research.

### Entropy of Individual Tree-level NDVI Image

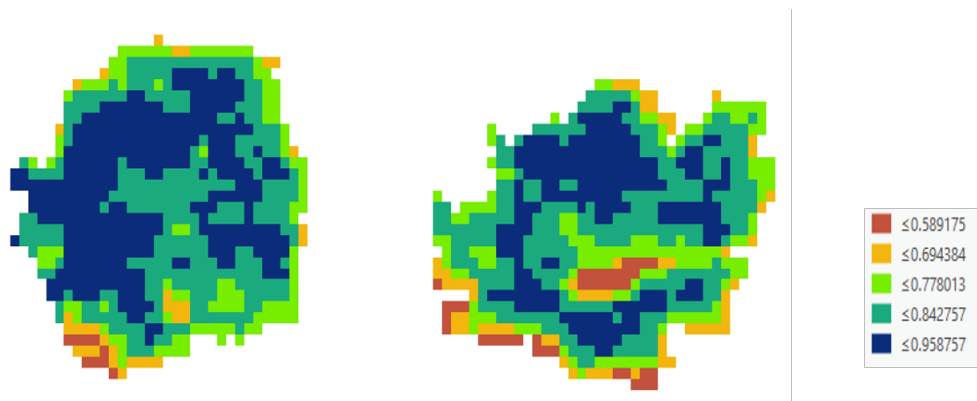
To characterize the texture of the individual tree-level NDVI image of the lysimeter trees, the author adopted the entropy method, which was a statistical measurement of the randomness in the image. Entropy was defined as -



(a) The NDVI distribution of individual lysimeter trees at 60 m flight height.

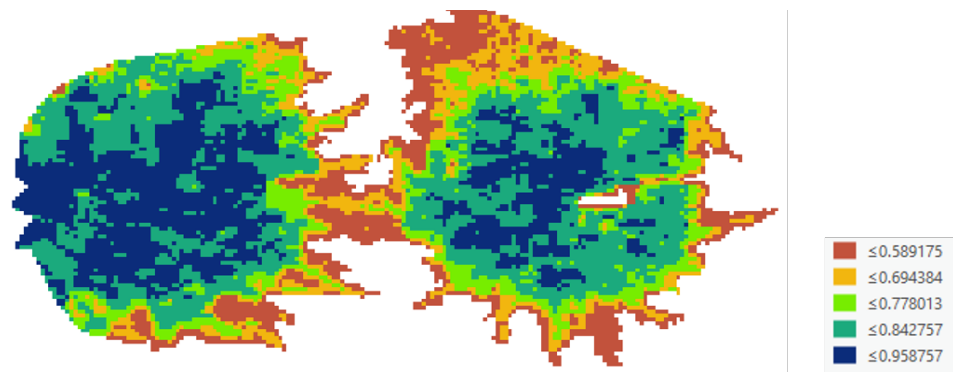


(b) The NDVI distribution of individual lysimeter trees at 90 m flight height.

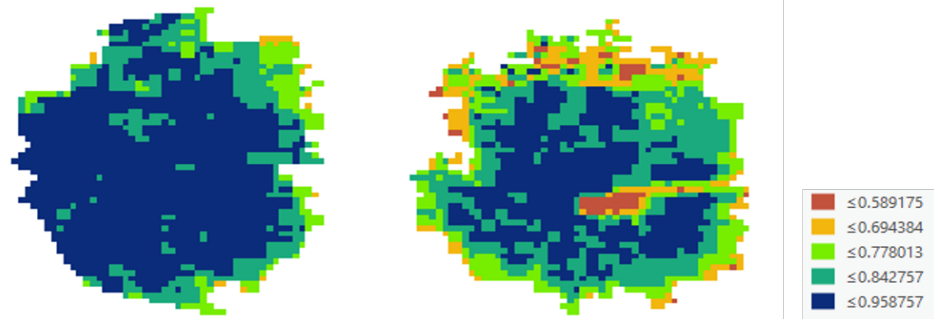


(c) The NDVI distribution of individual lysimeter trees at 120 m flight height.

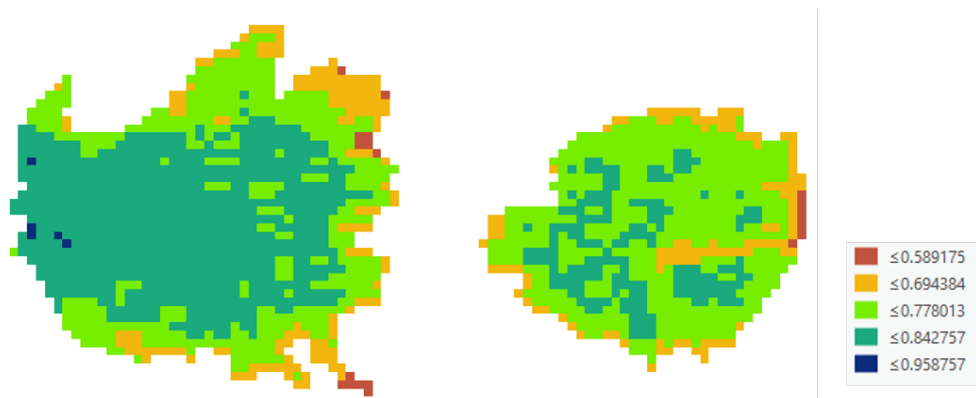
Figure 3.22: The NDVI distribution of two individual lysimeter trees at 60 m, 90 m and 120 m on May 8<sup>th</sup>, 2019.



(a) The NDVI distribution of individual lysimeter trees at 60 m flight height.

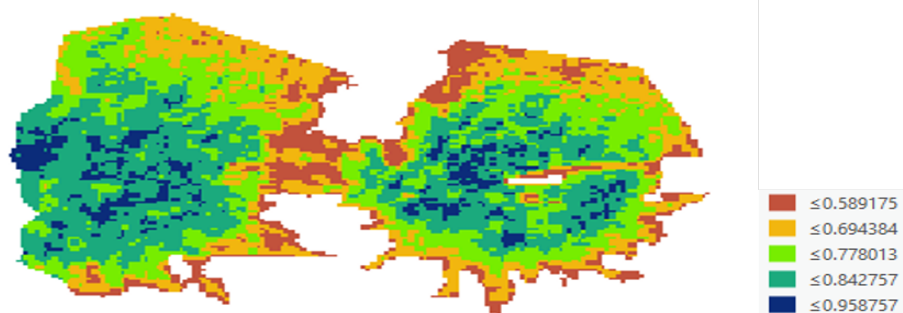


(b) The NDVI distribution of individual lysimeter trees at 90 m flight height.

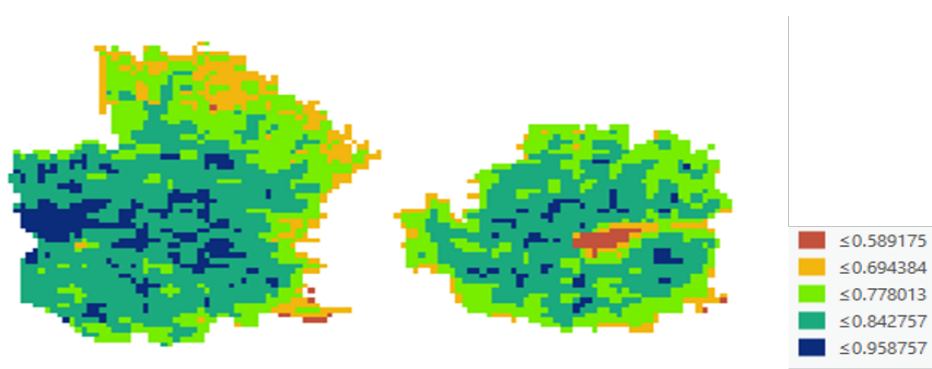


(c) The NDVI distribution of individual lysimeter trees at 120 m flight height.

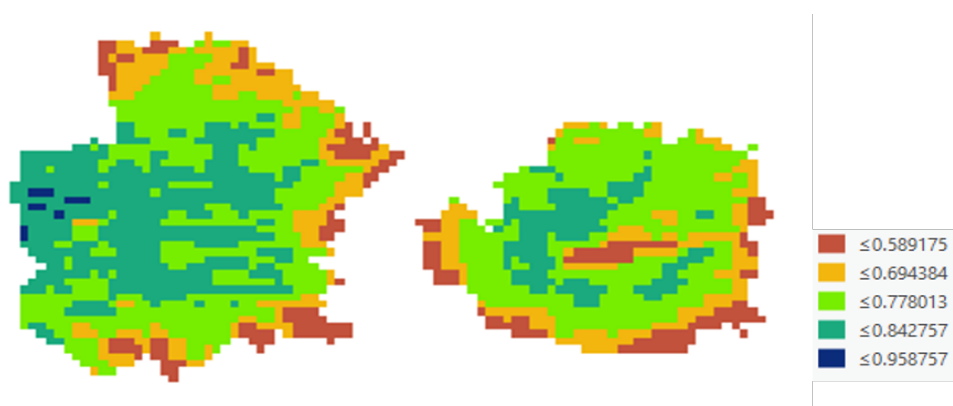
Figure 3.23: The NDVI distribution of two individual lysimeter trees at 60 m, 90 m and 120 m on Sep 19<sup>th</sup>, 2019.



(a) The NDVI distribution of individual lysimeter trees at 60 m flight height.



(b) The NDVI distribution of individual lysimeter trees at 90 m flight height.



(c) The NDVI distribution of individual lysimeter trees at 120 m flight height.

Figure 3.24: The NDVI distribution of two individual lysimeter trees at 60 m, 90 m and 120 m on Oct 3<sup>rd</sup>, 2019.

Table 3.13: Entropy was used in the quantitative analysis and evaluation of image information, because it provided better comparison of the image details. Higher value of entropy meant more detailed information in the image.

Dates	60 m	90 m	120 m
May 8 <sup>th</sup> , 2019	2.0176	2.0789	1.7984,
Sep 19 <sup>th</sup> , 2019	4.5861	3.7598	3.1027,
Oct 3 <sup>rd</sup> , 2019	3.2812	3.6725	4.0022.

$\text{sum}(p \cdot \log_2(p))$ , where  $p$  contained the normalized histogram counts returned from the MATLAB command “imhist” [252]. It was used in the quantitative analysis and evaluation of image details. Higher value of entropy meant more detailed information in the image.

**Key observation:** As shown in Table 3.13, the higher entropy value for lysimeter trees was obtained at 90 m on May 8<sup>th</sup>. However, the higher value entropy were at 60 m and 120 m on Sep 19<sup>th</sup> and Oct 3<sup>rd</sup>, respectively. Therefore, high spatial-resolution had low impact on the UAV-based individual tree-level NDVI images. There was no significant difference for image information in range of 60 m to 120 m of UAV flight height.

### 3.7.4 Conclusions and Future Work

In this study, UAV flight missions were conducted to collect multispectral imagery at different flight height (60 m, 90 m, and 120 m). After image processing, the author contributed a dataset on Dryad for a high-spatial-resolution UAV imagery research study.

Using the NDVI derived from UAV images, the author analyzed how spatial resolution could affect the NDVI values at the individual tree level. According to the results, there was no significant difference for mean NDVI value at individual tree level for different flight heights when the data was processed appropriately. The  $R^2$  of mean NDVI values between 90 m and 120 m was around 0.7, which

proved the multispectral sensor was reliable for data collection. However, the shade around the tree canopy could be a key factor for tree canopy segmentation (Fig. 3.19), which could reduce the mean NDVI significantly.

Lower flight height (60 m) did give a higher spatial resolution image. The NDVI distribution inside the canopy was more precise than that in higher flight height. Therefore, what the average tells us can be wrong. How to use this high-resolution benefit from UAV imagery can be discussed in the near future. Variability analysis may play an important role in individual tree-level research. In the future, the author will apply the conclusion to NDVI related research topics, such as evapotranspiration estimation, stem water potential, and yield estimation.

### 3.8 Conclusion and Future Research

Compared with traditional remote sensing tools, the UAV and lightweight payloads can be more flexible and frequent in the field. UAVs can fly at a lower altitude and can take higher spatial and temporal resolution images of crops. As a low-cost scientific data collection platform, UAVs also make data acquisition relatively less expensive. While there are many advantages by using UAVs for agricultural research, the author also discussed the challenges for UAV flight missions with different remote sensing payloads.

Based on the current research results, the author presents the following potential research directions for future investigation.

1. For future research, uncooled thermal cameras can be used to evaluate with other temperatures sensor information to acquire reliable thermal information, such as atmospherically corrected satellite images and temperature canopy sensors.
2. How to benefit the research study from high-resolution UAV imagery can be discussed in the near future.
3. Is there any optimal point where the data can be the best representation of crops or trees? As researchers try to understand the potential of the UAVs,

efficient workflow, image processing methods, and better software are still under developing.

# Chapter 4

## The Edge-AI Sensors and Internet of Living Things (IoLT)

### 4.1 Introduction

The term “Internet of things” was first created by Kevin Ashton of Procter & Gamble, later MIT’s Auto-ID Center, in 1999 [253]. The Internet of things (IoT) can describe physical objects that are embedded with sensors, software, and other technologies, which connect and exchange information with other equipment or systems over the Internet or other communication networks [254, 255, 256]. This research topic has been gaining interest because of the convergence of multiple technologies, such as ubiquitous computing, commodity sensors, embedded systems, and machine learning. There are extensive applications for IoT devices, such as agriculture, medical and healthcare [257, 258], and manufacturing [259]. For example, many researchers have been working on the application of the IoT technology in agriculture [260, 261, 262]. In [263], Zhao *et al.* selected mobile wireless communication technology to achieve greenhouse monitoring with IoT technology. Research results showed that the greenhouse monitoring system based on IoT technology could automatically control the environmental temperature and humidity factors. In [264], Hamad *et al.* emphasized the the role of smartphones for collecting agricultural parameters and its advantages in the field of agriculture. Using

the smartphone enabled the farmers to have a positive impact on communication with producer's network and improved the awareness of farming community.

Considering the author's research experience in agriculture, he proposed the concept of "Internet of Living Things (IoLT)" in this chapter. In the dictionary, a "living thing" pertains to any organism or a life form that possesses or shows the characteristics of life or being alive. The fundamental characteristics are 1.) having an organized structure, 2.) requiring energy, 3.) responding to stimuli and adapting to environmental changes, 4.) being capable of reproduction, growth, movement, metabolism, and death. For most of agricultural applications of IoT, it actually can also be considered as the IoLT. Researchers collect data of crops or trees, such as tree canopy temperature, rainfall, humidity, wind speed, soil moisture, and stem water potential, etc. After the analysis of recorded data, stakeholders or researchers can help make better decisions to increase the farm productivity, improve the sustainability, and reduce the costs.

The proximate sensors play a key role in IoLT. Therefore, in the rest of this chapter, the author introduced several sensors he commonly used in the research work.

## **4.2 Proximate Sensors**

### **4.2.1 The Spectrometer**

The spectrometer EPP2000-VIS-50 was used for the author's onion irrigation treatment inference research. The StellarNet EPP2000 Spectrometers (StellarNet, Inc., Tampa, Florida, USA) are miniature fiber optic instruments for ultraviolet (UV), visible (VIS), and near-infrared (NIR) measurements in 190 - 1700 nm ranges (Fig. 4.1). The technical specifications of EPP2000-VIS-50 was listed in Table 4.1 for reference.



Figure 4.1: The spectrometer EPP2000-VIS-50. The StellarNet EPP2000 Spectrometers are miniature fiber optic instruments for ultraviolet (UV), visible (VIS), and near-infrared (NIR) measurements in 190 - 1700 nm ranges.

Table 4.1: The specifications of spectrometer EPP2000-VIS-50.

<b>Specifications:</b>	
Wavelength range	190 - 1700 nm,
Base unit size	$15.5 \times 9.5 \times 4.0$ cm,
Base unit mass	500 g,
Detector	2048 pixel, $14 \times 200$ $\mu m$ ,
Linear range	0 - 2.1 absorbance units ( $< 0.5\%$ ),
Exposure range	4 milliseconds to 60 seconds,
Integration time range	4 - 6500 ms,
Wavelength accuracy	$< 0.25$ nm,
Wavelength repeatability	$< 0.05$ nm.
Wavelength stability	$< 0.001$ nm per $^{\circ}C$ .



Figure 4.2: A light and small near-infrared spectrometer, Scio. The low power consumption and zero warm up time make it highly responsive and extremely efficient, which allows it to perform hundreds of samplings from a small rechargeable battery. The Scio spectrometer works in NIR at wavelengths of 700 - 1100  $nm$ . It can also be integrated into smart phone as an Edge-AI device.

### 4.2.2 A Pocket-sized Spectrometer

Recently, a light and small near-infrared spectrometer, Scio (Consumer Physics, Israel) was released in the market (Fig. 4.2). They used advances in micro-optical technology to miniaturize the traditional near-infrared spectrometer. The optical head is just a few millimeters in size and can provide sensitivity and accuracy levels on par with the best bench spectrometers. The low power consumption and zero warm up time make it highly responsive and extremely efficient, which allows it to perform hundreds of samplings from a small rechargeable battery. The Scio spectrometer works in NIR at wavelengths of 700 - 1100  $nm$ . It is so small that it can even be integrated into the smartphone as an Edge-AI device. This system is a low-cost module, with a price less than \$300. The technical specifications of Scio was listed in Table 4.2 for reference.

### 4.2.3 A Microwave Radio Frequency 3D Sensor

The reflectance of the environment being sensed was collected with a radio frequency 3D sensor called Walabot Developer (Fig. 4.3) (Vayyar Imaging Ltd, Yehud-Monosson, Israel). The frequency range was 3.3 - 10 GHz for the US/FCC model and 6.3 - 8 GHz for the EU/CE model. The average transmitted energy of

Table 4.2: The specifications of spectrometer Scio.

<b>Technical specifications:</b>	
Wavelength range	700 - 1100 nm,
Dimensions Handheld Device	Cover: $67.7 \times 40.2 \times 18.8$ mm,
Weight handheld device	35 g,
Standalone sensor module	$27.5 \times 9.5 \times 3.15$ mm,
Operational distance	Contact to 2 cm,
Typical scan time	2 - 5 seconds,
Connectivity	Online and offline scanning supported,
Temperature range - operation	4 - 35 °C.

both models was below 41 dBm/MHz and did not constitute health concerns for the user, nor did it impact the tested tissues. Based on the technical specifications, the Walabot could sense the environment by transmitting, receiving, and recording signals from multiple antennas. Recordings of multiple transmit-receive antenna pairs were analyzed to build a 3D image of the examined environment. Changes in the environment were characterized by analyzing sequences of images. Then, researchers could detect changes in the environment by analyzing the sequences of images.

The Walabot used an antenna array to send radio frequency to the area in front of it and then captured the returning signals (reflectance or response). The citation signals were produced, and the reflectance was then recorded by integrated circuits (Fig. 4.4). The reflectance data were preprocessed by MATLAB 2020a. For example, records of the different reflectance strengths could be visualized in a graph (Fig. 4.5). The  $y$ -axis denoted the radio frequency reflectance from a walnut leaf. The  $x$ -axis meant the time. The research hypothesis was that the radio frequency reflectance of walnut leaves would be significantly different towards root-lesion nematode infection levels. Then, the spectral curve obtained from the leaves of walnut trees infected with nematodes could show the characteristic pattern of walnut under nematode stress. For more details of this research work, please refer

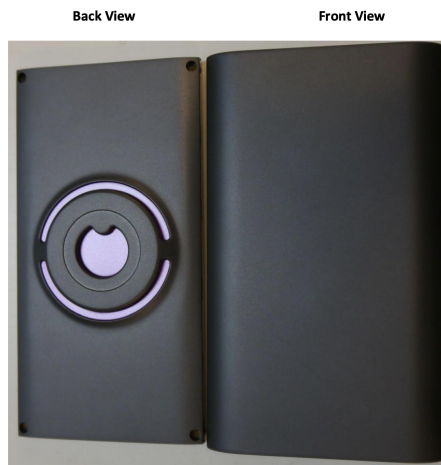


Figure 4.3: A radio frequency 3D sensor, Walabot Developer (Front and back view). The frequency range was 3.3 - 10 GHz for the US/FCC model and 6.3 - 8 GHz for the EU/CE mode. The average transmitted energy of both models was below 41dBm/MHz and did not constitute health concerns for the user, nor did it impact the tested tissues.

to Chapter 6.

## 4.3 Case Study: Onion Irrigation Treatment Inference Using A Low-cost Edge-AI Sensor

### 4.3.1 Introduction

Onions are produced and consumed throughout the world. It is worldwide used in different countries and cultures during all seasons in a year [227]. California produces the most onion in the US. In 2015, it produced around one third of the total onion crop in the US. It is the only state that can produce spring and summer-harvested onions [265]. Onions are shallow-rooted crop, and most of the roots can be found in the top 0.18 m of soil [266]. This makes it hard for onions to obtain enough soil water. Therefore, lighter and more frequent irrigation are recommended in onion cultural practices [267]. On the other hand, experimental results showed that water stress could also cause reduction in the yield at any growing stages [268].

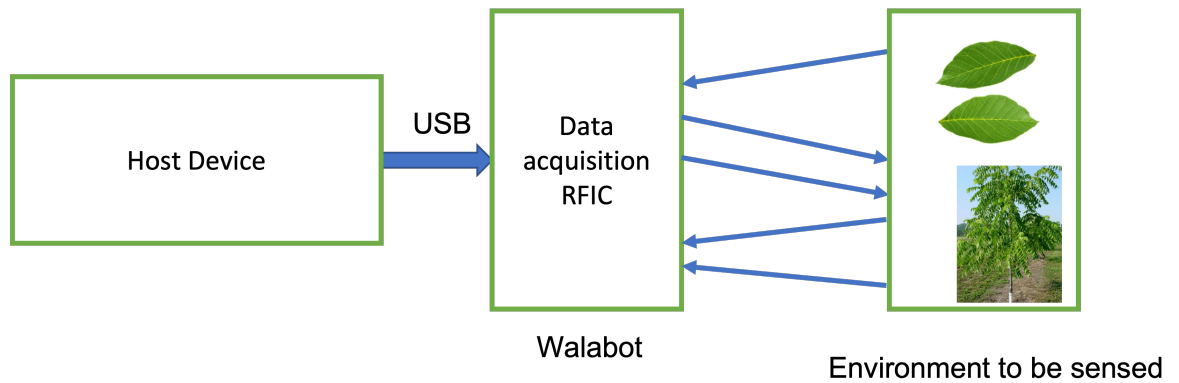


Figure 4.4: The principle of Walabot. The sensor uses an antenna array to send radio frequency to the area in front of it, e.g. walnut leaves, and then captures the returning signals (reflectance or response). The citation signals are produced, and the reflectance is then recorded by the radio frequency integrated circuits (RFIC).

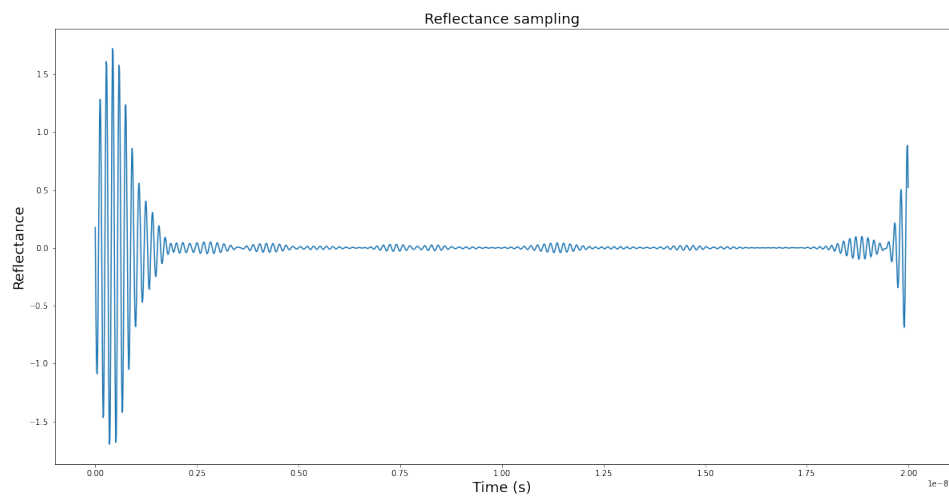


Figure 4.5: The measurement signal of the radio frequencies reflectance of the walnut leaves using Walabot. The research hypothesis is that the reflectance of walnut leaves will be significantly different towards root-lesion nematode infection levels. The spectral curve obtained from the leaves of walnut trees infected with nematodes could show the characteristic pattern of walnut under nematode stress. For more details of this research work, please refer to Chapter 6.

To optimize irrigation schedule, it is necessary to have accurate and reliable water stress monitoring methods. Many studies have been published on water stress detection using remote sensing, real-time and nondestructive methods [269]. Near-infrared cameras were used to detect water stress of almond trees [192, 229, 230, 231, 146, 232], where new types of spectral features were proposed to predict stem water potential. Hyperspectral sensors were also applied for water stress monitoring in apple trees [270], vineyard [271, 272], etc. For onions, studies of remote sensing were conducted on yield and biomass prediction using the spectroradiometer [273], biomass monitoring using UAVs and RGB cameras [233], detecting diseased onion tissues [234], quality inspections [274, 275]. However, to date, little research has been conducted on the irrigation treatment inference using the spectrometer. Furthermore, Scio, as a low-cost portable, light spectrometer, was also evaluated to infer irrigation treatments in onions for the first time.

### **4.3.2 Material and Methods**

#### **Onion Study Site**

The study field was in the USDA-ARS, San Joaquin Valley Agricultural Sciences Center (36.59°N, 119.51°W), Parlier, California (Fig. 4.6). Since 2016, an onion test field had been set up for research of biomass soil amendments and deficit irrigation. There were three irrigation treatment levels, High, Medium and Low, and four soil amendments, Biochar, Check, Biochar + Compost, and Biochar + Compost + Sulfur. There were three replicate plots for each treatment combination.

#### **The Spectrometer Scio**

Most recently, a light and small hyperspectral scanner called Scio (Consumer Physics, Israel) was released in the market. As a complete system, it included a spectrometer, a light source, and optimized algorithms in the cloud. The Scio spectrometer worked in NIR at wavelengths of 700 - 1100 nm (Fig. 4.7). It could also be integrated into the smartphone. This system was a low-cost module, with



Figure 4.6: The onion field (image taken by the “Hover” UAV platform). The study field was in the USDA-ARS, San Joaquin Valley Agricultural Sciences Center (36.59°N, 119.51°W), Parlier, California. Since 2016, an onion test field had been set up for research of biomass soil amendments and deficit irrigation. There were three irrigation treatment levels, High, Medium and Low.

the price less than \$300.

As a reference, the author also used a traditional handheld spectrometer EPP2000-VIS-50. Its wavelength sensitivity was from 190 nm to 1700 nm, with the wavelength accuracy of 0.25 nm.

### Field Measurement Collection

During the growing season, onions under different treatment were sampled once a month. The field measurements using the spectrometers were coordinated with these physiological measurements, including shoot length, root length, number of leaves, fresh weight, dry weight, and bulb diameter. There were three onion samples collected for each plot. For each onion sample, three measurements were made using both the EPP2000-VIS-50 (Fig. 4.8) and Scio at the same time in the field to reduce the likelihood of errors or anomalous results. In general, the author had 81 measurements for 27 onion samplings.

The Scio was an active sensing platform and it provided calibration case. The sensor was first calibrated using the white panel in the case. The measurement using Scio required the distance between onion leaves and the scanner as small

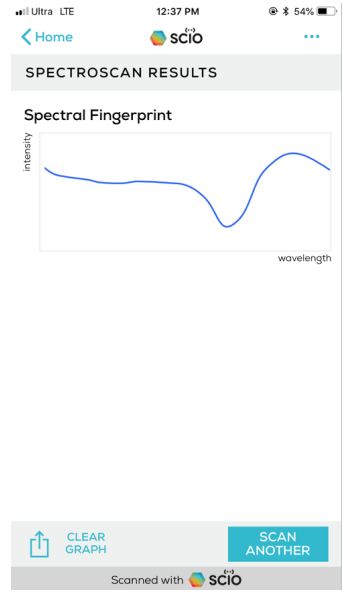


Figure 4.7: The NIR reflectance measurement of Scio using a smartphone.

as possible to minimize the disturbance of sun light source. On the other hand, EPP2000-VIS-50 was a passive sensing platform. The author needed to take the measurements of white panel and dark panel for calibration before measuring the onion leaves.

### The Principal Component Analysis

Both principal component analysis (PCA) and linear discriminant analysis (LDA) were methods for reducing dimensionality of a dataset to increase accuracy, speed up processing time, and generate visualization.

PCA is a linear transformation that rotates the axes of the data along the direction that maximizes its variance, allowing data to be projected onto a lower dimensional subspace [235]. These new axes, or “loadings,” are found by calculating the eigenvectors  $W$  of the covariance matrix of data, where  $X$  is an  $M \times N$  matrix representing  $M$  samples of size  $N$ :

$$X^T X = W\lambda. \quad (4.1)$$

The eigenvalues  $\lambda$  represented how “important” each loading was in transforming

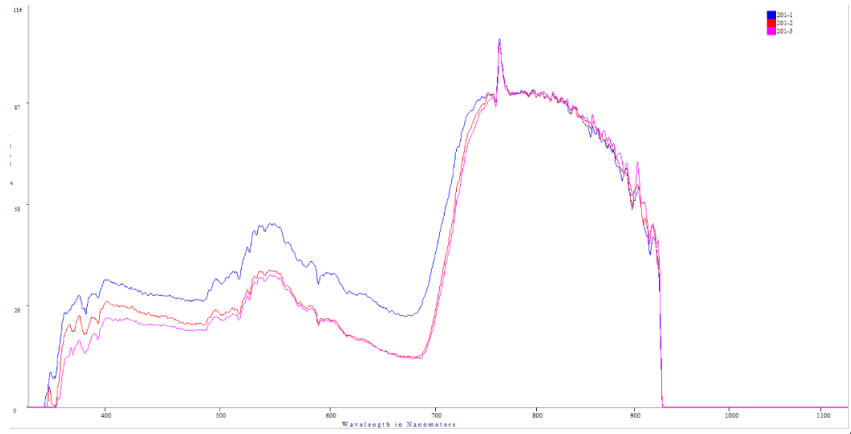


Figure 4.8: The reflectance measurement of EPP2000-VIS-50. Each onion sampling was measured three times to reduce the likelihood of errors or anomalous results.

the data, or how much variance the projection onto this axis contributed. As the loadings (and  $\lambda$ ) were sorted in descending order,  $W$  could be truncated to  $r$  columns, which could then be used to project data along  $r$  dimensions, preserving the dimensions that contributed most to the variance of distribution.  $W$  was often obtained with singular value decomposition (SVD) instead of performing the eigen decomposition of  $X^T X$ , as it was more computationally efficient.

### Linear Discriminant Analysis

LDA reduces dimensionality of data by finding new axes to project it onto that maximizes the separability between classes [276]. It does this by maximizing the distance between means of classes relative to some center point for all classes, while minimizing the variance, or scatter, within each category (equation (4.2)). In the following equation,  $C$  is the number of classes,  $N_i$  is the size of class  $i$ ,  $\mu$  is the mean of all data points,  $\mu_i$  is the mean of class  $i$ , and  $x_j$  is the  $j^{\text{th}}$  data point in class  $i$ ,

$$\frac{\sum_{i=1}^C N_i (\mu_i - \mu)(\mu_i - \mu)^T}{\sum_{i=1}^C \sum_{j=1}^{N_i} (x_j - \mu_i)(x_j - \mu_i)^T}. \quad (4.2)$$

The optimized solution contains eigenvectors that is descending order of their eigenvalues, which can be used to reduce the dataset similar to PCA. Optimizing for

both within and between-class scatter is important because only maximizing distance between means can lead to scenarios where the variance is high along the axis with large mean distances, increasing the chance that there are points from different classes overlapping. Minimizing the variance ensures data from each class is grouped tightly along the new axis, increasing separability.

### Multi-layer Perceptron Classifier

The single perceptron, or artificial neurons, are nodes with a number of weighted data inputs, a bias input, and an output [277]. The weighted inputs are summed up and fed through an activation function, used as a threshold to decide when the node should be active. They can be used for binary classification or regression problems by using activation functions (e.g. tanh, sigmoid). The function for a single perceptron is as follows, where  $a$  is the activation function,  $W$  is the input weights, and  $b$  is the bias,

$$f(x) = a(Wx + b). \quad (4.3)$$

The single perceptron cannot be used for many complex prediction tasks because they can only predict nonlinear patterns [278]. Multilayer Perceptrons (MLP) overcome this by constructing networks out of multiple perceptrons. An MLP is a supervised learning system consisting of an input layer,  $N$  number of hidden layers, and an output layer. Nonlinear activation functions used in the MLP introduce nonlinearity into the model, allowing it to make predictions on complex, nonlinear datasets, such as hyperspectral readings. MLPs are trained using a process called backpropagation, which updates the network's weights with respect to the error between its current output and the expected result.

### 4.3.3 Results and Discussion

To prepare the dataset of EPP2000-VIS-50, each 1675-dimension reading was loaded into a vector. The Scio measurements were obtained with the help of a smartphone application, and each reading was of 1060 dimensions. For the model evaluation, the dataset was split into 75% for training, and 25% for testing.

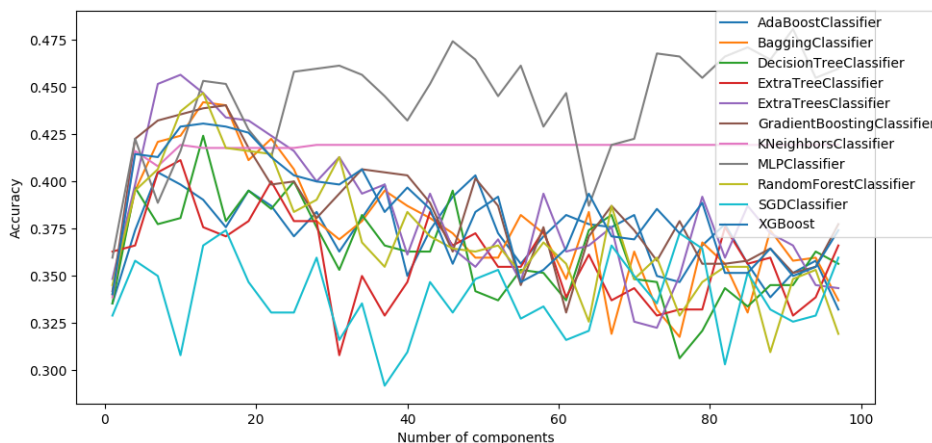


Figure 4.9: Classifier accuracy comparison on the PCA reduced Scio dataset.

All data was normalized with scikit-learn’s *normalize()* function, while the MLP classifier required normalization with the *StandardScaler()* module [279].

The evaluation stage was broken up into three steps: data preparation, classifier evaluation, and parameter grid search on the best performing classifiers. Classifier performance was ranked by the percentage of correctly predicted labels in the test dataset, averaged over 10 iterations. In the classifier evaluation stage, a number of classifiers were being applied with and without PCA and LDA dimensionality reduction.

### Results Using PCA Based Classifiers

Figure 4.9 showed the performance of several scikit-learn classifiers (and XGBoost) ranked against each other in terms of label prediction accuracy for the Scio dataset (reduced with PCA from 3 - 99 components). Most classifiers performed very poorly, with only the MLP classifier nearly breaking 50% accuracy, hitting a high score of 48.1% at 90 components, with the rest barely beating random guessing (33% for 3 labels). After MLP was determined to perform the best with PCA reduced data, the author performed parameter grid search to optimize its results, iterating through the parameters listed below, achieving a top accuracy of 53.1% (top 5 results and parameters are shown in Table 4.3).

- PCA components: 10, 20, 40, 80, 160
- Hidden layer sizes: 25, 50, 100, 200, 400
- Activation: relu, logistic, tanh
- Solver: lbfgs, adam
- Alpha: 0.00001, 0.0001, 0.001, 0.01, 0.1
- Batch size: 200, 100, 50, 25
- Max iterations: 200, 500, 1000

### Results Using LDA Based Classifiers

Each classifier was tested against reduced data with size ranging from 3 - 99 components, as with the PCA reduction in the previous section. This hurted performance relative to PCA reduction, with all classifiers again scoring only slightly above random guessing, with the exception of MLP which scored an average of 38.8% accuracy (see Fig. 4.10), with a best score of 39.5% at 6 components. Because these results were substantially less than the default results of MLP with PCA reduction, parameter grid search was not conducted.

### Results Using MLP

The MLP implementation was also tested with the raw, unreduced dataset, but performed substantially worse than PCA and LDA-reduced methods. MLP predicted the correct label 36.6% of the time with the unreduced data, essentially

Accuracy	PCA Components	Hidden Layer Sizes	Activation	Solver	Alpha	Batch Size	Max Iterations
0.53064	20	100	tanh	adam	0.001	25	500
0.52903	20	50	relu	lbfgs	0.1	50	500
0.52741	20	200	tanh	adam	1e-05	25	500
0.52741	20	400	relu	adam	0.01	100	500
0.52580	20	50	logistic	adam	1e-05	25	1000

Table 4.3: Top 5 performing classifiers using PCA and MLP and their grid search parameters.

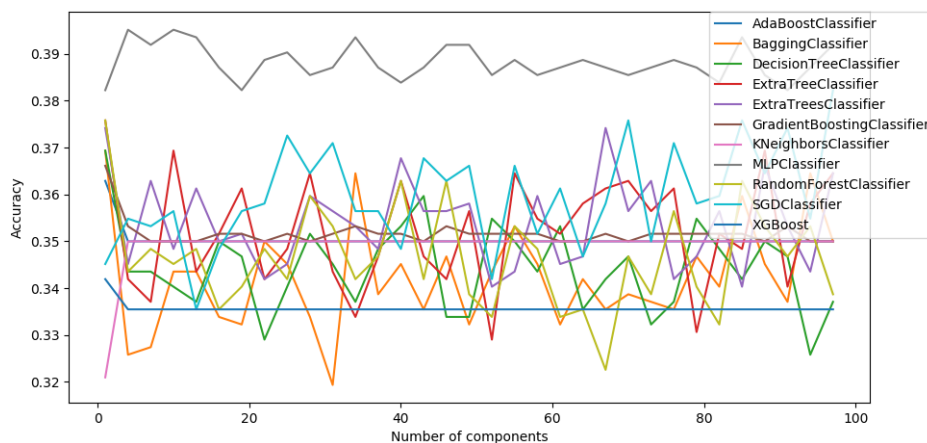


Figure 4.10: Classifier accuracy comparison on the LDA reduced Scio dataset.

randomly picking the result. This demonstrated that dimensionality reduction was necessary for MLP to provide any benefit for the onion dataset. For the unreduced data, scikit-learn Extra Trees implementation performed the best, predicting the correct label with an accuracy of 43.1%.

#### 4.3.4 Conclusions and Future Work

Data collection from the Scio sensor produced worse classification results as opposed to the spectrometer EPP2000-VIS-50. Using the data of EPP2000-VIS-50 increased MLP's prediction accuracy from 36.6% to 71.8% on unreduced data. Similar improvement was seen with dimensionally reduced data, improving the prediction accuracy of MLP from 48.1% (with 90 components) to 77.4% (with 30 components) for PCA, and 39.5% (with 6 components) to 58.5% (with 42 components) for LDA.

In the future, the author will collect more measurements in different growing stages of onions to make sure the model is robust to the different growth stages. As for the sensor Scio, the author will explore new machine learning methods to see if better algorithms can help improve prediction accuracy.

## 4.4 Conclusion and Future Research

In this chapter, the author proposed the concept of “Internet of Living Things (IoLT).” A “living thing” pertains to any organism or a life form that possesses or shows the characteristics of life or being alive. The fundamental characteristics are 1.) having an organized structure, 2.) requiring energy, 3.) responding to stimuli and adapting to environmental changes, 4.) being capable of reproduction, growth, movement, metabolism, and death. For most of agricultural applications of IoT, it actually can also be considered as the IoLT. Researchers collect data of crops or trees, such as tree canopy temperature, rainfall, humidity, wind speed, soil moisture, and stem water potential, etc. After the analysis of recorded data, stakeholders or researchers can help make better decisions to increase the farm productivity, improve the sustainability, and reduce the costs. For the future research, new sensors can be designed for specific agricultural applications. How to extract the most significant data using the ML algorithms can be an important research topic.

# Chapter 5

## The Unmanned Ground Vehicles (UGVs) for Precision Agriculture

### 5.1 Introduction

An unmanned ground vehicle (UGV) is an autonomous vehicle, capable of not only driving without a human driver, but can also include artificial intelligence to conduct search, proximate sensing, mapping and tracking mission without the need of human's control [280]. Current UGVs come in a variety of forms and capabilities, from full-sized tractor capable of replicating manned operations to miniature systems for agricultural environments [281]. Industry experts predicted a significant surge in UGVs deployment, especially within the agricultural industry. This exponential increase is expected from two major developments: the increase in availability of advanced sensor technology [282] and the cognitive applications allowing commercial use of UGVs [283]. Advanced sensing technology allows cameras to be automated, leading the way for UGVs to further reduce labor costs in agriculture. According to a robotic research report, agricultural robots can become a 45 billion industry by 2038 [284].

UGVs, equipped with sensors, have been used in several agricultural sensing applications for collecting data. For example, the CGMD302 spectrometer can be used to measure the leaf area index (LAI) for monitoring the rice growth conditions

[285]. Equipped with pan-tilt-zoom (PTZ) camera and Stereo cameras, Husky UGV from Clearpath Robotics can be used for optimized harvesting by isolating low yielding crops [286]. The Velodyne VLP-16 LiDAR, equipped with the IG52-DB4 UGV from Superdroid Robots, can be used for 3D mapping of plants [287]. Furthermore, equipped with a 2D laser rangefinder, a Kinect v2 camera and a set of robot navigation sensors, a commercial off-the-shelf mobile robot Summit XL HL can be used for assessing vines' canopy dimensions and estimating yield [288]. Pest population distribution and irrigation non-uniformity mapping are still new areas for UGVs, but they have more exact requirements than other sensing applications. For example, real-time management of irrigation systems require more and more precise information on water, soil, and plant conditions than most surveillance applications. Most current UGV sensing applications use expensive UGVs and cameras [286].

Pests are usually considered as the most economically important factor in agriculture because of their spatial coverage [289]. Early detection of pest population distribution in agricultural systems is critical to enabling timely interventions and reducing crop yield losses [290]. For example, estimates are that approximately 10.8% of global crop losses are due to pests [291]. Each year in California, eradication of pests is not always available, due to either the quickly expanding distribution of the pest or constraints regarding the tools available to attempt eradication. Pests can cause significant damage to the agricultural industry and natural environments [292].

The irrigation systems have been designed to apply water uniformly in the irrigation area. Uniformity of soil moisture under the sprinkler irrigation system is an important parameter for crop quality and yield. Non-uniformity irrigation can cause less yields than expected [293]. Smart irrigation management will enable growers to irrigate ideally in agricultural industry. For example, research in almond irrigation management has been accelerated to achieve sustainability and marketability since 2010 in California. There are around 7600 almond farms in California, which makes up almost 100% of commercial almond production in the US and about 80% of the global supply. Since there is limited water in CA,

it is important to move the almond industry forward toward sustainable water management. The Sustainable Ground Management Act (SGMA) defined a new industry goal for the almond water use efficiency by 2025 to “Reduce the amount of water used to grow a pound of almonds by 20%.” Smart irrigation management will enable growers to irrigate almonds ideally and keep CA as a global leader in sustainable almond production.

The current state-of-the-art methods to identify pest population distribution and non-uniformity irrigation system require farmers or growers to employ field scouts to identify visible symptoms or rely on remote sensing images from satellites or UAVs to identify crops [294]. Usually, when visual symptoms occur, the damages may have already occurred. Early detection of crop pest population distribution and irrigation non-uniformity mapping will directly or indirectly contribute to agricultural, environmental and economic sustainability due to rational irrigation water usage, minimized application of fertilizers and pesticides and improve yield estimation.

This chapter will first focus on how to build a low-cost UGV platform and its application for pest population distribution and irrigation non-uniformity mapping. The fundamental research proposed can also be used for other precision agriculture applications, such as leak detection. The UGV, as a data acquisition platform, will definitely play a key role in these agricultural applications.

## **5.2 The UGV as A Data Acquisition Platform**

Over the past decade, UGVs have shown much promise in their future role as a primary tool to collect critical information for precision agriculture [295]. Commercial UGVs have the potential to deal with rising demand for lowering labor cost in the world. Whether used as a smart farmer’s companion or a co-ecologist, cognitive swarming via UGVs with associated system applications is rapidly increasing in number and sophistication. We are limited only by our imagination for potential future applications, much like the dawn of personal computing.

The proposed UGVs in this chapter can run more than 6 hours in the field, and

have the ability to capture remarkably high resolution thermal, near infrared, red-green-blue standard video and imagery, and LIDAR for 3D mapping. These data can then be used for a variety of timely decisions, such as determining not only the species of plants, but also their water and nutrient stress status [296]. This type of applications is only the beginning, as we believe there are many more untapped agriculture and environmental research abilities, such as health-check for crops (disease detection), pest management, irrigation management, crop harvesting, mechanical weeding, and much more. Also, the world population increases fast, which is expected to reach about 9 billion by 2050 [297]. More food is in demand from agriculture. Labor shortages have been reported throughout agriculture in the United States again and again [298]. UGVs can decrease the need for labors in farms by mechanizing and automating agricultural processes such as harvesting, seeding, monitoring, and etc. [297].

### 5.2.1 Fundamental Research Questions for UGVs

Precision agricultural applications by using cognitive swarming of low-cost UGVs require spatial and temporal resolutions. Cognitive swarming of low-cost UGVs is promising but limited by its autonomous navigation controls, management methods and performances. The fundamental questions are

- How to use smart cognitive algorithms to make sure the UGVs can perform state-of-art movement in the field?
- How can UGVs/UAVs cooperate efficiently by using a swarming mechanism?
- How to make the UGVs taskable with little modification of current planning methodologies?
- How to lower the UGVs barriers (low-cost) to entry agricultural industry?
- How to early detect pest population and irrigation non-uniformity mapping based on data information collected from low-cost UGVs?
- How to use data collected from UGV sensors to acquire most related information about precision agriculture sensing and applications?

- How can the UGVs perform safely in emergency to avoid hurting people or crops?

### 5.2.2 Low Barriers to Entry

The personal UGV platforms are highly efficient for different agricultural sensing and applications. Specifically, the personal UGV can run more than 6 hours each time and 3 miles per hour, which makes it work more efficiently than most UAVs. Currently, one method to make the UAV fly longer is adding more batteries, such as NCFLY-Helios (Drone Technology Inc.). With eight motors and the diameter up to 2136 mm, UAVs can have the endurance of 60 minutes with 1 kilogram payload or 40 minutes with 7 kilograms payload. This is clearly not enough for many agricultural applications in the field. With a single, more cost-effective battery, a personal UGV can work more than 12 hours per day. This makes the UGV platform work much more efficiently in a variety of agricultural proximate sensing and applications. Affordability of the UGV platform is also a very important concern from agricultural industry [299]. Recently, most UGVs used in the research are very expensive, such as IG52-DB4, HD2-S UGV from Superdroid Robots [287] and Husky UGV from Clearpath Robotics [286]. To make it commercial, balancing the technology efficiency with cost is a study area for researchers.

Table 5.1: Specifications of several UGVs and the proposed Personal UGV.

UGVs	Price	Run time	Max speed	User power
Husky	more than \$20,000	3 hours	2.3 mph	5 V, 12 V, and 24 V fused at 5 A each
IG52-DB4	\$1613.55	5 - 5 hours	5.65 mph	24 V, SLA batteries with 18 A of capacity
HD2-S	\$32,500	up to 8 hours	2.7 mph	24 V, SLA batteries with 18 A of capacity
Personal UGV	less than \$1000	6 hours	3.7 mph	12 V fused at 7 A

As seen from Table 5.1, compared with Husky UGV, IG52-DB4 and HD2-S UGV, the proposed personal UGV had a much lower cost and better performance. For example, IG52-DB4 (Superdroid Robots) costed like \$1613.55, and it could only run like 2 to 5 hours without payload. The proposed personal UGV could run as long as 6 hours. The HD2-S UGV was even more expensive, as much as \$32500.

The performance was very similar with the proposed UGV platform, which was targeted to less than \$1000. The author believed this cost range made the proposed personal UGV achieved lowering barriers to entry and became more ubiquitous in precision agriculture industry.

As indicated in the above examples, only one camera is used to have longer endurance on the UAV platforms. However, for UGV platforms, there is more space for cameras. All kinds of cameras can be mounted on the UGV without concern about the endurance. For example, The GoPro Hero 6 is the newest product from GoPro technology company. It can shoot 4K video at 60 frames per second and slow-motion 1080P (240 fps), which is only \$399. To make it more cost effective, Gopro Hero 5 can be another choice, which is \$299. For another example, Survey 2 Camera (MAPIR, USA) is a visible light RGB camera. According to its official website, it is only \$280. The Survey 2 has a 16MP sensor and sharp non-fisheye lens make it easier to capture in the field. It captures photos on the default timer trigger or can be sent a PWM signal through the HDMI port. Similar size to a GoPro 6 (Gopro, USA), these small survey cameras can be attached to UGV platforms using various mounts. With more cameras, the UGV can become more taskable for farmers and growers.

TurtleBot is a low-cost, personal robot kit with open-source software. It was created at Willow Garage by Melonee Wise and Tully Foote in November 2010. There are mobile base, 3D sensor and a laptop computer in the TurtleBot kit. TurtleBot has many similar abilities of the large company's robot platforms, such as PR2. With the TurtleBot components, users can even create real-time obstacles avoidance and autonomous navigation. For the personal UGV platform, we can even use the TurtleBot to control the UGVs. Then, the TurtleBot becomes the "UGV brain" and monitor the UGV behaviors in the field. All the possible applications of the TurtleBot can be realized on the UGVs and can be much more powerful. The TurtleBot 2 and TurtleBot 3 are most commonly used in research. TurtleBot 2 consists of a Kobuki base, a 2200 mAh battery pack, a Kinect sensor, an Asus Xion Pro Live, fast charger, netbook (ROS compatible). The ROS stands for robot operation system, which is a flexible framework for writing robot software

[300]. Turtlebot 3 is the new generation mobile robot which is modular, compact and customizable. It reduced the size and lowered price without sacrificing function, capability, and quality. The Intel RealSense Depth Camera D435 has been used in several research areas. It can be used indoor and outdoor. The depth technology is active IR stereo. The processor used in this camera is Processor D4. The depth field of view can be up to  $1280 \times 720$ . The depth stream output frame rate can be up to 90 fps. It can be used in 3D point clouds and other research areas. The most important is that the price is only \$179. Mounted on the UGVs, it will be more powerful as part of the cognitive system.

### 5.2.3 Cognitive Algorithms by Deep Learning

Cognitive algorithm is one of the most important parts of the UGV platform. The inspiration of cognitive algorithms for UGV comes from the human drivers. Based on human cognitive mechanism, researchers lay the foundation for the development of cognitive algorithms. Typically, there are three steps of the UGV movement behaviors, stimulus perception, judgement and decision making, and stimulus performance [301]. In a recent cognitive algorithm, it could identify specific objects in the environment, using cognitive reasoning to develop a deeper understanding of the scene based on objects and their spatial relationships [302]. Reconstruction and mapping monocular simultaneous localization and mapping (SLAM) relies on cognition techniques to calculate the position of the robot and map the environment [303]. Real-time monocular SLAM was thought impossible due to high computational costs. However, there are many kinds of SLAM packages now, such as LSD-SLAM [304], RatSLAM [305], and SVO [306]. Many open source vision-based SLAM packages were compared in a paper at 2016 [307]. It turned out that ORB-SLAM is the best performing package [308]. The ORB-SLAM uses ORB features, which are binary features that are invariant to rotation and scale [303]. The ORB-SLAM also allows the robots to initialize with no user input, which is important for UGV platforms as an autonomous robot system. Additionally, when the ORB-SALM is matching features, the number of key frames increases because of the complexity of the images. This is done by “culling” key frames that are no

longer used, and allows for ORB-SLAM to run for longer periods of time [303].

Recognition using deep learning can bridge the gap between perception and intelligence. Perception missions can collect lots of data, but much of it is discarded to simplify interpretation by higher level tasks [309], e.g. a 3D object can become a point in space. In [309], it used a deep learning framework to replace these interfaces with learned interfaces. This allows for error back-propagation that can adapt each module to the robot's task. Deep learning is also a powerful state-of-art technique for image processing. It can target land cover and crop type classification from the images collected from sensors [310]. Safety is another concern by farmers and growers, the UGV should have the ability to detect workers and farmers, then make the right decision in the field.

#### 5.2.4 The Swarming Mechanism of UGVs

Technological advances are pushing the applications of UGVs in exciting directions [311]. Many different types of UGVs have been developed to address a variety of agricultural applications ranging from soil sampling, irrigation mapping and crop harvesting [312]. However, for a large scale of field where fleets of autonomous UGVs must be used to work together on a common goal, multiple UGVs can collaborate to form a swarming mechanism [313].

Recent swarming research has focused on aspects of communications and maintenance of connectivity [314], such as control and collision avoidance with the swarm [315], task allocation and strategies for solving multiple tasks [316], modeling of the swarm behavior by predicting individual behaviors [317]. In these papers [318, 319, 320, 321], control methodologies for swarms of UGVs were discussed. In this chapter, the research will be conducted based on the proposed UGV platform and provide swarm mechanism with multiple UGVs. In this mode, the followers can only follow the leader UGV according to its GPS position, although detailed functions will be developed depending on the requirement of proximate sensing. For example, several UGVs can work in a large scale field together, which makes a mission much shorter than normal time. The collected data can also be shared between UGVs in real-time mode, which makes the UGVs more intelligent.



Figure 5.1: The toy vehicle.

## 5.3 Case Study: Build A UGV platform for Agricultural Research from A Low-cost Toy Vehicle

### 5.3.1 Introduction

This section is for a short introduction of the UGV from a toy vehicle (Fig. 5.1). the UGV could navigate through its environment without the assistance or guidance of human intervention. This was done through the signal transmission between the vehicle controller and a program called Mission Planner, which was used to set up markers called waypoints that set up locations for the UGV to reach. For the research purpose, the UGV's main function was to survey and inspect different farmlands, performing large amounts of data collection for researchers to use. After data gathering is complete, they can perform data analysis and computer vision algorithms to gain more insight in crop growth, trends and pave the way to precision agriculture.

This tool is a great substitute for physical labor and minimizes expenses in the industry (Fig. 5.2). Besides research, UGV usage can transition to applications within the working sectors such as agriculture, emergency services, government



Figure 5.2: The UGV platform.

work, and much more. In terms of agriculture, the goal of this project is to create a low-cost (less than \$1000) UGV that local farmers in the Central Valley can use. With this affordable UGV, they have a device that does surveillance in their field, inspect for water pipe leakage, crop diseases, and perform human-based tasks such as spraying insecticides and mowing, especially in vineyards. For more information about this UGV application in agriculture, please refer to Chapter 10.

## 5.4 Conclusions and Future Research

Unlike other robots, UGVs post particular challenges for algorithms of automation, cognition and swarming. UGVs are operated in the environment with disturbances like weather condition, and decisions on the control actions have to be made instantaneously. Also, farmers and growers are worried about the profitability of UGVs implementation as well as safety. Therefore, it is necessary to develop a mixed-initiative planning system with adjustable autonomy to enable UGVs meet with their mission objectives within the physical dynamics.

More precisely, the architecture of UGV system should include three layers. The first layer includes a team of multiple UGVs with cost effective cameras and sensors.

Each camera sensing specific band of light is mounted on a single UGV. On this level, it supports direct precise teleoperation for a single UGV by providing guiding mode, loitering mode, or even stabilizing mode controller. In this scenario, the higher layer monitoring system keeps checking the status of the UGV and operation of the user and notifies the user about safety and corresponding suggestion on action.

The second layer is model based monitoring system to improve system safety and operator awareness. The control system is embedded with declarative model of its activities to detect constraint violations. On the one hand, the performance of UGVs, like position, speed, battery etc., will be compared with the prediction output based on the prior model of UGV. Once there are any strange behaviors, it will give warning or action suggestion to operators. Particularly, management-by-consent and management-by-exception should be involved to free operator's cognitive resources for higher priority operation. On the other hand, while mission planning, human command is also checked to prevent dangerous or conflict initiatives. Not normal interaction would be detected and displayed to the user, and only safe meaningful interaction will pass into the first layer.

The highest level is mixed-initiative planning system, which allows incremental interactive planning for pest population distribution and non-uniformity irrigation mapping. The scale adaptive searching algorithm is part of this layer for path planning. It orchestrates task assignment, task decomposition, overall path planning, and incremental planning. The user either generate mission plan by task assignment with the planning system or follow the plan sequence with just a few modifications. In addition, it permits incremental planning so the user can just focus local decisions without endanger the overall system constraints.

## Part III

# Advanced Big Data Analytics, Plant Physiology-informed Machine Learning, and Fractional-order Thinking

# Chapter 6

## A Low-cost Proximate Sensing Method for Early Detection of Nematodes in Walnut Using Machine Learning Algorithms

### 6.1 Introduction

Most of the high-value commodity walnuts of the US are grown in the fertile soils of the California Central Valley. The sustainability of walnut production is challenged by several pests and pathogen problems that can occur in walnut orchards [322, 323]. The plant-parasitic nematodes are one of these pest problems. There are many species of nematodes in California, but the root-knot nematodes (*Meloidogyne* spp.) and root-lesion nematodes (*Pratylenchus vulnus*) [324] are among the most damaging [325]. Plant-parasitic nematodes are difficult to control and can spread easily in soil on tools, boots, or infested plants [326]. Root-knot nematodes can attack many different crops, including nut and fruit trees. Root-knot nematodes usually cause distinctive swellings, called galls, on the roots of affected plants [327]. Many nut crop rootstocks used in California carry resistance towards root-knot nematodes, but nematode species new to California can occur

in the state and damage the nut crops based on their vulnerability. Root-lesion nematodes are also widely distributed and heavily damaging in walnut orchards, therefore causing widespread problems [328].

Recently, accurate nematode detection relies on soil collections, tedious nematode extraction procedures, and identification and enumeration under a microscope [324]. Infestations of nematode under field conditions are not diagnostic but need to be confirmed by laboratory procedures. These traditional nematode detection methods are tedious, need highly specialized personnel, equipment, and take time to complete. Detection of plant-parasitic nematodes by simple means is paramount to direct management strategy decisions.

With the development of remote sensing technology, satellite and unmanned aerial vehicles (UAVs) imagery have been commonly used in precision agriculture, such as early detection of nematodes [329, 330, 331], irrigation management [24, 27], and evapotranspiration estimation [142, 137, 28]. The walnut root infection by nematodes can induce spectral variation in leaves and define a special spatial configuration. Thus, Hillnhütter *et al.* reported that the induction of symptoms in leaves, the clustered occurrence, and the low level of mobility in the soil made nematodes ideal targets for remote sensing detection [332]. For example, Martins *et al.* detected and mapped the root-knot nematode infection in coffee crops using the hyperspectral data and RapidEye sensor to identify the most sensitive spectral ranges for nematode infection discrimination in coffee plants [329]. The multispectral classification method could classify the spatial distribution of healthy, moderately infected, and severely infected coffee plants with an overall accuracy of 78% [329].

However, satellite or UAVs could be limited by flight time or payload capability. Such limitations do not apply to proximate sensors. For instance, in [333], Li *et al.* adopted a non-invasive method of measuring leaf water content using terahertz (THz) radiation, which provided for repeated, non-destructive measurement of leaf water content. In [334], the author proposed a novel low-cost proximate radiofrequency tridimensional sensor Walabot to measure the stem water potential of walnut leaves. Results showed that the sensor could predict stem water potentials

with an accuracy of 78% using the decision tree classifier. The Walabot has also been used in many other research topics, such as battery management [335, 336]. For example, Wang *et al.* [336] compared the performance of three classifiers on Lithium-ion batteries (LIBs) voltage classification problem, which were principal component analysis (PCA) [235], linear discriminant analysis (LDA) [236], and stochastic gradient descent (SGD) classifiers. Experimental results showed that LDA was the most suitable for LIBs voltage classification. These findings highlighted the powerful potential for applying Walabot as a proximate sensor.

Inspired by previous research work, the **objectives of this chapter** are:

1. Investigate and validate the non-invasive approach of early detection of nematodes using a pocket-sized, cutting-edge technology radio frequency tridimensional sensor.
2. Implement several Scikit-learn classifiers, such as “Neural Net” [277], “Support Vector Machine” [337], “Random Forest” [338], “AdaBoost” [150], “Nearest Neighbors” [339], and “Decision Tree” [340] to classify the nematode infection levels of walnut trees.
3. Evaluate the prediction performance of the Deep Neural Networks (DNNs) model.

The **major contributions of this chapter** are:

1. Develop a reliable method for early detection of nematodes using a proximate sensor and ML algorithms.
2. Provide a DNN framework, which establishes a DNN model between the radio frequency reflectance of walnut leaves and nematode infection levels.

The rest of this chapter is organized as follows: the second section introduces material and methods for early detection of nematode infection levels. Several commonly used ML algorithms are also introduced in this section. Different results of early detection of nematode infection levels are then presented, compared, and discussed in the third section. In the end, the author shares views on the

early detection of nematodes with ML algorithms for future research and draws conclusive remarks.

## 6.2 Material and Methods

### 6.2.1 Study Area

The study was conducted in an experimental walnut orchard at the Kearney Agricultural Research and Extension Center, 9240 S Riverbend Ave, Parlier, CA, 93648, USA (36.595°N, 119.508°W). There were three replications to detect the nematode infection levels, Project 30 (a) and (b), Project 45, and Project Smith (Fig. 6.1). For example, in Project 45, the experimental orchard consisted of 90 trees in total, including experimental clonal hybrid walnut rootstock genotypes (originating from one cross) and some clonal controls (Fig. 6.1(b)). They foremost varied for their host status towards root-lesion nematode.

### 6.2.2 Reflectance Measurements with A Radio Frequency Sensor

The reflectance of the walnut leaves was collected with a radio frequency 3D sensor called Walabot Developer<sup>1</sup>. The Walabot used an antenna array to send radio frequency to the area in front of the walnut leaf and then captured the returning signals (See Chapter 4 for more details of the Walabot). The research hypothesis was that the radio frequency reflectance of walnut leaves would be significantly different towards root-lesion nematode infection levels. Then, the spectral curve obtained from the leaves of walnut trees infected with nematodes could show the characteristic pattern of walnut under nematode stress.

---

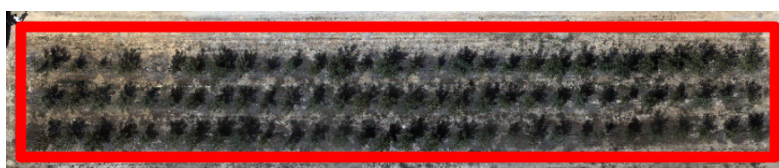
<sup>1</sup>Mention of trade names or commercial products in this publication is solely to provide specific information and does not imply recommendation or endorsement by the University of California or the Kearney Agricultural Research and Extension Center. The University of California and Kearney Center are equal opportunity providers and employers.



(a) The Project 30 (a) and (b).



(b) The Project 45.



(c) The Project Smith.

Figure 6.1: The study was conducted in an experimental walnut orchard at the Kearney Agricultural Research and Extension Center, 9240 S Riverbend Ave, Parlier, CA, 93648, USA (36.595°N, 119.508°W). There were three replications to detect the nematode infection levels, Project 30 (a, b), Project 45, and Project Smith.

Table 6.1: Nematode numbers per gram of root in rootstock genotypes examined by Walabot measurements (Project 45, 2019). “RLN per gram of root” meant the root-lesion nematode number per gram of root extracted in laboratory procedures.

Block	Genotype	RLN per gram of root
A	62	57.2
A	95	49.8
A	127	70.6
A	117	99.8
B	72	147.2
B	89	8.0
B	127	47.7
C	95	50.2
C	127	40.8
D	48	72.6
D	127	7.1
D	128	117.6
E	89	76.1
E	127	1.8
F	127	0

### 6.2.3 Groundtruth Data Collection and Processing

In this chapter, the Walabot was used to measure the radiofrequency reflectance of the walnut leaves in 2019 and 2020. For Project 45, there were 15 sampling trees from 6 different blocks in 2019 (Table 6.1) and 60 sampling trees from 4 different blocks in 2020 (Table 6.6). Each sampling tree was measured five times to reduce the likelihood of errors or anomalous results. Genotypes from one cross went into the analysis. “RLN per gram of root” meant the root-lesion nematode number per gram of root extracted in laboratory procedures. Based on the root-lesion nematode number, the walnut trees of 2019 were classified into four nematode infestation levels (Table 6.2).

Table 6.2: The classification of the nematode infestation levels (Project 45, 2019).

Nematode infestation levels	RLN per gram of root
Level 1	0 - 20,
Level 2	20 - 60,
Level 3	60 - 90,
Level 4	> 90.

### 6.2.4 Scikit-learn Classification Algorithms

Several different methods in generating classifiers were adopted to evaluate the detection performance for nematode infection levels. “Neural Net”, “Support Vector Machines (SVM)”, “Random Forest”, “AdaBoost”, “Nearest Neighbors”, and “Decision Tree” were chosen as the classification algorithms. In the “Neural Net” library, a multi-layer perceptron (MLP) classifier was used. This model optimized the log-loss function using stochastic gradient descent. The MLP trained iteratively because the partial derivatives of the loss function with respect to the model parameters were computed to update the parameters at every step. The SVMs are a set of supervised learning methods used for classification, regression, and outliers detection. The SVMs are effective in high dimensional spaces and effective in cases where the number of dimensions is greater than the number of samples.

For the “Random Forest” classifier, it is a meta-estimator that fits several decision tree classifiers on various sub-samples of the dataset and adopts averaging to improve the predictive accuracy and control overfitting. An “AdaBoost classifier” is also a meta-estimator that begins by fitting a classifier on the original dataset and then fits additional copies of the classifier on the same dataset but where the weights of incorrectly classified instances are adjusted such that subsequent classifiers focus more on complex cases.

The “Nearest Neighbors” method is to figure out a predefined number of training samples closest in the distance to the new point, and predict the label from these. The number of samples can be a constant ( $k$ -nearest neighbor learning) or

vary based on the local density of points (radius-based neighbor learning). Despite of its simplicity, the nearest neighbors method has been successfully applied for many research problems, such as the handwritten digits classification. As a non-parametric method, it is often successful in classification situations where the decision boundary is very irregular.

The “Decision Trees” are also non-parametric supervised learning methods commonly adopted for classification problems. The objective is to create a model that predicts the value of a target variable by learning simple decision rules inferred from the data features. A tree can be seen as a piecewise constant approximation. The “Decision Trees” usually use a white box model, which means the explanation for the condition is easily explained by boolean logic if a given situation is observable in a model. In contrast, results may be more challenging to interpret for a black-box model, such as an artificial neural network.

### 6.2.5 Deep Neural Networks (DNNs) and TensorFlow

A deep neural network (DNN) usually has two or more hidden layers, commonly used in agriculture-related research. For example, in [341], Boniecki *et al.* adopted the DNN as one of the classification tools, with the process of identifying selected apple tree orchard pests as an example. In [342], You *et al.* proposed a segmentation method using DNN that could recognize the weed precisely with arbitrary shape in complex environmental conditions and enabled the autonomous robot to reduce the density of weed more successfully.

In this research, the author trained a DNN with TensorFlow’s high-level application programming interface (API). For each training instance of the nematode dataset, the algorithm fed the instance into the DNN and predicted the nematode infection level. The DNN classifier could be trained with any number of hidden layers. Then, a softmax output layer was used to generate the estimated nematode infection level probabilities. During the training process, the authors trained a DNN for classification with two hidden layers, one with 300 neurons and the other with 100 neurons.

## 6.3 Results and Discussion

### 6.3.1 Data Visualization (Project 45, 2019)

Figure 4.5 was a measurement example of the time-domain reflectance signal using the Walabot. Records of the different reflectance strengths could be visualized. Based on the root-lesion nematode number, the walnut trees were classified into four levels of nematode infestation (Table 6.2). Each sampling was  $2 \times 2048$  dimension by default. Then, the collected nematode infestation data were converted into 2048-dimension vectors for data processing. For data visualization, the author applied the LDA method for dimension reduction, which learned the most critical axes between the classes [343]. The axes were then used to define hyperplane to project the high-dimensional training data into two dimensions, which gained important insight by visually detecting patterns (Fig. 6.2). The  $x$ -axis and  $y$ -axis had no scale because of hyperplane projection [20]. The nematode infection levels were successfully clustered into four levels. Although the two clusters of lower nematode infection levels (Level 1 and Level 2) were close to each other in Fig. 6.2, they were clustered very well in three-dimensional space (Fig. 6.3).

### 6.3.2 Performance of Classifiers (Project 45, 2019)

The collected data of nematode infestation levels were converted into 2048-dimension vectors for Scikit-learn algorithms data processing. The data was distributed as 75% for training and 25% for testing using the *train\_test\_split* method. For evaluating the trained models, a confusion matrix was used to compare the performances of different classifiers. A confusion matrix was a summary of prediction results on a classification problem. The number of correct and incorrect predictions was tallied with count values and divided into classes. The confusion matrix provided insight not only into the errors being made by a classifier but, more importantly, the types of errors that were being made. “True label” meant the ground truth of nematode infestation levels. “Predicted label” identified the nematode infestation levels predicted by the trained model.

The trained Scikit-learn classifiers had distinct test performance for early detec-

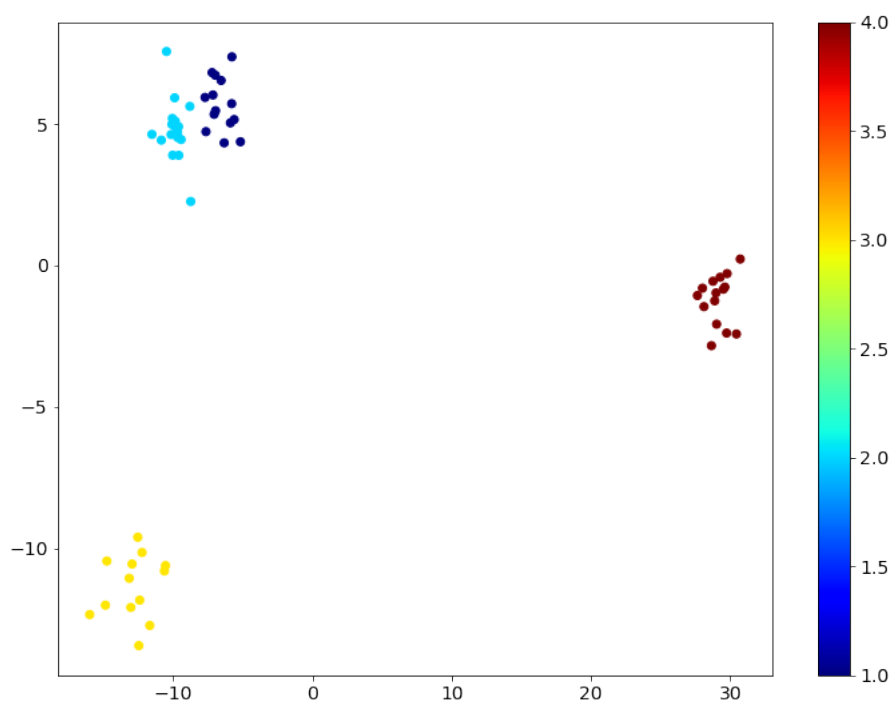


Figure 6.2: The Linear Discriminant Analysis (LDA) was used for data visualization, which learned the most critical axes between the classes. The axes were then used to define hyperplane to project the high-dimensional training data into two dimensions, which gained important insight by visually detecting patterns. The  $x$ -axis and  $y$ -axis had no scale because of hyperplane projection. The nematode infection levels were successfully clustered into four levels. The color bar values 1, 2, 3, and 4 represented the four nematode infection levels from 1 to 4 (low to high) (Table 6.2).

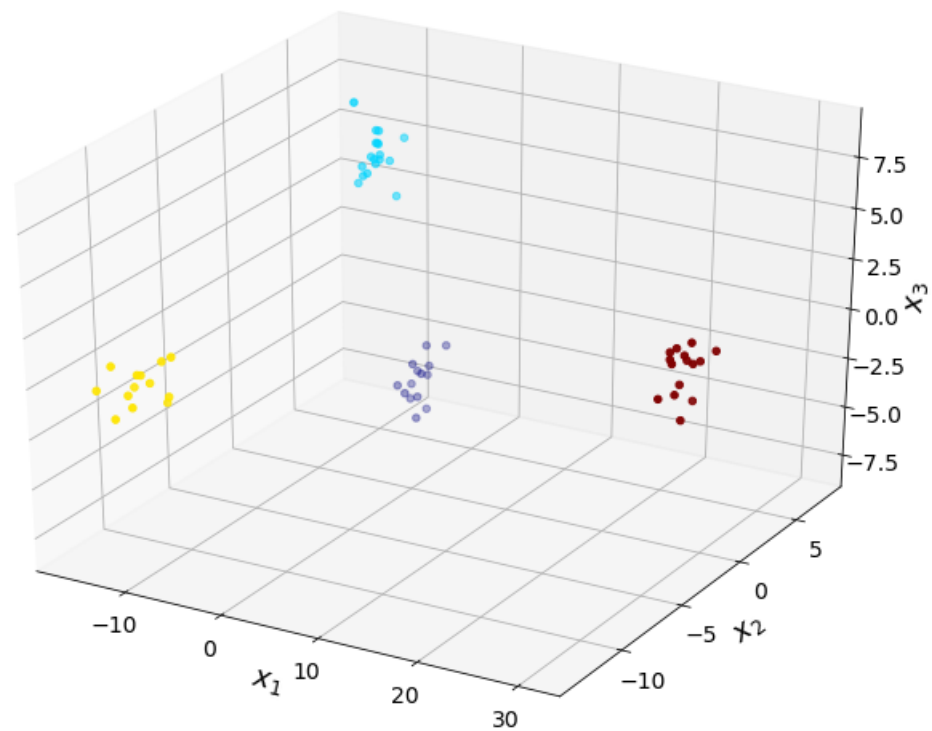


Figure 6.3: The Linear Discriminant Analysis (LDA) was used for three-dimensional data visualization. The  $x$ -axis and  $y$ -axis had no scale because of hyperplane projection. The nematode infection levels were successfully clustered into four levels. The clusters' color was related to Fig. 6.2.

Table 6.3: The performance of classification methods (Project 45, 2019).

Classification methods	Prediction accuracy
“Neural Network”	0.62
“Support Vector Machine”	0.57
“Random Forest”	0.76
“AdaBoost”	0.57
“Nearest Neighbors”	<b>0.95</b>
“Decision Tree”	0.81
“DNN with TensorFlow”	0.82

tion of nematode infection levels (Fig. 6.4 and Table 6.3). The  $k$ -nearest neighbors vote had the highest accuracy of 0.95. Table 6.4 showed the details of the test process of the  $k$ -nearest neighbors method, which was a type of instance-based learning that did not attempt to construct a general internal model, but simply stored instances of the nematode infection levels training data. The classification was computed from a simple majority vote of the nearest neighbors of each point. Then, a query point was assigned the data class that had the most representatives within the nearest neighbors of the point. For the other classifiers’ test performance, the accuracy of the “Support Vector Machine” was 0.57. The “Random Forest” had a test accuracy of 0.76. The “AdaBoost”, “Neural Network”, and “Decision Tree” had an accuracy of 0.57, 0.62, and 0.81, respectively.

During the training process of DNN with TensorFlow, the number of epochs was set as 200. The batch size was 10 since there was a small training dataset. As shown in Fig. 6.5, there were 100 models. The highest accuracy could be as high as 0.9. The lowest accuracy was around 0.58 when the training instances could not represent the nematode infection levels very well. To evaluate the trained model, the authors run the training process 100 times to reduce the randomness of the training instances selection. The mean accuracy was 0.82 for the DNN classifier model.

The experimental results proved that the walnut root infection by nematodes

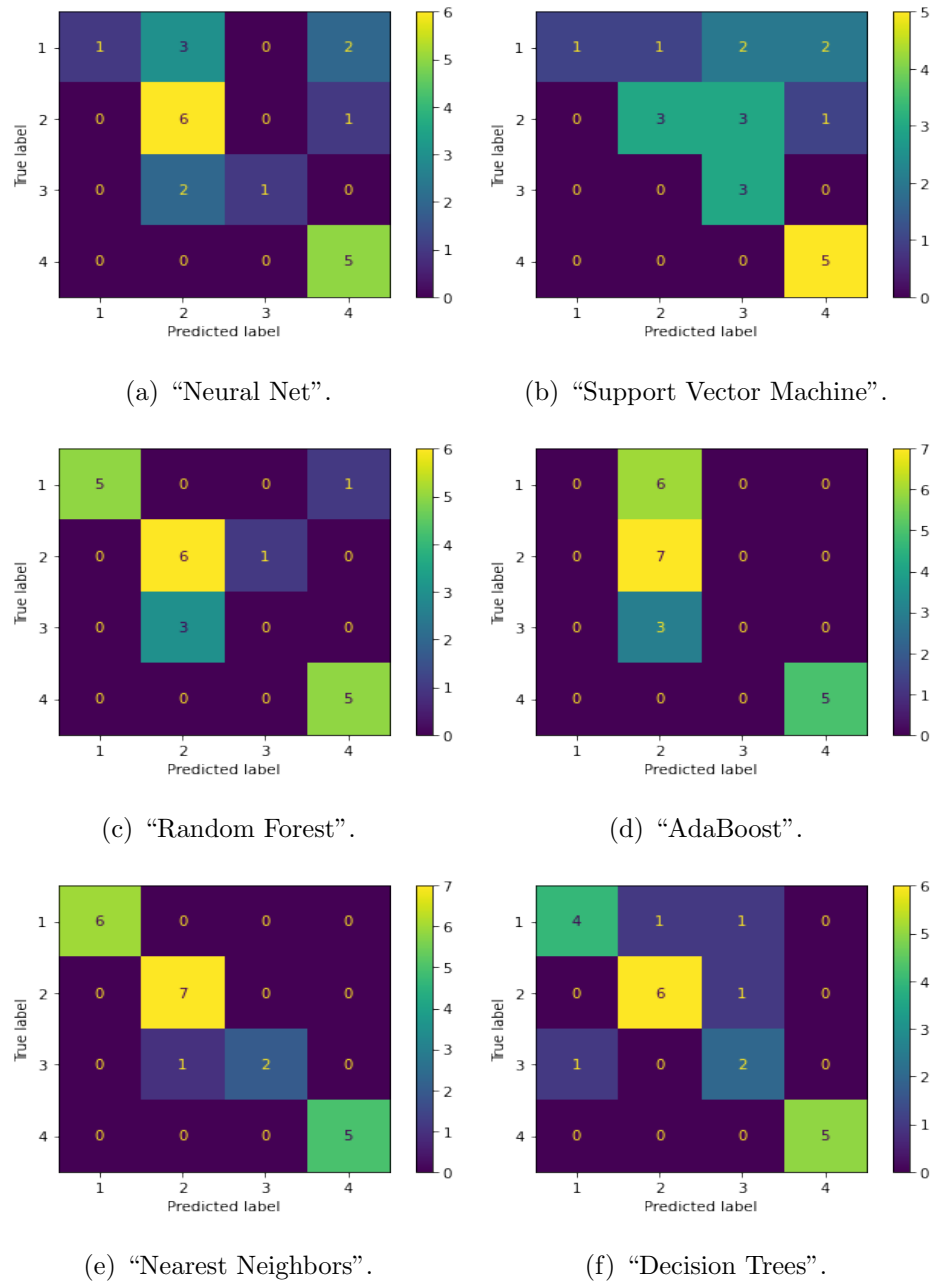


Figure 6.4: A comparison of six classifiers in Scikit-learn on nematode testing dataset (Project 45, 2019). A confusion matrix was a summary of prediction results on a classification problem. The “True label” meant the ground truth of nematode infestation levels. The “Predicted label” identified the nematode infestation levels predicted by the trained model.

Table 6.4: The  $k$ -nearest neighbors performance (Project 45, 2019).

Nematode infestation level	Precision	Recall	F1-score
Level 1	1	1	1
Level 2	0.88	1	0.93
Level 3	1	0.67	0.80
Level 4	1	1	1
Accuracy	NA	NA	<b>0.95</b>
Macro avg	0.97	0.92	0.93
Weighted avg	0.96	0.95	0.95

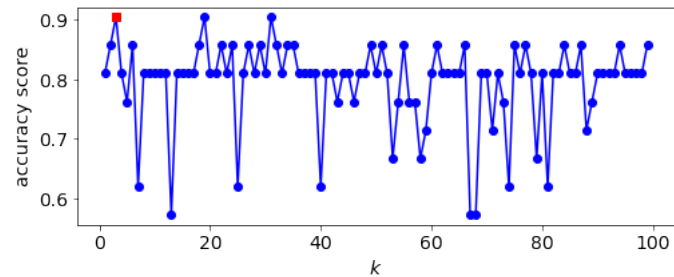


Figure 6.5: There were  $k$  models (in this case,  $k = 100$ ). The best accuracy could be as high as 0.9 (marked as a red dot). The lowest accuracy was around 0.58 when the training instances could not represent the nematode infestation levels dataset very well. The mean accuracy was 0.82 for the DNN classifier model.

could induce spectral variation in walnut leaves. The proximate sensor could send the radio frequency to the area in front of the walnut leaf and then captured the returning signals (reflectance). Then, waveforms generated by different signals could estimate the damage caused by nematodes in the walnut root. With the machine learning algorithms, the nematode infection levels could be classified with high accuracy of 95%. These findings emphasized the importance of applying phenotyping analysis for the early detection of nematode infection levels. Trees and crops severely infected by nematodes showed a significant reduction in leaf area similar to the plant response to other environmental stress, such as drought, nutrient deficiency, salinity, and other biotic stresses [344]. Several researchers reported the similar results [329, 330, 345, 346, 347]. For example, Matins *et al.* concluded that the multispectral classification with hyperspectral data could define the spatial distribution of healthy, moderately infected, and severely infected coffee plants, with an overall accuracy of 78% for detecting and mapping the root-knot nematode infection [329]. In [330], Palacharla *et al.* proposed an SVM regression method for the inversion and retrieval of key biophysical parameters that help understand and to quantify the nature of the nematode infested vegetation. Therefore, to guarantee the efficiency of early detection of nematode infection levels, efficient machine learning algorithms and sensing technology should be adopted according to the results from this study.

### 6.3.3 Performance of Classifiers (Project 45, 2020)

In order to obtain a complete understanding of the facts and circumstances about the early detection of nematode infection levels, the author also collected the data using the proximate sensor in 2020. For Project 45, there were 60 sampling trees from 4 different blocks in 2020 (Table 6.6). Each sampling tree was measured five times to reduce the likelihood of errors or anomalous results. Genotypes from one cross went into the analysis. Based on the root-lesion nematode number, the walnut trees of 2020 were classified into four levels of nematode infestation, from level 1 to level 4 (Table 6.5).

The machine learning algorithms were applied for nematode data processing

Table 6.5: The classification of the nematode infestation levels (Project 45, 2020). “RLN per gram of root” meant the root-lesion nematode number per gram of root that was extracted in laboratory procedures.

Nematode infestation levels	RLN per gram of root
Level 1	0 - 20,
Level 2	20 - 60,
Level 3	60 - 200,
Level 4	> 200.

and analysis. According to Fig. 6.6 and Table 6.7, the trained models had different prediction performance for early detection of nematode infection levels. Although the exact prediction accuracy was distinct, the experimental results of 2020 were pretty consistent with the analysis results of 2019. The  $k$ -nearest neighbors vote still had the highest accuracy of 0.95. Table 6.8 showed the details of the test process of the  $k$ -nearest neighbors method. For the other classifiers’ test performance, the accuracy of the “Support Vector Machine” was 0.58. The “Random Forest” had a test accuracy of 0.61. The “AdaBoost”, “Neural Network”, and “Decision Tree” had an accuracy of 0.63, 0.62, and 0.78, respectively.

For the training process of DNN with TensorFlow, the number of epochs was still set as 200 and the batch size was 10. As shown in Fig. 6.7, there were 100 models. The highest accuracy could be as high as 0.88. The lowest accuracy was around 0.4 when the training instances could not represent the nematode infection levels very well. To evaluate the trained model, the authors run the training process 100 times to reduce the randomness of the training instances selection. The mean accuracy was around 0.7 for the DNN classifier model.

As mentioned earlier in this section, the experimental results of 2020 were pretty consistent with the analysis results of 2019. Detecting the nematode disease in walnut roots with proximate sensing is usually based on changes in the spectral response of the walnut due to impairment of their leaf structure. The research consistency further enhanced the author’s discussion that the walnut root infection by nematodes could induce spectral variation in walnut leaves. The different signals

Table 6.6: Nematode numbers per gram of root in rootstock genotypes examined by Walabot measurements (Project 45, 2020). “RLN per gram of root” meant the root-lesion nematode number per gram of root that was extracted in laboratory procedures. “ID” is a short form for “identity”.

Tree ID	Genotype	RLN per gram of root	Tree ID	Genotype	RLN per gram of root
C1	MS1 48	243.8	A1	MS1 62	418.5
C2	I13-32	1005	A2	MS1 117	73.5
C3	Vlach	872.4	A3	MS1 117	43.5
C4	MS1 128	96	A4	MS1 95	205.5
C5	MS1 3	155.4	A5	MS1 48	82.5
C6	RX1	40.6	A6	MS1 128	355.5
C7	MS1 72	21	A7	Vlach	228
C8	MS1 117	4.5	A8	MS1 89	64.5
C9	MS1 31	207.6	A9	UZ229	172.5
C10	MS1 132	20	A10	MS1 127	37.5
C11	MS1 89	11.6	A11	MS1 3	1.4
C12	MS1 127	69	A12	RX1	1536
C13	MS1 95	201	A13	MS1 31	766.5
C14	VX211	19.5	A14	VX211	174
C15	MS1 62	462	A15	MS1 98	18
D1	Vlach	187.5	B1	MS1 31	67.5
D2	MS1 128	437.4	B2	MS1 48	111
D3	MS1 3	286.5	B3	MS1 95	57.4
D4	MS1 89	197.5	B4	MS1 127	15
D5	MS1 132	159	B5	MS1 132	23.2
D6	MS1 31	226.5	B6	VX211	36
D7	VX211	22.5	B7	MS1 62	141
D8	MS1 95	90	B8	Vlach	30
D9	MS1 127	114	B9	RX1	111
D10	MS1 72	931.5	B10	MS1 3	10.4
D11	MS1 122	201	B11	MS1 89	18
D12	I13-32	433.5	B12	MS1 72	27
D13	RX1	333	B13	MS1 117	12
D14	MS1 62	17.5	B14	UZ229	1090.5
D15	MS1 48	1599	B15	MS1 128	334.6

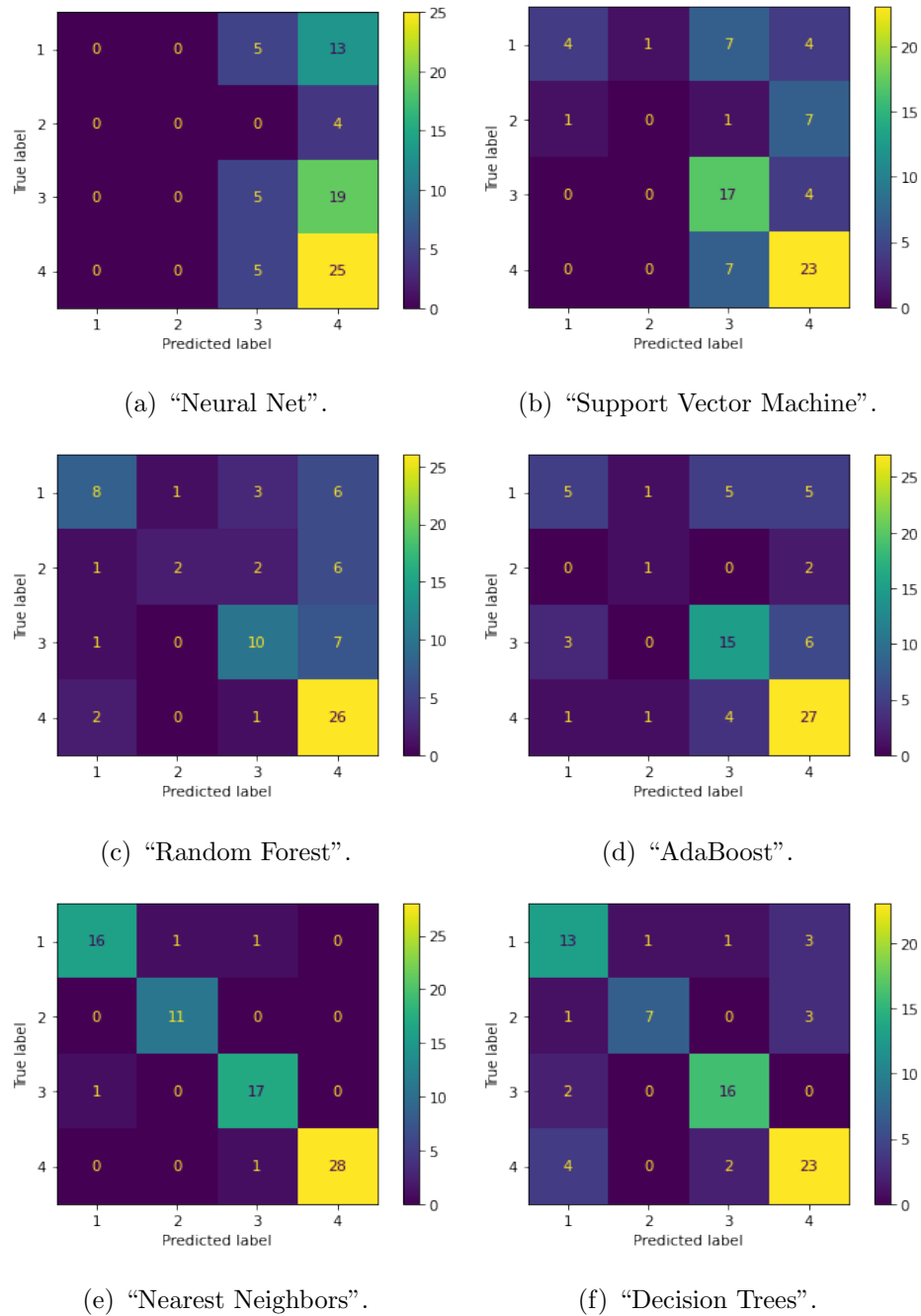


Figure 6.6: A comparison of six classifiers in Scikit-learn on nematode testing dataset (Project 45, 2020). Table 6.8 showed the details of the test process of the  $k$ -nearest neighbors method.

Table 6.7: The performance of classification methods (Project 45, 2020).

Classification methods	Prediction accuracy
“Neural Network”	0.63
“Support Vector Machine”	0.58
“Random Forest”	0.61
“AdaBoost”	0.63
“Nearest Neighbors”	<b>0.95</b>
“Decision Tree”	0.78
“DNN with TensorFlow”	0.7

Table 6.8: The  $k$ -nearest neighbors performance (Project 45, 2020).

Nematode infestation level	Precision	Recall	F1-score
Level 1	0.94	0.89	0.91
Level 2	0.92	1	0.96
Level 3	0.89	0.94	0.92
Level 4	1	0.97	0.98
Accuracy	NA	NA	<b>0.95</b>
Macro avg	0.94	0.95	0.94
Weighted avg	0.95	0.95	0.95

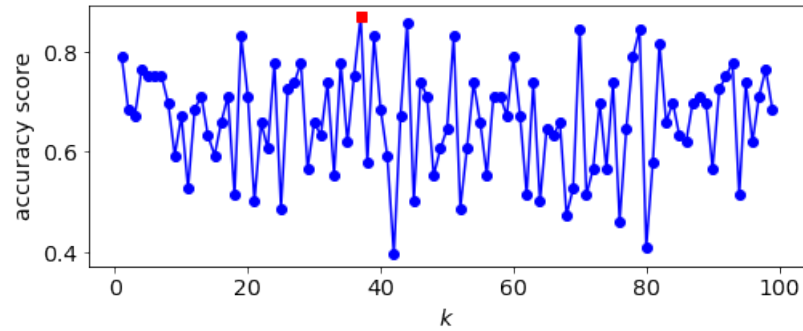


Figure 6.7: The test performance of DNN for Project 45, 2020. There were 100 models and the best accuracy could be as high as 0.88 (marked as a red dot). The lowest accuracy was around 0.4 when the training instances could not represent the nematode infection levels dataset very well. The mean accuracy was 0.7 for the DNN classifier model.

generated by the radio frequency proximate sensor could estimate the walnut root damage caused by nematodes. With the  $k$ -nearest neighbors method, the nematode infection levels could be classified with a high accuracy of 95%. These findings further emphasized the importance of applying phenotyping analysis by machine learning algorithms for the early detection of nematode infection levels.

To evaluate the hypothesis that remote sensing is the best approach to monitoring root-knot nematodes in coffee crops, Matins *et al.* also collected agronomical parameters from plots of healthy and infected coffee plants, such as leaf area index (LAI), chlorophyll relative content obtained by soil and plant development analyzer (SPDA), biomass measurements, and radiometric data [329]. For the spectral characterization, radiometric data of leaves enabled the identification of the most sensitive spectral ranges for discrimination of the infected coffee plots. Inspired by the research work by [329], the author will also collect agronomical parameters from the study site in the future and will further figure out the correlation between the radio frequency reflectance and the agronomical parameters, such as LAI and chlorophyll relative content of the walnut leaves.

## 6.4 Conclusions and Future Research

The aim of the present research was for the early detection of nematode infection levels in the walnut root by a non-invasive method. The author collected the radio frequency reflectance data of walnut leaves by using a proximate sensor. Then, machine learning algorithms were adopted for the nematode infection levels classification problem. The research results showed that the best classification accuracy of nematode infection levels was 95% when the  $k$ -nearest neighbors method was being adopted. The walnut root infection by nematodes could induce spectral variation in walnut leaves. The results of this research supported the idea that trees and crops severely infected by nematodes showed a significant reduction in leaf area similar to the plant response to other environmental stress, such as drought, nutrient deficiency, salinity, and other biotic stresses. Furthermore, the findings of this research provided insights for the early detection of nematodes using phenotyping and machine learning technology.

The study was limited by the lack of information on the biophysical explanation of what variations of the walnut leaves were responsive or sensitive to the radio frequency signal under the pressure of nematodes. Despite of its limitations, the study certainly added an understanding of the effect of nematode infection on walnut phenotyping analysis. In the future, the precise mechanism of the radio frequency sensor in the early detection of nematodes remains to be elucidated. The author will also collect agronomical parameters from the study site and figure out the correlation between the radio frequency reflectance and the agronomical parameters, such as LAI and chlorophyll relative content of the walnut leaves. The author will also perform similar data analysis for Project 30 (a, b) and Project Smith.

# Chapter 7

## Evapotranspiration Estimation with Small UAVs

### 7.1 Introduction

Evapotranspiration (ET) estimation is important for precision agriculture, especially precision water management. Mapping the ET temporally and spatially can identify variations in the field, which is useful for evaluating soil moisture [348, 349] and assessing crop water status [350]. ET estimation can also benefit the water resources management and weather forecast [351]. ET is a combination of two separate processes, evaporation (E) and transpiration (T). Evaporation is the process whereby liquid water is converted to water vapor through latent heat exchange [352]. Transpiration is the process of the vaporization of liquid water contained in plant tissues, and the vapor removal to the atmosphere [352]. The current theory for transpiration is constituted by the following three steps. First, the conversion of liquid-phase water to vapor water causes canopy cooling from latent heat exchange. Thus, canopy temperature can be used as an indicator of ET. Second, diffusion of water vapor from inside plant stomata on the leaves to the surrounding atmosphere. Third, atmospheric air mixing by convection or diffusion transports vapor near the plant surfaces to the upper atmosphere or off-site away from the plant canopy. Usually, evaporation and transpiration occur simultane-

ously.

Many approaches have been developed to estimate ET. Typically, there are direct and indirect methods. For direct methods, ET can be determined by water balance [353]:

$$ET = P + I - D - R - S, \quad (7.1)$$

where  $P$  (mm day<sup>-1</sup>) is precipitation,  $I$  (mm day<sup>-1</sup>) is irrigation,  $D$  (mm day<sup>-1</sup>) is drainage,  $R$  (mm day<sup>-1</sup>) is runoff, and  $S$  (mm day<sup>-1</sup>) is the soil moisture storage. These direct ET methods, however, are usually point-specific or area-weighted measurements and cannot be extended to a large scale because of the heterogeneity of the land surface. The experiment equipment is also costly and requires substantial expense and effort, such as lysimeters, which are only available for a small group of researchers. For indirect methods, there are energy balance methods [354] and remote sensing methods [355]. For energy balance methods, Bowen ratio [356, 357] and eddy covariance [358] have been widely used in ET estimation. However, they are also area-weighted measurements. Remote sensing techniques can detect variations in vegetation and soil conditions over space and time. Thus, they have been considered as one of the most powerful methods for mapping and estimating spatial ET over the past decades [359, 360]. Remote sensing models have been useful in accounting for the spatial variability of ET at regional scales when using satellite platforms such as Landsat and ASTER [361, 362, 206, 363]. Since the satellite was being applied [364], several remote sensing models have been developed to estimate ET, such as Surface Energy Balance Algorithm for Land (SEBAL) [362, 355], Mapping Evapotranspiration with Internalized Calibration (METRIC) [365], the Dual Temperature Difference (DTD) [366], and the Priestley-Taylor TSEB (TSEB-PT) [198]. Remote sensing techniques can provide information such as Normalized Difference Vegetation Index (NDVI), Leaf Area Index (LAI), surface temperature, and surface albedo. Related research on these parameters has been discussed by different researchers [367, 368, 369].

As a new remote sensing platform, researchers are more and more interested in the potential of small UAVs in precision agriculture [138, 139, 140, 141], especially

on heterogenous crops, such as vineyard and orchards [146, 26]. UAVs overcome some of the remote sensing limitations faced by satellite. For example, satellite remote sensing is prone to cloud cover; UAVs are below the clouds. Compared with the satellite, UAVs can be operated at any time if the weather is within operating limitations. The satellite has a fixed flight path, UAVs are more mobile and adaptive for site selection. Mounted on the UAVs, lightweight sensors, such as RGB cameras, multispectral cameras, and thermal infrared cameras, can be used to collect high-resolution images. The higher temporal and spatial resolution images, relatively low operational costs, and the nearly real-time image acquisition, make the UAV an ideal platform for mapping and monitoring ET. Many researchers have already used UAVs and lightweight sensors for ET estimation, as shown in Table 7.1 and Table 7.2. For example, in [203], Ortega-Farías *et al.* implemented a remote sensing energy balance (RSEB) algorithm for estimating energy components in an olive orchard, such as incoming solar radiation, sensible heat flux, soil heat flux, and latent heat flux. Optical sensors were mounted on a UAV to provide high spatial resolution images. By using the UAV platform, experimental results showed that the RSEB algorithm could estimate latent heat flux and sensible heat flux with errors of 7% and 5%, respectively. It demonstrated that UAV could be used as an excellent platform to evaluate the spatial variability of ET in the olive orchard.

The objective of this chapter is to investigate the advanced analytics for crop coefficient estimation and reliable tree-level ET estimation methods proposed by the author. The rest of the chapter is organized as follows: In Section 7.4, the author proposed to estimate crop coefficient with UAV-based imagery and SCNs model. Then, the author proposed reliable tree-level ET estimation methods in Section 7.5. Lastly, the author shares views in ET estimation with UAVs in the future research and draws conclusive remarks.

Table 7.1: ET estimation using UAV platforms.

Study sites	UAV Platforms	Sensors	Method	Crops	References
Ames, Iowa, USA	eBee Ag	Sequoia, Cannon S110 thermoMAP camera	SEBAL	Corn and soybean	[195]
Scipio, UT					
Lodi, CA, USA	AggieAir	Canno S-95 ICI thermal camera	METRIC	Vineyard	[196]
Pinto Bandeira city Rio Grande do Sul State, Brazil	AIBOTIX	Nikon CoolpixA Camera	METRIC	Vineyard	[197]
HOBE agricultural site, Denmark	Q300, QuestUAV	Optris Pi 450	TSEB	Barley	[198]
Lodi, CA, USA	Cessna TU206	ImperX Bobcat B8430 ThermaCAM SC640	TSEB	Vineyard	[199]
Lodi, CA, USA	AggieAir	NA	TSEB	Vineyard	[200]
Pinto Bandeira Serra Gaucha, Brazil	AIBOTIX Hexacoptero	Nikon CoolpixA camera	TSEB	Vineyard	[201]
Lodi, CA, USA	NA	NA	TSEB	Vineyard	[202]
Pencalhue Valley Región del Maule, Chile	NA	Mini MCA-6 EasIR-9	TSEB	Olive	[203]
Bushland, Texas, USA	AggieAir	Kodak thermal infrared model 760	TSEB	Sorghum and corn	[204]
Petit-Nobressart, Luxembourg	MikroKopter OktoXL	Samsung ES80 Optris Pi 400	TSEB	Grassland	[205]
Lodi, CA, USA	Cessna TU206	ImperX Bobcat B8430 ThermaCAM SC640	OSEB	Vineyard	[199]
Petit-Nobressart, Luxembourg	MikroKopter OktoXL	Samsung ES80 Optris Pi 400	OSEB	Grassland	[205]
Tatura, Victoria, Australia	DJI S1000	A65 and RedEdge M	HRMET	Peach, nectarine, and corn	[206]

Table 7.2: Multispectral and thermal infrared sensors on UAV platforms.

Sensor	Function	Resolution	Weights	Dimensions	Spectral bands	Accuracy
Rededge M	Multispectral	1280 × 960 pixels	231.9 g	8.7 × 5.9 × 4.54 cm	Blue, green, red, red edge, near infrared (NIR)	8.2 cm/pixel, per band at 120 m
MAPIR Survey 3	Multispectral	4608 × 3456 pixels	76 g	5.9 × 4.15 × 3.6 cm	375 - 650 nm	4.05 cm/pixel at 120 m
Mini MCA-6	Multispectral	1280 × 1024 pixels	700 g	13.14 × 7.83 × 8.76 cm	450 - 1000 nm	3.3 cm/pixel at 60 m
Tetracam ADC Lite	Multispectral	2048 × 1536 pixels	200 g	11.4 × 7.7 × 6.05 cm	Red, green, NIR	5 cm/pixel at 150 m
Sequoia	Multispectral	4608 × 3456 pixels	72 g	5.9 × 4.1 × 2.8 cm	Green, red, red edge and near infrared	17 cm/pixel at 100 m
Cannon S 110	Near infrared	4000 × 3000 pixels	198 g	9.9 × 5.9 × 2.7 cm	NIR	3.5 cm/pixel at 100 m
ICI SWIR 640 P	Short-wave infrared	640 × 512 pixel	130 g	4.6 × 4.6 × 2.95 cm	0.9 - 1.7 μm	±1 °C
ICI 9640 P	Thermal infrared	640 × 480 pixel	37 g	3.4 × 3.0 × 3.4 cm	7 - 14 μm	±1 °C
ICI 8640 P	Thermal infrared	640 × 480 pixel	74.5 g	4.5 × 4.5 × 3.9 cm	7 - 14 μm	±1 °C
FLIR Vue Pro R 640	Thermal infrared	640 × 512 pixel	72 g	5.74 × 4.44 cm	7.5 - 13.5 μm	±5 °C
Optris PI 450	Thermal infrared	382 × 288 pixels	240 g	4.6 × 5.6 × 6.8 cm	8 - 14 μm	±2 °C or ±2 %
ThermalCAM SC640	Thermal infrared	640 × 480 pixel	1.7 kg	28.2 × 14.4 × 14.7 cm	7.5 - 13 μm	±2 °C or ±2 %
EasIR-9	Thermal infrared	288 × 384 pixel	1 kg	11.2 × 18.2 × 25.2 cm	8 - 14 μm	±2 °C or ±2 %
thermoMAP	Thermal infrared	640 × 512 pixel	134 g	56 × 46 × 26 cm	7 - 15 μm	±5 °C
A65	Thermal infrared	640 × 512 pixel	200 g	29.5 × 20.0 × 10.5 cm	7.5 - 13 μm	±5 °C
Optris PI 400	Thermal infrared	382 × 288 pixel	240 g	4.6 × 5.6 × 6.8 cm	8 - 14 μm	±2 °C

## 7.2 ET Estimation Methods with UAVs: A Literature Review

Most ET estimation using UAVs is based on satellite remote sensing methods. One source energy balance (OSEB), High Resolution Mapping of Evapotranspiration (HRMET) [370], Machine Learning (ML) [371, 372, 373, 374, 375, 376], Artificial Neural Networks (ANN) [377], Two source energy balance (TSEB), Dual-Temperature-Difference (DTD) [378], Surface Energy Balance Algorithm for Land (SEBAL) [362, 355], and Mapping Evapotranspiration at high Resolution with Internalized Calibration (METRIC) [365] are introduced in this section. The discussed ET estimation methods with UAVs and their advantages and disadvantages are summarized in Table 7.3. This chapter is not intended to provide an exhausting review of all direct or indirect methods that have been developed for ET estimation, but rather to provide an overview on ET estimation with the UAV applications. Therefore, only those methods (Table 7.1) which have already been used with the UAV platform are discussed.

### 7.2.1 One Source Energy Balance (OSEB)

The one source energy balance (OSEB) model assumes the whole surface as a uniform layer, which does not differentiate potential sources, such as the soil and canopy [362, 359]. The OSEB model uses empirical parameters to explain differences in the aerodynamic and radiometric components [379, 380, 381, 382, 383]. The OSEB model uses the following equation to calculate the latent heat flux,

$$LE = R_n - G - H, \quad (7.2)$$

where  $LE$  is the latent heat flux ( $\text{W m}^{-2}$ ),  $R_n$  is the net radiation ( $\text{W m}^{-2}$ ),  $G$  is the soil heat flux ( $\text{W m}^{-2}$ ), and  $H$  is the sensible heat flux ( $\text{W m}^{-2}$ ). The sensible heat flux  $H$  is calculated by

Table 7.3: Comparisons of the different ET estimation methods.

Methods	Applications with UAVs	Advantages	Disadvantages
OSEB	Vineyard [199], grassland [205]	(1) Treat the surface as big leaf and therefore as a simple uniform layer.	(1) Uses empirical parameters to explain differences in the aerodynamic and radiometric components; (2) Assumes the whole surface as a uniform layer, which does not take advantage of UAV high-resolution imagery; (3) Less sensitive to land surface temperature variations than the TSEB model.
HRMET	Peach, nectarine [206], and corn	(1) Only requires basic meteorological data, spatial surface temperature, and canopy structure data; (2) Does not depend on wet and dry reference features to calculate turbulent fluxes.	(1) Needs more validation for clumped canopy structure, such as trees and vines.
ML/ANN	Vineyard [377]	(1) Capture non-linear crop characteristics	(1) Requires large amount of data for training models and validation
TSEB	Barley vineyard [198], [199, 200, 201, 202], olive [203], sorghum and corn [204], grassland [205]	(1) The calculation of sensible heat flux and latent heat flux for canopy and soil are separate; (2) Parameterization of resistances is easier compared with a single layer model	(1) Sensitive to the temperature difference between the land surface and air; (2) The measurement of the absolute land surface temperature is inaccurate
DTD	Barley [198], corn and soybean	(1) One more input dataset, the land surface temperature retrieved one hour after sunrise; (2) Minimizes the bias in the temperature estimation; (3) Separates the land surface temperature into vegetation and soil temperatures	(1) Requires flights at two times during the morning hours, thus complicating flight missions
SEBAL	Corn and soybean [195]	(1) Requires minimum ground-based data; (2) Automatic internal correction	(1) Selecting hot or cold pixels is subjective, which can cause variations in ET estimation
METRIC	Vineyard [196, 197]	(1) Eliminates the need for absolute surface temperature calibration; (2) Requires minimum ground-based data; (3) Automatic internal correction	(1) Selecting hot or cold pixels is subjective, which can cause variations in ET estimation

$$H = \rho C_p \frac{T_{aero} - T_{ac}}{R_{ah}}, \quad (7.3)$$

where  $\rho$  is the air density ( $\text{kg m}^{-3}$ ),  $C_p$  is the specific heat of air ( $\text{J kg}^{-1} \text{K}^{-1}$ ),  $T_{aero}$  is the aerodynamic temperature (K) [384], and  $T_{ac}$  is the air temperature (K) in the vegetation [385, 386, 387].  $R_{ah}$  is the aerodynamic resistance to heat flux ( $\text{s m}^{-1}$ ), which is calculated by

$$R_{ah} = \frac{[\ln(\frac{z_u-d}{z_{om}}) - \Psi_m][\ln(\frac{z_t-d}{z_{om}}) + \ln(\frac{z_{om}}{z_{oh}}) - \Psi_h]}{k^2 u}, \quad (7.4)$$

where  $z_u$  and  $z_t$  are the wind and air temperature measurement heights, respectively. The parameter  $d$  is the zero displacement height,  $z_{om}$  is the momentum transfer [388, 389],  $\Psi_m$  and  $\Psi_h$  are the diabatic correction factors for momentum and heat [390],  $z_{oh}$  is the resistance to heat,  $k$  is the Karman constant, and  $u$  is the wind speed.

The parameter  $kB^{-1}$  is also used in OSEB model to adjust the radiometric to the aerodynamic temperature. The measured radiometric temperature can be used in equation (7.3) instead of  $T_{aero}$ . The parameter  $kB^{-1}$  is calculated by

$$kB^{-1} = \ln\left(\frac{z_{om}}{z_{oh}}\right). \quad (7.5)$$

There are also some other types of OSEB models. For example, deriving atmosphere turbulent transport useful to dummies using temperature (DATUTDUT) [391] is an energy balance model which only needs the land surface temperature as the input for ET estimation. The DATUTDUT estimates ET by scaling the energy fluxes between the hot and cold pixels. The DATUTDUT model is similar to the simplified surface energy balance index (S-SEBI) proposed by Roerink [392]. However, the DATUTDUT model is more simplified to acquire the radiometric temperature. More details can be found in [391].

## 7.2.2 High Resolution Mapping of ET (HRMET)

For most current ET models such as METRIC and SEBAL, they are highly relied on selecting hot and cold pixels to separate energy fluxes between latent and

sensible heat in the images. Therefore, their ability is limited to map ET throughout the growing season at extremely high spatial resolutions. Thus, Zipper *et al.* developed a field-validated surface energy balance model, which was called High Resolution Mapping of Evapotranspiration (HRMET) [370]. The HRMET only requires basic meteorological data, spatial surface temperature, and canopy structure data. For more detailed calculation steps about the HRMET, please refer to [370].

### 7.2.3 Machine Learning (ML) and Artificial Neural Networks (ANN)

Machine learning techniques and ANN models have already been used for estimating hydrological parameters [371, 372, 373, 374, 375, 376], ecological variables [393]. Because of the ML's ability to capture non-linear characteristics, many research results suggest that machine learning methods can provide better ET estimates than empirical equations based on different meteorological parameters [394, 395, 396, 397, 398, 399, 400, 401]. Traditional multispectral indices have limitations to assess water status. Therefore, artificial neural networks (ANN) were used in [377] to improve the estimation of spatial variability of vine water status. In [402], Dou *et al.* used four different machine learning approaches in different terrestrial ecosystems for ET estimation. The ANN, support vector machine (SVM), extreme learning machine (ELM) [403] and adaptive neuro-fuzzy inference system (ANFIS) [404, 405, 406, 407, 400, 408] were compared with each other on estimating ET. In [409], Torres-Rua *et al.* built a narrowband and broadband emissivities model for UAV thermal imagery using a deep learning (DL) model. The resulting emissivities were incorporated into the TSEB model to analyze their effect on the estimation of instantaneous energy balance components against ground measurements.

### 7.2.4 Two Source Energy Balance (TSEB) Models

The TSEB model is developed to improve the accuracy of  $LE$  estimation [369, 366, 385, 410], using the assumptions of canopy transpiration in Priestley and Taylor potential evapotranspiration [411] calculations. Therefore, this TSEB model is also called TSEB-PT to differentiate it from other TSEB methods. The calculation of sensible heat flux and latent heat flux for canopy and soil are separate, which makes the parameterization of resistances easier compared with a single layer model. Based on [412, 413], the TSEB is effective over homogeneous land and environmental conditions. The TSEB model reproduces fluxes with similar results to tower-based observations.

The TSEB model separates the land surface temperature into soil surface temperature  $T_s$  and vegetation surface temperature  $T_c$ . Subscripts “s” and “c” mean soil and canopy. It considers sensible and latent heat fluxes are transferred to the atmosphere from both surface temperature components, as shown in the following equations [199],

$$R_n = R_{ns} + R_{nc}, \quad (7.6)$$

$$R_{ns} = H_s + LE_s + G, \quad (7.7)$$

$$R_{nc} = H_c + LE_c. \quad (7.8)$$

The net radiation  $R_n$  is divided into two parts, the soil net radiation  $R_{ns}$  and the canopy net radiation  $R_{nc}$  [414, 415],

$$R_{ns} = \tau_l L_d + (1 - \tau_l)\varepsilon_c \sigma T_c^4 - \varepsilon_s \sigma T_s^4 + \tau_s(1 - \alpha_s)S_d, \quad (7.9)$$

$$R_{nc} = (1 - \tau_l)(L_d + \varepsilon_s \sigma T_s^4 - 2\varepsilon_c \sigma T_c^4) + (1 - \tau_s)(1 - \alpha_c)S_d, \quad (7.10)$$

where  $\tau_l$  and  $\tau_s$  are the longwave and shortwave radiation transmittances through the canopy, respectively.  $L_d$  and  $S_d$  are the incoming longwave and shortwave radiation ( $\text{W m}^{-2}$ ), which are usually measured from a nearby weather station. The Stefan-Boltzmann constant is given by  $\sigma$ , which is approximately  $5.67 \times 10^{-8}$

(W m<sup>-2</sup> K<sup>-4</sup>). The surface emissivity is denoted by  $\varepsilon$ ,  $\alpha$  is the surface albedo, and  $T$  is the surface temperature (K).

For the soil sensible heat flux  $H_s$  and canopy sensible heat flux  $H_c$ , they can be calculated based on the following equations,

$$H_s = \rho C_p \frac{T_s - T_{ac}}{R_s}, \quad (7.11)$$

$$H_c = \rho C_p \frac{T_c - T_{ac}}{R_x}, \quad (7.12)$$

where  $\rho$  is the air density (kg m<sup>-3</sup>),  $C_p$  is the specific heat of air (J kg<sup>-1</sup> K<sup>-1</sup>),  $T_{ac}$  is the air temperature in the vegetation [385, 386, 387],  $R_s$  is the resistance to heat flux above the soil surface (s m<sup>-1</sup>), and  $R_x$  is the boundary layer resistance of the canopy leaves (s m<sup>-1</sup>).

### 7.2.5 Dual-Temperature-Difference (DTD) Model

The DTD model separates the land surface temperature into vegetation and soil temperatures [378]. Then, it calculates the surface energy balance components by using the same procedures as the TSEB. The TSEB model is very sensitive to the temperature difference between the land surface and air, which makes the absolute land surface temperature inaccurate. To solve this problem, the DTD model added one more input dataset, the land surface temperature retrieved one hour after sunrise. The energy fluxes are minimal at sunrise, which minimizes the bias in the temperature estimation. For the soil sensible heat flux  $H_s$  and canopy sensible heat flux  $H_c$ , equation (7.11) and (7.12) become

$$H_s = \rho C_p \frac{(T_{s_i} - T_{s_o}) - (T_{ac_i} - T_{ac_o})}{R_s}, \quad (7.13)$$

$$H_c = \rho C_p \frac{(T_{c_i} - T_{c_o}) - (T_{ac_i} - T_{ac_o})}{R_x}, \quad (7.14)$$

where subscript  $i$  means the measurements are at midday and subscript  $o$  refers to observations one hour after the sunrise.

In [416], Guzinski *et al.* produced surface energy flux successfully by using the DTD model with satellite images, who used night observations to substitute

for the early morning observation. However, the temporal resolution of the satellite observations is limited, especially when the weather conditions are limiting. For example, satellite thermal infrared observations cannot penetrate clouds when there is a cloud cover. The incapacity to collect data in overcast situations applies to all satellite sensors except for those operating in the microwaves region [416].

The calculation of soil heat flux  $G$  is different between midday and sunrise observations. This difference can be used to estimate the soil surface temperature variations. Soil heat flux is calculated based on the model of [417]. The soil heat flux equation is

$$G = R_{ns} A \cos\left(2\pi \frac{(t + 10800)}{B}\right), \quad (7.15)$$

$$A = 0.0074\Delta T_R + 0.088, \quad (7.16)$$

$$B = 1729\Delta T_R + 65013, \quad (7.17)$$

where  $\Delta T_R$  is the diurnal variation in the soil surface temperature, and  $t$  is the time between the data collection time and the solar noon. For more details about the TSEB and DTD equations, see [418, 419].

## 7.2.6 Surface Energy Balance Algorithm for Land (SEBAL)

The Surface Energy Balance Algorithm for Land (SEBAL) model uses surface temperature  $T_s$ , visible, near-infrared, thermal infrared radiation, albedo maps, and NDVI to estimate surface fluxes with many different land cover types [362, 420]. SEBAL is currently one of the most reliable algorithms to estimate actual ET ( $ET_a$ ), and it is one of the most promising approaches currently for local and regional estimation with minimum ground data [354]. SEBAL has been validated in many different climatic conditions around the world [421, 422, 423, 424, 425]. Typically, the SEBAL's accuracy is around 85% and 95% at daily and seasonal scales, respectively [421, 426]. To calculate ET as a residual of the energy balance model, the sensible heat flux  $H$  needs to be estimated first.

In the SEBAL model, two reference air temperatures are measured to compute the air temperature difference ( $dT$ ). One air temperature is measured at the height  $h_1$  close to the surface. The other is measured at an upper height of  $h_2$ . To calculate  $dT$  for each pixel, SEBAL assumes that there is a linear relationship between  $dT$  and the surface temperature  $T_s$  as

$$dT = a + bT_s, \quad (7.18)$$

where  $a$  and  $b$  are derived parameters empirically based on two extreme hot and cold pixels, also called “anchor” pixels [420]. These hot and cold pixels defined the boundary of the sensible heat flux. The cold pixel is usually selected from a well-watered area with no water stress. The  $H$  is assumed to be minimum, and ET should be maximum. The hot pixel is taken from a dry and bare field where  $H$  is maximum, and ET is almost zero. Hot and cold pixels are usually selected by an empirical method.

Most SEBAL applications for estimating energy fluxes and ET have used space-borne platforms with a relatively low spatial resolution. There is not much published work related to the use of the SEBAL model to estimate ET using UAVs. Selecting hot or cold pixels is subjective, which can cause variations in ET estimation. Estimated sensible heat flux  $H$  is easily affected by the surface-air temperature differences or surface temperatures measurements. The radiometer’s viewing angle can also cause variations in  $T_s$  by several degrees for some images.

Although SEBAL has limitations, there are also several advantages of SEBAL for estimating land surface fluxes from thermal remote sensing data. First, SEBAL does not need a lot of ground-based data. Second, SEBAL has an automatic internal correction. Third, every image has an internal calibration in SEBAL.

### **7.2.7 Mapping Evapotranspiration at High Resolution with Internalized Calibration (METRIC)**

METRIC is originally a satellite image processing model for estimating ET as a residual of the energy balance [365], which is based on SEBAL. The METRIC

can generate ET maps with a 30-meter spatial resolution by using Landsat images. METRIC has a self-calibration process which contains ground-based hourly reference ET and the selection of hot, cold pixels [427]. It eliminates the need for absolute surface temperature calibration [355].

SEBAL uses  $T_s$ ,  $\rho$ , NDVI and their relationships to calculate the surface fluxes [362], which has been evaluated all over the world [421, 422, 423, 425, 424]. The METRIC model uses the same method with the SEBAL to estimate  $dT$ . Thus, there is no need to get an accurate aerodynamic surface temperature. In [354], Liou *et al.* summarized three differences between the SEBAL and METRIC. First, for the cold pixel, the METRIC does not consider sensible heat flux as zero. Instead, a surface soil water balance is applied to set ET as 1.05 times reference ET at cold pixels. Reference ET is calculated by using the standardized American Society of Civil Engineers (ASCE) Penman-Monteith equation. Second, in METRIC, cold pixels are selected in agricultural settings instead of biophysical characteristics. Third, the extrapolation of instantaneous ET is based on reference ET instead of the actual evaporative fraction.

METRIC estimates ET using the energy balance equation (7.2). For the net radiation  $R_n$  ( $\text{W m}^{-2}$ ), it can be calculated by adding all the incoming radiation and subtracting all the outgoing radiation based on the following equation [365],

$$R_n = (1 - \alpha)R_{s\downarrow} + R_{L\downarrow} - R_{L\uparrow} - (1 - \varepsilon_o)R_{L\downarrow}, \quad (7.19)$$

where  $R_{s\downarrow}$  is the incoming short-wave radiation ( $\text{W m}^{-2}$ ),  $\alpha$  is the surface albedo,  $R_{L\downarrow}$  and  $R_{L\uparrow}$  are the incoming longwave radiation ( $\text{W m}^{-2}$ ) and outgoing longwave radiation ( $\text{W m}^{-2}$ ), respectively.  $\varepsilon_o$  is the thermal emissivity, which is also dimensionless. These parameters can be calculated in METRIC with several sub-models that use other parameters derived from the ground-based weather data, digital elevation model (DEM), and satellite images [365].

Sensible heat flux  $H$  ( $\text{W m}^{-2}$ ) is computed from surface roughness, wind speed, surface temperature ranges,

$$H = \rho_{air} C_p \frac{dT}{r_{ah}}, \quad (7.20)$$

where  $r_{ah}$  is the aerodynamic resistance ( $\text{s m}^{-1}$ ) between two surface height. In METRIC,  $r_{ah}$  is usually calculated by using the wind speed, LAI or NDVI, and an iterative stability correction, as shown in the following equation,

$$r_{ah} = \frac{\ln(z_2/z_1)}{u_* k}, \quad (7.21)$$

where  $z_1$  and  $z_2$  are heights above the zero-plane displacement of the vegetation.  $k$  is the von Karman constant (0.41).  $u_*$  is the friction velocity ( $\text{m s}^{-1}$ ), which is calculated by using

$$u_* = \frac{ku_{200}}{\ln(200/z_{om})}, \quad (7.22)$$

where  $u_{200}$  is the wind speed at a blending height 200m, and  $z_{om}$  is the momentum roughness length (m).

The temperature difference between the air and the surface is represented by  $dT$ . A strong linear relationship between the  $dT$  and the surface temperature were found in [365, 362, 426, 428], as shown in equation (7.18). The sensible heat fluxes for the cold and hot pixels are calculated by equation (7.2). According to [429], for the cold pixel, the ratio  $LE$  and  $ET_r$  is assumed to be 1.05. However, this assumption is not always true at the beginning or outside of the growing season when the vegetation is much less than the alfalfa [364]. Therefore, the ratio of the  $LE$  and  $ET_r$  for the cold and hot pixels are calculated by NDVI [365]. Then, the  $dT$  and land surface temperature  $T_s$  for the cold and hot pixels are applied for calculating the  $a$  and  $b$  in equation (7.18) as

$$a = \frac{dT_{hot} - dT_{cold}}{T_{shot} - T_{scold}}, \quad (7.23)$$

$$b = \frac{dT_{hot} - a}{T_{shot}}, \quad (7.24)$$

where  $T_{shot}$  and  $T_{scold}$  are the land surface temperature (K) at the hot and cold pixels, respectively.

Table 7.4: Comparisons of the different ET estimation methods with UAVs.

Methods	Applications with UAVs	Accuracy of $R_n$	Accuracy of $G$	Accuracy of $LE$	Accuracy of $H$
OSEB TSEB	Grassland [205]	$R^2$ of 0.98 $R^2$ of 0.99	$R^2$ of 0.73 $R^2$ of 0.83	$R^2$ of 0.92 $R^2$ of 0.93	$R^2$ of 0.79 $R^2$ of 0.84
TSEB DTD	Barley [198]	RMSE of 44 W m <sup>-2</sup> RMSE of 44 W m <sup>-2</sup>	RSME of 38 W m <sup>-2</sup> RSME of 48 W m <sup>-2</sup>	RMSE of 94 W m <sup>-2</sup> RSME of 67 W m <sup>-2</sup>	RMSE of 85 W m <sup>-2</sup> RSME of 59 W m <sup>-2</sup>
TSEB DATTUTDUT	Vineyard [199]	RMSE of 33 W m <sup>-2</sup> RMSE of 66 W m <sup>-2</sup>	RSME of 33 W m <sup>-2</sup> RSME of 40 W m <sup>-2</sup>	RMSE of 87 W m <sup>-2</sup> RSME of 150 W m <sup>-2</sup>	RMSE of 42 W m <sup>-2</sup> RSME of 68 W m <sup>-2</sup>
TSEB	Olive [203]	RMSE of 38 W m <sup>-2</sup>	RMSE of 19 W m <sup>-2</sup>	RMSE of 50 W m <sup>-2</sup>	RMSE of 56 W m <sup>-2</sup>
SEBAL	Corn, soy-bean [195]	$R^2$ of 0.71	$R^2$ of 0.17 and 0.22	$R^2$ of 0.82	$R^2$ of 0.5

## 7.3 Existing ET Estimation Methods with UAVs: Results and Discussion

Compared with traditional satellite remote sensing approaches, the UAVs platform and the lightweight cameras can estimate the surface energy fluxes with similar accuracy. Therefore, the UAVs can be used for modeling ET estimation with high confidence. In this section, different crops ET estimation with UAV platforms (Table 7.4) are compared with each other. The reasons behind the errors of ET estimation are also discussed in related sections.

### 7.3.1 OSEB and TSEB Models

In [205], Brenner *et al.* compared the OSEB model with the TSEB model by using an octocopter MikroKopter OktoXL (HiSystems GmbH, Moormerland, Germany). This UAV platform could carry a payload of 4 kg for each flight mission. An ES80 camera (Samsung, Seoul, South Korea) and an Optris Pi 400 thermal camera were mounted on the UAV to collect images. According to the specification, Pi 400 had an accuracy of  $\pm 2$  °C. The thermal image resolution was  $382 \times 288$  pixels with a field of view  $38^\circ \times 29^\circ$ . Approximately 700 to 1000 thermal images were collected for every flight mission. The eddy covariance system was used to evaluate the UAV ET estimation.

Based on the comparison between UAV fluxes and eddy covariance (EC) fluxes,

the net radiation  $R_n$  for TSEB was in good agreement with  $R_n$  measured from EC with an R-squared value ( $R^2$ ) of 0.99. The  $R^2$  value for OSEB was 0.98. The sensible heat flux ( $H$ ) for TSEB had a  $R^2$  value of 0.84, and the OSEB had a  $R^2$  value of 0.79. For the soil heat flux  $G$ , the  $R^2$  value for OSEB was 0.73. The TSEB had a  $R^2$  value of 0.83. Both models underestimated the ground heat flux compared with the eddy covariance system. For the latent heat flux  $LE$ , OSEB had a  $R^2$  value of 0.92. The TSEB had a  $R^2$  value of 0.93.

**Remark:** The results showed that the OSEB model significantly underestimated measured values for flux conditions. The poor performance of the OSEB model mainly resulted from an underestimation of high fluxes. Different from the TSEB model, the OSEB model needs an empirical adjustment parameter  $kB^{-1}$  to explain the difference between the radiometric and aerodynamic surface temperature. The parameter  $kB^{-1}$  is usually overestimated in case of strong temperature gradients between the surface and the atmosphere [205].

### 7.3.2 HARMET Model

In [206], Park *et al.* used the HARMET model when flying a DJI S1000 UAV. A thermal infrared camera A65 and a multispectral camera Rededge M were mounted on the UAV to collect thermal and multispectral images. The thermal camera image resolution was  $640 \times 512$  pixels with a field of view of  $25^\circ \times 20^\circ$ . The Rededge had a spatial resolution of  $1280 \times 960$  pixels. The UAV was flown at solar noon for capturing the period of high ET and for minimizing tree canopy shadows.

The energy fluxes were estimated in the HRMET model. For the reference trees, the estimated ET was around  $0.62 \text{ mm h}^{-1}$ . The study site was small and the UAV flight time was less than 15 minutes; thus, the meteorological data, such as incoming shortwave radiation, wind speed, and vapor pressure, were considered to be consistent during the UAV flight mission. The different ET rates along the trees were mainly decided by the differences in tree canopy temperature and LAI. The estimated ET had a strong linear relationship with leaf transpiration ( $R^2 = 0.9$ ).

**Remark:** Although it was challenging to evaluate the results because of the absence of sufficient data such as the directly measured ET or multi-seasonal UAV data, the HARMET model still showed a great potential to estimate tree-by-tree ET and capturing intra-field variability.

### 7.3.3 Machine Learning and Neural Networks

In [377], Poblete *et al.* used the ANN and multispectral images from a UAV platform to predict vine water status. A multispectral camera MCA-6 (Tetracam Inc, Chatsworth, CA, USA) was mounted on an octocopter Mikrokopter OktoXL for data collection. The data were grouped into training and validation, where 80% was used for the ANN model calibration, and 20% was used to validate the model. Although this research was not exactly for ET estimation, it proved that Neural Networks, such as ANN, had a great potential for ET estimation when combining with high-resolution multispectral UAV images.

In [402], four machine learning methods, ANN, SVM, ELM, and ANFIS, were used to estimate ET. Results showed that all four models could detect the variations of ET. The reason is that ML algorithms can identify complex non-linear relationships between ET and environmental variables. As a new model, the ELM exhibits strong modeling accuracy for daily ET estimation. The ANFIS can estimate ET more efficiently than the ANN and SVM. More importantly, these new machine learning approaches show a novel perspective for ET estimation with remote sensing data. Therefore, UAV platforms should be used with ML algorithms together, which will have great potential for ET estimation in the future.

### 7.3.4 TSEB and DTD Models

The UAVs can help generate more accurate maps of NDVI, LAI,  $f_c(\theta)$ , and  $T_R(\theta)$ , which are the critical input data for the TSEB and DTD models [430]. In [198], Hoffmann *et al.* used the TSEB model and the DTD model when flying a Q300, which has a 2.2 meters wingspan and can carry a payload of 2 kg for a 25-minute flight. An Optris PI 450 camera was mounted on the UAV to collect

thermal images. Hoffmann *et al.* concatenated the LST thermal images into the orthomosaic, which were applied as the input for TSEB model [198]. According to the specifications, the thermal camera has an accuracy of  $\pm 2$  °C or  $\pm 2\%$  at an ambient temperature of  $23 \pm 5$  °C. The thermal image resolution is  $382 \times 288$  pixels at 90m flying height. Around 700 to 1000 thermal images were collected for every flight mission. The eddy covariance system was used to compare with the UAV results.

Based on the comparison between UAV fluxes and eddy covariance (EC) fluxes, the net radiation  $R_n$  for TSEB was in good agreement with  $R_n$  measured from EC with a root mean square error (RMSE) of  $44 \text{ W m}^{-2}$  (11%), the correlation coefficient was 0.98. The sensible heat flux ( $H$ ) for DTD has RMSE of  $59 \text{ W m}^{-2}$  (64%), and the mean absolute error (MAE) value was  $49 \text{ W m}^{-2}$  (52%). Compared with DTD, the TSEB model had a RMSE of  $85 \text{ W m}^{-2}$  (91%) and the MAE was  $75 \text{ W m}^{-2}$  (81%). The TSEB had a better linear relationship between measured sensible heat flux  $H$  and modeled  $H$ . The soil heat fluxes ( $G$ ) were underestimated, which had RMSE and MAE of  $48 \text{ W m}^{-2}$  (91%) and  $45 \text{ W m}^{-2}$  (86%) for DTD, respectively. The RSME and MAE for TSEB were  $38 \text{ W m}^{-2}$  (72%) and  $35 \text{ W m}^{-2}$  (66%), respectively. The correlation between the modeled  $G$  and measured  $G$  was very poor. Soil heat flux  $G$  was measured with the heat flux plates, which could lead to uncertainties in measured  $G$  [431]. For the latent heat flux  $LE$ , DTD had RMSE and MAE of  $67 \text{ W m}^{-2}$  (26%) and  $57 \text{ W m}^{-2}$  (22%), respectively. The TSEB had RMSE and MAE values of  $94 \text{ W m}^{-2}$  (37%) and  $84 \text{ W m}^{-2}$  (33%), respectively.

**Remark:** The results showed that the DTD model predicted the energy fluxes better than TSEB, which demonstrated that adding another input, the land surface temperature retrieved one hour after sunrise, made the DTD model more robust. It concluded that the thermal camera placed on a UAV platform could provide high spatial and temporal resolution data for estimating energy balance fluxes of ET. Calibration of the thermal camera was also likely to improve TSEB heat flux computations. This study showed similar results with Guzinski's work [418], who applied the TSEB at the same site but using satellite images instead of UAV

images. In [418], the RMSE was  $46 \text{ W m}^{-2}$  for  $R_n$ ,  $56 \text{ W m}^{-2}$  for  $H$ , and  $66 \text{ W m}^{-2}$  for  $LE$ . The DTD model in [198] achieved RMSE of  $44 \text{ W m}^{-2}$  for  $R_n$ ,  $59 \text{ W m}^{-2}$  for  $H$  and  $67 \text{ W m}^{-2}$  for  $LE$ .

### 7.3.5 TSEB and DATTUTDUT Models

Xia *et al.* used the TSEB model and DATTUTDUT model for a sub-field and plant canopy scale ET monitoring over vineyards [199]. Based on the results, the TSEB model estimated sensible heat flux and latent heat flux with the RMSE ranging from 20 to  $60 \text{ W m}^{-2}$ . DATTUTDUT estimated heat fluxes with a larger error, the RMSE for latent heat flux LE was  $105 \text{ W m}^{-2}$ . The net radiation  $R_n$  had an RMSE of  $65 \text{ W m}^{-2}$ . It concluded that the TSEB model could simulate the energy balance components in two vineyards with MAE ranging from 15 to  $90 \text{ W m}^{-2}$ . They found that the TSEB model was fairly robust and was able to calculate LE and ET values under varying environmental conditions. By using the TSEB, the  $T_s$  and  $T_c$  had a bias of  $0.5 \text{ }^\circ\text{C}$  and RMSE on the order of  $2.5 \text{ }^\circ\text{C}$ . The accuracy was similar with [432, 410, 385, 386], in which the RMSE values were between 2.4 to  $5.0 \text{ }^\circ\text{C}$  for  $T_s$  and 0.83 to  $6.4 \text{ }^\circ\text{C}$  for  $T_c$ .

**Remark:** In general, the TSEB has a better performance than the DATTUTDUT model. The reason might be that the TSEB has a better physical representation of the energy exchange. The DATTUTDUT, as a single-source model, is more sensitive when the surface temperature pixels are selected [433, 434]. The actual extremes may not even exist in the thermal images. Besides, the effect of aerodynamic resistance (surface roughness) is also not considered in the DATTUTDUT model.

Ortega *et al.* [203] used the TSEB model to estimate the energy balance fluxes over a drip-irrigated olive orchard by using a helicopter-based UAV platform. The UAV flight height was at 60 m, which enabled the thermal camera's image at 6 cm spatial resolution. For the multispectral camera Mini MCA-6, the resolution was 3.3 cm. The remote sensing energy balance (RSEB) algorithm was well implemented, and only the climatic parameters, such as air temperature  $T_a$ , wind speed  $u$  were measured as the input data. The UAV images were used for calculating

the NDVI and soil temperature  $T_s$ . Ortega *et al.* used the Bowen ratio approach to balance  $(R_n - G)$  and  $(H + LE)$  to close the energy balance.

For the net radiation  $R_n$ , the RMSE and MAE were  $38 \text{ W m}^{-2}$  and  $33 \text{ W m}^{-2}$ , respectively. For the estimated soil heat flux  $G$  by TSEB, the RMSE and MAE were  $19 \text{ W m}^{-2}$  and  $16 \text{ W m}^{-2}$ , respectively. Results showed that the algorithm estimated  $LE$  and  $H$  with errors of 7% and 5%, respectively. The RMSE and MAE for the sensible heat flux  $H$  were  $56 \text{ W m}^{-2}$  and  $46 \text{ W m}^{-2}$ , respectively. The RMSE and MAE for latent heat flux  $LE$  were  $50 \text{ W m}^{-2}$  and  $43 \text{ W m}^{-2}$ , respectively. It showed that the largest differences for  $H$  and  $LE$  were found when the wind speed was greater than  $2.7 \text{ m s}^{-1}$ .

**Remark:** The results indicated that the UAV could be an excellent tool to evaluate the effects of spatial variability for ET estimation. The high spatial resolution images were able to show significant differences between the energy balance fluxes above the tree canopy and the soil surface. It concluded that the TSEB model was fairly robust and could estimate ET at a sub-field scale level under different environmental conditions. The UAV can also help the satellite platforms for estimating intra-field spatial variability of the energy fluxes to improve the estimation of water requirements of sparse canopies, for example, orchards and vineyards, which have different plant densities and fractional covers.

### 7.3.6 The SEBAL Model

In [195], Montibeller *et al.* used the SEBAL model to estimate energy fluxes and ET of corn and soybean in Ames, Iowa. The UAV being used was the eBee Ag (SenseFly, Cheseaux-sur-Lausanne, Switzerland), which weighed about 700 grams and could cover a  $12 \text{ km}^2$  area in one flight. A modified S110 camera (Canon Inc, Ota City, Tokyo, Japan), the Sequoia multispectral sensor (MicaSense, Seattle, WA, USA), and the thermoMAP camera (SenseFly, Cheseaux-sur-Lausanne, Switzerland) were equipped with the UAV to collect data for running the SEBAL model. The thermal and multispectral images are the most important data for this project. UAV images were collected from different growing stages of the crops, such as flowering, yield formation, and the ripening. The seasonal variability of ET and

energy fluxes were also considered. The surface albedo and surface reflectance were measured by a spectroradiometer.

To evaluate the accuracy of estimated energy fluxes, [195] used linear regression models and residual plots methods. All pixels in the energy flux images were averaged to compare with the observed values measured from the flux towers. The  $R^2$  for the net radiation  $R_n$  predicted by SEBAL was 0.71, which was underestimated by about 17% compared with the flux towers. Underestimation was most likely caused by clouds at the time when UAV was flying. The net radiation  $R_n$  ranged from  $427.24 \text{ W m}^{-2}$  to  $688.76 \text{ W m}^{-2}$  during the UAV flight missions, with a RMSE of  $6.09 \text{ W m}^{-2}$ .

Estimating soil heat flux  $G$  was the most challenging part. The estimated soil heat flux was compared with two soil heat plates in the test field. For the soil heat flux  $G$ , the  $R^2$  for the plate 1 was 0.17, with the RMSE of  $11.23 \text{ W m}^{-2}$ . The  $R^2$  for the plate 2 was 0.22, with the RMSE of  $31.02 \text{ W m}^{-2}$ . Both showed a poor correlation. There were mainly two reasons behind it. First, the accuracy of the soil heat flux plates was very low. The grown canopy could cover the soil surface, which gave errors for soil heat flux estimations. The soil heat flux plates could detect the heat rate flow difference when the canopy was developing during the growing season. Second, the flux plates depth and the soil types also affected the heat flux estimation [431]. The soil heat flux  $G$  ranged from  $14.57 \text{ W m}^{-2}$  to  $119.76 \text{ W m}^{-2}$  for the whole growing season, which was not a good estimation. Several factors could affect the soil heat flux values, such as the quality of the UAV images, the spatial distribution of surface albedo. The SEBAL model estimates  $G$  as the function of surface albedo, vegetation index, and surface temperature, which depended on the empirical equation developed by [420]. This equation was originally developed for the Mediterranean regions; thus, different climatic conditions may have different results.

For the sensible heat flux, it requires an internal calibration method. The challenge is how to select hot and cold pixels appropriately. To solve this challenge, Montibeller *et al.* [195] created a water body for the cold pixel selection by placing an evaporative pan. The evaporative pan, however, differed from a natural water

body, which affected the calculation of net radiation  $R_n$  and soil heat flux  $G$ . Therefore, the anchor pixels were usually selected from the coldest pixels in the UAV images. The  $R^2$  for the sensible heat flux  $H$  was 0.5, with the RMSE of  $8.84 \text{ W m}^{-2}$ . The estimated value by SEBAL overestimated the sensible heat flux by 5%. The sensible heat flux within the field was around  $91.84 \text{ W m}^{-2}$  during the growing season.

The  $R^2$  of the latent heat flux  $LE$  was 0.82, with an RMSE of  $2.67 \text{ W m}^{-2}$ . The research result showed that the  $LE$  varied as the crop grew. The ET rate was also relevant to the crop growth stage. Corn, for example, had higher ET rates up until the tassel appeared. The maximum mean for  $LE$  was  $564.90 \text{ W m}^{-2}$ , and the minimum mean was  $256.22 \text{ W m}^{-2}$ .

The relationship between NDVI and ET was also evaluated by the author while using the SEBAL. It assumed that there was a linear relationship between NDVI and ET. However, the correlation between the NDVI and ET was very poor; the  $R^2$  was around 0.01. One of the reasons was that soil wetting might affect NDVI prediction [361]. Further study needs to be explored.

**Remark:** Overall, the research proves that the SEBAL model can be used for estimating ET with UAVs. The MAE and RMSE values show that SEBAL can estimate ET with the UAV images very well. UAVs platform also has great potential to help farmers making decisions with real-time crop conditions in the near future, which can monitor the water consumption of each crop in the field. The SEBAL algorithms being used by [195] were automated by reprogramming the model with Python, which improved the data processing for ET estimation.

### 7.3.7 METRIC and METRIC-HR Models

The METRIC is discussed here because of its potential in UAV applications. For satellite images, monthly images can be effective for estimating seasonal ET [365] by the METRIC model. However, during times of rapid vegetative growth, multiple dates of satellite images may be needed, which is usually not available because of limitations on the satellite revisit cycles. UAVs have a more flexible flight schedule. Since METRIC is designed to use satellite images as inputs, several

adjustments are usually needed for the high-resolution UAV input data [195].

In [196], a modified METRIC model called METRIC High Resolution (METRIC-HR) was proposed to use the UAV high-resolution images. There are several differences between the METRIC and METRIC-HR. First, the digital elevation model (DEM) has a higher image resolution in METRIC-HR. Manal *et al.* replaced the original DEM with a 15 cm resolution DEM, which was generated by using the Photoscan (Agisoft, St.Petersburg, Russia). Second, the National Land Cover Database (NLCD) was also replaced by a 15 cm NLCD in METRIC-HR, which could be used to develop NLCD high-resolution maps. Third, METRIC used shortwave infrared (SWIR) bands generated by Landsat 8. SWIR is usually used for calculating the normalized difference water index. SWIR value is usually less than zero for water, which can help identify water more accurately than NDVI. In METRIC-HR, SWIR was neglected because there was no water in the study site. The thermal band (TIR) resampling of METRIC-HR is also different from the METRIC model. The thermal band resolution being used in METRIC-HR is acquired by AggieAir, which has a 60 cm resolution. Since METRIC requires all bands to have identical resolutions, TIR resampling is necessary. Nearest Neighbor Resampling was performed in ArcGIS software, which did not change the original pixel values [435, 436]. The shortwave radiance images (BGR) also have higher reflectance than Landsat 8 images. Therefore, upscaling BGR with Landsat 8 PSF and developing correction equations are necessary for the METRIC-HR model.

As mentioned earlier in the METRIC model section, selecting hot and cold pixels as anchor pixels can be subjective and requires experience. Different hot and cold pixels can lead to significant deviations in the final ET estimation [437]. METRIC recommends selecting cold pixels in a homogenous, well-watered place where the range of NDVI is from 0.76 to 0.84. The surface albedo range is from 0.18 to 0.24. Hot pixels are selected in a homogeneous bare, dry soil location with NDVI less than 0.2. The surface albedo for hot pixels is recommended to be from 0.17 to 0.23. More information about anchor pixels selection can be found in [365, 438]. After METRIC and METRIC-HR models were run, the final output was the instantaneous  $ET_r F$  (fraction of the alfalfa-based reference ET).

For the METRIC-HR results, the  $ET_rF$  values ranged from 0 to 1.15. Lower values represented hotter areas, such as bare soil. Higher values meant wet areas. Compared with METRIC, METRIC-HR had a higher  $ET_rF$  estimated; this could be caused by the presence of pixels of multiple vegetation growth with significant differences in some covers. The maximum difference was around 20%.

**Remark:** The results showed the values estimated between METRIC and METRIC-HR had a 0.9 coefficient of correlation. This proves that METRIC-HR has a similar performance with METRIC. Higher resolution images in the METRIC-HR model has a better performance in mixed areas. This work demonstrates that UAVs equipped with lightweight cameras can estimate ET quantitatively. However, cameras need further calibration to relate spectral response to METRIC-HR models.

## 7.4 Estimating Actual Crop Evapotranspiration Using the Stochastic Configuration Networks and UAV-based Crop Coefficients

### 7.4.1 Introduction

Estimating evapotranspiration ( $ET$ ) by crop coefficient ( $K_c$ ) is one of the most commonly used methods for water irrigation management. The crop evapotranspiration ( $ET_c$ ) is determined by the  $K_c$  approach whereby the effect of the various weather conditions are incorporated into reference  $ET$  ( $ET_o$ ) and the crop characteristics into the  $K_c$  [352]:

$$ET_c = K_c \times ET_o. \quad (7.25)$$

The  $K_c$  curve is the crop coefficient distribution during a growing season. At the beginning of the growing season, the value of  $K_c$  increases from a minimum value. When the canopy cover is full, the  $K_c$  reaches a maximum around the mid-season. Then, the  $K_c$  starts decreasing before the end of the growing season.

The normalized difference vegetation index (NDVI) has been commonly used for vegetation monitoring, such as water stress detection [192, 232], crop yield

assessment [224], and  $ET$  estimation [142, 28]. The NDVI is calculated by

$$NDVI = \frac{\rho_{NIR} - \rho_R}{\rho_{NIR} + \rho_R}, \quad (7.26)$$

where  $\rho_{NIR}$  and  $\rho_R$  are the reflectance of near-infrared and red wavebands, respectively. NDVI is a standardized method to measure healthy vegetation. When the NDVI is high, it indicates the vegetation has a higher level of photosynthesis.

Many studies have used satellite-derived NDVI to estimate crop coefficient values [244, 245, 246]. For example, Trout *et al.* [247] and Zhang *et al.* [248] applied a remote sensing method using NDVI to estimate canopy ground cover as a basis for generating  $K_c$ . Kamble *et al.* [244] used a simple linear regression model to establish a relationship between NDVI and  $K_c$ . Satellite imagery can provide spatially distributed measurements, though, they cannot acquire useful spatio-temporal resolution images for precision agriculture applications [249]. The timing of satellite overpass is not always synchronous with research requirements, either.

As a new remote sensing platform, the UAVs have been commonly used in agricultural applications, such as crop yield estimation [224], irrigation managements [24, 27], water stress estimation [146], and pest management [225, 250]. Compared with the satellite, the flight of UAVs can be more flexible and frequent in the field. The UAVs fly at a lower altitude and take higher resolution imagery of crops [190]. The UAVs also make data acquisition relatively less expensive.

The objective of this study was to investigate the approaches of estimating  $K_c$  using UAV-based NDVI for an experimental pomegranate orchard. The pomegranate is widely grown all over the world, which has drought resistance and high economic value. There are approximately 11,000 ha of pomegranate in the semi-arid and arid areas of California [248]. The spatial and temporal variability of  $K_c$  and NDVI are analyzed by using the Stochastic Configuration Networks (SCNs). A regression model is established between the NDVI and  $K_c$ . The performance of the new regression model was evaluated by the data collected by the UAVs.



Figure 7.1: Pomegranate test site. The pomegranate was planted in 2010 with a 5 m spacing between rows and 2.75 m within-row tree spacing in a 1.3 ha field. There were two large weighing lysimeters, which were 2 m  $\times$  4 m by 3 m deep. The lysimeters had a resolution of 0.1 mm of water loss, which were located in the center of the field, marked in red boxes.

## 7.4.2 Material and Methods

### Pomegranate Study Area

As shown in the Fig. 7.1, this study was conducted in an experimental pomegranate orchard at the USDA-ARS, San Joaquin Valley Agricultural Sciences Center (36.594°N, 119.512°W), Parlier, California, 93648, USA. The pomegranate was planted in 2010 with a 5 m spacing between rows and 2.75 m within-row tree spacing in a 1.3 ha field. There were two large weighing lysimeters [248], which were 2 m  $\times$  4 m by 3 m deep. The lysimeters had a resolution of 0.1 mm of water loss, which were located in the center of the field, marked in red boxes in Fig. 7.1.

### The UAV Platform and Multispectral Camera

In this study, the author used a quadcopter, called “Hover”, as the UAV platform. The “Hover” was controlled by a Pixhawk flight controller, which could

fly over the pomegranate field by waypoints mode for 30 minutes. Multispectral imagery was collected by the Rededge M camera (MicaSense, Seattle, WA, USA). The Rededge M has five bands, which are Blue, Green, Red, Near-infrared, and Red edge. It has a spectral resolution of  $1280 \times 960$  pixel, with a  $46^\circ$  field of view. (See more details of the UAV and sensor in Chapter 3)

### **UAV Image Collection and Preprocessing**

Flight missions were programmed by using the Mission Planner. The flight height was set up as 60 m. The overlapping of UAV images was set up as 80%, so that the UAV imagery of the pomegranate could be stitched together during image processing. The image of a calibrated reflectance panel (CRP) was taken before and after the flight missions, servicing as the reflectance reference.

The author flew the UAV bi-weekly over the pomegranate field at noon during the growing season in 2019. The successful data collections were shown in Table 7.5. After the flight missions, all of the aerial images were stitched together to generate the orthomosaick images in PhotoScan (Agisoft LLC, Russian).

### **Deep Stochastic Configuration Networks (DeepSCNs)**

The Deep Stochastic Configuration Networks (DeepSCNs) was first proposed by Wang *et al.* in 2017 [169]. Compared with the known randomized learning algorithms for single hidden layer feed-forward neural networks, the DeepSCNs randomly assign the input weights and biases of the hidden nodes in the light of a supervisory mechanism. The output weights are analytically evaluated in a constructive or selective method. DeepSCNs have better performance than other randomized neural networks in terms of the fast learning, scope of the random parameters, and the required human intervention. Therefore, it has already been used in many data processing projects, such as [173, 176].

The simple linear regression model could only plot the best fit line which showed that the model was not a good fit for the data because the data had a non-linear pattern. Therefore, in this study, the DeepSCNs were used to derive a better regression model than the simple linear regression model.

Table 7.5: The UAV flight schedule. The flight height was set up as 60 m. The overlapping of UAV images was set up as 80%, so that the UAV imagery of the pomegranate could be stitched together during image processing. The author flew the UAV bi-weekly over the pomegranate field at noon during the growing season in 2019.

Dates	Flight time	Flight height
May 8 <sup>th</sup> , 2019	12 - 1 pm	60 m,
Jun 5 <sup>th</sup> , 2019	12 - 1 pm	60 m,
Jul 25 <sup>th</sup> , 2019	12 - 1 pm	60 m,
Aug 7 <sup>th</sup> , 2019	12 - 1 pm	60 m,
Aug 29 <sup>th</sup> , 2019	12 - 1 pm	60 m,
Sep 19 <sup>th</sup> , 2019	12 - 1 pm	60 m,
Oct 3 <sup>rd</sup> , 2019	12 - 1 pm	60 m,
Oct 29 <sup>th</sup> , 2019	12 - 1 pm	60 m.

### 7.4.3 Results and Discussion

#### Seasonal $K_c$ and NDVI

The values of  $K_c$  and NDVI were shown in Fig. 7.2. The values of  $K_c$  were derived using equation (7.25). The  $ET_c$  was recorded by the weighing lysimeter in the center of the pomegranate field. The  $ET_o$  was calculated by the California Irrigation Management Information System (CIMIS) near the pomegranate field. The NDVI was derived by image processing tools in MATLAB.

A strong correlation was shown between the  $K_c$  and NDVI during the growing season in 2019. The maximum values of  $K_c$  and NDVI were 1.0069 and 0.8429 on July 25<sup>th</sup> (DOY 206), respectively. The high values of  $K_c$  and NDVI showed that the trees in the lysimeter were in a well-irrigated condition. The  $K_c$  increased fast at the beginning of the growing season. After the peak of the mid-season,  $K_c$  started decreasing. Both  $K_c$  and NDVI had very low values on October 29<sup>th</sup> (DOY 302). The reason was that most leaves fell off the pomegranate trees after the harvest. Therefore, the data of DOY 302 was not used for the data analysis.

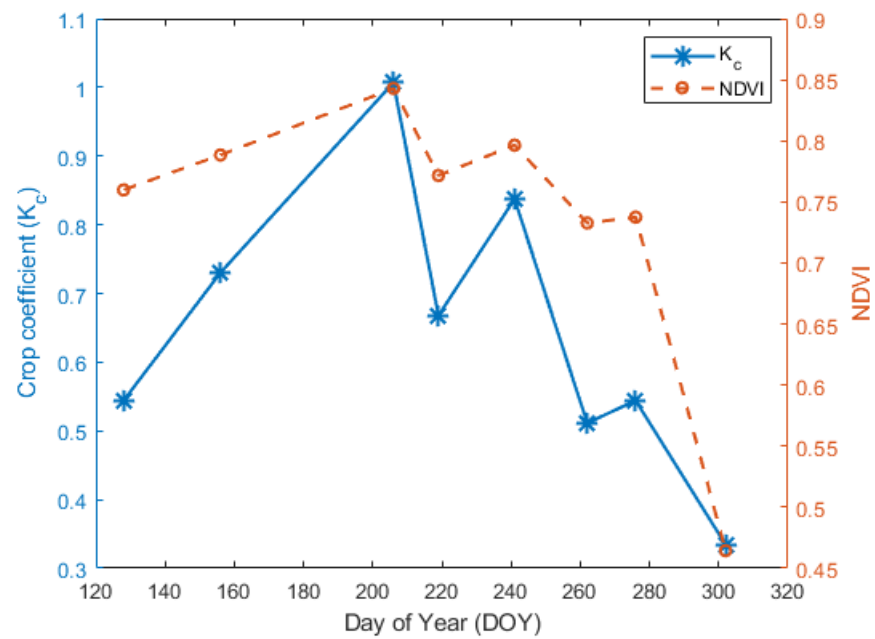


Figure 7.2: Seasonal  $K_c$  and NDVI at the pomegranate field in 2019. The values of  $K_c$  were derived using equation (7.25). The  $ET_c$  was recorded by the weighing lysimeter in the center of the pomegranate field. The  $ET_o$  was calculated by the CIMIS near the pomegranate field. The NDVI was derived by image processing tools in MATLAB.

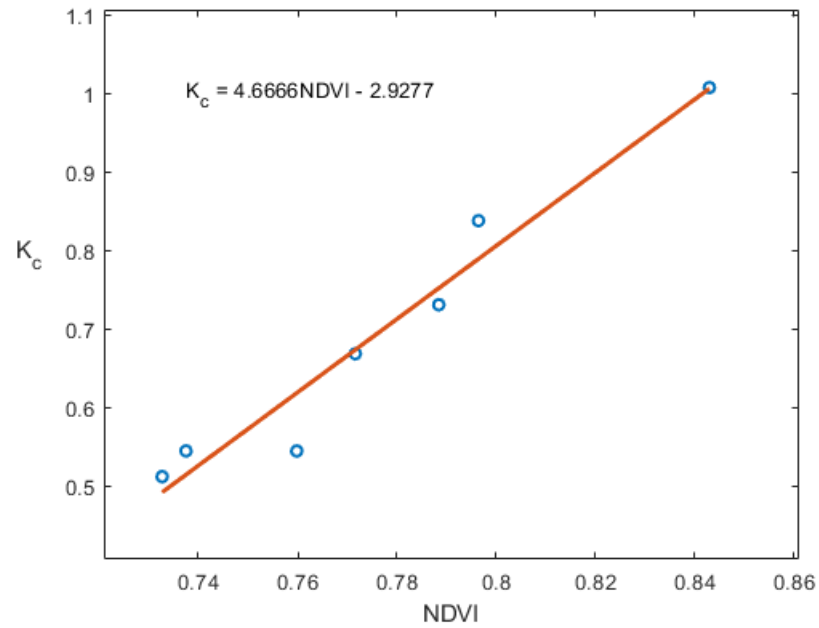


Figure 7.3: Linear regression model for  $K_c$  and NDVI. A strong correlation was shown between the  $K_c$  and NDVI during the growing season in 2019.

### Regression Models for $K_c$ and NDVI

As shown in Fig. 7.3, there was a strong correlation between the  $K_c$  and NDVI. A simple linear regression model was built using the NDVI values derived from the UAV imagery and the  $K_c$  from field measurement,

$$K_c(NDVI) = 4.6666NDVI - 2.9277, \quad (7.27)$$

where 4.6666 and -2.9277 were the slope and intercept coefficients, respectively. The correlation coefficient ( $R^2$ ) was 0.975. The root mean square error (RMSE) was 0.05.

With the development of machine learning technology, many neural networks have been applied for agricultural applications [23, 26]. Since the dataset of  $K_c$  and NDVI was not large, in this study, DeepSCNs was used for building the regression model between  $K_c$  and NDVI. Four out of seven days of data were used for training the DeepSCNs regression model. All the data points were fitted very well in the

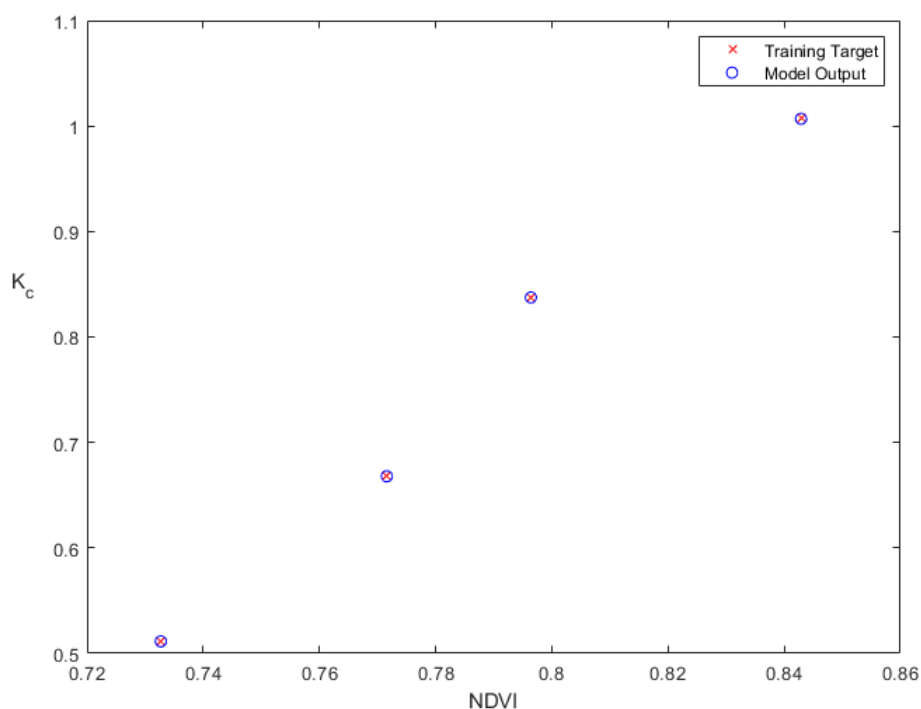


Figure 7.4: DeepSCNs training model. Since the dataset of  $K_c$  and NDVI was not large, in this study, DeepSCNs was used for building the regression model between  $K_c$  and NDVI. Four out of seven days of data were used for training the DeepSCNs regression model. All the data points were fitted very well in the trained model.

trained model, as shown in Fig. 7.4. The weights and bias were shown in Table 7.6. The parameter L meant that there were four hidden nodes of the trained DeepSCNs model. For the other parameters in the DeepSCNs model, please refer to [169].

Three days of data were used to evaluate the trained model, as shown in Fig. 7.5. The value of  $R^2$  was 0.995. The value of RMSE was 0.046. Both showed good performance for estimating  $K_c$  by using NDVI. The variations of  $K_c$  were well explained by using the NDVI from UAV images. The trained model was used to generate the  $K_c$ . For example, the spatial mapping of NDVI and  $K_c$  on September 19<sup>th</sup> were shown in Fig. 7.6. The spatial mapping of ET on September 19<sup>th</sup> was shown in Fig. 7.7.

Table 7.6: DeepSCNs with properties. For example, the maximum times of random configuration  $T_{max}$  was set as 100. The scale factor  $\Lambda$  in the activation function, which directly determined the range for the random parameters, was examined by performing different settings (0.5 - 200). The tolerance was set as 0.001.

Properties	Values
Name:	“Stochastic Configuration Networks”
version:	“1.0 beta”
L:	4
W:	[0.4924 -0.4987 -4.3543 9.2007]
b:	[-0.4650 -0.4197 -4.7048 -9.2846]
Beta:	[4 x 1 double]
r:	[0.9000 0.9900 0.9990 0.9999 1.0000 1.0000]
tol:	1.0000e-03
Lambdas:	[0.5000 1 5 10 30 50 100 150 200 250]
$L_{max}$ :	250
$T_{max}$ :	100
nB:	1
verbose:	50
COST:	5.5250e-13

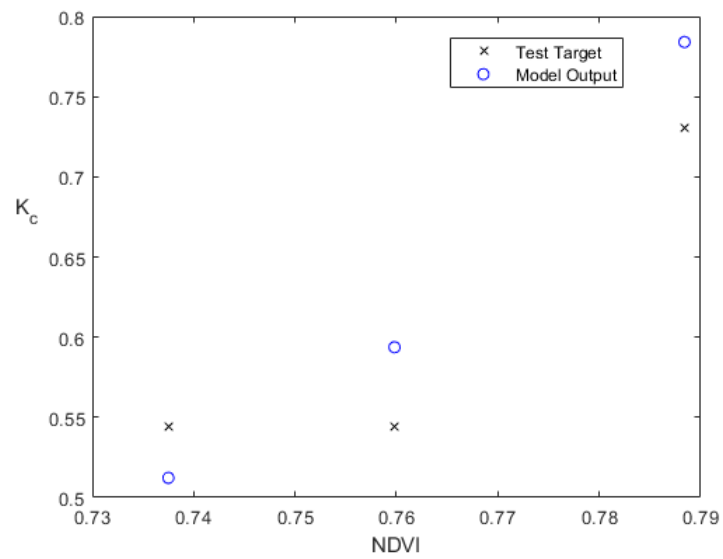


Figure 7.5: The SCNs model evaluation performance. Three days of data were used to evaluate the trained model. The value of  $R^2$  was 0.995. The value of RMSE was 0.046. Both of them showed good performance for estimating  $K_c$  by using NDVI. The variations of  $K_c$  were well explained by using the NDVI from UAV images.

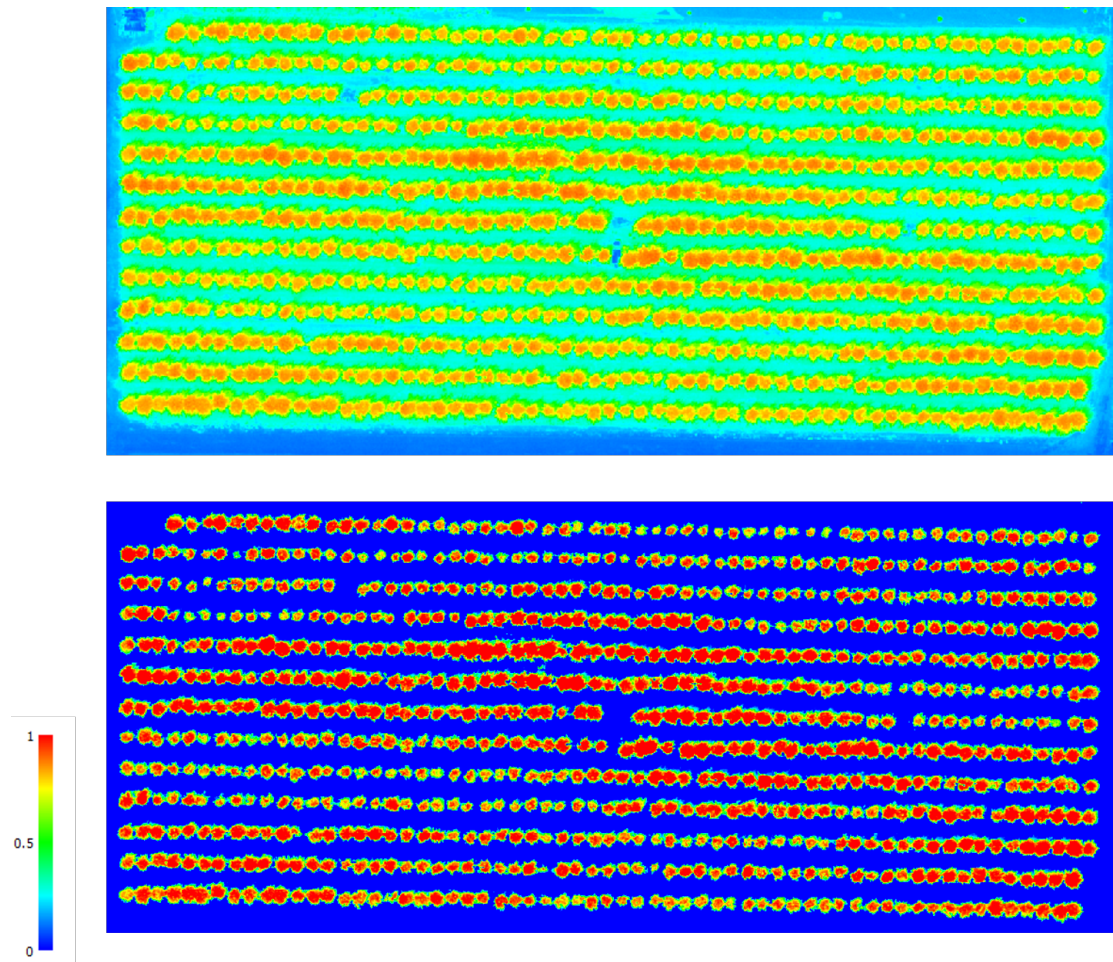


Figure 7.6: NDVI (top) and  $K_c$  (bottom) maps of the pomegranate using UAVs. (Sept. 19<sup>th</sup>, 2019)

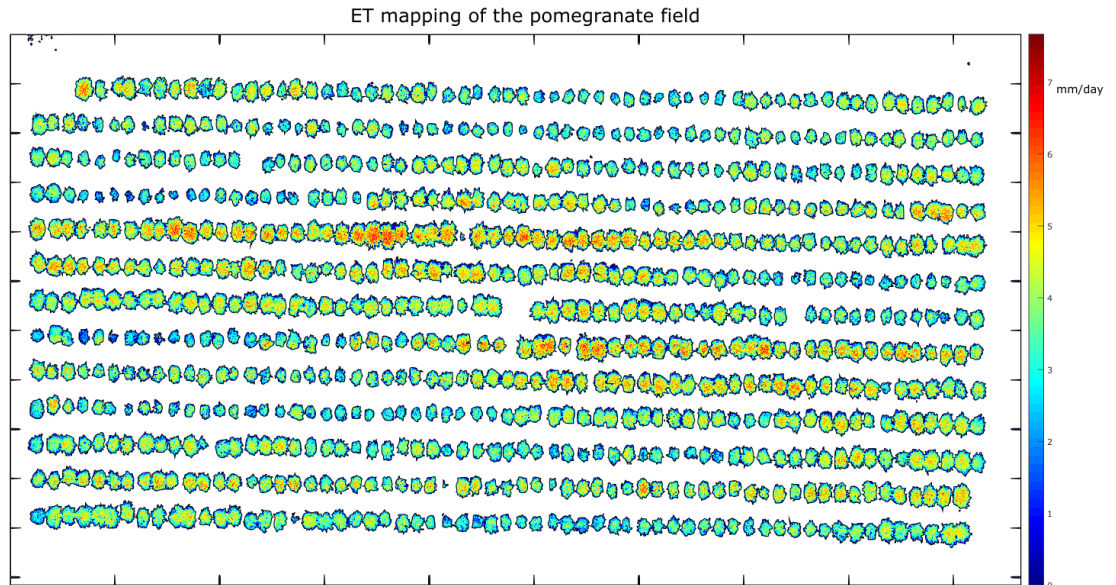


Figure 7.7: Spatial and tree-by-tree view of ET distribution.

#### 7.4.4 Conclusions

In this study, UAV flight missions were conducted to collect remote sensing multispectral images in a pomegranate orchard at USDA. Using the NDVI derived from the multispectral imagery, the author could apply DeepSCNs for a regression model between NDVI and  $K_c$ . The parameters of the DeepSCNs model was shown in Table 7.6. The  $K_c$  represents the actual growth conditions in the field. Therefore,  $K_c$  can be used for estimating the  $ET$  temporally and spatially in the pomegranate field.

The simple linear regression model was  $K_c(NDVI) = 4.6666NDVI - 2.9277$ . Compared with the simple linear regression model, the DeepSCNs model could better fit the data points in the training dataset. The simple linear regression model had  $R^2$  and RMSE of 0.975 and 0.05, respectively. The DeepSCNs regression model had  $R^2$  and RMSE of 0.995 and 0.046. The DeepSCNs showed a better performance than the linear regression model.

Although only the data of 2019 was used for analysis, the study had provided evidence that variations of NDVI from UAV imagery could be used to explain the

variations of  $K_c$ . In the future, the data of 2017 and 2018 will be added to train a more robust DeepSCNs model.

## 7.5 Reliable Tree-level Evapotranspiration Estimation of Pomegranate Trees Using Lysimeter and UAV Multispectral Imagery

### 7.5.1 Introduction

Because of the recurring water shortages in California, many growers started growing crops that have drought resistance and high economic value to a certain degree [439], such as pomegranate. There is around 11,000 ha of pomegranate in California [248]. Evidence suggests that evapotranspiration (ET) estimation is among the most important factors to manage limited water effectively in agriculture [352]. Mapping the ET temporally and spatially can identify variations in the field, which is useful for evaluating soil moisture [348, 349] and assessing crop water status [350].

Using crop coefficient ( $K_c$ ) to estimate ET is a common method for water irrigation management. The actual crop evapotranspiration ( $ET_c$ ) is determined by the  $K_c$  approach whereby the effect of the various weather conditions are incorporated into reference ET ( $ET_o$ ) and the crop characteristics into the  $K_c$  [352]. At the beginning of the growing season,  $K_c$  increases from a minimum value. When the canopy cover is full, the  $K_c$  reaches a maximum around the mid-season. Then, the  $K_c$  starts decreasing before the end of the growing season. The normalized difference vegetation index (NDVI) has been commonly used for vegetation monitoring, such as water stress detection [192, 232], crop yield assessment [224], and ET estimation [142, 28, 27, 137, 143]. The value of NDVI is a standardized method to measure healthy vegetation. When the NDVI is high, it indicates the vegetation has a higher level of photosynthesis. Many studies have used satellite-derived NDVI to estimate crop coefficient values [244, 245, 246]. For example, Trout *et al.* [247] and Zhang *et al.* [248] applied a remote sensing method using NDVI to

estimate canopy ground cover as a basis for generating  $K_c$ . Kamble *et al.* [244] used a simple linear regression model to establish a relationship between NDVI and  $K_c$ . Although satellite imagery can provide spatially distributed measurements, it cannot acquire useful spatio-temporal resolution images for precision agriculture applications [249]. The timing of satellite overpass is not always synchronous with research requirements, either. To date, few studies have investigated the association between the  $K_c$  and NDVI at the individual-tree level.

Recently, UAVs have been emerging as powerful platforms in agricultural applications, such as crop yield estimation [224], irrigation management [24, 27], water stress estimation [146], and pest management [225, 250]. With lightweight sensors being mounted on UAVs, high-resolution imagery has been taken in massive amounts [190]. The spatial resolution of the UAV imagery can be at the centimeter-level and help identify, standardize, and validate methods to calculate the spatial variability for clumped canopy structures, such as trees and vines.

The **objectives of this study** are: 1. To investigate and validate the approaches of estimating  $K_c$  using UAV-based NDVI for an experimental pomegranate orchard. 2. To establish a linear regression model between the NDVI and  $K_c$  in the individual-tree level. 3. To evaluate the performance of the new regression model on estimating 100% ET irrigation sampling trees. The **major contributions of this section** are: 1. Develop a reliable tree-level ET estimation method using UAV high-resolution multispectral images. 2. Provide a framework to establish a linear regression model between the NDVI and  $K_c$  to estimate the actual daily ET. Results show that the linear regression model can estimate tree-level ET with an  $R^2$  and mean absolute error (MAE) of 0.9143 and 0.39 mm/day, respectively, which shows a state-of-art performance.

## 7.5.2 Material and Methods

### Study Site Description

Field studies were conducted in an experimental pomegranate (*Punica granatum L.*, cv ‘Wonderful’) field (Fig. 7.8) at the USDA-ARS, San Joaquin Valley Agricultural Sciences Center (36.59°N, 119.51°W), Parlier, California, 93648, USA.



Figure 7.8: The Pomegranate study site. Field studies were conducted in an experimental pomegranate (*Punica granatum L.*, cv ‘Wonderful’) field at the USDA-ARS, San Joaquin Valley Agricultural Sciences Center (36.59°N, 119.51°W), Parlier, California, 93648, USA. The pomegranate field was randomly designed into 16 equal blocks, with four replications, to test four irrigation levels. The irrigation volumes are 35%, 50%, 75%, and 100% of  $ET_c$ , which was measured by the weighing lysimeter in the field. There were five sampling trees in each block, 80 sampling trees in total, marked with red labels.

The San Joaquin Valley has a Mediterranean climate with hot and dry summers. Rainfall is insignificant, and irrigation is the only source of water for pomegranate growth [440]. There are two large weighing lysimeters installed at the center of the experimental field [441]. According to [439], the lysimeters have a resolution of approximately 0.1 mm of water loss. The soil types are a Hanford fine sandy loam (coarse-loamy, mixed, thermic Typic Xerorthents). The meteorological data was generated by the CIMIS weather station 39, which is about 700 m far from the experimental field.

The pomegranate field was randomly designed into 16 equal blocks, with four replications, to test four irrigation levels. The irrigation volumes are 35%, 50%, 75%, and 100% of  $ET_c$ , which was measured by the weighing lysimeter in the field. There were five sampling trees in each block, 80 sampling trees in total, marked with red labels in Fig. 7.8.

Table 7.7: Flight missions at the USDA in 2019. The UAV flight missions were configured by using the MissionPlanner (Ardupilot, USA). The flight altitude was set up as 60 m. The overlapping of UAV images was set up as 80% forward and 70% by the side.

Dates	Flight time	Flight altitude
May 8 <sup>th</sup> , 2019	12 - 1 pm	60 m,
Jul 25 <sup>th</sup> , 2019	12 - 1 pm	60 m,
Aug 7 <sup>th</sup> , 2019	12 - 1 pm	60 m,
Aug 29 <sup>th</sup> , 2019	12 - 1 pm	60 m,
Sep 19 <sup>th</sup> , 2019	12 - 1 pm	60 m,
Oct 3 <sup>rd</sup> , 2019	12 - 1 pm	60 m,
Oct 29 <sup>th</sup> , 2019	12 - 1 pm	60 m.

### UAV Image Collection and Processing

A UAV platform, called “Hover”, was deployed for imagery data acquisition. The Rededge M (MicaSense, Seattle, WA, USA) was used for collecting multispectral images (See more details of the UAV and sensor in Chapter 3).

The UAV flight missions were configured by using the MissionPlanner (Ardupilot, USA). The flight altitude was set up as 60 m. The overlapping of UAV images was set up as 80% forward and 70% by the side. Then, the UAV imagery of the pomegranate can be stitched together during image processing with high confidence. The image of a calibrated reflectance panel (CRP) was taken before and after the flight missions, servicing as the reflectance reference. The author flew the UAV bi-weekly over the pomegranate field at noon during the growing season in 2019. The successful data collections were shown in Table 7.7. After the flight missions, all aerial images were stitched together to generate the orthomosaick images in PhotoScan (Agisoft LLC, Russian).

### 7.5.3 Results and Discussion

#### Determination of Individual-tree $K_c$ from NDVI

The correlation between the  $K_c$  and NDVI of an individual tree was analyzed. Daily  $K_c$  for the individual tree was calculated as [352]:

$$K_c = ET_c/ET_o, \quad (7.28)$$

where the actual ET ( $ET_c$ ) was measured by the weighing lysimeter and the reference ET ( $ET_o$ ) was obtained from the CIMIS weather station near the field. The mean NDVI values for the lysimeter tree were calculated by  $\rho_{NIR}$  and  $\rho_R$ , where  $\rho_{NIR}$  and  $\rho_R$  were the reflectance of near-infrared and red wavebands, respectively. NDVI is a standardized method to measure healthy vegetation. When the NDVI is high, it indicates the vegetation has a higher level of photosynthesis (One of our demos is an NDVI mapping for May 8<sup>th</sup>, 2019). According to the demo, most NDVI values of the tree canopies range from 0.468 to 1. It is interesting to point out that the shade of the trees had a mean NDVI value around 0.5.

$$NDVI = \frac{\rho_{NIR} - \rho_R}{\rho_{NIR} + \rho_R}. \quad (7.29)$$

**Key observation:** Fig. 7.9 showed the relationship between the daily  $K_c$  and the derived mean NDVI for the tree in the lysimeter with 100% irrigation treatment. The sampling data started on May 8<sup>th</sup> and ended on Oct 29<sup>th</sup>. The linear relationship had an intercept of 0.6114 and a slope of 1.6493. It also had a high correlation coefficient of 0.8865, indicating a significant correlation between the  $K_c$  and NDVI at the individual-tree level during the growing season in 2019.

#### The Spatial Variability Mapping of $K_c$ and $ET_c$

**Key observation:** Inspired by the strong linear correlation between the  $K_c$  and NDVI for the individual lysimeter tree, the author calculated the  $K_c$  for all the trees in the experimental field using the linear regression model. The mapping of  $K_c$  and  $ET_c$  was generated, respectively (Fig. 7.10 is an example for  $K_c$  and  $ET_c$

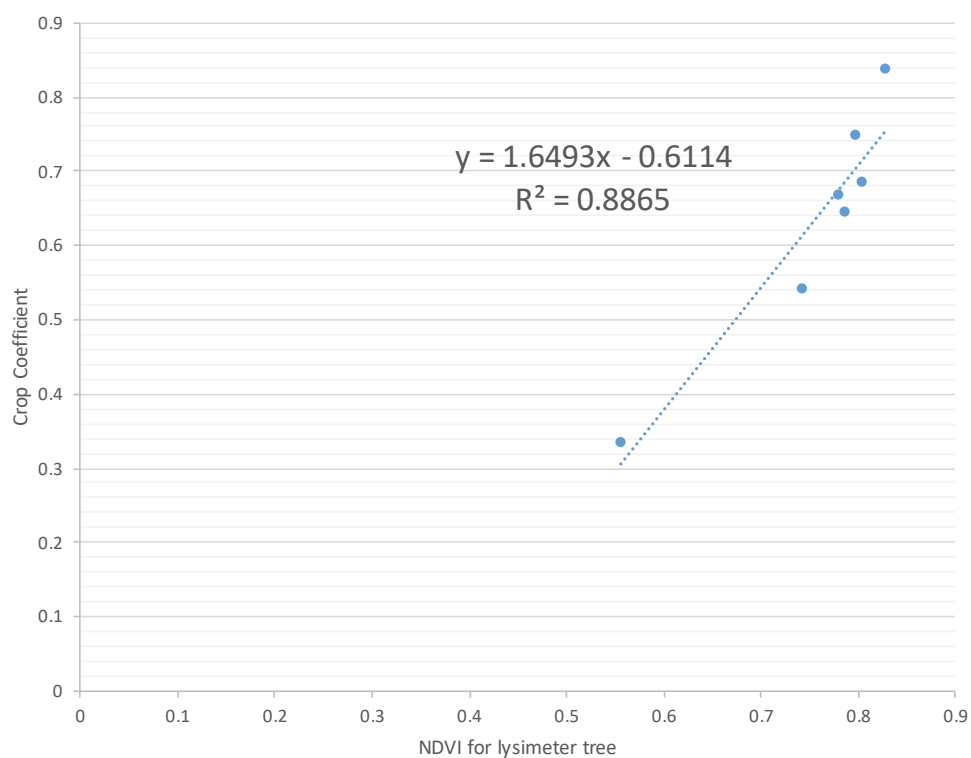


Figure 7.9: Seasonal  $K_c$  and NDVI for the tree in lysimeter. The sampling data started on May 8<sup>th</sup> and ended on Oct 29<sup>th</sup>. The linear relationship had an intercept of 0.6114 and a slope of 1.6493. It also had a high correlation coefficient of 0.8865, indicating a significant correlation between the  $K_c$  and NDVI at the individual-tree level during the growing season in 2019.

spatial variability mapping on May 8<sup>th</sup>). The values of  $K_c$  were mostly between 0.578 and 1.039 on May 8<sup>th</sup>. For the  $ET_c$ , it ranged from 3.2 to 6.0 mm/day.

### Performance of the Individual Tree-level ET Estimation

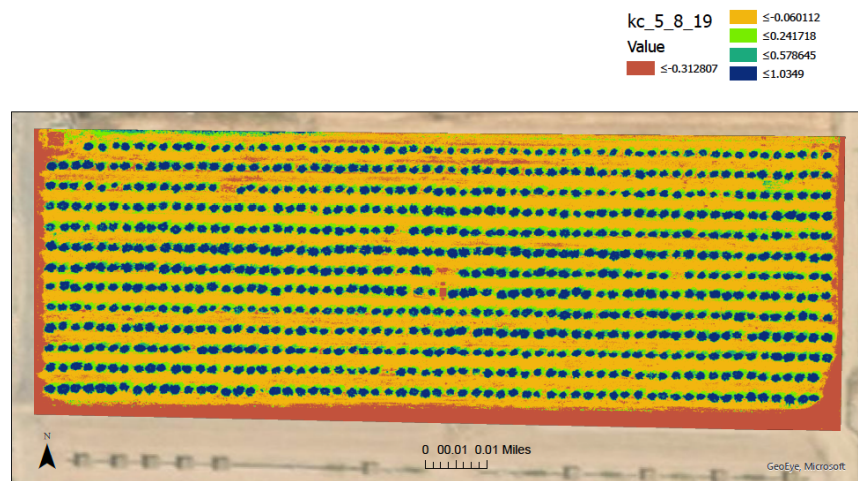
As mentioned earlier, there were 80 sampling trees in the pomegranate field. Twenty of them were irrigated with 100% of  $ET_c$ , same with the lysimeter tree.

**Key observation:** To validate the linear regression model on individual-tree-level ET estimation, the author compared the 20 sampling trees with the lysimeter daily  $ET_c$  for the UAV flight dates (almost the whole growing season). The trends of the daily  $ET_c$  for the 20 sampling trees (100% irrigation ) and the lysimeter tree were shown in Fig. 7.11. Each ‘Serie’ meant an individual tree in the field. Then, the boxplot of Fig. 7.12 was generated for analysis. Compared with the lysimeter tree, the linear regression model estimated tree-level ET with an  $R^2$  and mean absolute error (MAE) of 0.9143 and 0.39 mm/day, respectively.

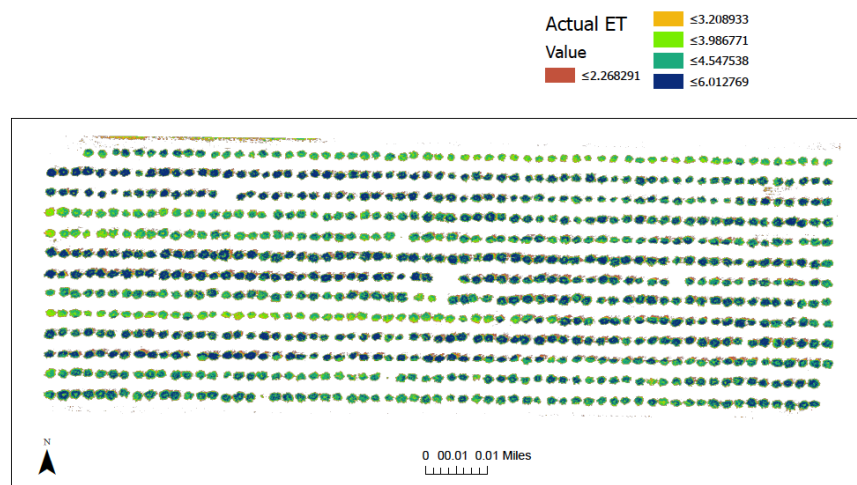
### 7.5.4 Conclusions

In this study, UAV flight missions were conducted to collect high-resolution multispectral imagery in a pomegranate orchard at USDA. Using the NDVI derived from the multispectral imagery, the author applied a regression model between NDVI and  $K_c$  to estimate the individual tree-level ET estimation. The linear regression model was  $K_c(NDVI) = 1.6493NDVI - 0.6114$ , which had an  $R^2$  of 0.8865. Then,  $ET_c$  for all the 100% ET irrigation trees were generated individually. Experimental results showed that the estimated daily  $ET_c$  has an  $R^2$  and mean absolute error (MAE) of 0.9143 and 0.39 mm/day for 100% irrigated sampling trees, which showed a state-of-art performance.

Only the data of 2019 was used for analysis; the study had provided evidence that variations of NDVI from UAV imagery could be used to explain the variations of  $K_c$  and  $ET_c$  at the individual tree level. In the future, the data of 2017 and 2018 will be added for further analysis.



(a) The  $K_c$  map of May 8<sup>th</sup>, 2019. Inspired by the strong linear correlation between the  $K_c$  and NDVI for the individual lysimeter tree, the author calculated the  $K_c$  for all the trees in the experimental field using the linear regression model. The mapping of  $K_c$  was generated. The values of  $K_c$  were mostly between 0.578 and 1.039 on May 8<sup>th</sup>.



(b) The  $ET_c$  map of May 8<sup>th</sup>, 2019. Inspired by the strong linear correlation between the  $K_c$  and  $ET_c$  for the individual lysimeter tree, the author calculated the  $ET_c$  for all the trees in the experimental field using the linear regression model. The mapping of  $ET_c$  was generated. For the  $ET_c$ , it ranged from 3.2 to 6.0 mm/day.

Figure 7.10: The  $K_c$  and  $ET_c$  maps of May 8<sup>th</sup>, 2019.

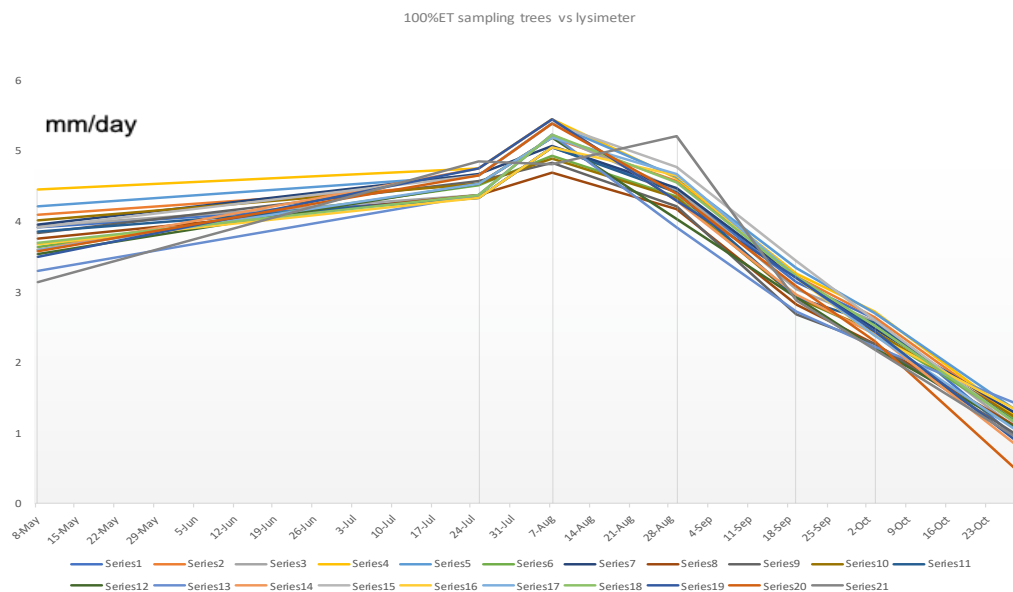


Figure 7.11: 100% ET irrigation sampling trees vs lysimeter tree. To validate the linear regression model on individual-tree-level ET estimation, the author compared the 20 sampling trees with the lysimeter daily  $ET_c$  for the UAV flight dates (almost the whole growing season). The trends of the daily  $ET_c$  for the 20 sampling trees (100% irrigation) and the lysimeter tree were shown. Each ‘Serie’ meant an individual tree in the field.

## 7.6 Conclusion and Future Research

As a new remote sensing platform, researchers are gaining interest in the potential of UAVs in precision agriculture. Compared with traditional remote sensing platforms, the UAVs can be more flexible in the field. For example, UAVs can be operated at any time if the weather is within the operating limitations. The satellite has a fixed flight path, UAVs are mobile and flexible for site selection. Mounted on the UAVs, lightweight sensors, such as RGB cameras, multispectral cameras, and thermal infrared cameras, can be used to collect high-resolution images. While there are many advantages with using UAVs, there are still challenges for UAVs when used for estimating ET. Many researchers fly the UAVs at different height, using specialized equipment and relying on data analysis expertise. As researchers try to understand and realize the potential of the UAVs for ET estimation, efficient

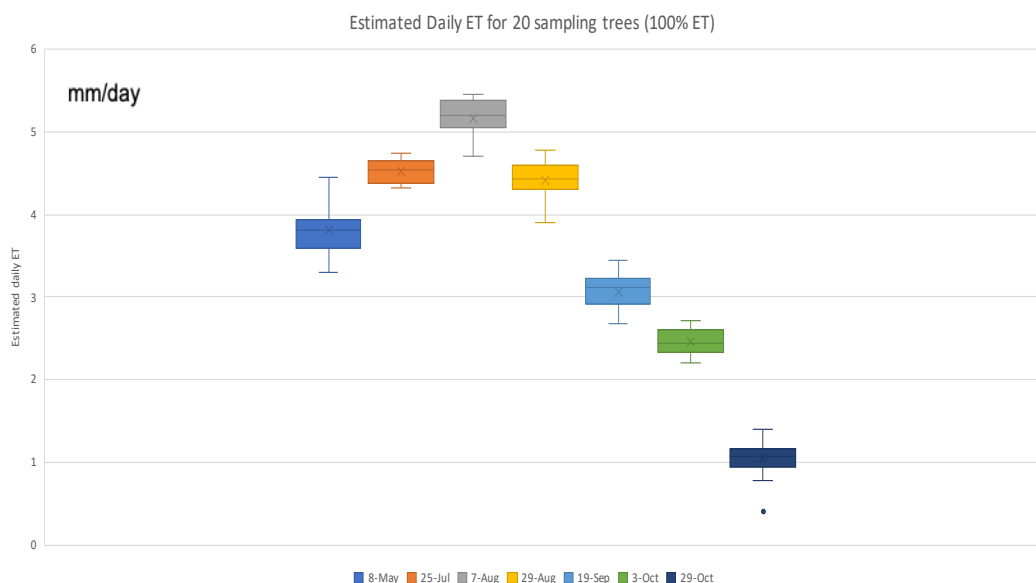


Figure 7.12: The boxplot of 100% ET sampling trees vs lysimeter tree. Compared with the lysimeter tree, the linear regression model estimated tree-level ET with an  $R^2$  and mean absolute error (MAE) of 0.9143 and 0.39 mm/day, respectively.

workflow, image processing, and better software are still under developing.

No existing methods can fully satisfy the spatial, temporal, spectral, and accuracy requirements for ET-based science and applications. Therefore, innovative methods or models for ET estimation are required by using UAVs. There are five requirements to map ET with high fidelity in the future [442], which are high frequency, high spatial resolution, high temporal resolution, large spatial coverage, and long-term monitoring. High frequency will improve the differentiation of water stress between crops, which enables more efficient water management. High spatial resolution can help detect spatially heterogeneous responses to water stress. Because ET is highly variable within and among days, high temporal resolution can help detect crop ET in real-time. Large spatial coverage can help detect large scale drought. Long term monitoring will be important to record ET variability overtime.

Compared with other satellite-based remote sensing methods, the UAV platform and lightweight sensors can provide better quality, higher spatial, and tem-

poral resolution images. The UAVs can be used to estimate ET on an excellent spatial scale and with flexible flight schedules. In the future, (1) The two-source energy balance (TSEB) and dual temperature difference (DTD) models have great potential for ET estimation since they can separate the soil and canopy with high-resolution UAV imagery; (2) Taking advantage of the UAV high-resolution imagery, research related to individual tree-level ET estimation will be possible and useful for analyzing the temporal and spatial variability of the crops in the field; (3) Deep learning algorithms can be used for processing high-resolution UAV imagery, such as individual tree-level canopy or soil segmentation; (4) The author's research results [28] showed that there was strong correlation between the NDVI and crop coefficient at individual tree-level ET estimation. Further study can be conducted to create new generation of vegetation index using machine learning and deep learning algorithms.

## Chapter 8

# Individual Tree-level Water Status Inference Using High-resolution UAV Thermal Imagery and Complexity-informed Machine Learning

### 8.1 Introduction

There is around 11,000 ha of pomegranate in California because of its drought resistance and high economic value [439]. Considering the recurring water shortage in California, it is essential to find effective methods to optimize irrigation water use. Research results suggested that the evapotranspiration (ET) estimation is one of the most critical factors to help manage water use efficiency in agriculture [352]. Mapping the ET temporally and spatially can identify variations in the field, which helps evaluate crop water status [350].

The tree canopy temperature from infrared thermometer (IRT) sensors is an ef-

fective tool for detecting plant water stress. Research has been conducted on crops and trees to relate the  $\Delta T$  to irrigation management. The main reason is that a significant increase in the midday infrared canopy to air temperature difference ( $\Delta T$ ) will indicate stomata closure and water stress conditions [443, 444, 445]. For example, Zhang *et al.* evaluated the performance of using  $\Delta T$  to manage postharvest deficit irrigation of nectarine trees [446]. The results demonstrated that the measured  $\Delta T$  values above the tree canopy showed consistent differences among irrigation treatment levels. Clawson *et al.* used canopy temperature variability and average canopy temperature to schedule irrigation in corn (*Zea mays* L.). They remarked that canopy temperature variability could show the plant water stress and the need to schedule an irrigation event [447]. Furthermore, Wang *et al.* investigated the infrared canopy temperature of early ripening peach trees under postharvest deficit irrigation and monitored the stem water potential. The strong correlation between stem water potential and  $\Delta T$  ( $R^2 \approx 0.7$ ) indicated that canopy temperature could be used for water stress estimation.

However, little research could be found in the literature on using midday  $\Delta T$  derived from UAV thermal infrared (TIR) image as a primary input for mapping irrigation treatment levels of a pomegranate field at individual tree levels. This article evaluated the feasibility and performance of using midday  $\Delta T$  (UAV-TIR) and machine learning algorithms for spatial mapping of irrigation treatments. Recently, UAVs have been emerging as powerful platforms in agricultural applications, such as irrigation management [24, 27], and water stress estimation [146]. With lightweight sensors being mounted on UAVs, high spatial and temporal resolution imagery has been taken in massive amounts with low-cost [190, 448]. Because of the lightweight and low power consumption, the thermal camera has been commonly used in agriculture research [191, 198]. The spatial resolution of the UAV-based thermal imagery can be at the centimeter level and help identify, standardize, and validate methods to calculate the spatial variability for clumped canopy structures, such as trees and vines [449].

Machine learning (ML) models have been widely used in real-world applications, for example, image processing [23], natural language processing [25], and

precision agriculture [137]. ML algorithms can simplify a solution and perform better than traditional statistical approaches, which may require more hand-tuning rules. However, training ML models may require a large amount of data, which may not always be available for scientific problems [450]. Then, the smaller dataset may cause ML models to lack robustness and cannot guarantee convergence. Therefore, in this article, the authors proposed the concept of complexity-informed machine learning (CIML) and the principle of tail matching (POTM). The original dataset can exhibit a heavy-tailed distribution phenomenon, and tail-index analysis can be used for ML algorithms [451, 12]. Specifically, tail information in the training dataset variability and diversity should indicate the data representativeness. In this sense, we can expect a “smaller dataset” rather than “big data” for ML under the same performance requirement. In summary, we pursue “tail matching” between the dataset and the ML algorithms.

The convolutional neural network (CNN) is one of the most common architectures, which includes the input layer, the convolution layer, the pooling layer and the fully connected layer [452]. Because of its powerful ability for complex data analysis, CNN models have been commonly used in agricultural applications, such as yield estimation [453], water stress analysis [454], and pest management [455]. For example, Yang *et al.* proposed to estimate corn yield by using the hyperspectral imagery and a CNN model in [456]. Research results showed that the spectral and color image-based integrated CNN model had a classification accuracy of 75.5%. In [455], Li *et al.* proposed an effective data augmentation strategy for CNN-based method for pest detection. In the training phase, they adopted data augmentation by rotating images with several degrees followed by cropping into different grids. Then, a large number of extra multi-scale examples were obtained and could be used to train a multi-scale pest detection model. Experimental results showed that their data augmentation strategy with CNN model achieved the pest detection accuracy of 81.4%. Advances in CNN models have been leading to significantly promising progress for agricultural research.

The **objectives of this study** were: 1. Evaluated the reliability of the UAV thermal camera on individual tree canopy temperature measurements. 2. Inves-

tigated and validate the approaches of irrigation treatment inference using UAV-based  $\Delta T$  at individual tree level. 3. Demonstrated the performance of the CIML models on irrigation treatment inference. 4. Demonstrated the performance of the CNN model on irrigation treatment inference. The **major contributions of this chapter** were: 1. Developed a reliable tree-level water stress detection method using UAV-based high-resolution thermal images. 2. Proposed the concept of CIML and proved its performance on the classification of tree-level irrigation treatments. The rest of the chapter is organized as follows. 3. Proposed a CNN model and proved its performance on the classification of tree-level water status. The rest of the chapter is organized as follows. Section 2 introduces the materials and methods being used for UAV-based irrigation treatment inference. Results and discussion are presented in Section 3. In Section 4, the author draws conclusive remarks.

## 8.2 Material and Methods

### 8.2.1 Experimental Site and Irrigation Management

The study was conducted in a 1.3 ha pomegranate field in 2019 at the USDA-ARS San Joaquin Valley Agricultural Sciences Center in Parlier, CA (36.594°N, 119.512°W). The pomegranate (*Punica granatum* L., cv 'Wonderful') was planted in 2010 with a 5 m spacing between rows and a 2.75 m within-row tree spacing [439]. The soil type was a Hanford fine sandy loam (coarse-loamy, mixed, thermic Typic Xerorthents). There are also two large weighing lysimeters, which are 2 m  $\times$  4 m by 3 m in depth and have a resolution of 0.1 mm of water loss. As shown in Fig. 8.1, the weighing lysimeters are located in the center of the pomegranate field. The experimental site was randomly designed into 16 blocks, with four replications, to test four irrigation rates on the pomegranate growth. As measured by the lysimeter, the irrigation volumes were set up as 35%, 50%, 75%, and 100% of  $ET_c$ . The trees in the lysimeter were irrigated at the 100% treatment level. For each irrigation treatment block, there were three rows with around 15 trees per row. Only the central row of each block was used as the experimental row. The height of trees was pruned and maintained at approximately 3 m.



Figure 8.1: The pomegranate field at the USDA-ARS (36.594°N, 119.512°W). The weighing lysimeter is located in the center of the pomegranate field, marked as a red box. The blue marks are where the 14 IRT sensors were installed.

### 8.2.2 Ground Truth: Infrared Canopy and Air Temperature

The tree canopy temperature was measured with 14 IRT sensors (Model SI-100 series, Apogee Instruments, Inc., Logan, UT), which were installed 4.5 m above the soil surface. The field of view (FOV) of the IRT sensor was 20° (Fig. 8.2). The air temperature and relative humidity were also measured with a sensor in the experimental site. Then, the author could evaluate the performance of using midday infrared canopy to air temperature difference ( $\Delta T$ ) to detect or classify deficit irrigation of pomegranate trees.

### 8.2.3 The Thermal Infrared Remote Sensing Data

A quadcopter named “Hover” was used as the low-cost UAV platform (less than \$1000) to collect high-resolution thermal images at the height of 60 m. The thermal camera ICI 9640P (Infrared Cameras Inc, Beaumont, TX, USA.) was equipped with the UAV for collecting thermal images for the experimental field (See more details of the UAV and sensor in Chapter 3).



Figure 8.2: The IRT sensor was installed 4.5 m above the soil surface, with a FOV of  $20^\circ$ . A quadcopter was used as the low-cost UAV platform (less than \$1000) to collect high-resolution thermal images at the height of 60 m.

### **The UAV Thermal Image Collection and Processing**

The author used the Mission Planner to program all flight missions. The flight height was set up as 60 m. The overlapping of UAV imagery was set up as 80% so that the UAV imagery of the pomegranate could be stitched together more successfully during image processing. The UAV was flying at noon with clear sky conditions to minimize the shading effect on the thermal images. Since the thermal camera type is uncooled, it usually takes around 20 minutes to warm up the thermal camera before flight missions. To calibrate the thermal camera, the author took thermal images of ice water immediately before and after the flight missions as the reference temperature. After the flight missions, all UAV thermal images were stitched together to generate the orthomosaick images in Metashape (Agisoft LLC, Russian).

### **The Tree Canopy Segmentation Using Support Vector Machine (SVM)**

There were 746 trees in total for the pomegranate field. As mentioned earlier, there were three rows with around 15 trees per row for each irrigation treatment block. Only the central row of each block was used as the experimental row. To obtain the individual tree canopy images of the 250 sampling trees (Fig. 8.3(B)),

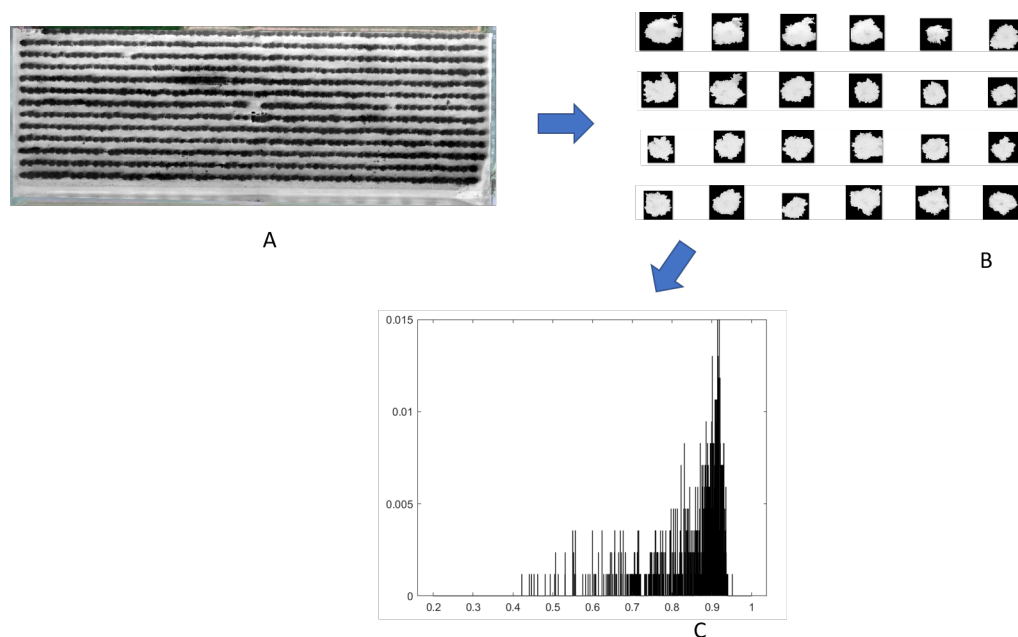


Figure 8.3: **(A)** All of the UAV thermal images were stitched together to generate the orthomosaick images in Metashape (Agisoft LLC, Russian); **(B)** To obtain the individual tree canopy images of the 250 sampling trees, the author used the SVM for classifying the tree canopy. **(C)** Histogram was generated for each tree canopy to check the variability of each tree canopy temperature.

the author used the SVM for classifying the tree canopy with ArcGIS Pro. Using the SVM classifier could map the input data vectors into a higher dimensional feature space. Then, the SVM optimally separated the data into different classes. Since the file size of UAV-based thermal imagery was large, the SVM classifier was adopted, which was less susceptible to noise, unbalanced number, or size of training sites within each class. All the sampling trees were successfully segmented using the SVM classifier. Then, the mean, variance, and histogram information (Fig. 8.3(C)) were calculated using MATLAB 2021b as input features for CIML models.

#### 8.2.4 The Complexity-informed Machine Learning (CIML)

When the author discusses complexity-informed machine learning, he focuses on variability analysis using the histogram information of individual tree canopy.

Variability refers to several properties of the ML dataset. First, it refers to the number of inconsistencies in the data, which needs to be understood by using anomaly- and outlier-detection methods for any meaningful analytics to be performed. Second, variability can also refer to diversity. For example, when the author studied the individual tree-level ET estimation [449], it turned out that the evapotranspiration for each tree is very close to each other. The reason was that the mean pixel values were used for data analysis, making the ET classification challenging to implement. Considering the complexity of each tree canopy, embedding the complex information into the ML training process may have great potential to detect or classify deficit irrigation for pomegranate trees. To analyze the complex information in each tree, we need to use tail-index analysis methods.

### 8.2.5 The Principle of Tail Matching

In probability theory, heavy-tailed distributions are PDFs whose tails do not decay exponentially [81]. The distribution of a real-valued random variable  $X$  is said to have a heavy right tail if the tail probabilities  $P$  decay more slowly than those of any exponential distribution. Consequently, they have more weight in their tails than does an exponential distribution,

$$\lim_{x \rightarrow \infty} \left( \frac{P(X > x)}{e^{-\lambda x}} \right) = \infty, \quad (8.1)$$

for every  $\lambda > 0$  [85]. The tail information in the training dataset variability and diversity should be used to indicate the data representativeness. In this article, the Generalized Pareto distribution (GP) was developed to model tail index for individual tree canopy thermal imagery.

#### The Pareto Distribution

A random variable is said to be described by a Pareto probability density distribution (PDF) if its cumulative distribution function (CDF) is

$$F(x) = \begin{cases} 1 - \left(\frac{b}{x}\right)^a, & x \geq b, \\ 0, & x < b, \end{cases} \quad (8.2)$$

where  $b > 0$  is the scale parameter, and  $a > 0$  is the shape parameter which is the Pareto's index of inequality [99]. The tail data of the tree canopy temperature were fitted using the generalized Pareto distribution by maximum likelihood estimation. Many fitting models may agree well with the data in high-density regions but poorly in low-density areas. However, in many applications, fitting the data in the tail may also contribute to model performance. The GP was developed as a distribution that can model tails of a wide variety of distributions based on theoretical arguments.

### 8.2.6 Machine Learning Classification Algorithms

Several classification algorithms were adopted to evaluate the detection performance for irrigation treatment levels. “Neural Net”, “Support Vector Machines (SVM)”, “Random Forest”, “AdaBoost”, “Nearest Neighbors”, “Gaussian Process”, “Naive Bayes”, “Quadratic Discriminant Analysis”, and “Decision Tree” were chosen as the classification algorithms. A more detailed introduction can be found in Chapter 6.

### 8.2.7 Image Preprocessing for the CNN Model

The individual tree canopy images were extracted from the UAV thermal imagery, 250 in total. Then, the dataset was distributed as 67% for training and 33% for testing using the *train\_test\_split* method. To verify that the dataset looks correct, the authors plotted the first 25 images from the training set and displayed the class name below each image (Fig. 8.4). All the images were resized into  $32 \times 32 \times 3$  in order to input into our CNN model using TensorFlow 2.0. The summary of the CNN model is shown in Table 8.1. The output of every Conv2D and MaxPooling2D layer is a 3D tensor of shape (height, width, channels). The width and height dimensions tend to shrink as we go deeper in the network. The number of output channels for each Conv2D layer is controlled by the first argument. The authors fed the last output tensor from the convolutional base into the Dense layers to perform classification. Dense layers take vectors as input (which are 1D),

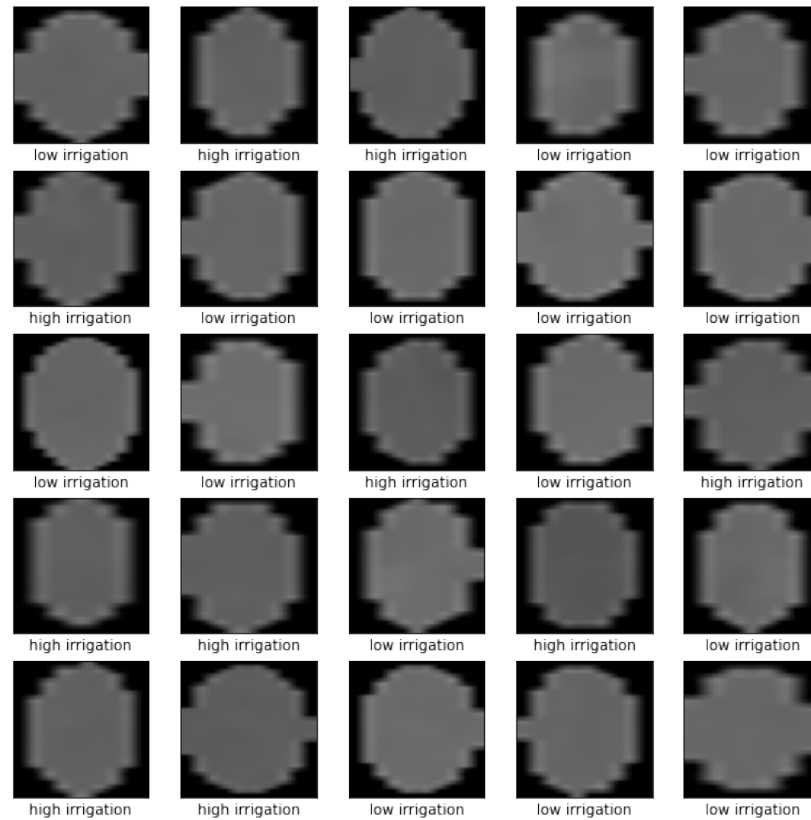


Figure 8.4: 25 images were randomly selected from the training set and the class name for each image was displayed below. All the images were resized into  $32 \times 32 \times 3$  in order to input into the CNN model.

while the current output is a 3D tensor. Considering the dataset has two classes, the authors used a final Dense layer with 2 outputs.

## 8.3 Results and Discussion

### 8.3.1 Comparison of Canopy Temperature Per Tree Based on Ground Truth and UAV Thermal Imagery

To evaluate the reliability of UAV thermal remote sensing, the author first compared the canopy temperature per tree acquired by IRT sensors and the UAV thermal camera. The correlation between the canopy temperature per tree mea-

Table 8.1: The architecture of the CNN model.

Layer Type	Output Shape	Parameter Numbers
Conv2D	(None, 30, 30, 32)	896
MaxPooling2D	(None, 15, 15, 32)	0
Conv2D	(None, 13, 13, 64)	18496
MaxPooling2D	(None, 6, 6, 64)	0
Conv2D	(None, 4, 4, 64)	36928
Flatten	(None, 1024)	0
Dense	(None, 64)	65600
Dense	(None, 2)	130

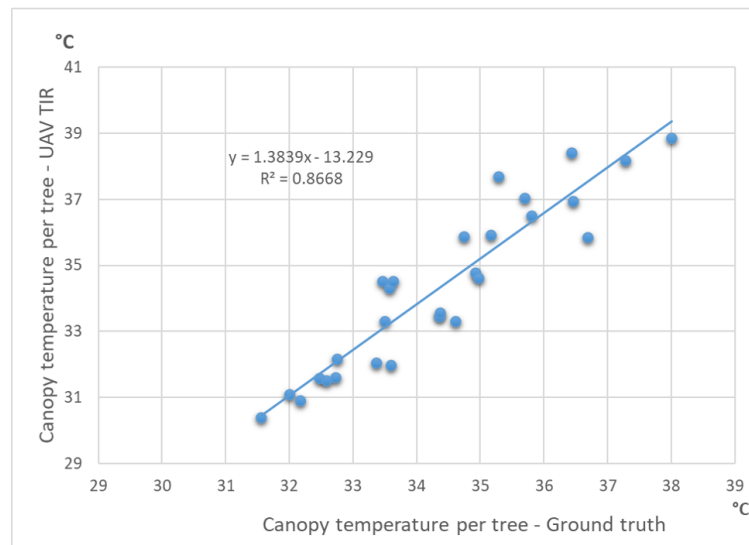


Figure 8.5: The correlation between the canopy temperature per tree measured by the IRT sensors and UAV thermal camera. The coefficient of determination ( $R^2$ ) was 0.8668, which indicated that the difference between the ground truth and UAV thermal camera was acceptable. The method was reliable for monitoring tree-level canopy temperature.

sured by the IRT sensors and UAV thermal camera was shown by their scatter-related plot and the established regression equation (Fig. 8.5). The coefficient of determination ( $R^2$ ) was 0.8668, which indicated that the difference between the ground truth and UAV thermal camera was acceptable. The method was reliable for monitoring tree-level canopy temperature.

### 8.3.2 The Relationship Between $\Delta T$ and Irrigation Treatment

The effect of irrigation treatment on canopy-to-air temperature ( $\Delta T$ ) was plotted in this section (7-25-2019 and 8-7-2019). As shown in Fig. 8.6, the  $\Delta T$  was significantly higher in the 35% irrigation treatment than the 100% irrigation treatment on different days. The values of  $\Delta T$  decreased as the irrigation increased. This finding emphasized the importance of irrigation on the tree canopy temperature response. Several researchers reported similar results [439, 446, 457]. At the USDA-ARS, all the pomegranate trees were fully irrigated before 2012, which did not show any significant difference for  $\Delta T$  [439]. After the deficit irrigation started in early 2012, the difference of  $\Delta T$  was more significant.

### 8.3.3 The Classification Performance of CIML on Irrigation Treatment Levels

For the CIML algorithms, the author focused on the variability analysis. Variability refers to the individual tree canopy temperature spatial diversity. Different types of tree canopy temperature data were used as the primary input for training, including (1.) mean and variance, (2.) tail index, mean, and variance, (3.) histogram of tree canopy temperature. The tree canopy temperature of 250 sampling trees was distributed as 75% for training and 25% for testing using the *train\_test\_split* method. For evaluating the trained CIML models, a confusion matrix was used to compare the performances of different classifiers. A confusion matrix was a summary of prediction results on a classification problem. The number of correct and incorrect predictions was tallied with count values and divided

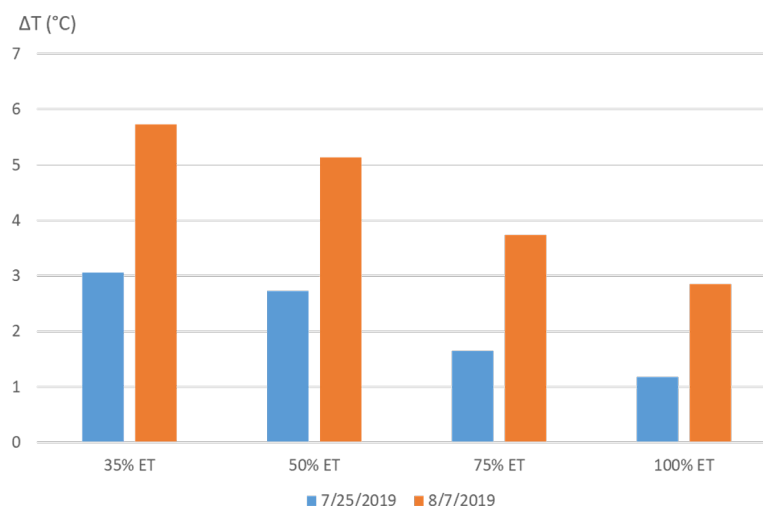


Figure 8.6: The  $\Delta T$  was significantly higher in the 35% irrigation treatment than the 100% irrigation treatment on different days. The values of  $\Delta T$  decreased as the irrigation increased. This finding emphasized the importance of irrigation on the tree canopy temperature response.

into classes. The confusion matrix provided insight not only into the errors being made by a classifier but, more importantly, the types of errors that were being made. “True label” meant the ground truth of  $ET_c$  based irrigation treatment levels. “Predicted label” identified the irrigation treatment levels predicted by the trained model. To simplify the visualization, 30% and 50% ET irrigation were labeled as “0”, denoting low-level irrigation; 75% and 100% ET irrigation were labeled as “1”, which meant high-level irrigation.

The trained models had distinct test performance for irrigation treatment prediction at tree level (Fig. 8.7, Table 8.2, and Fig. 8.8). First of all, the most important finding was that using the UAV-based tree canopy to air temperature ( $\Delta T$ ) and machine learning algorithms could successfully classify the irrigation treatment or water stress at the individual tree level. The research results demonstrated that  $\Delta T$  was highly related to irrigation management. As mentioned earlier, the main reason was that a significant increase  $\Delta T$  would indicate stomata closure and water stress conditions [443, 444, 445]. Thus, UAV-based thermal remote sensing is a reliable tool for tree irrigation management. The results were highly consistent for

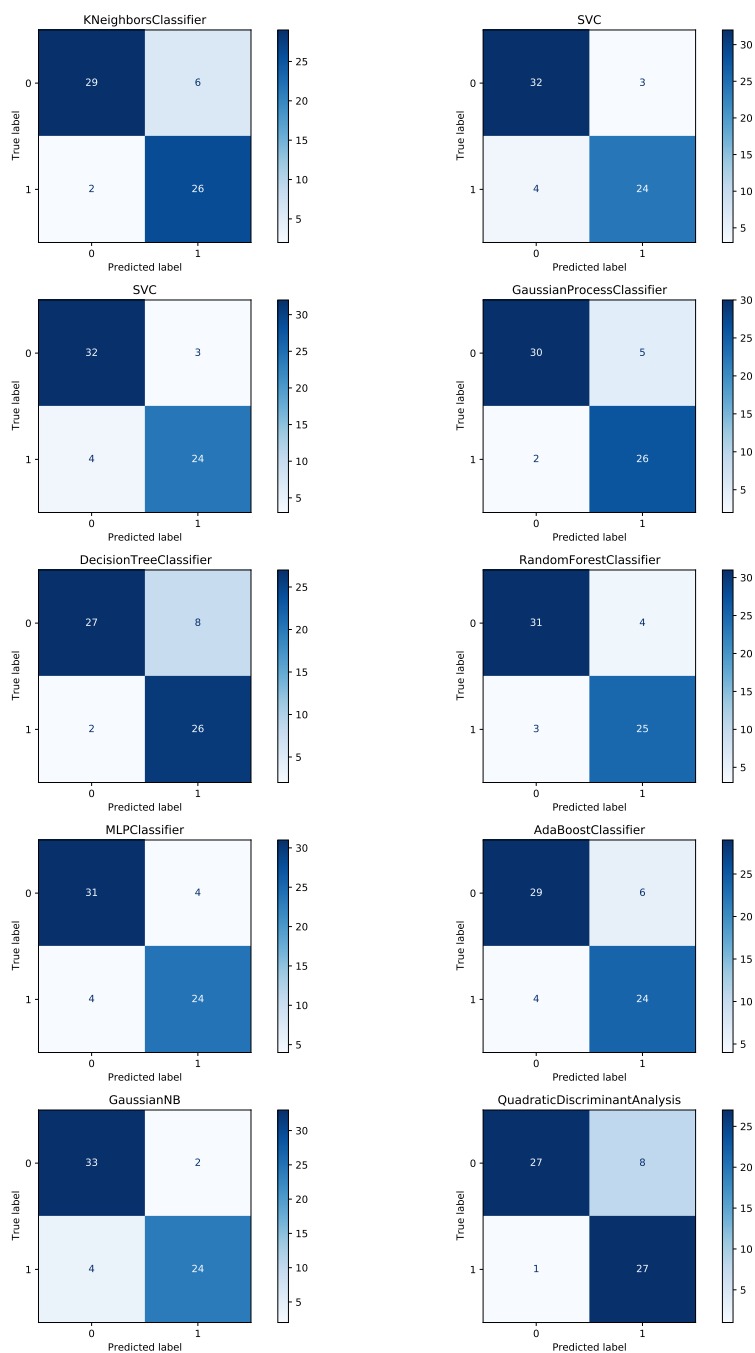


Figure 8.7: The summary of prediction results using histogram information on the tree-level irrigation treatment inference. “True label” meant the ground truth of  $ET_c$  based irrigation treatment levels. “Predicted label” identified the irrigation treatment levels predicted by the trained model.

Table 8.2: The classification performance of CIML algorithms on irrigation treatment levels at individual tree level. All the methods showed a state-of-art performance, with an overall accuracy of 87%. The “Naive Bayes” had the highest accuracy of 0.90.

Classification methods	Prediction accuracy (histogram)	Prediction accuracy (mean, variance, and tail index)	Prediction accuracy (mean + variance)
“KNeighborsClassifier”	0.87	0.86	0.84
“Linear SVM”	0.89	0.86	0.84
“RBF SVM”	0.89	0.84	0.84
“Gaussian Process”	0.89	0.86	0.86
“Decision Tree”	0.84	0.89	0.87
“Random Forest”	0.89	0.87	0.89
“Neural Net”	0.87	0.89	0.44
“AdaBoost”	0.84	0.87	0.89
“Naive Bayes”	<b>0.90</b>	0.81	0.68
“QDA”	0.86	0.83	0.73

different methods. For example, when histogram information was used for training and testing. All the methods showed a state-of-art performance, with an overall accuracy of 87%. The “Naive Bayes” had the highest accuracy of 0.90.

Another finding was that tail-index information had great potential to benefit training and testing performance. The mean and variance were a simplification of complex information. By adding the tail information into the training dataset, the prediction accuracy of some methods was increased, as shown in Table 8.2. It inspired us that the tail information in the training dataset variability and diversity should be used to indicate the data representativeness. Then, with more complex information, the histogram information of tree canopy temperature had the best prediction accuracy, without a doubt. In summary, all three situations had overall accuracy above 80%, mainly because the  $\Delta T$  was very sensitive to irrigation treatments.

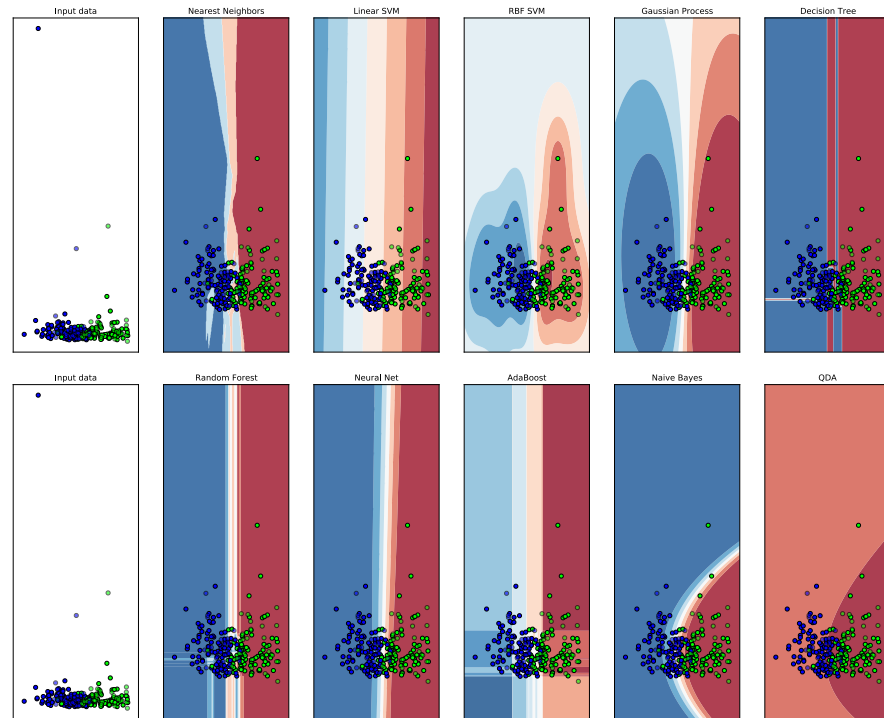


Figure 8.8: The test performance for the histogram dataset. The t-distributed stochastic neighbor embedding (TSNE) method was used for data visualization, which learned the most critical axes between the classes. The axes were then used to define the hyperplane to project the high-dimensional training data into two dimensions, which gained important insight by visually detecting patterns. The  $x$ -axis and  $y$ -axis had no scale because of hyperplane projection. The irrigation treatment levels were successfully clustered into low-level (blue) and high-level (green).

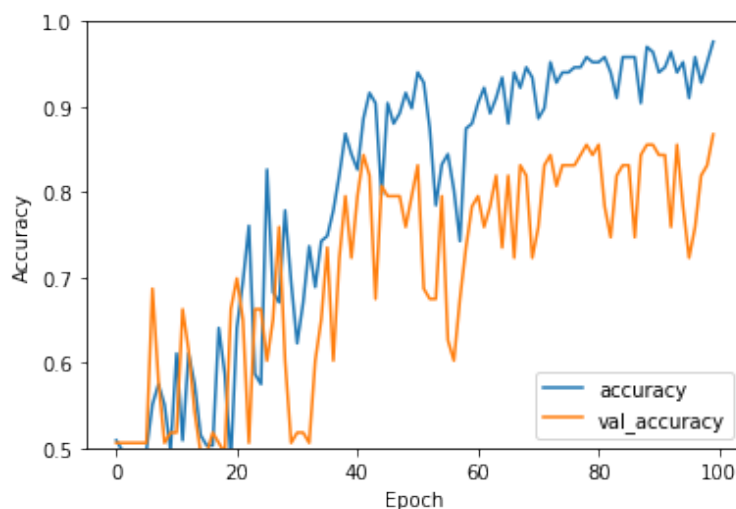


Figure 8.9: The performance of the CNN model, training and validation accuracy curves.

### 8.3.4 The Performance of the CNN Model

As mentioned earlier, there were 250 tree canopy images in total, which were distributed as 67% for training and 33% for testing using the *train\_test\_split* method. To train the CNN model, the ‘adam’ optimizer and the cross entropy loss function were adopted during the training process. The epoch was set up as 100. For evaluating the trained CNN models, the authors plotted the training and validation accuracy curves with the epochs increasing (Fig. 8.9). The test accuracy was 87%. To visualize the trained CNN model performance, the authors made predictions about some images in the test dataset (Fig. 8.11). Correct prediction labels are blue and incorrect prediction labels are red. The number gives the percentage (out of 100) for the predicted label. A confusion matrix was also used, which was a summary of prediction results on a classification problem. “True label” meant the ground truth of  $ET_c$  based irrigation treatment levels. “Predicted label” identified the irrigation treatment levels predicted by the trained CNN model. To simplify the visualization, low irrigation (30% and 50% ET) were labeled as “0”; high irrigation (75% and 100% ET) were labeled as “1” (Fig. 8.10). The detailed information of precision and recall was shown in Table 8.3.

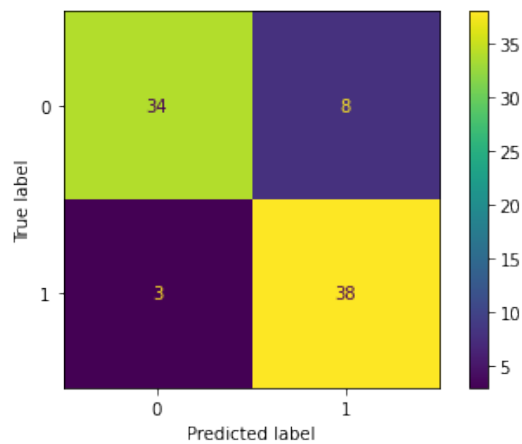


Figure 8.10: The summary of prediction results on the irrigation treatment classification problem. “True label” meant the ground truth of  $ET_c$  based irrigation treatment levels. “Predicted label” identified the irrigation treatment levels predicted by the trained CNN model. To simplify the visualization, low irrigation (30% and 50% ET) were labeled as “0”; high irrigation (75% and 100% ET) were labeled as “1”.

Table 8.3: The CNN model performance.

Irrigation level	Precision	Recall	F1-score
Low irrigation	0.92	0.81	0.86
High irrigation	0.83	0.93	0.87
Accuracy	NA	NA	<b>0.87</b>
Macro avg	0.87	0.87	0.87
Weighted avg	0.87	0.87	0.87

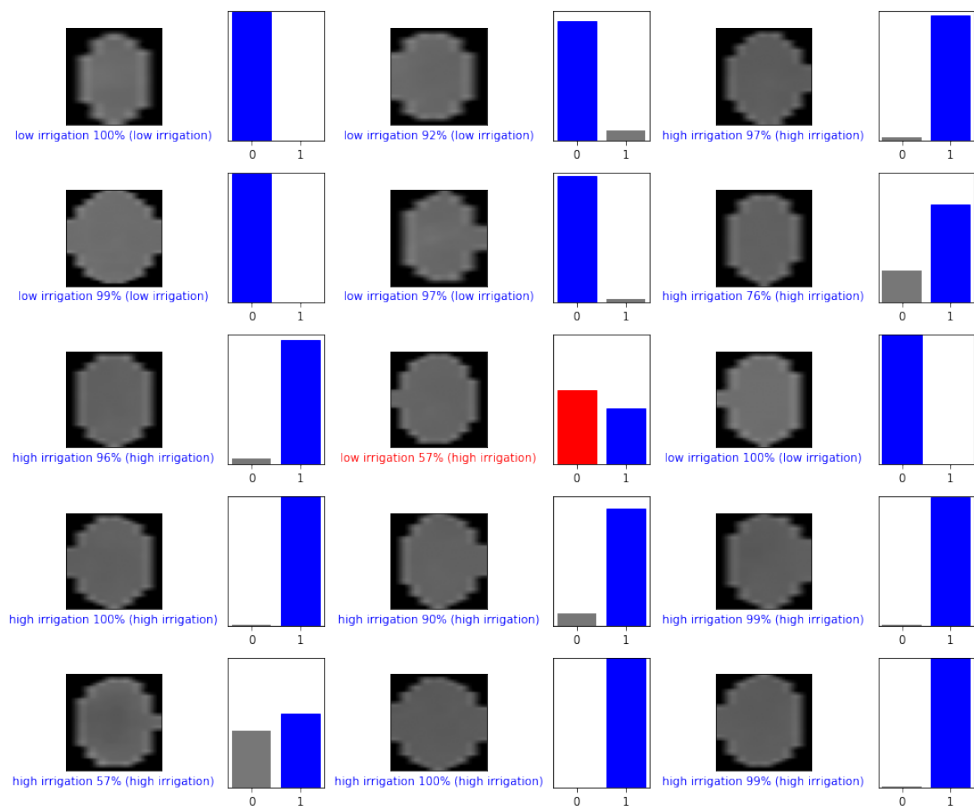


Figure 8.11: To visualize the trained CNN model performance, the authors made predictions about some images in the test dataset. Correct prediction labels are blue and incorrect prediction labels are red. The number gives the percentage (out of 100) for the predicted label.

## 8.4 Conclusion and Future Research

The aim of this chapter was for irrigation treatment levels inference in the pomegranate field at the individual tree level by using UAV-based thermal images and machine learning algorithms. The author collected the  $\Delta T$  by using a UAV-based high-resolution thermal camera. Then, CIML algorithms were adopted for the tree-level irrigation treatment classification problem. The author developed a reliable tree-level irrigation treatment inference method using UAV-based high-resolution thermal images. The research results showed that the best classification accuracy of irrigation treatment levels was 90% when the “Naive Bayes” method was adopted. The results of this research supported the idea that a significant increase in the midday infrared canopy to air temperature difference ( $\Delta T$ ) will indicate stomata closure and water stress conditions. The author also proposed the concept of CIML and proved its performance on the classification of tree-level irrigation treatments. CIML models have great potential for future agriculture research. With more complex information, it will benefit the training and testing process of machine learning algorithms.

## Chapter 9

# Scale-aware Pomegranate Yield Prediction Using UAV Imagery and Machine Learning

Monitoring the development of trees and accurately estimating the yield are important to improve orchard management and production. Growers need to estimate the yield of trees at the early stage to make smart decisions for field management. However, methods to predict the yield at the individual tree level are currently not available because of the complexity and variability of each tree. This study aimed to evaluate the performance of an unmanned aerial vehicle (UAV)-based remote sensing system and machine learning (ML) approaches for tree-level pomegranate yield estimation. Lightweight sensors, such as multispectral camera, were mounted on the UAV platform to acquire high-resolution images. Eight features were extracted, including normalized difference vegetation index (NDVI), green normalized vegetation index (GNDVI), red-edge normalized difference vegetation index (NDVI<sub>re</sub>), red-edge triangulated vegetation index (RTVI<sub>core</sub>), individual tree canopy size, the modified triangular vegetation index (MTVI<sub>2</sub>), the chlorophyll index-green (CI<sub>g</sub>), and the chlorophyll index-rededge (CI<sub>re</sub>). First, direct correlations were made, and correlation coefficient ( $R^2$ ) was determined between these vegetation indices and tree yield. Then, machine learning approaches were applied with the extracted features to predict the yield at the individual

tree level. Results showed that the decision tree classifier had the best prediction performance, with an accuracy of 85%. The study demonstrated the potential of using UAV-based remote sensing methods, coupled with ML algorithms, for pomegranate yield estimation. Predicting the yield at the individual tree level will enable the stakeholders to manage the orchard at different scales, thus improving the field management efficiency.

## 9.1 Introduction

Due to the recurring water shortages in California, many growers started growing crops that have drought resistance and high economic value to a certain degree, such as pomegranate [439]. There is around 11,000 ha of pomegranate in California, evidence suggests that the pomegranate trees have strong adaptability to a wide range of soil conditions and climates [440, 458]. Research results show that pomegranate has great potential for human disease treatment and prevention, such as cancer [459, 460]. Pomegranate yield estimation can provide critical information for stakeholders and help them make better decisions on field operations. Therefore, efficient pomegranate yield prediction is economically important in pomegranate production.

The yield of field and woody crops is usually determined by their genotype and environmental conditions, such as soil physical and chemical properties, irrigation management, weather conditions, etc., making the yield prediction complicated and inaccurate [461, 462]. Thus, many researchers have been working on the yield prediction using a plethora of approaches [463, 464, 465, 466, 467]. For example, [463] developed statistical models using the stochastic gradient boosting method for early and mid-season yield prediction of almond in the central valley of California. Multiple variables were extracted from the remote sensing images, such as canopy cover percentage (CCP) and vegetation indices (VIs). Research results demonstrated the potential of automatic almond yield prediction at the individual orchard level. In [456], Yang *et al.* estimated the corn yield by using the hyperspectral imagery and convolutional neural networks (CNNs). Results showed

that the spectral and color image-based integrated CNN model has a classification accuracy of 75% for corn yield prediction.

Recently, UAVs and lightweight payloads have been used as a reliable remote sensing platform by many researchers to monitor the crop status temporally and spatially [449, 137, 468, 140]. Equipped with lightweight payloads, such as RGB camera, multispectral camera, and thermal camera, UAV-based remote sensing system can provide low-cost and high-resolution images for data analysis. For example, in [464], Yang *et al.* proposed an efficient CNN for rice grain yield estimation. A fixed-wing UAV was adopted to collect RGB and multispectral images to derive the vegetation indices. Results showed that the CNNs trained by RGB and multispectral imagery had better performance than the VIs-based regression model. In [465], Stateras *et al.* defined the geometry of olive tree configurations and developed a forecasting model of annual production in a non-linear olive grove. Digital terrain model (DTM) and digital surface model (DSM) were generated with high-resolution multispectral imagery. Results showed that the forecasting model could predict the olive yield in kilograms per tree.

However, few studies have investigated the correlation between the tree canopy characteristics and yield prediction at the individual tree level. Thus, this article aims to estimate the pomegranate tree yield with ten different tree canopy characteristics, which are normalized difference vegetation index (NDVI), green normalized vegetation index (GNDVI), red-edge normalized difference vegetation index (NDVI<sub>re</sub>), red-edge triangulated vegetation index (RTVI<sub>core</sub>), canopy size, canopy temperature, irrigation level, the modified triangular vegetation index (MTVI<sub>2</sub>), the chlorophyll index-green (CI<sub>g</sub>) and the chlorophyll index-rededge (CI<sub>re</sub>). For example, the NDVI has been commonly used for vegetation monitoring, such as water stress detection [232], crop yield assessment [224], and evapotranspiration (ET) estimation [28]. The value of NDVI is a standardized method to measure healthy vegetation. When the NDVI is high, it indicates that the vegetation has a higher level of photosynthesis. In [461], Feng *et al.* demonstrated that the NDVI and yield had a Pearson correlation coefficient of 0.80. The GNDVI and yield had a correlation of 0.53.

The objectives of this chapter were: 1.) To investigate the correlation between the pomegranate yield and eight different features extracted from UAV high-resolution images. 2.) To establish a scale-aware yield prediction model using machine learning approaches. Estimating the yield with scale-aware models will help stakeholders make better decisions for field management at the block or orchard levels.

## 9.2 Material and Methods

### 9.2.1 Experimental Field and Ground Data Collection

This study was conducted in a pomegranate research field at the USDA-ARS, San Joaquin Valley Agricultural Sciences Center (36.594 °N, 119.512 °W), Parlier, California, 93648, USA. The soil types are a Hanford fine sandy loam (coarse-loamy, mixed, thermic Typic Xerorthents). The San Joaquin Valley has a Mediterranean climate with hot and dry summers. Rainfall is insignificant during the growing season, and irrigation is the only source of water for pomegranate growth [440]. Pomegranate (*Punica granatum* L., cv ‘Wonderful’) was planted in 2010 with a 5 m spacing between rows and a 2.75 m within-row tree spacing in a 1.3 ha field [439].

The pomegranate field was randomly designed into 16 equal blocks, with four replications, to test four irrigation levels (Fig. 9.1). The irrigation volumes were 35%, 50%, 75%, and 100% of crop evapotranspiration (ET<sub>c</sub>), measured by the weighing lysimeter in the field. There were five yield sampling trees in each block, 80 sampling trees in total, marked with red labels in Fig. 9.2.

### 9.2.2 UAV Platform and Imagery Data Acquisition

The UAV-based remote sensing system consisted of a UAV platform, called “Hover”, and a multispectral camera (Rededge M, Micasense, Seattle, WA, USA). See more details of the UAV and sensor in Chapter 3. A software Mission Planner was used to design the flight missions. The flight height was designed as 60 m above

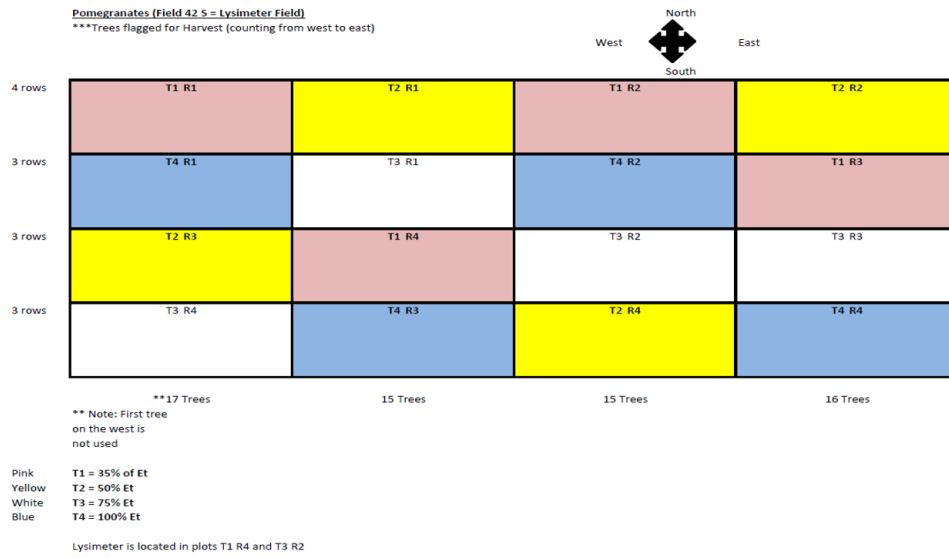


Figure 9.1: The pomegranate field was randomly designed into 16 equal blocks, with four replications, to test four irrigation levels. The irrigation volumes were 35%, 50%, 75%, and 100% of  $ET_c$ , which were measured by the weighing lysimeter in the field.



Figure 9.2: There were five sampling trees in each block, 80 sampling trees in total, marked with red labels.

Table 9.1: UAV image features used in this study.

Features	Equations	Related traits	References
NDVI	Equation (9.1)	Yield, leaf chlorophyll content, biomass	[469, 475, 461]
GNDVI	Equation (9.2)	Yield, leaf chlorophyll content, biomass	[470, 461]
NDVIre	Equation (9.3)	Nitrogen, yield	[471, 476]
RTVIcore	Equation (9.4)	Leaf area index, biomass, nitrogen	[472, 477]
MTVI2	Equation (9.5)	Leaf chlorophyll content	[473, 478]
CIg	Equation (9.6)	Yield, leaf chlorophyll content	[474, 479]
CIre	Equation (9.7)	Yield, leaf chlorophyll content	[480, 481]

ground level (AGL). The UAV image overlapping was designed as 75% in forward and 70% sideward to stitch UAV images successfully by Agisoft Metashape.

### 9.2.3 UAV Image Feature Extraction

The orthomosaick image was used to extract image features defined in Table 9.1. Seven image features were extracted from the multispectral orthomosaick image acquired by the UAV platform. All the vegetation indices or features have been commonly used in monitoring the plant health, nitrogen, biomass, and yield estimation [469, 470, 471, 472, 473, 474].

#### The Normalized Difference Vegetation Index (NDVI)

The NDVI has been commonly used for vegetation monitoring, such as water stress detection [232], crop yield assessment [224], and ET estimation [143]. The value of NDVI is a standardized method to measure healthy vegetation, allowing to generate an image displaying greenness (relative biomass). The NDVI takes advantage of the contrast of the characteristics of two bands, which are the chlorophyll pigment absorptions in the red band (R) and the high reflectivity of plant materials in the near-infrared band (NIR). When the NDVI is high, it indicates that the vegetation has a higher level of photosynthesis. The NDVI is usually calculated by

$$NDVI = \frac{NIR - R}{NIR + R}, \quad (9.1)$$

where  $NIR$  and  $R$  are the reflectance of near-infrared and red band, respectively.

### **The Green Normalized Difference Vegetation Index (GNDVI)**

The GNDVI is commonly used to estimate photosynthetic activity and determine water and nitrogen uptake into the plant canopy [470, 461]. The GNDVI is calculated by

$$GNDVI = \frac{NIR - G}{NIR + G}, \quad (9.2)$$

where  $G$  stands for the reflectance of the green band.

### **The Red-Edge Normalized Difference Vegetation Index (NDVI<sub>re</sub>)**

The NDVI<sub>re</sub> is a method for estimating vegetation health using the red-edge band. The chlorophyll concentration is usually higher at the late stages of plant growth; the NDVI<sub>re</sub> can then be used to map the within-field variability of nitrogen foliage to help better understand the fertilizer requirements of crops [471, 476]. The NDVI<sub>re</sub> is calculated by

$$NDVI_{re} = \frac{NIR - RedEdge}{NIR + RedEdge}, \quad (9.3)$$

where  $RedEdge$  is the reflectance of the red-edge band.

### **The Red-Edge Triangulated Vegetation Index (RTVI<sub>core</sub>)**

The RTVI<sub>core</sub> is usually used for estimating the leaf area index and biomass [472, 477]. It uses the reflectance in the NIR, RedEdge, and G spectral bands, calculated by

$$100(NIR - RedEdge) - 10(NIR - G). \quad (9.4)$$

### The Modified Triangular Vegetation Index (MTVI2)

The MTVI2 method usually detects the leaf chlorophyll content at the canopy scale, which is relatively insensitive to the leaf area index [473]. MTVI2 uses the reflectance in the G, R and NIR bands, calculated by

$$\frac{1.5[1.2(NIR - G) - 2.5(R - G)]}{\sqrt{(2NIR + 1)^2 - (6NIR - 5\sqrt{R}) - 0.5}}. \quad (9.5)$$

### The Green Chlorophyll Index (CIg)

The CIg is for estimating the chlorophyll content in leaves using the ratio of the reflectivity in the NIR and G bands [474], which is calculated by

$$\frac{NIR}{G - 1}. \quad (9.6)$$

### The Red-Edge Chlorophyll Index (CIre)

The CIre is for estimating the chlorophyll content in leaves using the ratio of the reflectivity in the NIR and RedEdge bands [474], which is calculated by

$$\frac{NIR}{RedEdge - 1}. \quad (9.7)$$

## 9.2.4 The Machine Learning Methods

Several ML classifiers were adopted to evaluate the performance of pomegranate yield estimation, such as “Random Forest” [338], “AdaBoost” [150], “Nearest Neighbors” [339], and “Decision Tree” [340]. Please refer to Chapter 6 for more details of the ML methods.

## 9.3 Results and Discussion

### 9.3.1 The Pomegranate Yield Performance in 2019

The pomegranate fruit was harvested from 80 sampling trees in 2019. As mentioned earlier, there were four different irrigation levels in the field, 35%, 50%,

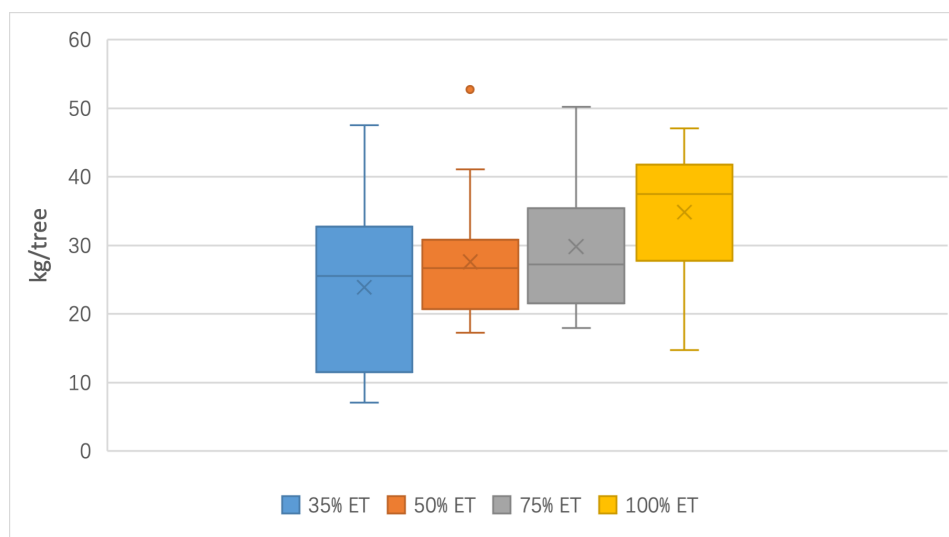


Figure 9.3: The pomegranate yield performance at the individual tree level in 2019. For the 35% irrigation treatment, the total fruit weight per tree was 23.92 kg, which produced the lowest yield. For the 50% irrigation treatment, the total fruit weight per tree was 27.63 kg. For 75% and 100% irrigation treatment, the total fruit weight per tree was 29.84 kg and 34.85 kg, respectively.

75%, and 100% of ET. The author then calculated the total fruit weight per tree (kg) and drew the boxplot for each irrigation level (Fig. 9.3). For the 35% irrigation treatment, the total fruit weight per tree was 23.92 kg, which produced the lowest yield. For the 50% irrigation treatment, the total fruit weight per tree was 27.63 kg. For 75% and 100% irrigation treatment, the total fruit weight per tree was 29.84 kg and 34.85 kg, respectively. The pomegranate yield performance at the USDA was consistent with previous research work [439]. Since the author had the yield data for each sampling tree, machine learning algorithms were used for individual tree level yield estimation with the eight image features mentioned earlier.

### 9.3.2 The Correlation between the Image Features and Pomegranate Yield

Before the vegetation indices were used as input features for ML algorithms, the author first investigated the correlation ( $R^2$ ) between the vegetation index and the

pomegranate yield (Fig. 9.4). Each dot represented a mean value of 20 sampling trees. According to the research results, the NDVI<sub>re</sub> and CI<sub>re</sub> had relatively higher  $R^2$ , which were 0.6963 and 0.6772, respectively. Research results showed that the NDVI and the pomegranate yield had an  $R^2$  of 0.6273. The GNDVI and the yield had an  $R^2$  of 0.5166. The MTVI2 and CI<sub>g</sub> had  $R^2$  of 0.4293 and 0.5059, respectively. The RTVI<sub>core</sub> had the lowest  $R^2$  of 0.1216. The canopy size had an  $R^2$  of 0.6192. These findings emphasized the importance of yield estimation using vegetation indices. Several researchers reported that vegetation indices could be used for yield estimation [469, 475, 470, 471, 472, 473, 480, 479, 461]. The performance of ML algorithms on yield prediction is discussed in the following section.

### 9.3.3 The ML Algorithm Performance on Yield Estimation

The pomegranate yield data (80 sampling trees) was distributed as 75% for training and 25% for testing using the *train\_test\_split* method. Considering the dataset was relatively small, the author used  $K$ -fold cross-validation, splitting the training dataset into  $K$  folds, then making predictions and evaluating each fold using an ML model trained on the remaining folds [20]. The classes were defined as low yield and high yield for yield prediction based on a threshold value of 25 kg per tree. For evaluating the trained models, a confusion matrix was used to compare the performances of different classifiers. The “True label” meant the ground truth of the yield. The “Predicted label” identified the individual tree yield predicted by the trained model.

The trained ML classifiers had distinct test performance for individual tree level yield prediction. The “Decision Trees” classifier had the highest accuracy of 0.85. Table 9.2 and Fig. 9.5 showed the details of the “Decision Trees” method, a non-parametric supervised learning methods commonly adopted for classification problems. The objective was to create an ML model that predicted the value of a target variable by learning simple decision rules inferred from the data features (Fig. 9.5). A tree can be seen as a piecewise constant approximation. “Decision Trees” usually uses a white box model, which means the explanation for the con-

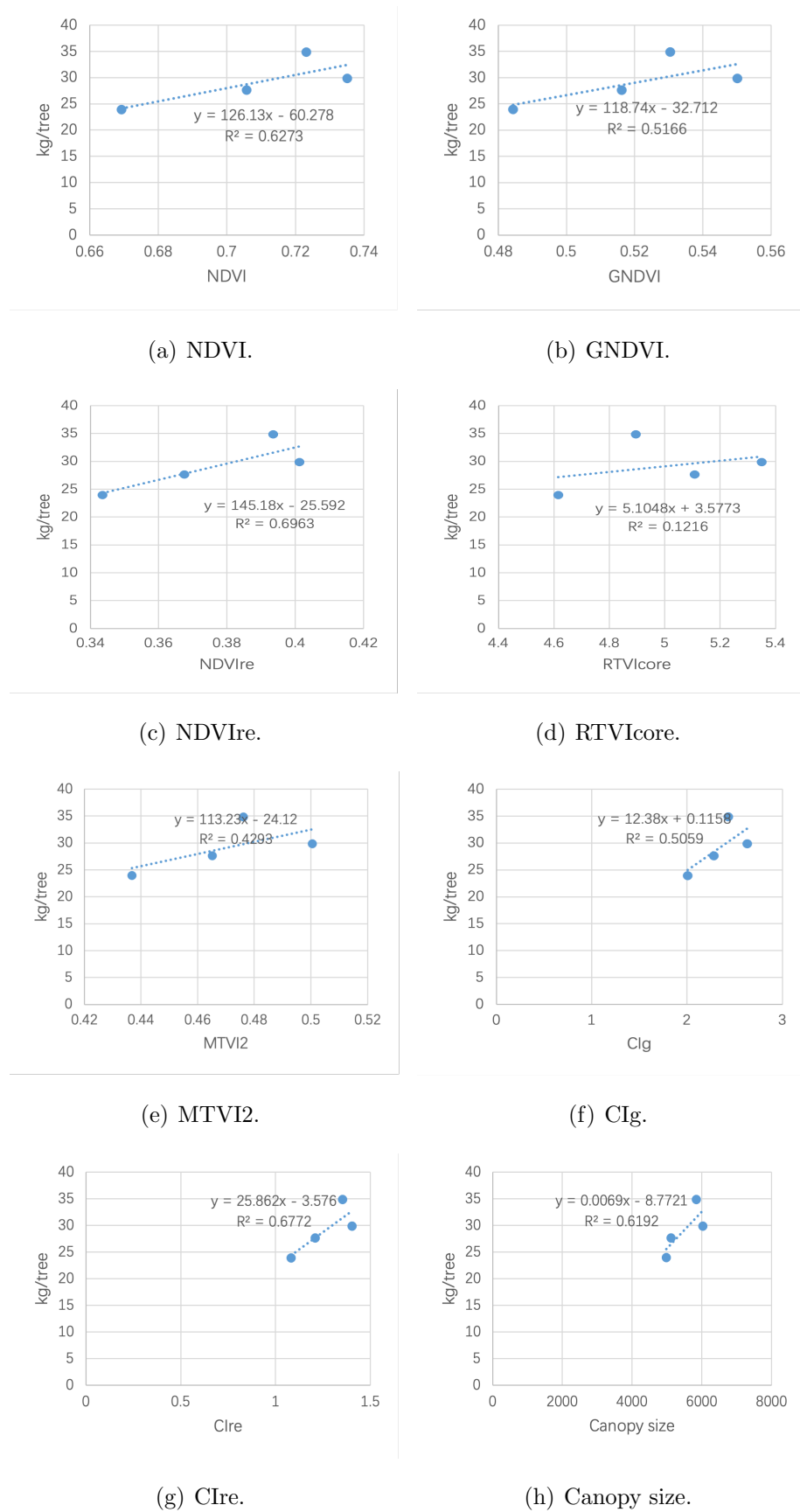


Figure 9.4: The correlation between the vegetation index and yield.

Table 9.2: The “Decision Tree” performance on yield prediction. “NA” stands for “Not available”.

Yield prediction	Precision	Recall	F1-score
Low yield	0.92	0.85	0.88
High yield	0.75	0.86	0.80
Accuracy	NA	NA	<b>0.85</b>
Macro avg	0.83	0.85	0.84
Weighted avg	0.86	0.85	0.85

dition is easily explained by Boolean logic if a given situation is observable in a model. As shown in Fig. 9.5, the “Decision Trees” ML model started at the root node, if the NDVI<sub>re</sub> value were less than 0.334, the prediction process would move to the leaf child node. In this case, the model would predict that the input was a low-yield pomegranate tree. A node’s gini attribute measures its impurity: a node is “pure (gini = 0)” if all the training instances it applies are from the same class.

For the other classifiers’ test performance, the accuracy of the  $k$ -nearest neighbor was 0.8. “Support Vector Classification (SVC)” had an accuracy of 0.7. The “Random Forest” had a test accuracy of 0.65. The “AdaBoost”, “Gaussian Process”, and “Gaussian Naive Bayes” had an accuracy of 0.8, 0.75, and 0.6, respectively. The “Quadratic Discriminant Analysis (QDA)” also had a prediction accuracy of 0.8 (Table 9.3 and Fig. 9.6).

## 9.4 Conclusion and Future Research

The aim of the research was for individual tree level yield prediction in the pomegranate field using a UAV-based remote sensing method. The author collected the yield data and calculated the vegetation indices derived from the high-resolution UAV imagery. Then, machine learning algorithms were adopted for the yield prediction classification. The research results showed that the best classification accuracy of yield was 85% when the “Decision Trees” method was being adopted. For the other ML models’ test performance, the accuracy of the  $k$ -nearest



Figure 9.5: The “Decision Trees” method training process. The “Decision Trees” usually uses a white box model, which means the explanation for the condition is easily explained by Boolean logic if a given situation is observable in a model. As shown here, the “Decision Trees” ML model started at the root node, if the NDVire value were less than 0.334, the prediction process would move to the leaf child node. In this case, the model would predict that the input was a low-yield pomegranate tree. A node’s gini attribute measures its impurity: a node is “pure (gini = 0)” if all the training instances it applies are from the same class.

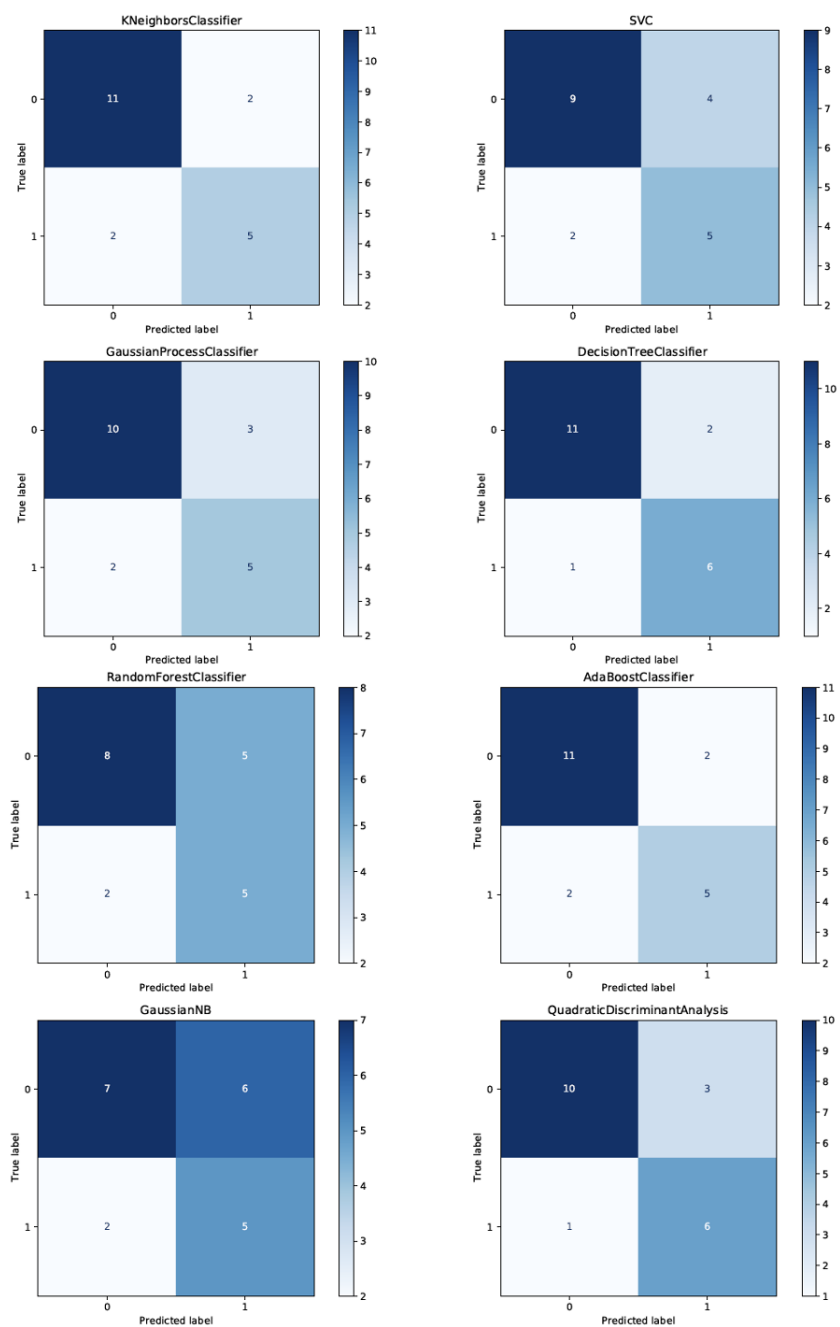


Figure 9.6: The comparison of the eight different ML classifiers on individual tree level yield prediction. “True label” meant the ground truth of the yield. “Predicted label” identified the individual tree yield predicted by the trained model. The value 0 meant the low yield; value 1 meant the high yield.

Table 9.3: The performance of ML methods on yield prediction.

Classification methods	Prediction accuracy
“Decision Trees”	<b>0.85</b>
“Nearest Neighbors”	0.80
“Support Vector Machine”	0.70
“Random Forest”	0.65
“AdaBoost”	0.80
“Gaussian Process”	0.75
“Gaussian Naive Bayes”	0.60

neighbor was 0.8. “Support Vector Classification (SVC)” had an accuracy of 0.7. The “Random Forest” had a test accuracy of 0.65. The “AdaBoost”, “Gaussian Process”, and “Gaussian Naive Bayes” had an accuracy of 0.8, 0.75, and 0.6, respectively. The “QDA” also had a prediction accuracy of 0.8. The pomegranate yield information could be reflected by vegetation index data. The research results supported the idea that vegetation indices could be used for yield estimation. Furthermore, the findings of this research provided insights for the scale-aware yield prediction using phenotyping and machine learning technology.

## Part IV

# Towards Smart Big Data in Precision Agriculture

# Chapter 10

## Intelligent Bugs Mapping and Wiping (iBMW): An Affordable Robot-driven Robot for Farmers

### 10.1 Introduction

Navel orangeworm (NOW) is a common pest of almonds in California. According to [482], California almond harvests is worth of more than five billion dollars before processing. The NOW can cause around 30 percent product loss in almonds from direct consumption [483]. First-instar larvae can bore into the nutmeat, then, the larvae can consume most of the nut, which will produce lots of webbing and frass. Later, the larvae damage can also cause fungal infections as soon as hull splits occur. With 2% total damage from the NOW, almond growers' loss can be \$158.75 per acre. For those who had 20% total damage, the loss can be as high as \$1742.50 per acre, which is 24% of the total profit \$7200 per acre [484]. This summer's NOW threat to almond orchards could rival that of 2017, when damage to almonds by the pest was at historic levels. Therefore, NOW is economically important in California and early detection of pest population distribution in agricultural system is critical to enabling timely interventions and reducing crop yield losses [290]. Each year in California, eradication of pests is not always available,

because of either the fast expanding distribution of the pest or restrictions regarding the tools available to attempt eradication. As mentioned about NOW, they can fly a quarter-mile or more to find new host, which makes it more difficult mapping their distribution. Monitoring is able to give some warnings, but the growers have to respond fast. Traditionally, people use pheromone traps to monitor the flights of NOW, but it needs labors counting the number of moths and tracking the data, which is time consuming and needs a lot of labor effort.

Typically, growers must take four critical steps in their Integrated Pest Management (IPM) program to reduce NOW damage:

1. Winter sanitation to remove mummy nuts.
2. Mapping NOW population and timing of moth flights.
3. Pesticide applications or biological control.
4. Prompt harvest before a third generation of NOW.

In this chapter, the author will focus on the second and third section. The goal is to develop an intelligent bugs mapping and wiping (iBMW) robot to perform pest population spatial and temporal distribution and “surgical precision spraying” for pest wipeout. The iBMW is an affordable (less than \$1000) robot-driven robot, which has a Turtlebot 3 worked as the robot’s brain and an unmanned ground vehicle serviced as the work platform. According to the design, the robot will be capable to recognize and classify the NOW by using deep learning neural networks. Several iBMWs can also work in the field together in swarming mode day and night, so that it can realize temporal and spatial bugs mapping. Then, based on the mapping results, the iBMWs can determine which areas are at the greatest risk and whether wiping treatment is needed in those areas.

Being able to target treatment of infestations will result in lower use of toxic insecticide, time saving, reduced production costs, and greater crop yields. Less pesticide usage can also reduce both air and water contamination so that it can reduce the environmental impact. All of these make farming more economically viable, and have the potential to provide us safety, health, and sustainability in food systems for our growing world population.

## 10.2 Existing Solutions

The current state-of-the-art methods to identify pest population distribution require farmers to use egg traps, pheromone traps, or degree-day calculations to monitor the first and second generations of navel orangeworm.

Egg traps usually have a mixed of almond meal and almond oil. They will encourage female moths to lay eggs on the traps. The egg traps are usually placed with a density of 1 trap per 5 acres. Farmers or growers usually check the traps twice a week to get the eggs data and determine the egg-laying peaks. Pheromone traps are mainly placed in the tree canopies at around 6 to 8 feet to map the flights of adult male moths [485]. Farmers need to count the number of moths in the trap and identify peaks in adult activity in the orchard. Although these methods can help prevent almonds from NOW damage in some degree, scouting in the field and collecting data is still very time consuming. It also needs lots of labor to finish the field work. Also, counting the number of moths is an empirical job, even experienced farmers may make mistakes. For example, meal moth (*Pyralis farinalis*) is also attracted to the traps, which looks very similar with navel orangeworm. Another disadvantage is the traps are point measurement, which can hardly stand for the temporal and spatial distribution for a whole orchard.

After collecting the data from egg or pheromone traps, researchers or farmers will make treatment decisions. The first hullsplit is the most effective timing to apply for insecticide. Spraying the pesticide at the beginning of hullsplit if eggs are laid on egg traps. Researchers or farmers can also spray pesticide if pheromone traps indicate that the second flight is starting. Usually, commercial spray rigs are used in almond orchards, such as D2-40 engine driven or GB-36 power take-off (PTO), manufactured by Air-O-Fan (Reedley, CA, USA) [486]. The Progressive Ag tower is another top choice for spraying applications. Cone-jet nozzles (Teejet Technologies, Wheaton, IL, USA) have also been widely used. Spraying speed for those machines is usually set up as 2 to 4 mph. Spray applications of insecticides are mostly empirically based on crop phenology and degree-days using a lower threshold of 55°F and an upper threshold of 94°F. Mating disruption, which uses female-moth pheromones to confuse male moths, is another tool used with insecti-

cides together. The cost estimation for mating disruption is \$120 to \$160 per acre. For insecticide application, it's \$40 to \$60 per spraying.

Researchers or farmers usually spray a whole orchard to deal with potential pest risks, for which the insecticide is not used efficiently. Research results [487] proved that much of the pesticide was not used on the target trees. Seiber found that 88% of pesticide was on the orchard floor instead of the trees [488]. Cross also investigated the effects of spray droplet size and application volumes of 10 to 80 gallons per acre on spray deposition in an orchard [489]. The results showed that 43% to 61% of the applied spray was lost to ground deposit within 15 feet of the row being sprayed. The off-target pesticides result in a significant waste of money as well as environmental issues, such as air pollution and water contamination.

To reduce the pesticide usage and to improve the efficiency, researchers tried several different new technologies. For example, sensor-equipped sprayers, also called “Smart sprayer”, use ultrasonic or optical sensors to detect the presence or absence trees [490]. Giles found that this technology could save 28% to 34% of pesticide when using this system. The basic idea is to turn on the spray nozzles when the target trees show up in the spray zones [487]. The sprayer will turn off when it's between trees or where trees are absent. The experiment was designed in a commercial almond orchard near Modesto, CA. The majority of the trees were about 20 years, which are planted on a 23-foot diamond pattern. In principle, however, these sprayers are the same with conventional sprayers. They did not consider the pests population temporal and spatial distribution. In this chapter, the author believes iBMWs can improve pesticide spraying efficiency a lot based on the innovations mentioned in the next section.

### 10.3 iBMW Innovation

As mentioned previously, the iBMW is an intelligent robot which can recognize and classify the NOW by using deep learning neural networks. As shown in Fig. 10.1, by using swarming mechanism, several iBMWs can scout in orchard together to realize pest population mapping in a large scale. Based on the map-

ping analysis, the iBMWs can determine which areas are at the greatest risk and whether wiping treatment is needed. Once the whole system is working, the final goal is to use the iBMWs system to monitor more kinds of trees, such as walnut, pistachio, and pomegranate. Such flexibility can make iBMWs have impact on more than just one type of field. Based on farmers' requirements, the author will add more agricultural applications, such as soil moisture monitoring, water stress detection [232] and 3D modelling of canopies, on this taskable robot platform.

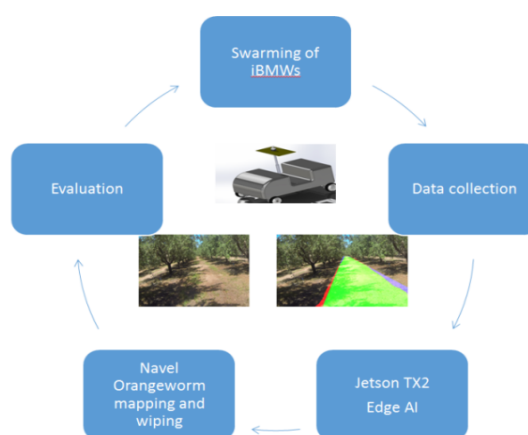


Figure 10.1: The iBMW workflow. The iBMW is an intelligent robot which can recognize and classify the NOW by using deep learning neural networks. By using swarming mechanism, several iBMWs can scout in orchard together to realize pest population mapping in a large scale. Based on the mapping analysis, the iBMWs can determine which areas are at the greatest risk and whether wiping treatment is needed.

Currently, the objective is to make the iBMWs work perfectly in an almond orchard in Merced (37.493°N, -120.634°W). There are three kinds of almonds: Nonpareil, Carmel, and Monterey, all planted on Lovell peach rootstock, spaced at 5.5 m × 6.1 m, with Rocklin loam and Greenfield sandy soil [232]. In order to achieve the pest mapping and wiping, our team has been working in the almond orchard several times to collect videos and images to feed into the deep learning algorithms to realize the cognition of the iBMW. We will collect more data in different almond orchards in the future to make iBMWs more robust and adaptive.



Figure 10.2: The concept of the iBMW.

### 10.3.1 Cognitive of Pest Population Mapping and Wiping

Instead of set up in the almonds' canopies, the egg traps or pheromone traps will be equipped on iBMW's deluxe rod actuator, as shown in Fig. 10.2, which can change the height to six or eight feet when running in the field. Then, iBMWs can scout in orchard together to record number of moths in the traps by using high resolution RGB cameras mounted on the iBMWs. High resolution images enable that eggs and adult moths can be seen clearly in images. Then, deep learning neural networks, such as Faster RCNN [491], Fully Convolutional Neural Networks [492], can be used to train images datasets to get a NOW detection model. The model will be used to recognize and classify the NOW in the images.

Several iBMWs can work in the field together in swarming mode day and night if necessary. Thus, it can map the NOW in almond orchard temporally and spatially. The high temporal and spatial resolution images will help the farmers to determine where, when, and what kind of treatments are needed. For example, the iBMW can pinpoint infestations and problems areas, so that it's unnecessary to treat all areas in a large scale of field. Sprayer system can be mounted on the iBMWs to realize pesticide applications. This will definitely save lots of labors

for scouting in the field and less pesticide will be used. It will directly or indirectly contribute to agricultural, environmental and economic sustainability due to minimized application pesticides and improve yields estimation.

The challenges for NOW detection highly depend on how accurate our deep learning algorithms will be. During the image processing, NOW may not be treated as bugs or other pests on traps may be recognized as NOW, both could happen during the training process. We will carefully select training and testing data samples during the image processing. Several image processing techniques will be applied to make sure we can get the best accuracy results.

### **10.3.2 iBMW with TurtleBot 3 as “Brain”**

For the iBMW platform, we used a TurtleBot 3 which is operated by ROS (Robot Operating System), as the robot’s brain and control the iBMW’s behaviors in the field. ROS is a flexible framework for writing robot software, so that it can save us a lot of time on software development. TurtleBot 3 is a low cost robot platform with open-source software. There are mobile base, 3D sensor and laptop computer in the TurtleBot 3 kit. TurtleBot 3 has many similar abilities of the large company’s robot platforms, such as PR2. With the TurtleBot 3 components, we can even create real-time obstacles avoidance and autonomous navigation.

### **10.3.3 Real-time Vision Processing**

We will also use the Jetson TX2 to realize cognition mechanism by deep learning algorithms. Field road detection experiment results are shown in Fig. 10.3. Jetson TX2 is the fastest, most power-efficient embedded AI computing device. It is built around an NVIDIA GPU, loaded with 8GB of memory, and 59.7GB/s of memory bandwidth, which will benefit the iBMWs to react faster in a real time pest monitoring. Deep learning can allow the iBMW to adapt to field conditions based on computer vision instead of only relying on GPS (GPS sometimes is weak under tree canopies). The iBMW currently can run 3.7 miles per hour. Emergency shut-off can also avoid injury to workers or crops if an object shows up in iBMW’s

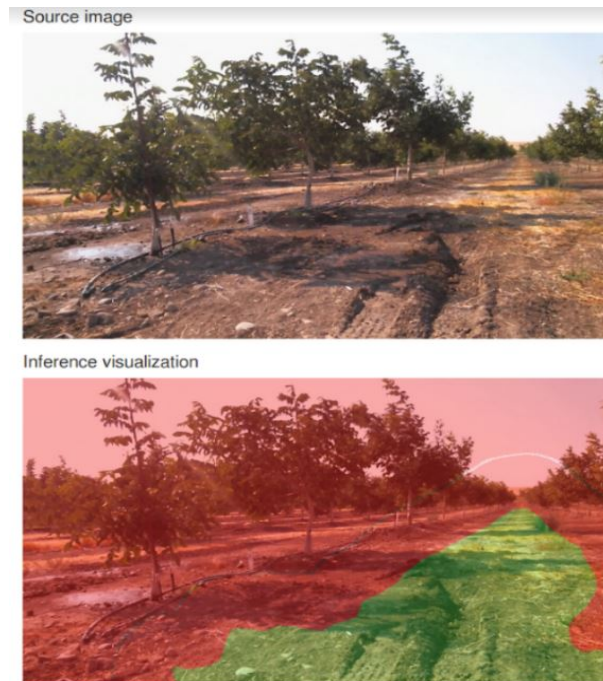


Figure 10.3: Road detection by Jetson TX2.

path accidentally. All of these advantages will make the iBMW more time efficient, consistent and reliable.

iBMW, which includes artificial intelligence platform, can also enable researchers to conduct proximate sensing and mapping missions without human intervention. Real-time vision processing enabled by cognition algorithms is one of the most important factor. Typically, there are three steps of the iBMW movement behaviors, stimulus perception, judgement and decision making, and stimulus performance. In a recent cognitive algorithm used by robot, it can even recognize specific objects in the environment, by using cognitive algorithms to develop a deeper understanding of the scene based on objects and their spatial relationships.

Reconstruction and mapping Monocular Simultaneous Localization and Mapping (SLAM) can also be applied on iBMW platform. SLAM relies on cognition techniques to calculate the position of the robot and to map the environment [303]. Real-time monocular SLAM was thought not possible because of the high computational cost. However, there are many kinds of SLAM packages now, such as

LSD-SLAM [304], RatSLAM [305], and SVO [306]. Researchers compared many different open-source vision-based SLAM packages in a paper at 2016 [307]. It turned out that ORB-SLAM [308] is the best performing package. ORB-SLAM uses ORB features, which are binary features that are invariant to rotation and scale [303]. ORB-SLAM also allows the robots to initialize with no user input, which is important for iBMW platforms as an autonomous robot system. Additionally, when the ORB-SLAM is matching features, the number of key frames increases because of the complexity of the images. This is done by “culling” key frames that are not used, and allows for ORB-SLAM to run for longer periods of time [303].

Using deep learning, recognition can bridge the gap between perception and intelligence. For example, perception missions can collect lots of data, but much of it was discarded to simplify interpretation by higher level tasks [309], e.g. a 3D object can become a point in space. In Arne’s paper [309], it used a deep learning framework to replace these interfaces with learned interfaces. This allows for error back-propagation that can adapt each module to the robot’s task. Deep learning is also a state-of-art technique for image processing. It can target land cover and crop type classification from the images collected from sensors and cameras [23]. Safety is another concern by farmers and growers, the iBMW should have the ability to detect workers and farmers, then will make the right decision in the field.

### 10.3.4 Optimal Path Planning Enabled by iBMW

The iBMW can also contribute to optimal path planning research. Traditionally, there is not much path planning knowledge for field operations [493]. Researchers execute field operations based on experience. According to a study of spraying vehicles with a positioning system, it showed that 16% of the driving distance could be saved, which expressed a clear need for robot path planning. In the past few years, many algorithms have been developed to realize real time path planning systems for robots. For example, in [494], the author used a visibility graph algorithm and Dijkstra’s algorithm to choose optimal path for a robot to traverse in the environment.

Usually, a path planning algorithm needs to meet the following rules [495]:

1. The path planning should have the lowest cost.
2. The resulting path should be fast and accurate.
3. The algorithm should be adaptive with different maps.

The iBMW, as a low-cost robot platform, can be used for basic research of path planning. As mentioned in previous section, iBMWs use Turtlebot 3 components to control the robot's behavior. We can create real-time obstacles avoidance and autonomous navigation based on the ROS. With the Jetson TX2, the iBMW currently can do emergency shut-off, which avoids injury to workers or crops if an object shows up in iBMW's path accidentally. All of these advantages will make the iBMW more time efficient, consistent and reliable for path planning research.

### **10.3.5 Ethical, Cultural and Legal Matters**

With any new practice growers are concerned about if it works and will it save them time and money. Growers would probably worry there is no time or money saved, as any time or money spent checking traps or setting up pheromone traps would just be spent maintaining machines. This would probably be a big concern, as these are unfamiliar and perceptually more complex machines for growers. We are competing with a large market that has been promising a lot with automation and mechanization over the years and have not really delivered. Thus, growers are getting more skeptical. Getting Bowles Farming Company involved is a good step as we need to get growers to buy-in to get other growers to buy into the concept. We will prefer to spend more time convincing one grower than a full room of growers. If we can convince one person and he or she use it and it works, they will go about convincing other growers, as well as, this naturally happening when a neighbor uses something and it works.

## 10.4 Measuring Success

There are three outcome indicators that the author will be monitoring throughout the iBMWs project, the pest population temporal and spatial distribution, the amount of pesticide being used, and the target trees almond yield.

### 10.4.1 NOW Population Temporal and Spatial Distribution

The egg traps are usually placed in the orchard on March at a rate of 1 trap per 10 acres. Researchers also hang one pheromone traps per 50 acre and at least two traps per orchard. Farmers usually monitor the traps once a week. The pest population distribution data acquired by using the above method will be used as groundtruth. The author will compare the iBMW's pest population temporal and spatial distribution with the groundtruth to see if we can get similar or even better results. This will definitely reduce the labor cost, and early detection of the pest will also reduce crop losses made by NOW.

### 10.4.2 The Amount of Pesticide Being Used

The pesticide usage is another indicator to measure during the growing season. The author will set up several homogeneous almond blocks. The author will use commercial spray rigs to spray half of the almond blocks. The iBMWs will be used to spray the rest according to iBMWs pest population distribution results. Each spray amount will be recorded during the growing season. The total amount of pesticide for both methods will be calculated after the last spray at the end of growing season. As mentioned in the existing solution section, Giles found that his technology could save 28% to 34% of pesticide when using his system [490]. In principle, however, these sprayers are the same with conventional sprayers. They did not consider the pests population temporal and spatial distribution. The author believes iBMWs can improve pesticide spraying efficiency by reduced use of large-scale pesticide. This low-environmental impact solution will reduce air and water contamination resulting from orchard pesticide usage. Therefore,

it can provide us a safe, healthy and sustainable food systems. The reduction of pesticide cost can be substantial. Based on UC Cooperative publications, the estimate pesticide costs per acre in California orchard crops can be around \$250 [496]. Based on [487], their method saved 10% - 20% pesticide in Sacramento Valley almonds. The author will evaluate iBMWs in the following season to see our results.

### **10.4.3 The Target Trees Almond Yield**

The almond yield will be measured by the researchers or farmers in orchard. The author will compare the results between conventional method and iBMWs to see if iBMWs have any benefit to the almond yield when applied iBMWs spray system.

## **10.5 Conclusions and Future Research**

In general, this chapter proposed an intelligent bugs mapping and wiping (iBMW) robot concept to perform pest population spatial and temporal distribution and “surgical precision spraying” for pest wipeout. Based on the design, the robot will be able to recognize and classify the NOW by using an innovative method for NOW population temporal and spatial distribution. Several iBMWs can also work in the field together in swarming mode. Then, based on the mapping results, the iBMWs can determine which areas are at the greatest risk and whether wiping treatment is needed in those areas.

Being able to target treatment of infestations will result in lower use of toxic insecticide, time saving, reduced production costs, and greater crop yields. Less pesticide usage can also reduce both air and water contamination so that it can reduce the environmental impact. All of these make farming more economically viable, and have the potential to provide us safety, health, and sustainability in food systems for our growing world population. Based on research purpose, the author can also use this iBMW robot platform for more agricultural applications, such as onion irrigation treatment detection [24], tree canopies segmentation [23, 26] and

so on.

# Chapter 11

## A Non-invasive Stem Water Potential Monitoring Method Using Proximate Sensor and Machine Learning Algorithms

### 11.1 Introduction

Improving the capacity to determine plant water status is critical to solve the drought responses and water requirements of crops and trees [497]. The stem water potential (SWP) is a direct measure of water tension within the plant, implying the water status directly in the plant-soil-atmospheric continuum [498]. The SWP also summarizes the effects of both soil moisture and evapotranspiration. These advantages make it a popular index in crops and trees. The details of SWP measurement methods can be referred to [499]. The water mass per leaf area (WMA) and relative water content (RWC) are also critical indices. The WMA represents the absolute tissue water content normalized by the leaf area. The RWC is normalized by the saturated water content, which provides information about cell volume shrinkage [500]. However, those traditional methods require the excision of tissues and laboratory analysis, either gravimetric in the case of WMA and RWC, or using

the pressure chamber for SWP [501]. For example, it is labor-intensive and time consuming to conduct the SWP measurement, requiring at least 10 minutes after the leaf being covered with a foil bag until the water potential is well balanced all around the leaf. Thus, measurement of plant water status has commonly been limited to small study scales [502].

Compared with the traditional methods, noninvasive methods have great potential for improving ground-based and remote sensing in water relations research and their applications in agriculture. In [502], Browne *et al.* demonstrated a refined method and physical model to predict WMA, RWC, and leaf water potential using terahertz transmission. With the development of UAVs technology, UAVs have been commonly used in water stress related research, such as irrigation management [24], evapotranspiration estimation [137], and tree canopy detection [23]. However, UAVs are limited by flight time and payload capability. Such limitations do not apply to proximate sensors. It was the objective of this study to collect data with a pocket-sized, cutting-edge technology radio frequency tridimensional sensor, and then implement several scikit-learn classifiers to detect SWP in a walnut orchard.

In this study, the author proposed a low-cost proximate radio frequency tridimensional sensor “Walabot” and machine learning classification algorithms to predict the walnut SWP. Walnut leaves from trees of different SWP were placed on this sensor to test if the Walabot can detect small changes in the water stress levels. Hypothetically, waveforms generated by different signals may be useful to classify SWP levels. Scikit-learn classification algorithms, such as “Neural Networks,” “Random forest,” “Adam optimizer,” “Decision Tree,” “Support Vector Machine,” and “Nearest Neighbors” were applied for data processing and evaluation.

## 11.2 Material and Methods

### 11.2.1 Walnut Study Area

This study was conducted in a walnut orchard at Merced, CA, 95340, USA (37.47°N, 120.45°W). There were three types of spacing treatment, 22' × 22',

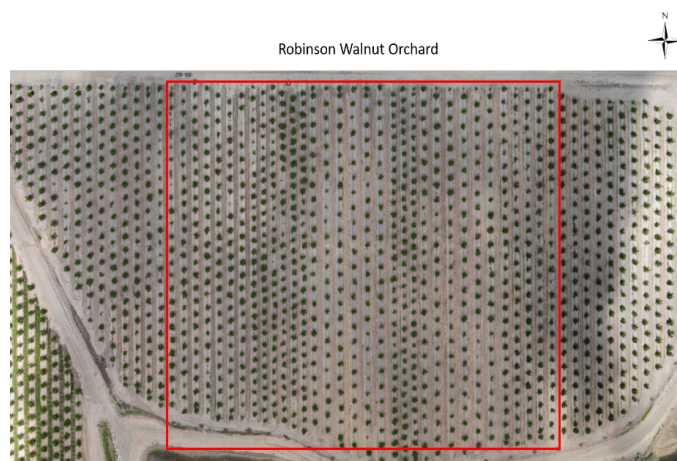


Figure 11.1: This study was conducted in a walnut orchard at Merced, CA, 95340, USA ( $37.47^{\circ}\text{N}$ ,  $120.45^{\circ}\text{W}$ ). There were three types of spacing treatment,  $22' \times 22'$ ,  $26' \times 26'$ , and  $30' \times 30'$ . The region of interest was marked with the red box. To determine the SWP of a walnut tree, midday SWP was measured by using a pressure chamber weekly from May to September 2018.

$26' \times 26'$ , and  $30' \times 30'$ . The region of interest was marked with the red box (Fig. 11.1). To determine the SWP of a walnut tree, midday SWP was measured by using a pressure chamber weekly from May to September 2018.

### 11.2.2 Reflectance Measurements with A Radio Frequency Sensor

The SWP data was collected with a radio frequency 3D sensor called Walabot (Vayyar Imaging Ltd, Yehud-Monosson, Israel). The Walabot was used to measure the reflectance of radio frequencies of the walnut leaves. Then, the reflectance was visualized using PyTorch. For each measurement, a time-domain reflectance signal was recorded. Records of the different reflectance strengths were visualized in the dataset. See more details about the sensor in Chapter 6.

### 11.2.3 Data Collection and Processing

In this study, the Walabot was used to measure radio frequency reflectance from the walnut leaves in 8-28-18 and 9-10-18. There were 16 sampling trees, which had

Table 11.1: The stem water potential of walnut leaves. There were 16 sampling trees, which had unique ID numbers. For example, “20-4” meant the fourth tree on row 20. Each sampling tree was measured five times to reduce the likelihood of errors or anomalous results.

Sampling trees	SWP (8-28-2018)	SWP (9-10-2018)
20-4	4.14	5.67
20-12	4.53	4.95
20-20	4.63	4.26
26-4	5.10	4.95
26-12	3.76	4.17
26-20	4.25	4.02
26-28	5.25	4.44
32-4	3.53	4.85
32-12	2.84	1.36
32-20	3.78	5.27
38-4	5.06	5.37
38-12	3.46	3.56
38-20	3.64	4.28
44-4	4.60	4.58
44-12	3.45	4.49
44-20	4.07	4.29

unique ID numbers (Table 11.1). For example, “20-4” meant the fourth tree on row 20. Each sampling tree was measured five times to reduce the likelihood of errors or anomalous results. Based on the SWP range, the walnut trees were classified into three levels (Table 11.2).

#### 11.2.4 Scikit-learn Classification Algorithms

Six different methods in generating classifiers were used to evaluate the detection performance for SWP levels. “Neural Net,” “Random Forest,” “AdaBoost,” “Support Vector Machine,” “Nearest Neighbors,” and “Decision Trees” were used

Table 11.2: The SWP levels of walnut leaves. Based on the SWP range, the walnut trees were classified into three levels.

SWP levels	Pressure applied (Bar)
Level 1	< 3.5
Level 2	3 - 5
Level 3	> 5

as classification algorithms. For example, the “Decision Trees” are a non-parametric supervised learning method used for classification and regression. The goal was to create a model that predicted the value of a target variable by learning simple decision rules inferred from the data features.

### 11.3 Results and Discussion

The collected SWP data were converted into 2048-dimension vectors for scikit-learn algorithms data processing. The data was distributed as 70% for training and 30% for testing. For evaluating the trained models, a confusion matrix was used to compare performances of different classifiers. The ML models had different levels of performance (Fig. 11.2). The confusion matrix provided insight not only into the errors being made by a classifier but, more importantly, the types of errors that were being made. The “True label” meant the ground truth of SWP levels. The “Predicted label” identified the SWP levels predicted by the trained model. The “Decision Tree” had the highest accuracy of 0.78 (Table 11.3). The accuracy of the “Support Vector Machine” was 0.62. The “Random Forest” also had a low prediction accuracy of 0.60. The “AdaBoost,” “Nearest Neighbors,” and “Neural Network” had an accuracy of 0.60, 0.65, and 0.62, respectively.

In the analysis as “Decision Tree” for the SWP Level 1, the trained model predicted the test data was in the range of Level 3 (Table 11.4). Therefore, the prediction accuracy (F1-score) of Level 1 was zero. The model successfully classified 22 out of 25 samplings in Level 2. For the Level 2, the model had performance with an F1-score of 0.92. For the Level 3, the model classified 9 out of 10 sam-

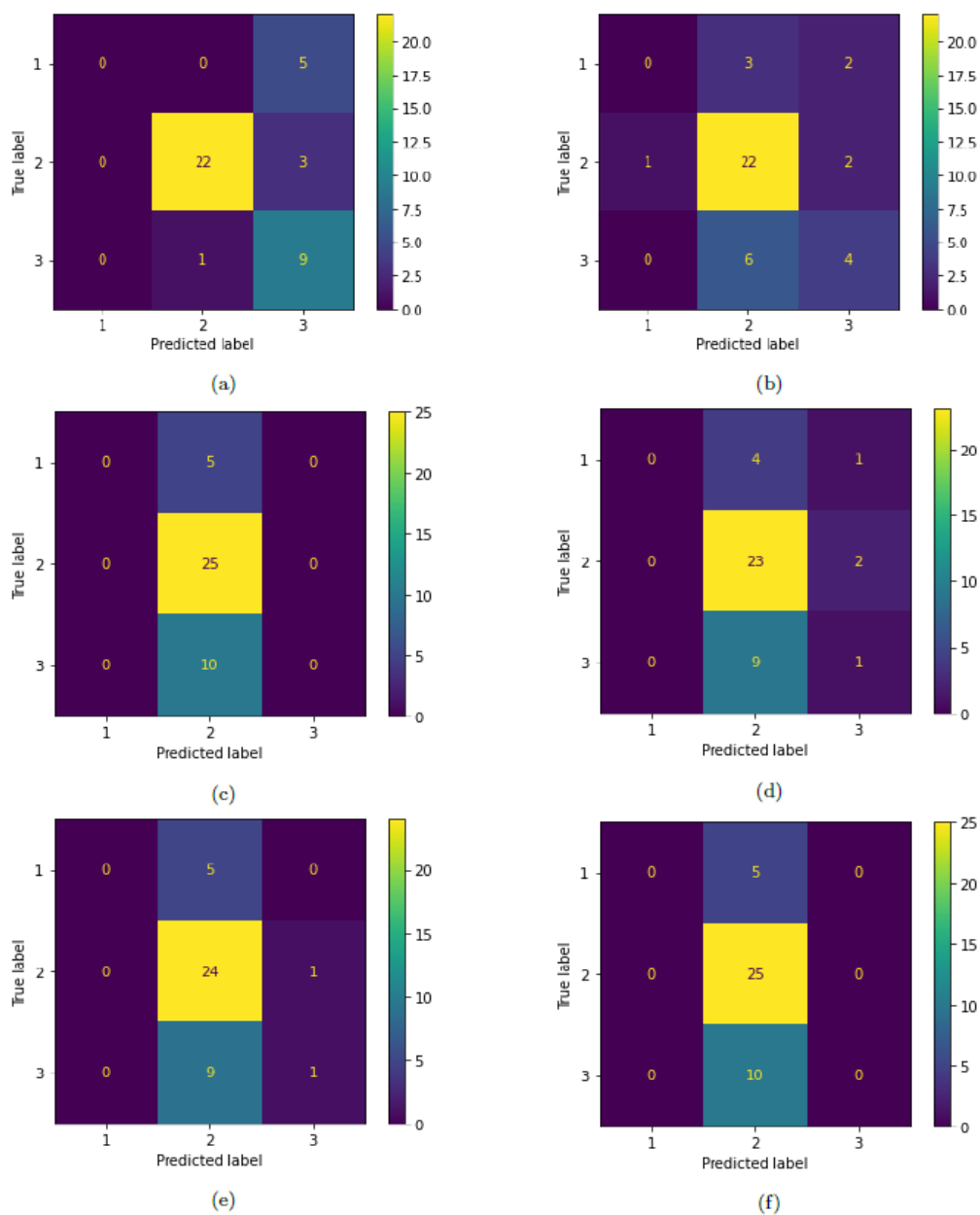


Figure 11.2: A comparison of six classifiers in Scikit-learn on SWP prediction. (a) “Decision Trees”; (b) “Nearest Neighbors”; (c) “Neural Net”; (d) “AdaBoost”; (e) “Random Forest”; (f) “Support Vector Machine”. “True label” meant the ground truth of SWP levels. “Predicted label” identified the SWP levels predicted by the trained model.

Table 11.3: The performance of classification methods. The accuracy of the “Support Vector Machine” was 0.62. The “Random Forest” also had a low prediction accuracy of 0.60. The “AdaBoost,” “Nearest Neighbors,” and “Neural Network” had an accuracy of 0.60, 0.65, and 0.62, respectively.

Classification methods	Prediction accuracy
“Neural Network”	0.62
“Support Vector Machine”	0.62
“Random Forest”	0.60
“AdaBoost”	0.60
“Nearest Neighbors”	0.65
“Decision Tree”	<b>0.78</b>

plings. The overall prediction accuracy of the trained model was 0.78. The model had poor performance when the SWP was low. Perhaps the difference between features was minimal when the SWP was at this low level and could not be detected. Another reason might be the performance of the “Decision Tree” classifier. Further study needed to be conducted to find better algorithms for SWP detection. The dataset was also very small. More data will be collected and added to train a more robust model for SWP detection.

## 11.4 Conclusion and Future Work

The detection of walnut SWP is important in the walnut industry for management decision support. In this study, a proximate sensor was used to classify different walnut SWP levels. By using the “Decision Tree” classifier, the Walabot could classify the walnut SWP levels with an accuracy of 78%. As a cutting-edge technology for radio sensing, the sensor could be used flexibly in walnut orchards and provided accurate data information. In the future, more data will be collected for training the model. With more data from the walnut trees, more training data will hypothetically improve the accuracy of the model.

Table 11.4: The “Decision Trees” performance on SWP prediction. In the analysis as “Decision Tree” for the SWP Level 1, the trained model predicted the test data was in the range of Level 3. Therefore, the prediction accuracy (F1-score) of Level 1 was zero. The model successfully classified 22 out of 25 samplings in Level 2. For the Level 2, the model had performance with an F1-score of 0.92. For the Level 3, the model classified 9 out of 10 samplings. The overall prediction accuracy of the trained model was 0.78.

SWP levels	Precision	Recall	F1-score
Level 1	0	0	0
Level 2	0.96	0.88	0.92
Level 3	0.53	0.90	0.67
Accuracy	NA	NA	<b>0.78</b>
Macro avg	0.50	0.59	0.53
Weighted avg	0.73	0.78	0.74

# Chapter 12

## A Low-cost Soil Moisture Monitoring Method by Using Walabot and Machine Learning Algorithms

### 12.1 Introduction

In [503], Engman *et al.* defined soil moisture as the temporary storage of precipitation within a shallow layer of the earth. The soil moisture plays an important role in hydrological applications, such as agriculture [24], climate change [504], and meteorology [505]. For example, the data analysis from soil moisture monitoring can be used for crop yield estimation, irrigation treatment inference [27], and warning of drought [503]. Soil moisture monitoring can also be applied for pest management [506] and evapotranspiration estimation [142]. Therefore, it is important to monitor the soil moisture accurately. Typically, there are two types of methods for monitoring the soil moisture, proximate sensing and remote sensing.

Proximate sensing methods for soil moisture are currently restricted to point-specific measurements [507]. For example, researchers usually put the soil moisture

probes in the test field for monitoring. However, these discrete measurements can not represent the spatial and temporal soil moisture distribution for the whole field.

With the development of remote sensing technology, the satellite has been widely used for soil moisture remote sensing [508]. Many researchers have proved that optical and thermal remote sensing can be used for soil moisture measurements. For example, in [509], Wang *et al.* proposed the normalized multiband drought index (NMDI) for remotely sensing the soil based on the soil spectral characteristic. Since variations of soil moisture have a significant influence on soil surface temperature [510], thermal infrared remote sensing is also used for measuring the soil temperature to correlate it with soil moisture. Active and passive microwave remote sensing techniques are also commonly used for soil moisture measurements [511]. For passive microwave sensors, they can measure the intensity of microwave emission from the soil, which is proportional to the brightness temperature, a product of the surface temperature and emissivity [507, 512]. However, there are disadvantages to these methods. Limited surface penetration can be a problem both for optical and thermal remote sensing. Cloud contamination can be another issue [507]. The data acquired from the microwave has a low spatial resolution.

Therefore, in this study, the author proposed a new low-cost (less than \$1000) soil moisture monitoring method by using a Walabot sensor and machine learning algorithms. Walabot is a pocket-sized device and cutting-edge technology for Radio Frequency tridimensional sensing, which has already been used in many research topics, such as nematodes detection [334], and battery voltage detection [336]. It can work flexibly in the field and provide data information accurately than remote sensing methods with machine learning algorithms. First, the sensor was used to collect radio frequency reflectance of sampling soil, which could detect the physical structure of the soil moisture. Second, the collected data were pre-processed by data enhancement or a wavelet transform. Third, processed data was used by PCA [513] and LDA [514] for analysis. Results showed that the Walabot successfully classified the different levels of soil moisture with a state-of-art

performance. Moreover, with the development of wireless technology and micro-electromechanical systems, and computer vision, we might even use the Walabot to recognize real-time soil moisture monitoring in future research.

## 12.2 Material and Methods

### 12.2.1 Study Site

This research was conducted at Mechatronics, Embedded Systems and Automation (MESA) Lab in Atwater, California, USA (37.37°N, 120.57°W).

### 12.2.2 The Proximate Sensor

The sensor being used was Walabot Developer (Vayyar Imaging Ltd), as shown in Fig. 12.1. Based on the technical specs [484], the Walabot can sense the environment by transmitting, receiving, and recording signals from multiple antennas. Multiple transmit-receive antenna pairs' recordings are analyzed to build a 3D image of the environment. Then, researchers can detect changes in the environment by analyzing the sequences of images. The sensor is also capable of short-range imaging into dielectric environments, such as drywall and concrete. Therefore, it can be used in many study areas as follows:

1. In room/wall imaging.
2. Object detection, location and tracking.
3. Speed measurement and motion sensing.
4. Dielectric properties of materials sensing.

### 12.2.3 The Experiment Setup

In this study, the author used Walabot to detect different levels of soil moisture. The experiment was conducted in the MESA Lab. The soil was sampled in an almond field near the lab and was divided into 3 cups, as shown in Fig. 12.1. All the soil samplings were from the same spot in the almond field to make sure they are homogeneous. The soil was dried out to make sure all the 3 cups of soil were

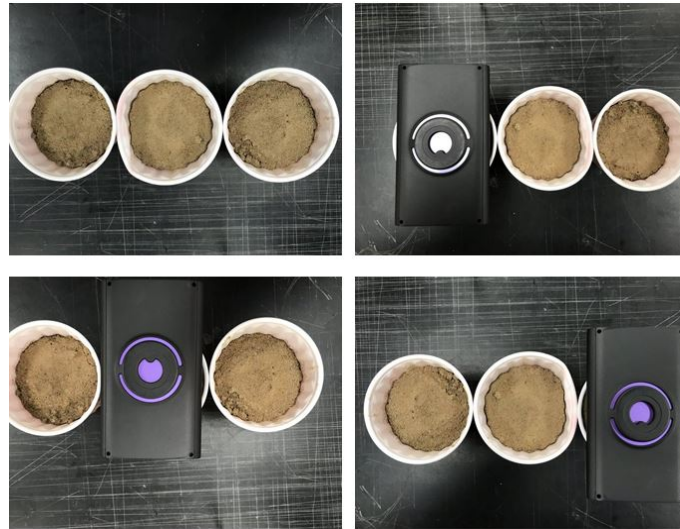


Figure 12.1: Walabot data collection. The experiment was conducted in the MESA Lab. The soil was sampled in an almond field near the lab and was divided into 3 cups.

at the same lowest moisture level. The weights of three cups of dry soil were 632 grams, 630 grams, and 634 grams. 6 g or 8 g water was added in every cup each time (10 times in total) to increase the soil moisture until the soil moisture was saturated, as shown in Table 12.1.

#### 12.2.4 Data Collection and Processing

The Walabot was used to measure the soil moisture every time after the water was added. Each measurement by the Walabot was repeated ten times to reduce the likelihood of errors or anomalous results so that it could increase the confidence interval. For image processing, the author used two different machine learning methods, the Principal Component Analysis (PCA) and Linear Discriminant Analysis (LDA). Both of them could reduce the dimensionality of the datasets and increase the classification accuracy. More details about PCA and LDA definitions can be found in Chapter 4.

Table 12.1: Soil samplings. All the soil samplings were from the same spot in the almond field to make sure they are homogeneous. The soil was dried out to make sure all the 3 cups of soil were at the same lowest moisture level. The weights of three cups of dry soil were 632 grams, 630 grams, and 634 grams. 6 g or 8 g water was added in every cup each time (10 times in total) to increase the soil moisture until the soil moisture was saturated

Soil condition	Soil sample 1	Soil sample 2	Soil sample 3
Dry	632g	630g	634g
1	640g	638g	642g
2	648g	646g	648g
3	654g	652g	656g
4	660g	660g	664g
5	668g	668g	670g
6	676g	674g	678g
7	682g	682g	686g
8	690g	690g	692g
9	696g	696g	700g
10 (Saturated)	704g	704g	708g

## 12.3 Results and Discussion

Each radio frequency reflectance image was converted into a 2048-dimension vector for data processing. The data was distributed as 67% for training and 33% for testing. Since the dataset was small for training eleven classifiers, the author distributed the eleven soil conditions into five different levels from dry to saturation. As shown in Fig. 12.2 and Fig. 12.3, “Dry” meant the dry soil. “WetTotal” stood for the saturated soil. Soil conditions 1, 2, and 3 were included in “Wet1”. “Wet2” contained the soil conditions 4, 5, and 6. “Wet3” included the soil conditions 7, 8, and 9.

Several classifiers in scikit-learn were used for comparison, such as “Nearest Neighbors,” “Linear SVM,” “RBF SVM,” “Gaussian Process,” “Decision Tree,” “Random Forest,” “Neural Net,” “AdaBoost,” “Naive Bayes,” and “QDA”. In this soil moisture monitoring problem, the accuracy of these classifiers was shown in Table 12.2. The best classifiers were “Nearest Neighbors,” “Gaussian Process,” “Decision Tree,” “Random Forest,” “Neural Net,” and “Naive Bayes” with an accuracy of 95%. The “QDA” was with 90% accuracy. The “Linear SVM” and “AdaBoost” were worst with 55% accuracy.

Scikit-learn’s accuracy classification score function evaluated the performance of the classifiers. This function computed the subset accuracy, in which the labels predicted for sampling must exactly match the corresponding true labels. Estimators used this score method as the evaluation criterion for the classification problems. All scorer objects followed the convention that higher return values were better than lower return values.

### 12.3.1 The Linear Discriminant Analysis Performance

Several LDA methods were used for soil moisture classification, as shown in Table 12.3. `decision_function(X)` was for predicting confidence scores of soil samples. `fit(X, y[, store_covariance, tol])` was for fitting the LDA model according to the given soil images training data and parameters. `fit_transform(X[, y])` was for fitting data and transform it. `get_params([deep])` was used for setting param-

Table 12.2: The classifier accuracy. The best classifiers were “Nearest Neighbors,” “Gaussian Process,” “Decision Tree,” “Random Forest,” “Neural Net,” and “Naive Bayes” with an accuracy of 95%. The “QDA” was with 90% accuracy. The “Linear SVM” and “AdaBoost” were worst with 55% accuracy.

Classifiers	Accuracy
“Nearest Neighbors”	0.95
“Linear SVM”	0.40
“RBF SVM”	0.95
“Gaussian Process”	0.95
“Decision Tree”	0.95
“Random Forest”	0.95
“Neural Net”	0.95
“AdaBoost”	0.55
“Naive Bayes”	0.95
“QDA”	0.90

Table 12.3: The LDA Methods. Several LDA methods were used for soil moisture classification.

Methods
decision_function(X)
fit(X, y[, store_covariance, tol])
fit_transform(X[, y])
get_params([deep])
predict(X)
predict_log_proba(X)
predict_proba(X)
score(X, y[, sample_weight])
set_params(**params)
transform(X)

eters for the estimator. Then, `predict(X)` could predict the class labels for soil samples. `predict_log_proba(X)` and `predict_proba(X)` could estimate the probability. Finally, `score(X, y[, sample_weight])` could return the mean accuracy on the given soil images test data and labels. `set_params(**params)` was for setting estimator parameters. `transform(X)` was for projecting data to maximize soil class separation.

The performance of the LDA for soil moisture monitoring was shown in Fig. 12.2. There were five different soil moisture levels with different colors, “Dry,” “Wet1,” “Wet2,” “Wet3,” and “WetTotal”, which meant the soil sampling was saturated. LDA classifiers firstly reduced the original dimension to 2 components. As seen from Fig. 12.2, different colors meant different soil moisture levels and the axes of the figure were dimensionless. The LDA could classify the five different levels of soil moisture in different areas of the coordinate, so that the LDA could classify the soil moisture with an state-of-art performance.

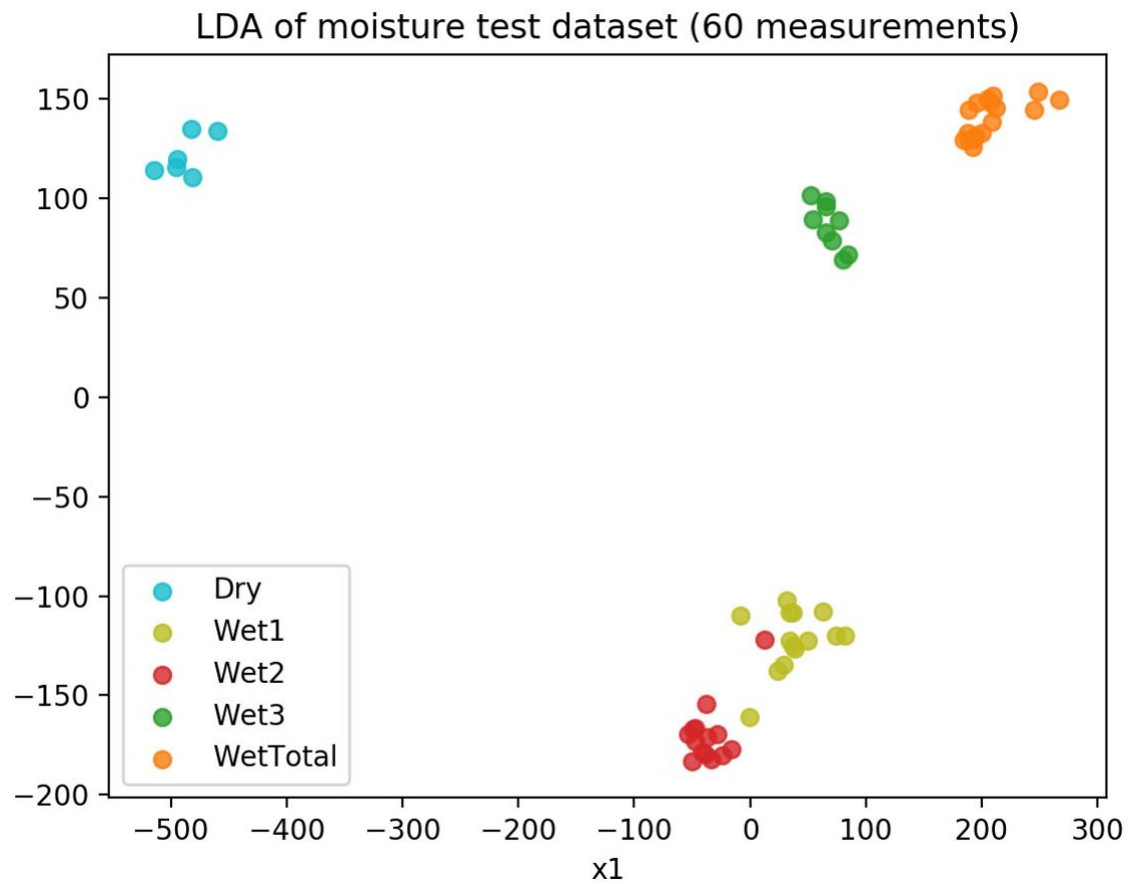


Figure 12.2: LDA results for soil moisture measurement. There were five different soil moisture levels with different colors, “Dry,” “Wet1,” “Wet2,” “Wet3,” and “WetTotal”, which meant the soil sampling was saturated. LDA classifiers firstly reduced the original dimension to 2 components. Different colors meant different soil moisture levels and the axes of the figure were dimensionless. The LDA could classify the five different levels of soil moisture in different areas of the coordinate, so that the LDA could classify the soil moisture with an state-of-art performance.

Table 12.4: The PCA Methods.

Methods
<code>fit(self, X[, y])</code>
<code>fit_transform(self, X[, y])</code>
<code>get_covariance(self)</code>
<code>get_params(self[,deep])</code>
<code>get_precision(self)</code>
<code>inverse_transform(self, X)</code>
<code>score(self, X[, y])</code>
<code>score_samples(self, X)</code>
<code>set_params(self, params)</code>
<code>transform(self, X)</code>

### 12.3.2 The Principal Component Analysis Performance

In PCA methods, `fit(self, X[, y])` was to fit the model with the input soil images data  $X$ . `fit_transform(self, X[, y])` was for fitting the model with  $X$  and apply the dimensionality reduction on  $X$ . `get_covariance(self)` was for computing the data covariance with the generative model. `get_params(self[,deep])` was to get parameters for the estimator. `get_precision(self)` was for computing the data precision matrix with the generative model. Then, `inverse_transform(self, X)` could transform the data back to its original space. Finally, `score(self, X[, y])` could return the average log-likelihood of all samples. `score_samples(self, X)` could return the log-likelihood of each sample. `set_params(self, params)` could help set the parameters of the estimator. `transform(self, X)` was being used for applying dimensionality reduction to soil images input.

In Fig. 12.3, PCA could also classify the soil moisture successfully but not entirely. As shown in Fig. 12.3, “WetTotal” points were on the left and right sides of the image. The “Wet3” and “Wet2” data points did not drop in the same area. The reason might be that the PCA could not detect the features difference from the

data. Similar to LDA, the PCA classifiers firstly reduced the original dimension to 2 components. Then, each classifier was tested against reduced dimensionality data with the component as 2. Results showed that LDA performs much better than the PCA method.

## 12.4 Conclusion and Future Research

Soil moisture monitoring is essential in precision agriculture, which has a significant effect on crop evapotranspiration, the exchange of water, and energy fluxes. Soil moisture can be measured by many remote sensing or proximate sensing techniques, such as thermal, optical, and microwave measurements. However, there are limiting factors for the applications of these methods, such as low spatial resolution, limited surface penetration and vegetation. In this study, the author used a portable sensor to classify different soil moisture successfully. By using the PCA and LDA machine learning methods, the Walabot could recognize small changes in different levels of soil moisture and could detect soil moisture difference with a state-of-art performance. As a pocket-sized device cutting-edge technology for radio frequency tridimensional sensing, the author believes the sensor can work flexibly in the field and provide data information more promptly and accurately than traditional remote sensing or proximate sensing method.

So far, the Walabot can only detect the difference in soil moisture. In the future, the author will compare it with different soil moisture sensors to see if one can find the regression model and quantify the soil moisture measurements by using the Walabot. With the development of wireless technology, and computer vision, it might be able to be mounted on UGVs for proximate sensing [250, 515]. Thus, we can use the sensor to recognize real-time soil moisture monitoring.

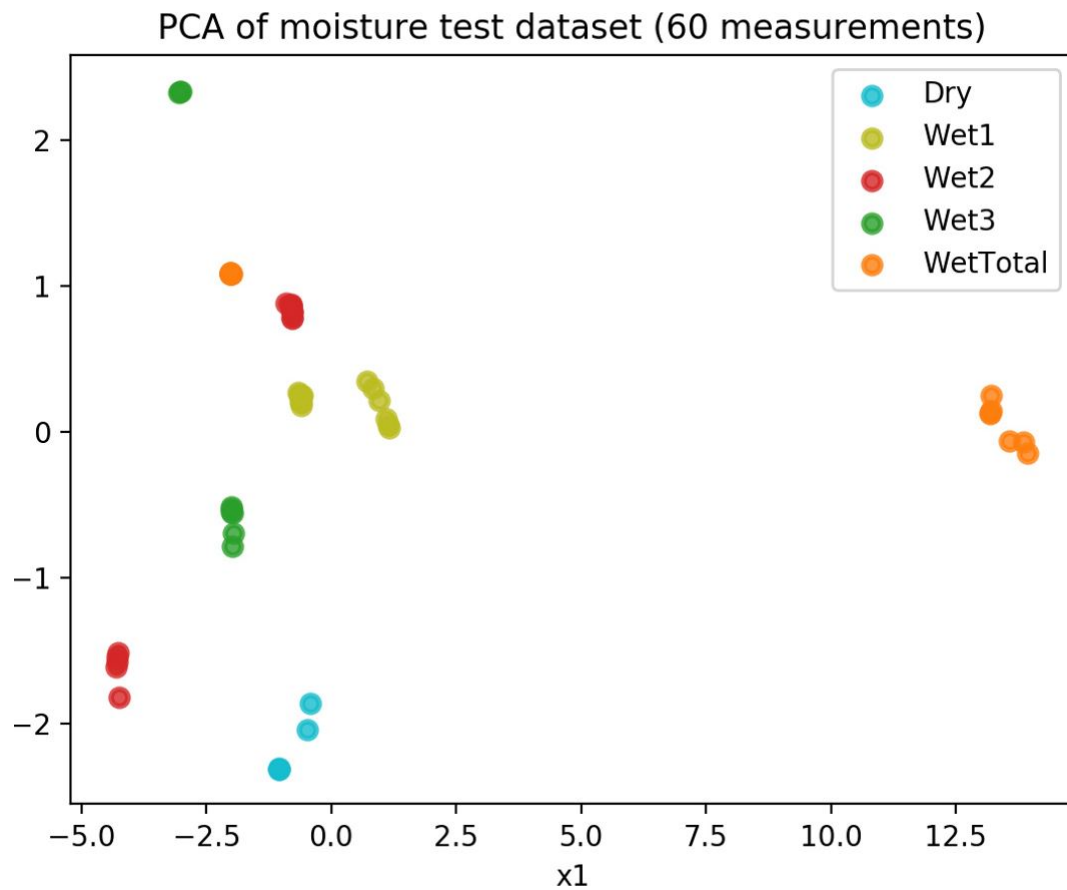


Figure 12.3: PCA results for soil moisture measurement. “WetTotal” points were on the left and right sides of the image. The “Wet3” and “Wet2” data points did not drop in the same area. The reason might be that the PCA could not detect the features difference from the data. Similar to LDA, the PCA classifiers firstly reduced the original dimension to 2 components. Then, each classifier was tested against reduced dimensionality data with the component as 2.

# Chapter 13

## Conclusions and Future Research

### 13.1 Concluding Remarks

This dissertation presented the concept and importance of smart big data towards precision agricultural applications. Smart big data restructures and enhances the dataset that AI and ML algorithms use. In this dissertation, the smart big data acquisition platforms were introduced, such as small UAVs and Edge-AI sensors. Smart big data cleans and transforms the data into useful information that is valuable and relevant to crops and trees growing status.

In this dissertation, the concept of plant physiology-informed machine learning and how to use advanced analytics and fractional-order thinking to make contributions are proposed in Chapter 1 and Chapter 2. Smart big data acquisition platforms are mainly discussed. A UAV platform for remote sensing data collection and a reliable image processing workflow are proposed. The challenges and opportunities for UAV image processing are also discussed in Chapter 3. In Chapter 4, the concept of IoLT is proposed and several proximate sensors are introduced. The potential of UGV platforms for agriculture is briefly discussed in Chapter 5.

In Chapter 6, a non-invasive proximate sensing method for early detection of nematodes was proposed. Microwave reflectance from walnut leaves was analyzed using ML algorithms to classify the nematode infection levels in the walnut roots. In Chapter 7, reliable tree-level ET estimation methods were proposed using the UAV high-resolution imagery, ML algorithms and platforms, such as

Python, MATLAB, Pytorch, and TensorFlow. In Section 7.4, the author proposes to estimate crop coefficient with UAV-based imagery and the SCN model. Then, the reliable tree-level ET estimation methods are proposed in Section 7.5. In Chapter 8, individual tree-level water status inference was performed using the high-resolution UAV thermal imagery and complexity-informed machine learning. The performance of the CNN model on irrigation treatment inference is demonstrated. In Chapter 9, a scale-aware pomegranate yield prediction method using UAV imagery and machine learning was proposed. Predicting the yield at the individual tree level will enable the stakeholders to manage the orchard at different scales, thus improving the field management efficiency. Then, an intelligent bugs mapping and wiping robot for farmers is discussed in Chapter 10, which has great potential for pest management in the future. A non-invasive stem water potential monitoring method using proximate sensor and ML algorithms for a walnut orchard is proposed in Chapter 11 and a low-cost soil moisture monitoring method is proposed in Chapter 12.

Smart big data is the use of various methods, such as ML algorithms and artificial intelligence, to analyze and transform the agricultural data into information from which valuable insight can be drawn. It incorporates advanced analytics to enhance plant physiology-informed machine learning. The application of smart big data can help researchers and stakeholders develop a better understanding of the data with the goal of developing better precision agriculture. So far, these are still the initial steps for the development of the smart big data applications in precision agriculture. More explicit definition of the steps of the smart big data framework integrated with advanced analytics, ML algorithms, and AI is required to demonstrate the capabilities of this innovative methodology.

## **13.2 Future Research Towards Smart Big Data in Precision Agricultural Applications**

Based on the research presented, a comprehensive work has been done towards the smart big data in precision agricultural applications. There is still plenty of

work. Thus, the future research plans will be:

- Further investigate the necessity of smart big data and the correlation between smart big data, machine learning, and plant physiology.
- Design and test a UGV platform for agricultural applications, such as pest management.
- Develop an intelligent bugs mapping and wiping system using UGVs for pest management.
- Evaluate the remote sensing methods of early detection of nematode using small UAVs and lightweight sensors, such as SWIR, TIR and multispectral cameras.
- Combine the proximate sensing methods and remote sensing methods to generate a comprehensive framework for early detection of nematodes.
- Develop a computer vision-based nematode counting and segmentation method using ML algorithms for nematode image processing.
- Investigate TSEB and DTD methods for reliable tree-level ET estimation using small UAVs and remote sensing sensors.
- Demonstrate the importance of spatial and temporal analysis for tree-level yield estimation using small UAVs and remote sensing sensors.
- Develop a robust and adaptive individual tree-level irrigation treatment inference system using high-resolution UAV thermal imagery and complexity-informed machine learning.
- Define and implement the concept of complexity-informed machine learning and principle of tail matching with Edge-AI sensors for more agricultural applications, such as soil moisture monitoring and stem water potential measurement.
- Further improve the concept of IoLT and demonstrate its key role with ML and Edge-AI sensors.

# Bibliography

- [1] M. Hilbert and P. López, “The world’s technological capacity to store, communicate, and compute information,” *Science*, vol. 332, no. 6025, pp. 60–65, 2011.
- [2] J. S. Ward and A. Barker, “Undefined by data: A survey of big data definitions,” *arXiv preprint arXiv:1309.5821*, 2013.
- [3] D. Reinsel, J. Gantz, and J. Rydning, “Data Age 2025: The evolution of data to life-critical,” *Don’t Focus on Big Data*, pp. 2–24, 2017.
- [4] G. Firican, “The 10 Vs of Big Data.” <https://tdwi.org/articles/2017/02/08/10-vs-of-big-data.aspx>, 2017.
- [5] H. Zhang, X. Wei, T. Zou, Z. Li, and G. Yang, “Agriculture big data: Research status, challenges and countermeasures,” in *International Conference on Computer and Computing Technologies in Agriculture*, pp. 137–143, Springer, 2014.
- [6] P. Maya-Gopal, B. R. Chintala, *et al.*, “Big data challenges and opportunities in agriculture,” *International Journal of Agricultural and Environmental Information Systems*, vol. 11, no. 1, pp. 48–66, 2020.
- [7] J. R. Mintert, D. Widmar, M. Langemeier, M. Boehlje, and B. Erickson, “The challenges of precision agriculture: Is big data the answer?,” tech. rep., Southern Agricultural Economics Association (SAEA) Annual Meeting, San Antonio, Texas, February 6-9, 2015, 2016.
- [8] Y. Nakahira, Q. Liu, T. J. Sejnowski, and J. C. Doyle, “Diversity-enabled sweet spots in layered architectures and speed-accuracy trade-offs in sensorimotor control,” *arXiv preprint arXiv:1909.08601*, 2019.
- [9] J. Arabas and K. Opara, “Population diversity of non-elitist evolutionary algorithms in the exploration phase,” *IEEE Transactions on Evolutionary Computation*, vol. 24, no. 6, pp. 1050–1062, 2019.

- [10] M. Ko, B. Stark, M. Barbadillo, and Y. Chen, "An evaluation of three approaches using Hurst estimation to differentiate between normal and abnormal HRV," in *Proceedings of the International Design Engineering Technical Conferences and Computers and Information in Engineering Conference*, American Society of Mechanical Engineers, 2015.
- [11] N. Li, J. Cruz, C. S. Chien, S. Sojoudi, B. Recht, D. Stone, M. Csete, D. Bahmiller, and J. C. Doyle, "Robust efficiency and actuator saturation explain healthy heart rate control and variability," *Proceedings of the National Academy of Sciences*, vol. 111, no. 33, pp. E3476–E3485, 2014.
- [12] H. Niu, Y. Chen, and B. J. West, "Why do big data and machine learning entail the fractional dynamics?," *Entropy*, vol. 23, no. 3, p. 297, 2021.
- [13] A. Sourav and A. Emanuel, "Recent trends of big data in precision agriculture: A review," in *IOP Conference Series: Materials Science and Engineering*, vol. 1096, p. 012081, IOP Publishing, 2021.
- [14] J. Granda-Cantuna, C. Molina-Colcha, S.-E. Hidalgo-Lupera, and C.-D. Valarezo-Varela, "Design and implementation of a wireless sensor network for precision agriculture operating in API mode," in *2018 International Conference on eDemocracy & eGovernment (ICEDEG)*, pp. 144–149, IEEE, 2018.
- [15] S. Rajeswari, K. Suthendran, and K. Rajakumar, "A smart agricultural model by integrating IoT, mobile and cloud-based big data analytics," in *2017 International Conference on Intelligent Computing and Control (I2C2)*, pp. 1–5, IEEE, 2017.
- [16] P. Zhang, Q. Zhang, F. Liu, J. Li, N. Cao, and C. Song, "The construction of the integration of water and fertilizer smart water saving irrigation system based on big data," in *2017 IEEE International Conference on Computational Science and Engineering (CSE) and IEEE International Conference on Embedded and Ubiquitous Computing (EUC)*, vol. 2, pp. 392–397, IEEE, 2017.
- [17] C. Li and B. Niu, "Design of smart agriculture based on big data and Internet of things," *International Journal of Distributed Sensor Networks*, vol. 16, no. 5, p. 1550147720917065, 2020.
- [18] F.-H. Tseng, H.-H. Cho, and H.-T. Wu, "Applying big data for intelligent agriculture-based crop selection analysis," *IEEE Access*, vol. 7, pp. 116965–116974, 2019.
- [19] R. Kaur, R. Garg, and H. Aggarwal, "Big data analytics framework to identify crop disease and recommendation a solution," in *2016 International Conference on Inventive Computation Technologies (ICICT)*, vol. 2, pp. 1–5, IEEE, 2016.

- [20] A. Géron, *Hands-on Machine Learning with Scikit-Learn, Keras, and TensorFlow: Concepts, Tools, and Techniques to Build Intelligent Systems*. O'Reilly Media, 2019.
- [21] T. M. Mitchell, *Machine Learning*. McGraw-hill New York, 1997.
- [22] G. E. Hinton, S. Osindero, and Y. W. Teh, “A fast learning algorithm for deep belief nets,” *Neural Computation*, vol. 18, no. 7, pp. 1527–1554, 2006.
- [23] T. Zhao, Y. Yang, H. Niu, D. Wang, and Y. Chen, “Comparing U-Net convolutional network with mask R-CNN in the performances of pomegranate tree canopy segmentation,” in *Multispectral, Hyperspectral, and Ultraspectral Remote Sensing Technology, Techniques and Applications VII*, International Society for Optics and Photonics, 2018.
- [24] T. Zhao, A. Koumis, H. Niu, D. Wang, and Y. Chen, “Onion irrigation treatment inference using a low-cost hyperspectral scanner,” in *Multispectral, Hyperspectral, and Ultraspectral Remote Sensing Technology, Techniques and Applications VII*, vol. 10780, p. 107800D, International Society for Optics and Photonics, 2018.
- [25] J. Hirschberg and C. D. Manning, “Advances in natural language processing,” *Science*, vol. 349, no. 6245, pp. 261–266, 2015.
- [26] T. Zhao, H. Niu, E. de la Rosa, D. Doll, D. Wang, and Y. Chen, “Tree canopy differentiation using instance-aware semantic segmentation,” in *2018 ASABE Annual International Meeting*, American Society of Agricultural and Biological Engineers, 2018.
- [27] H. Niu, T. Zhao, D. Wang, and Y. Chen, “A UAV resolution and waveband aware path planning for onion irrigation treatments inference,” in *2019 International Conference on Unmanned Aircraft Systems (ICUAS)*, pp. 808–812, IEEE, 2019.
- [28] H. Niu, D. Wang, and Y. Chen, “Estimating actual crop evapotranspiration using deep stochastic configuration networks model and UAV-based crop coefficients in a pomegranate orchard,” in *Autonomous Air and Ground Sensing Systems for Agricultural Optimization and Phenotyping V*, International Society for Optics and Photonics, 2020.
- [29] B. J. West, E. L. Geneston, and P. Grigolini, “Maximizing information exchange between complex networks,” *Physics Reports*, vol. 468, no. 1-3, pp. 1–99, 2008.
- [30] B. J. West, “Sir Isaac Newton stranger in a strange land,” *Entropy*, vol. 22, no. 11, p. 1204, 2020.

- [31] B. J. West and P. Grigolini, *Complex Webs: Anticipating the Improbable*. Cambridge University Press, 2010.
- [32] A. L. Barabási and R. Albert, “Emergence of scaling in random networks,” *Science*, vol. 286, no. 5439, pp. 509–512, 1999.
- [33] W. Sun, Y. Li, C. Li, and Y. Chen, “Convergence speed of a fractional order consensus algorithm over undirected scale-free networks,” *Asian Journal of Control*, vol. 13, no. 6, pp. 936–946, 2011.
- [34] B. Pesquet-Popescu and J. C. Pesquet, “Synthesis of bidimensional  $\alpha$ -stable models with long-range dependence,” *Signal Processing*, vol. 82, no. 12, pp. 1927–1940, 2002.
- [35] M. Li, “Modeling autocorrelation functions of long-range dependent teletraffic series based on optimal approximation in Hilbert space—A further study,” *Applied Mathematical Modelling*, vol. 31, no. 3, pp. 625–631, 2007.
- [36] Z. Zhao, Q. Guo, and C. Li, “A fractional model for the allometric scaling laws,” *The Open Applied Mathematics Journal*, vol. 2, no. 1, pp. 26–30, 2008.
- [37] H. Sun, Y. Chen, and W. Chen, “Random-order fractional differential equation models,” *Signal Processing*, vol. 91, no. 3, pp. 525–530, 2011.
- [38] R. Metzler and J. Klafter, “The random walk’s guide to anomalous diffusion: A fractional dynamics approach,” *Physics Reports*, vol. 339, no. 1, pp. 1–77, 2000.
- [39] B. M. Vinagre and Y. Chen, “Lecture notes on fractional calculus applications in automatic control and robotics,” in *Proceedings of the 41st IEEE CDC Tutorial Workshop*, vol. 2, pp. 1–310, 2002.
- [40] D. Valério, J. Machado, and V. Kiryakova, “Some pioneers of the applications of fractional calculus,” *Fractional Calculus and Applied Analysis*, vol. 17, no. 2, pp. 552–578, 2014.
- [41] N. Abel, “Solution of a couple of problems by means of definite integrals,” *Magazin for Naturvidenskaberne*, vol. 2, no. 55, p. 2, 1823.
- [42] I. Podlubny, R. L. Magin, and I. Trymorush, “Niels Henrik Abel and the birth of fractional calculus,” *Fractional Calculus and Applied Analysis*, vol. 20, no. 5, pp. 1068–1075, 2017.
- [43] B. Ross, “The development of fractional calculus 1695–1900,” *Historia Mathematica*, vol. 4, no. 1, pp. 75–89, 1977.

- [44] V. E. Tarasov, *Fractional Dynamics: Applications of Fractional Calculus to Dynamics of Particles, Fields and Media*. Springer Science & Business Media, 2011.
- [45] J. Klafter, S. Lim, and R. Metzler, *Fractional Dynamics: Recent Advances*. World Scientific, 2012.
- [46] P. Pramukul, A. Svenkeson, P. Grigolini, M. Bologna, and B. West, “Complexity and the fractional calculus,” *Advances in Mathematical Physics*, vol. 2013, pp. 1–7, 2013.
- [47] D. Chen, D. Xue, and Y. Chen, “More optimal image processing by fractional order differentiation and fractional order partial differential equations,” in *Proceedings of the International Symposium on Fractional PDEs*, 2013.
- [48] D. Chen, S. Sun, C. Zhang, Y. Chen, and D. Xue, “Fractional-order TV-L2 model for image denoising,” *Central European Journal of Physics*, vol. 11, no. 10, pp. 1414–1422, 2013.
- [49] Q. Yang, D. Chen, T. Zhao, and Y. Chen, “Fractional calculus in image processing: A review,” *Fractional Calculus and Applied Analysis*, vol. 19, no. 5, pp. 1222–1249, 2016.
- [50] V. Seshadri and B. J. West, “Fractal dimensionality of Lévy processes,” *Proceedings of the National Academy of Sciences of the United States of America*, vol. 79, no. 14, p. 4501, 1982.
- [51] R. Metzler, W. G. Glöckle, and T. F. Nonnenmacher, “Fractional model equation for anomalous diffusion,” *Physica A: Statistical Mechanics and its Applications*, vol. 211, no. 1, pp. 13–24, 1994.
- [52] H. Sheng, Y. Chen, and T. Qiu, *Fractional Processes and Fractional-order Signal Processing: Techniques and Applications*. Springer Science & Business Media, 2011.
- [53] B. B. Mandelbrot and J. R. Wallis, “Robustness of the rescaled range  $r/s$  in the measurement of noncyclic long run statistical dependence,” *Water Resources Research*, vol. 5, no. 5, pp. 967–988, 1969.
- [54] J. Geweke and S. Porter-Hudak, “The estimation and application of long memory time series models,” *Journal of Time Series Analysis*, vol. 4, no. 4, pp. 221–238, 1983.
- [55] K. Liu, Y. Chen, and X. Zhang, “An evaluation of ARFIMA (autoregressive fractional integral moving average) programs,” *Axioms*, vol. 6, no. 2, p. 16, 2017.

- [56] E. W. Montroll and G. H. Weiss, “Random walks on lattices. II,” *Journal of Mathematical Physics*, vol. 6, no. 2, pp. 167–181, 1965.
- [57] K. G. Liakos, P. Busato, D. Moshou, S. Pearson, and D. Bochtis, “Machine learning in agriculture: A review,” *Sensors*, vol. 18, no. 8, p. 2674, 2018.
- [58] Y. Nesterov, “A method for unconstrained convex minimization problem with the rate of convergence  $O(1/k^2)$ ,” *Doklady Akademii Nauk, Russian Academy of Sciences*, vol. 269, pp. 543–547, 1983.
- [59] L. A. Zadeh, “Fuzzy logic,” *Computer*, vol. 21, no. 4, pp. 83–93, 1988.
- [60] M. Unser and T. Blu, “Fractional splines and wavelets,” *SIAM Review*, vol. 42, no. 1, pp. 43–67, 2000.
- [61] G. Samoradnitsky, *Stable non-Gaussian Random Processes: Stochastic Models with Infinite Variance*. Routledge, 2017.
- [62] M. E. Crovella and A. Bestavros, “Self-similarity in World Wide Web traffic: Evidence and possible causes,” *IEEE/ACM Transactions on Networking*, vol. 5, no. 6, pp. 835–846, 1997.
- [63] K. Burnecki and A. Weron, “Lévy stable processes. From stationary to self-similar dynamics and back. An application to finance,” *Acta Physica Polonica Series B*, vol. 35, no. 4, pp. 1343–1358, 2004.
- [64] T. T. Hartley and C. F. Lorenzo, “Fractional-order system identification based on continuous order-distributions,” *Signal Processing*, vol. 83, no. 11, pp. 2287–2300, 2003.
- [65] R. L. Wolpert and M. S. Taqqu, “Fractional Ornstein–Uhlenbeck Lévy processes and the telecom process: Upstairs and downstairs,” *Signal Processing*, vol. 85, no. 8, pp. 1523–1545, 2005.
- [66] G. Bahg, D. G. Evans, M. Galdo, and B. M. Turner, “Gaussian process linking functions for mind, brain, and behavior,” *Proceedings of the National Academy of Sciences*, vol. 117, no. 47, 2020.
- [67] M. Csete and J. Doyle, “Bow ties, metabolism and disease,” *Trends in Biotechnology*, vol. 22, no. 9, pp. 446–450, 2004.
- [68] J. Zhao, H. Yu, J.-H. Luo, Z.-W. Cao, and Y.-X. Li, “Hierarchical modularity of nested bow-ties in metabolic networks,” *BMC Bioinformatics*, vol. 7, no. 1, pp. 1–16, 2006.
- [69] J. Doyle, “Universal laws and architectures,” *CDS 212 Lect. Notes*, 2011.

- [70] J. C. Doyle and M. Csete, “Architecture, constraints, and behavior,” *Proceedings of the National Academy of Sciences*, vol. 108, no. Supplement 3, pp. 15624–15630, 2011.
- [71] H. Sheng, Y. Q. Chen, and T. Qiu, “Heavy-tailed distribution and local long memory in time series of molecular motion on the cell membrane,” *Fluctuation and Noise Letters*, vol. 10, no. 01, pp. 93–119, 2011.
- [72] T. Graves, R. Gramacy, N. Watkins, and C. Franzke, “A brief history of long memory: Hurst, mandelbrot and the road to ARFIMA, 1951–1980,” *Entropy*, vol. 19, no. 9, p. 437, 2017.
- [73] C. T. Kello, G. D. Brown, R. Ferrer Cancho, J. G. Holden, K. Linkenkaer Hansen, T. Rhodes, and G. C. Van Orden, “Scaling laws in cognitive sciences,” *Trends in Cognitive Sciences*, vol. 14, no. 5, pp. 223–232, 2010.
- [74] R. Gorenflo and F. Mainardi, “Fractional calculus and stable probability distributions,” *Archives of Mechanics*, vol. 50, no. 3, pp. 377–388, 1998.
- [75] F. Mainardi, “The fundamental solutions for the fractional diffusion-wave equation,” *Applied Mathematics Letters*, vol. 9, no. 6, pp. 23–28, 1996.
- [76] Y. Luchko, F. Mainardi, and Y. Povstenko, “Propagation speed of the maximum of the fundamental solution to the fractional diffusion–wave equation,” *Computers & Mathematics with Applications*, vol. 66, no. 5, pp. 774–784, 2013.
- [77] Y. Luchko and F. Mainardi, “Some properties of the fundamental solution to the signalling problem for the fractional diffusion-wave equation,” *Open Physics*, vol. 11, no. 6, pp. 666–675, 2013.
- [78] Y. Luchko and F. Mainardi, “Cauchy and signaling problems for the time-fractional diffusion-wave equation,” *Journal of Vibration and Acoustics*, vol. 136, no. 5, 2014.
- [79] E. W. Montroll and B. J. West, “On an enriched collection of stochastic processes,” *Fluctuation Phenomena*, vol. 66, p. 61, 1979.
- [80] Z. Li, L. Liu, S. Dehghan, Y. Chen, and D. Xue, “A review and evaluation of numerical tools for fractional calculus and fractional order controls,” *International Journal of Control*, vol. 90, no. 6, pp. 1165–1181, 2017.
- [81] S. Asmussen, “Steady-state properties of of  $GI/G/1$ ,” *Applied Probability and Queues*, pp. 266–301, 2003.

- [82] M. Bernardi and L. Petrella, “Interconnected risk contributions: A heavy-tail approach to analyze US financial sectors,” *Journal of Risk and Financial Management*, vol. 8, no. 2, pp. 198–226, 2015.
- [83] S. Ahn, J. H. Kim, and V. Ramaswami, “A new class of models for heavy tailed distributions in finance and insurance risk,” *Insurance: Mathematics and Economics*, vol. 51, no. 1, pp. 43–52, 2012.
- [84] S. I. Resnick, *Heavy-tail Phenomena: Probabilistic and Statistical Modeling*. Springer Science & Business Media, 2007.
- [85] T. Rolski, H. Schmidli, V. Schmidt, and J. L. Teugels, *Stochastic Processes for Insurance and Finance*, vol. 505. John Wiley & Sons, 2009.
- [86] S. Foss, D. Korshunov, and S. Zachary, *An Introduction to Heavy-tailed and Subexponential Distributions*, vol. 6. Springer, 2011.
- [87] H. Niu, Y. Chen, and Y. Chen, “Fractional-order extreme learning machine with Mittag-Leffler distribution,” in *International Design Engineering Technical Conferences and Computers and Information in Engineering Conference*, American Society of Mechanical Engineers, 2019.
- [88] Y. Hariya, T. Kurihara, T. Shindo, and K. Jin’no, “Lévy flight PSO,” in *Proceedings of the IEEE Congress on Evolutionary Computation (CEC)*, 2015.
- [89] X. S. Yang, *Nature-inspired Metaheuristic Algorithms*. Luniver Press, 2010.
- [90] X.-S. Yang and S. Deb, “Engineering optimisation by cuckoo search,” *International Journal of Mathematical Modelling and Numerical Optimisation*, vol. 1, no. 4, pp. 330–343, 2010.
- [91] H. J. Haubold, A. M. Mathai, and R. K. Saxena, “Mittag-Leffler functions and their applications,” *Journal of Applied Mathematics*, 2011. doi:10.1155/2011/298628.
- [92] K. Jayakumar, “Mittag-Leffler process,” *Mathematical and Computer Modelling*, vol. 37, no. 12-13, pp. 1427–1434, 2003.
- [93] J. Wei, Y. Chen, Y. Yu, and Y. Chen, “Improving cuckoo search algorithm with Mittag-Leffler distribution,” in *Proceedings of the International Design Engineering Technical Conferences and Computers and Information in Engineering Conference*, pp. 1–9, American Society of Mechanical Engineers, 2019.
- [94] H. Rinne, *The Weibull Distribution: A Handbook*. CRC Press, 2008.
- [95] N. L. Johnson, S. Kotz, and N. Balakrishnan, *Continuous Univariate Distributions*. John Wiley & Sons, Ltd, 1995.

- [96] W. Feller, *An Introduction to Probability Theory and its Application Vol II*. John Wiley and Sons, 1971.
- [97] T. Liu, P. Zhang, W.-S. Dai, and M. Xie, “An intermediate distribution between Gaussian and Cauchy distributions,” *Physica A: Statistical Mechanics and its Applications*, vol. 391, no. 22, pp. 5411–5421, 2012.
- [98] D. Bahat, A. Rabinovitch, and V. Frid, *Tensile Fracturing in Rocks*. Springer, 2005.
- [99] F. Geerolf, “A theory of Pareto distributions,” *UCLA Manuscript*, 2016.
- [100] B. Mandelbrot, “The Pareto-Lévy law and the distribution of income,” *International Economic Review*, vol. 1, no. 2, pp. 79–106, 1960.
- [101] M. Lévy and S. Solomon, “New evidence for the power-law distribution of wealth,” *Physica A: Statistical Mechanics and its Applications*, vol. 242, no. 1-2, pp. 90–94, 1997.
- [102] J. Lu and J. Ding, “Mixed-distribution-based robust stochastic configuration networks for prediction interval construction,” *IEEE Transactions on Industrial Informatics*, vol. 16, no. 8, pp. 5099–5109, 2019.
- [103] M. R. Spiegel, J. J. Schiller, and R. Srinivasan, *Probability and Statistics*. New York: McGraw-Hill, 2013.
- [104] E. L. Hutton, *Xunzi: The Complete Text*. Princeton University Press, 2014.
- [105] C. B. Boyer, *The History of the Calculus and its Conceptual Development: (The Concepts of the Calculus)*. Courier Corporation, 1959.
- [106] J. S. Bardi, *The Calculus Wars: Newton, Leibniz, and the Greatest Mathematical Clash of All Time*. Hachette UK, 2009.
- [107] R. I. Tanner and K. Walters, *Rheology: An Historical Perspective*. Elsevier, 1998.
- [108] Y. Chen, R. Sun, and A. Zhou, “An improved Hurst parameter estimator based on fractional fourier transform,” *Telecommunication Systems*, vol. 43, no. 3-4, pp. 197–206, 2010.
- [109] H. Sheng, H. Sun, Y. Chen, and T. Qiu, “Synthesis of multifractional Gaussian noises based on variable-order fractional operators,” *Signal Processing*, vol. 91, no. 7, pp. 1645–1650, 2011.

- [110] R. Sun, Y. Chen, N. Zaveri, and A. Zhou, “Local analysis of long range dependence based on fractional Fourier transform,” in *Proceedings of the IEEE Mountain Workshop on Adaptive and Learning Systems*, pp. 13–18, IEEE, 2006.
- [111] V. Pipiras and M. S. Taqqu, *Long-range Dependence and Self-similarity*, vol. 45. Cambridge University Press, 2017.
- [112] G. Samorodnitsky, “Long range dependence,” *Wiley StatsRef: Statistics Reference Online*, 2014.
- [113] J. A. Gubner, *Probability and Random Processes for Electrical and Computer Engineers*. Cambridge University Press, 2006.
- [114] R. G. Clegg, “A practical guide to measuring the Hurst parameter,” *arXiv preprint math/0610756*, 2006.
- [115] L. Decreusefond, “Stochastic analysis of the fractional Brownian motion,” *Potential Analysis*, vol. 10, no. 2, pp. 177–214, 1999.
- [116] D. Koutsoyiannis, “The Hurst phenomenon and fractional Gaussian noise made easy,” *Hydrological Sciences Journal*, vol. 47, no. 4, pp. 573–595, 2002.
- [117] B. B. Mandelbrot and J. W. Van Ness, “Fractional Brownian motions, fractional noises and applications,” *SIAM Review*, vol. 10, no. 4, pp. 422–437, 1968.
- [118] M. D. Ortigueira and A. G. Batista, “On the relation between the fractional Brownian motion and the fractional derivatives,” *Physics Letters A*, vol. 372, no. 7, pp. 958–968, 2008.
- [119] Y. Chen, R. Sun, and A. Zhou, “An overview of fractional order signal processing (FOSP) techniques,” in *Proceedings of the International Design Engineering Technical Conferences and Computers and Information in Engineering Conference*, 2007.
- [120] K. Liu, P. D. Domański, and Y. Chen, “Control performance assessment with fractional lower order moments,” in *Proceedings of the 7th International Conference on Control, Decision and Information Technologies (CoDIT)*, vol. 1, pp. 778–783, IEEE, 2020.
- [121] G. Cottone and M. Di Paola, “On the use of fractional calculus for the probabilistic characterization of random variables,” *Probabilistic Engineering Mechanics*, vol. 24, no. 3, pp. 321–330, 2009.
- [122] G. Cottone, M. Di Paola, and R. Metzler, “Fractional calculus approach to the statistical characterization of random variables and vectors,” *Physica A: Statistical Mechanics and its Applications*, vol. 389, no. 5, pp. 909–920, 2010.

- [123] X. Ma and C. L. Nikias, “Joint estimation of time delay and frequency delay in impulsive noise using fractional lower order statistics,” *IEEE Transactions on Signal Processing*, vol. 44, no. 11, pp. 2669–2687, 1996.
- [124] F. RongHua, “Modeling and application of theory based on time series arma,” *Science & Technology Information*, vol. 2012, no. 19, p. 153, 2012.
- [125] L. Shalalfeh, P. Bogdan, and E. Jonckheere, “Fractional dynamics of PMU data,” *IEEE Transactions on Smart Grid*, 2020.
- [126] F. Harmantzis, “Heavy network traffic modeling and simulation using stable FARIMA processes,” in *Proceedings of the 19th International Teletraffic Congress (ITC19)*, 2005.
- [127] H. Sheng and Y. Chen, “FARIMA with stable innovations model of Great Salt Lake elevation time series,” *Signal Processing*, vol. 91, no. 3, pp. 553–561, 2011.
- [128] Q. Li, C. Tricaud, R. Sun, and Y. Chen, “Great Salt Lake surface level forecasting using FIGARCH model,” in *Proceedings of the International Design Engineering Technical Conferences and Computers and Information in Engineering Conference*, vol. 4806, pp. 1361–1370, 2007.
- [129] P. J. Brockwell, R. A. Davis, and S. E. Fienberg, *Time Series: Theory and Methods*. Springer Science & Business Media, 1991.
- [130] M. Boutahar, G. Dufrénot, and A. Péguin-Feissolle, “A simple fractionally integrated model with a time-varying long memory parameter  $d_t$ ,” *Computational Economics*, vol. 31, no. 3, pp. 225–241, 2008.
- [131] H. L. Gray, N.-F. Zhang, and W. A. Woodward, “On generalized fractional processes,” *Journal of Time Series Analysis*, vol. 10, no. 3, pp. 233–257, 1989.
- [132] W. A. Woodward, Q. C. Cheng, and H. L. Gray, “A  $k$ -factor GARMA long-memory model,” *Journal of Time Series Analysis*, vol. 19, no. 4, pp. 485–504, 1998.
- [133] B. J. West, *Fractional Calculus View of Complexity: Tomorrow’s Science*. CRC Press, 2016.
- [134] G. M. Zaslavsky, R. Sagdeev, D. Usikov, and A. Chernikov, *Weak Chaos and Quasi-regular Patterns*. Cambridge University Press, 1992.
- [135] R. Hilfer and L. Anton, “Fractional master equations and fractal time random walks,” *Physical Review E*, vol. 51, no. 2, p. R848, 1995.

- [136] R. Gorenflo, F. Mainardi, and A. Vivoli, “Continuous-time random walk and parametric subordination in fractional diffusion,” *Chaos, Solitons & Fractals*, vol. 34, no. 1, pp. 87–103, 2007.
- [137] H. Niu, D. Hollenbeck, T. Zhao, D. Wang, and Y. Chen, “Evapotranspiration estimation with small UAVs in precision agriculture,” *Sensors*, vol. 20, no. 22, p. 6427, 2020.
- [138] R. Díaz-Varela, R. de la Rosa, L. León, and P. Zarco-Tejada, “High-resolution airborne UAV imagery to assess olive tree crown parameters using 3D photo reconstruction: Application in breeding trials,” *Remote Sensing*, vol. 7, no. 4, pp. 4213–4232, 2015.
- [139] V. Gonzalez-Dugo, D. Goldhamer, P. J. Zarco-Tejada, and E. Fereres, “Improving the precision of irrigation in a pistachio farm using an unmanned airborne thermal system,” *Irrigation Science*, vol. 33, no. 1, pp. 43–52, 2015.
- [140] K. C. Swain, S. J. Thomson, and H. P. Jayasuriya, “Adoption of an unmanned helicopter for low-altitude remote sensing to estimate yield and total biomass of a rice crop,” *Transactions of the ASABE*, vol. 53, no. 1, pp. 21–27, 2010.
- [141] P. J. Zarco-Tejada, V. González-Dugo, L. Williams, L. Suárez, J. A. Berni, D. Goldhamer, and E. Fereres, “A PRI-based water stress index combining structural and chlorophyll effects: Assessment using diurnal narrow-band airborne imagery and the CWSI thermal index,” *Remote Sensing of Environment*, vol. 138, pp. 38–50, 2013.
- [142] H. Niu, T. Zhao, D. Wang, and Y. Chen, “Estimating evapotranspiration with UAVs in agriculture: A review,” in *Proceedings of the ASABE Annual International Meeting*, American Society of Agricultural and Biological Engineers, 2019.
- [143] H. Niu, D. Wang, and Y. Chen, “Estimating crop coefficients using linear and deep stochastic configuration networks models and UAV-based normalized difference vegetation index (NDVI),” in *Proceedings of the 2020 International Conference on Unmanned Aircraft Systems (ICUAS)*, pp. 1485–1490, IEEE, 2020.
- [144] Y. Che, Q. Wang, Z. Xie, L. Zhou, S. Li, F. Hui, X. Wang, B. Li, and Y. Ma, “Estimation of maize plant height and leaf area index dynamic using unmanned aerial vehicle with oblique and nadir photography,” *Annals of Botany*, 2020.
- [145] R. Deng, Y. Jiang, M. Tao, X. Huang, K. Bangura, C. Liu, J. Lin, and L. Qi, “Deep learning-based automatic detection of productive tillers in rice,” *Computers and Electronics in Agriculture*, vol. 177, p. 105703, 2020.

- [146] T. Zhao, Y. Chen, A. Ray, and D. Doll, “Quantifying almond water stress using unmanned aerial vehicles (UAVs): Correlation of stem water potential and higher order moments of non-normalized canopy distribution,” in *Proceedings of the ASME 2017 International Design Engineering Technical Conferences and Computers and Information in Engineering Conference*, American Society of Mechanical Engineers, 2017.
- [147] B. T. Polyak, “Some methods of speeding up the convergence of iteration methods,” *USSR Computational Mathematics and Mathematical Physics*, vol. 4, no. 5, pp. 1–17, 1964.
- [148] J. Duchi, E. Hazan, and Y. Singer, “Adaptive subgradient methods for online learning and stochastic optimization,” *Journal of Machine Learning Research*, vol. 12, no. 7, pp. 2121–2159, 2011.
- [149] G. Hinton and T. Tieleman, “Slide 29 in lecture 6, 2012, rmsprop: “Divide the gradient by a running average of its recent magnitude”..”
- [150] D. P. Kingma and J. Ba, “Adam: A method for stochastic optimization,” *arXiv preprint arXiv:1412.6980*, 2014.
- [151] G. M. Viswanathan, V. Afanasyev, S. Buldyrev, E. Murphy, P. Prince, and H. E. Stanley, “Lévy flight search patterns of wandering albatrosses,” *Nature*, vol. 381, no. 6581, pp. 413–415, 1996.
- [152] C. Zeng and Y. Chen, “Optimal random search, fractional dynamics and fractional calculus,” *Fractional Calculus and Applied Analysis*, vol. 17, no. 2, pp. 321–332, 2014.
- [153] J. Wei, Y. Chen, Y. Yu, and Y. Chen, “Optimal randomness in swarm-based search,” *Mathematics*, vol. 7, no. 9, p. 828, 2019.
- [154] J. Wei and Y. Yu, “A novel cuckoo search algorithm under adaptive parameter control for global numerical optimization,” *Soft Computing*, pp. 1–24, 2019.
- [155] J. Wei and Y. Yu, “An adaptive cuckoo search algorithm with optional external archive for global numerical optimization,” in *Proceedings of the International Conference on Fractional Differentiation and its Applications (ICFDA)*, 2018.
- [156] A. C. Wilson, B. Recht, and M. I. Jordan, “A Lyapunov analysis of momentum methods in optimization,” *arXiv preprint arXiv:1611.02635*, 2016.
- [157] R. P. Feynman, “The principle of least action in quantum mechanics,” in *Feynman’s Thesis—A New Approach to Quantum Theory*, pp. 1–69, World Scientific, 2005.

- [158] S. W. R. Hamilton, *On a General Method in Dynamics*. Richard Taylor, 1834.
- [159] S. W. Hawking, “The path-integral approach to quantum gravity,” in *General Relativity: An Einstein Centenary Survey*, pp. 746–789, United Kingdom: University Press, 1979.
- [160] E. Kerrigan, “What the machine should learn about models for control.” <https://www.ifac2020.org/program/workshops/machine-learning-meets-model-based-control>, 2020.
- [161] B. A. Francis and W. M. Wonham, “The internal model principle of control theory,” *Automatica*, vol. 12, no. 5, pp. 457–465, 1976.
- [162] G. Vinnicombe, *Uncertainty and Feedback:  $H_\infty$  Loop-shaping and the  $\nu$ -gap Metric*. World Scientific, 2001.
- [163] J. Viola, Y. Chen, and J. Wang, “Information-based model discrimination for digital twin behavioral matching,” in *Proceedings of the International Conference on Industrial Artificial Intelligence (IAI)*, pp. 1–6, IEEE, 2020.
- [164] K. Kashima and Y. Yamamoto, “System theory for numerical analysis,” *Automatica*, vol. 43, no. 7, pp. 1156–1164, 2007.
- [165] W. An, H. Wang, Q. Sun, J. Xu, Q. Dai, and L. Zhang, “A PID controller approach for stochastic optimization of deep networks,” in *Proceedings of the IEEE Conference on Computer Vision and Pattern Recognition*, pp. 8522–8531, 2018.
- [166] Y. Fan and J. Koellermeier, “Accelerating the convergence of the moment method for the Boltzmann equation using filters,” *Journal of Scientific Computing*, vol. 84, no. 1, pp. 1–28, 2020.
- [167] K. L. Kuhlman, “Review of inverse Laplace transform algorithms for Laplace-space numerical approaches,” *Numerical Algorithms*, vol. 63, no. 2, pp. 339–355, 2013.
- [168] D. Xue and Y. Chen, *Solving Applied Mathematical Problems with MATLAB*. CRC Press, 2009.
- [169] D. Wang and M. Li, “Stochastic configuration networks: Fundamentals and algorithms,” *IEEE Transactions on Cybernetics*, vol. 47, no. 10, pp. 3466–3479, 2017.
- [170] D. Broomhead and D. Lowe, “Multivariable functional interpolation and adaptive networks,” *Complex Systems*, 1988.

- [171] Y.-H. Pao and Y. Takefuji, “Functional-link net computing: Theory, system architecture, and functionalities,” *Computer*, vol. 25, no. 5, pp. 76–79, 1992.
- [172] D. Wang and M. Li, “Deep stochastic configuration networks with universal approximation property,” in *Proceedings of the International Joint Conference on Neural Networks (IJCNN)*, pp. 1–8, IEEE, 2018.
- [173] M. Li and D. Wang, “2-D stochastic configuration networks for image data analytics,” *IEEE Transactions on Cybernetics*, 2019.
- [174] W. Wang and D. Wang, “Prediction of component concentrations in sodium aluminate liquor using stochastic configuration networks,” *Neural Computing and Applications*, pp. 1–14, 2020.
- [175] J. Lu, J. Ding, X. Dai, and T. Chai, “Ensemble stochastic configuration networks for estimating prediction intervals: A simultaneous robust training algorithm and its application,” *IEEE Transactions on Neural Networks and Learning Systems*, 2020.
- [176] C. Huang, Q. Huang, and D. Wang, “Stochastic configuration networks based adaptive storage replica management for power big data processing,” *IEEE Transactions on Industrial Informatics*, vol. 16, no. 1, pp. 373–383, 2019.
- [177] S. Scardapane and D. Wang, “Randomness in neural networks: An overview,” *Wiley Interdisciplinary Reviews: Data Mining and Knowledge Discovery*, vol. Volume 7, no. 2, 2017.
- [178] Y.-H. Pao, G.-H. Park, and D. J. Sobajic, “Learning and generalization characteristics of the random vector functional-link net,” *Neurocomputing*, vol. 6, no. 2, pp. 163–180, 1994.
- [179] M. Lukoševičius and H. Jaeger, “Reservoir computing approaches to recurrent neural network training,” *Computer Science Review*, vol. 3, no. 3, pp. 127–149, 2009.
- [180] D. D. Lee, P. Pham, Y. Largman, and A. Ng, “Advances in neural information processing systems,” in *Neural Information Processing Systems*, 2009.
- [181] J. Wei, *Research on Swarm Intelligence Optimization Algorithms and Their Applications to Parameter Identification of Fractional-order Systems*. PhD thesis, Beijing Jiaotong University, 2020.
- [182] I. Y. Tyukin and D. V. Prokhorov, “Feasibility of random basis function approximators for modeling and control,” in *Proceedings of the IEEE Control Applications, (CCA) & Intelligent Control, (ISIC)*, 2009.

- [183] Y. Chen, *Fundamental Principles for Fractional Order Gradient Methods*. PhD thesis, University of Science and Technology of China, 2020.
- [184] S. Nagaraj, “Optimization and learning with nonlocal calculus,” *arXiv preprint arXiv:2012.07013*, 2020.
- [185] V. E. Tarasov, “Fractional vector calculus and fractional Maxwell’s equations,” *Annals of Physics*, vol. 323, no. 11, pp. 2756–2778, 2008.
- [186] M. Ortigueira and J. Machado, “On fractional vectorial calculus,” *Bulletin of the Polish Academy of Sciences: Technical Sciences*, vol. 66, no. 4, pp. 389–402, 2018.
- [187] J. Feliu Faba, Y. Fan, and L. Ying, “Meta-learning pseudo-differential operators with deep neural networks,” *Journal of Computational Physics*, vol. 408, p. 109309, 2020.
- [188] D. L. Hall, *Dao De Jing: A Philosophical Translation*. Random House Digital, Inc., 2003.
- [189] A. Torres-Rua, “Vicarious calibration of sUAS microbolometer temperature imagery for estimation of radiometric land surface temperature,” *Sensors*, vol. 17, no. 7, p. 1499, 2017.
- [190] T. Zhao, H. Niu, A. Anderson, Y. Chen, and J. Viers, “A detailed study on accuracy of uncooled thermal cameras by exploring the data collection workflow,” in *Autonomous Air and Ground Sensing Systems for Agricultural Optimization and Phenotyping III*, International Society for Optics and Photonics, 2018.
- [191] K. Ribeiro-Gomes, D. Hernández-López, J. F. Ortega, R. Ballesteros, T. Poblete, and M. A. Moreno, “Uncooled thermal camera calibration and optimization of the photogrammetry process for UAV applications in agriculture,” *Sensors*, vol. 17, no. 10, p. 2173, 2017.
- [192] T. Zhao, B. Stark, Y. Chen, A. L. Ray, and D. Doll, “A detailed field study of direct correlations between ground truth crop water stress and normalized difference vegetation index (NDVI) from small unmanned aerial system (sUAS),” in *Proceedings of the 2015 International Conference on Unmanned Aircraft Systems (ICUAS)*, pp. 520–525, IEEE, 2015.
- [193] C. Lelong, P. Burger, G. Jubelin, B. Roux, S. Labbé, and F. Baret, “Assessment of unmanned aerial vehicles imagery for quantitative monitoring of wheat crop in small plots,” *Sensors*, vol. 8, no. 5, pp. 3557–3585, 2008.

- [194] H. Xiang and L. Tian, "Method for automatic georeferencing aerial remote sensing (RS) images from an unmanned aerial vehicle (UAV) platform," *Biosystems Engineering*, vol. 108, no. 2, pp. 104–113, 2011.
- [195] Á. G. Montibeller, "Estimating energy fluxes and evapotranspiration of corn and soybean with an unmanned aircraft system in Ames, Iowa," Master's thesis, University of Northern Iowa, 2017.
- [196] M. Elarab, *The Application of Unmanned Aerial Vehicle to Precision Agriculture: Chlorophyll, Nitrogen, and Evapotranspiration Estimation*. PhD thesis, Utah State University, 2016.
- [197] T. dos Reis, R. Monteiro, E. Garcia, M. Albuquerque, J. Espinoza, and J. Ferreira, "Actual evapotranspiration estimated by orbital sensors, UAV and meteorological station for vineyards in the southern Brazil," in *IV Ino-vagri International Meeting*, 2017.
- [198] H. Hoffmann, H. Nieto, R. Jensen, R. Guzinski, P. Zarco-Tejada, and T. Friborg, "Estimating evaporation with thermal UAV data and two-source energy balance models," *Hydrology and Earth System Sciences*, vol. 20, no. 2, pp. 697–713, 2016.
- [199] T. Xia, W. P. Kustas, M. C. Anderson, J. G. Alfieri, F. Gao, L. McKee, J. H. Prueger, H. M. Geli, C. M. Neale, L. Sanchez, *et al.*, "Mapping evapotranspiration with high-resolution aircraft imagery over vineyards using one-and two-source modeling schemes," *Hydrology and Earth System Sciences*, vol. 20, no. 4, p. 1523, 2016.
- [200] H. Nieto, J. Bellvert, W. P. Kustas, J. G. Alfieri, F. Gao, J. Prueger, A. Torres-Rua, L. E. Hipps, M. Elarab, and L. Song, "Unmanned airborne thermal and multispectral imagery for estimating evapotranspiration in irrigated vineyards," in *Proceedings of the 2017 IEEE International Geoscience and Remote Sensing Symposium (IGARSS)*, pp. 5510–5513, IEEE, 2017.
- [201] C. Monteiro, "Evapotranspiration estimate using energy balance two source model with UAV images: A study in vineyard," *American Journal of Engineering Research (AJER)*, vol. 8, no. 21, pp. 60–69, 2019.
- [202] H. Nieto, W. P. Kustas, A. Torres-Rúa, J. G. Alfieri, F. Gao, M. C. Anderson, W. A. White, L. Song, M. del Mar Alsina, J. H. Prueger, *et al.*, "Evaluation of TSEB turbulent fluxes using different methods for the retrieval of soil and canopy component temperatures from UAV thermal and multispectral imagery," *Irrigation Science*, vol. 37, no. 3, pp. 389–406, 2019.
- [203] S. Ortega-Farías, S. Ortega-Salazar, T. Poblete, A. Kilic, R. Allen, C. Poblete-Echeverría, L. Ahumada-Orellana, M. Zuñiga, and D. Sepúlveda,

- “Estimation of energy balance components over a drip-irrigated olive orchard using thermal and multispectral cameras placed on a helicopter-based unmanned aerial vehicle (UAV),” *Remote Sensing*, vol. 8, no. 8, p. 638, 2016.
- [204] J. L. Chávez, P. Gowda, T. Howell, C. Neale, and K. Copeland, “Estimating hourly crop ET using a two-source energy balance model and multispectral airborne imagery,” *Irrigation Science*, vol. 28, no. 1, pp. 79–91, 2009.
- [205] C. Brenner, C. E. Thiem, H.-D. Witzmann, M. Bernhardt, and K. Schulz, “Estimating spatially distributed turbulent heat fluxes from high-resolution thermal imagery acquired with a UAV system,” *International Journal of Remote Sensing*, vol. 38, no. 8-10, pp. 3003–3026, 2017.
- [206] S. Park, *Estimating Plant Water Stress and Evapotranspiration Using Very-high-resolution (VHR) UAV Imagery*. PhD thesis, University of Melbourne, 2018.
- [207] A. S. Laliberte, A. Rango, and J. Herrick, “Unmanned aerial vehicles for rangeland mapping and monitoring: A comparison of two systems,” in *Proceedings of the ASPRS Annual Conference*, 2007.
- [208] P. J. Hardin and T. J. Hardin, “Small-scale remotely piloted vehicles in environmental research,” *Geography Compass*, vol. 4, no. 9, pp. 1297–1311, 2010.
- [209] P. J. Hardin and R. R. Jensen, “Small-scale unmanned aerial vehicles in environmental remote sensing: Challenges and opportunities,” *GIScience & Remote Sensing*, vol. 48, no. 1, pp. 99–111, 2011.
- [210] B. Stark and Y. Chen, “A framework of optimal remote sensing using small unmanned aircraft systems,” in *Proceedings of the 12th IEEE/ASME International Conference on Mechatronic and Embedded Systems and Applications (MESA)*, pp. 1–6, IEEE, 2016.
- [211] S. Harwin and A. Lucieer, “Assessing the accuracy of georeferenced point clouds produced via multi-view stereopsis from unmanned aerial vehicle (UAV) imagery,” *Remote Sensing*, vol. 4, no. 6, pp. 1573–1599, 2012.
- [212] A. Lucieer, Z. Malenovsky, T. Veness, and L. Wallace, “HyperUAS—Imaging spectroscopy from a multicopter unmanned aircraft system,” *Journal of Field Robotics*, vol. 31, no. 4, pp. 571–590, 2014.
- [213] D. Turner, A. Lucieer, and C. Watson, “An automated technique for generating georectified mosaics from ultra-high resolution unmanned aerial vehicle (UAV) imagery, based on structure from motion (SfM) point clouds,” *Remote Sensing*, vol. 4, no. 5, pp. 1392–1410, 2012.

- [214] L. Wallace, A. Lucieer, C. Watson, and D. Turner, "Development of a UAV-LiDAR system with application to forest inventory," *Remote Sensing*, vol. 4, no. 6, pp. 1519–1543, 2012.
- [215] G. M. Smith and E. J. Milton, "The use of the empirical line method to calibrate remotely sensed data to reflectance," *International Journal of Remote Sensing*, vol. 20, no. 13, pp. 2653–2662, 1999.
- [216] B. Stark, T. Zhao, and Y. Chen, "An analysis of the effect of the bidirectional reflectance distribution function on remote sensing imagery accuracy from small unmanned aircraft systems," in *Proceedings of the 2016 International Conference on Unmanned Aircraft Systems (ICUAS)*, pp. 1342–1350, IEEE, 2016.
- [217] J. A. Berni, P. J. Zarco-Tejada, L. Suárez, and E. Fereres, "Thermal and narrowband multispectral remote sensing for vegetation monitoring from an unmanned aerial vehicle," *IEEE Transactions on Geoscience and Remote Sensing*, vol. 47, no. 3, pp. 722–738, 2009.
- [218] K. Brown and N. J. Rosenberg, "A resistance model to predict evapotranspiration and its application to a sugar beet field 1," *Agronomy Journal*, vol. 65, no. 3, pp. 341–347, 1973.
- [219] H. Sheng, H. Chao, C. Coopmans, J. Han, M. McKee, and Y. Chen, "Low-cost UAV-based thermal infrared remote sensing: Platform, calibration and applications," in *Proceedings of the 2010 IEEE/ASME International Conference on Mechatronics and Embedded Systems and Applications (MESA)*, pp. 38–43, IEEE, 2010.
- [220] R. Gade and T. B. Moeslund, "Thermal cameras and applications: A survey," *Machine Vision and Applications*, vol. 25, no. 1, pp. 245–262, 2014.
- [221] H. G. Jones, R. Serraj, B. R. Loveys, L. Xiong, A. Wheaton, and A. H. Price, "Thermal infrared imaging of crop canopies for the remote diagnosis and quantification of plant responses to water stress in the field," *Functional Plant Biology*, vol. 36, no. 11, pp. 978–989, 2009.
- [222] A. Gowen, B. Tiwari, P. Cullen, K. McDonnell, and C. O'Donnell, "Applications of thermal imaging in food quality and safety assessment," *Trends in Food Science & Technology*, vol. 21, no. 4, pp. 190–200, 2010.
- [223] F. Martinelli, R. Scalenghe, S. Davino, S. Panno, G. Scuderi, P. Ruisi, P. Villa, D. Stroppiana, M. Boschetti, L. R. Goulart, *et al.*, "Advanced methods of plant disease detection. A review," *Agronomy for Sustainable Development*, vol. 35, no. 1, pp. 1–25, 2015.

- [224] T. Zhao, Z. Wang, Q. Yang, and Y. Chen, “Melon yield prediction using small unmanned aerial vehicles,” in *Autonomous Air and Ground Sensing Systems for Agricultural Optimization and Phenotyping II*, International Society for Optics and Photonics, 2017.
- [225] R. Näsi, E. Honkavaara, P. Lyytikäinen-Saarenmaa, M. Blomqvist, P. Litkey, T. Hakala, N. Viljanen, T. Kantola, T. Tanhuanpää, and M. Holopainen, “Using UAV-based photogrammetry and hyperspectral imaging for mapping bark beetle damage at tree-level,” *Remote Sensing*, 2015.
- [226] B. Rodriguez Galdon, C. Tascon Rodriguez, E. Rodriguez Rodriguez, and C. Diaz Romero, “Organic acid contents in onion cultivars (*Allium cepa* L.),” *Journal of Agricultural and Food Chemistry*, vol. 56, no. 15, pp. 6512–6519, 2008.
- [227] J. I. Córcoles, J. F. Ortega, D. Hernández, and M. A. Moreno, “Estimation of leaf area index in onion (*Allium cepa* L.) using an unmanned aerial vehicle,” *Biosystems Engineering*, vol. 115, no. 1, pp. 31–42, 2013.
- [228] P. Lazicki, D. Geisseler, and W. R. Horwath, “Onion production in California,” *CDFCA*, June, 2016.
- [229] T. Zhao, B. Stark, Y. Chen, A. Ray, and D. Doll, “More reliable crop water stress quantification using small unmanned aerial systems (sUAS),” *IFAC-Papers on Line*, vol. 49, no. 16, pp. 409–414, 2016.
- [230] T. Zhao, B. Stark, Y. Chen, A. L. Ray, and D. Doll, “Challenges in water stress quantification using small unmanned aerial system (sUAS): Lessons from a growing season of almond,” *Journal of Intelligent & Robotic Systems*, vol. 88, no. 2-4, pp. 721–735, 2017.
- [231] T. Zhao, D. Doll, D. Wang, and Y. Chen, “A new framework for UAV-based remote sensing data processing and its application in almond water stress quantification,” in *Unmanned Aircraft Systems (ICUAS), 2017 International Conference on*, pp. 1794–1799, IEEE, 2017.
- [232] T. Zhao, D. Doll, and Y. Chen, “Better almond water stress monitoring using fractional-order moments of non-normalized difference vegetation index,” in *2017 ASABE Annual International Meeting*, p. 1, American Society of Agricultural and Biological Engineers, 2017.
- [233] R. Ballesteros, J. F. Ortega, D. Hernandez, and M. A. Moreno, “Onion biomass monitoring using UAV-based RGB imaging,” *Precision Agriculture*, vol. 19, no. 5, pp. 840–857, 2018.

- [234] W. Wang, C. Li, and R. D. Gitaitis, “Optical properties of healthy and diseased onion tissues in the visible and near-infrared spectral region,” *Transactions of the ASABE*, vol. 57, no. 6, pp. 1771–1782, 2014.
- [235] I. Jolliffe, *Principal Component Analysis*. Springer, 2011.
- [236] J. Friedman, T. Hastie, and R. Tibshirani, *The Elements of Statistical Learning*, vol. 1. Springer Series in Statistics New York, 2001.
- [237] A. Soliman, R. J. Heck, A. Brenning, R. Brown, and S. Miller, “Remote sensing of soil moisture in vineyards using airborne and ground-based thermal inertia data,” *Remote Sensing*, vol. 5, no. 8, pp. 3729–3748, 2013.
- [238] A. M. Jensen, M. McKee, and Y. Chen, “Procedures for processing thermal images using low-cost microbolometer cameras for small unmanned aerial systems,” in *Geoscience and Remote Sensing Symposium (IGARSS), 2014 IEEE International*, pp. 2629–2632, IEEE, 2014.
- [239] C. M. Bishop, *Neural Networks for Pattern Recognition*. Oxford University Press, 1995.
- [240] K. F. Wallis, “Seasonal adjustment and relations between variables,” *Journal of the American Statistical Association*, vol. 69, no. 345, pp. 18–31, 1974.
- [241] R. A. Burckle and V. WinSystems, “Pc/104 embedded modules: The new systems components,” 2003.
- [242] J. Berni, P. Zarco-Tejada, L. Suárez, V. González-Dugo, and E. Fereres, “Remote sensing of vegetation from UAV platforms using lightweight multispectral and thermal imaging sensors,” *Int. Arch. Photogramm. Remote Sens. Spatial Inform. Sci*, vol. 38, no. 6, 2009.
- [243] R. A. Wood, “Uncooled thermal imaging with monolithic silicon focal planes,” in *Infrared Technology XIX*, vol. 2020, pp. 322–330, International Society for Optics and Photonics, 1993.
- [244] B. Kamble, A. Kilic, and K. Hubbard, “Estimating crop coefficients using remote sensing-based vegetation index,” *Remote Sensing*, vol. 5, no. 4, pp. 1588–1602, 2013.
- [245] A. Reyes-Gonzalez, C. Hay, J. Kjaersgaard, and C. Neale, “Use of remote sensing to generate crop coefficient and estimate actual crop evapotranspiration,” in *Proceedings of the 2015 ASABE Annual International Meeting*, p. 1, American Society of Agricultural and Biological Engineers, 2015.
- [246] D. J. Hunsaker, P. J. Pinter, E. M. Barnes, and B. A. Kimball, “Estimating cotton evapotranspiration crop coefficients with a multispectral vegetation index,” *Irrigation Science*, vol. 22, no. 2, pp. 95–104, 2003.

- [247] T. J. Trout, L. F. Johnson, and J. Gartung, "Remote sensing of canopy cover in horticultural crops," *HortScience*, vol. 43, no. 2, pp. 333–337, 2008.
- [248] H. Zhang, R. G. Anderson, and D. Wang, "Satellite-based crop coefficient and regional water use estimates for Hawaiian sugarcane," *Field Crops Research*, vol. 180, pp. 143–154, 2015.
- [249] A. Ershadi, M. F. McCabe, J. P. Evans, and J. P. Walker, "Effects of spatial aggregation on the multi-scale estimation of evapotranspiration," *Remote Sensing of Environment*, vol. 131, pp. 51–62, 2013.
- [250] H. Niu, T. Zhao, and Y. Chen, "Intelligent bugs mapping and wiping (iBMW): An affordable robot-driven robot for farmers," in *IEEE International Conference on Mechatronics and Automation (ICMA)*, pp. 397–402, IEEE, 2019.
- [251] M. Awais, W. Li, M. M. Cheema, S. Hussain, A. Shaheen, B. Aslam, C. Liu, and A. Ali, "Assessment of optimal flying height and timing using high-resolution unmanned aerial vehicle images in precision agriculture," *International Journal of Environmental Science and Technology*, pp. 1–18, 2021.
- [252] C. Rafael Gonzalez, E. R. Woods, and L. S. Eddins, "Digital image processing using MATLAB," *Prentice Hall, USA., ISBN*, vol. 10, p. 0130085197, 2003.
- [253] K. Ashton *et al.*, "That 'Internet of Things' thing," *RFID Journal*, vol. 22, no. 7, pp. 97–114, 2009.
- [254] S. Madakam, V. Lake, V. Lake, V. Lake, *et al.*, "Internet of Things (IoT): A literature review," *Journal of Computer and Communications*, vol. 3, no. 05, p. 164, 2015.
- [255] I. T. Union, "Internet of Things global standards initiative," 2012.
- [256] W. H. Hassan *et al.*, "Current research on Internet of Things (IoT) security: A survey," *Computer Networks*, vol. 148, pp. 283–294, 2019.
- [257] C. A. Da Costa, C. F. Pasluosta, B. Eskofier, D. B. Da Silva, and R. da Rosa Righi, "Internet of health things: Toward intelligent vital signs monitoring in hospital wards," *Artificial Intelligence in Medicine*, vol. 89, pp. 61–69, 2018.
- [258] A. Gatouillat, Y. Badr, B. Massot, and E. Sejdić, "Internet of medical things: A review of recent contributions dealing with cyber-physical systems in medicine," *IEEE Internet of Things Journal*, vol. 5, no. 5, pp. 3810–3822, 2018.

- [259] C. Yang, W. Shen, and X. Wang, "The Internet of Things in manufacturing: Key issues and potential applications," *IEEE Systems, Man, and Cybernetics Magazine*, vol. 4, no. 1, pp. 6–15, 2018.
- [260] F. Balducci, D. Impedovo, and G. Pirlo, "Machine learning applications on agricultural datasets for smart farm enhancement," *Machines*, vol. 6, no. 3, p. 38, 2018.
- [261] M. Paustian and L. Theuvsen, "Adoption of precision agriculture technologies by German crop farmers," *Precision Agriculture*, vol. 18, no. 5, pp. 701–716, 2017.
- [262] P. P. Jayaraman, A. Yavari, D. Georgakopoulos, A. Morshed, and A. Zaslavsky, "Internet of Things platform for smart farming: Experiences and lessons learnt," *Sensors*, vol. 16, no. 11, p. 1884, 2016.
- [263] J. Zhao, J. Zhang, Y. Feng, and J. Guo, "The study and application of the IOT technology in agriculture," in *2010 3rd International Conference on Computer Science and Information Technology*, vol. 2, pp. 462–465, IEEE, 2010.
- [264] M. A. Hamad, M. E. S. Eltahir, A. E. M. Ali, and A. M. Hamdan, "Efficiency of using smart-mobile phones in accessing agricultural information by smallholder farmers in north Kordofan–Sudan," *Available at SSRN 3240758*, 2018.
- [265] P. Lazicki, D. Geisseler, and W. R. Horwath, "Onion production in California." CDFA, June 2016, [https://apps1.cdfa.ca.gov/FertilizerResearch/docs/Onion\\_Production\\_CA.pdf](https://apps1.cdfa.ca.gov/FertilizerResearch/docs/Onion_Production_CA.pdf). (Accessed: 16 August 2018).
- [266] W. Drinkwater and B. Janes, "Effects of irrigation and soil moisture on maturity, yield and storage of two onion hybrids," in *Proceedings of the American Society for Horticultural Science*, vol. 66, pp. 267–278, 1955.
- [267] L. D. Doneen and J. H. MacGillivray, *Suggestions on irrigating commercial truck crops*. University of California, College of Agriculture, Agricultural Experiment Station, 1943.
- [268] R. Singh and R. Alderfer, "Effects of soil-moisture stress at different periods of growth of some vegetable crops," *Soil Science*, vol. 101, no. 1, pp. 69–80, 1966.
- [269] M. Govender, P. Govender, I. Weiersbye, E. Witkowski, and F. Ahmed, "Review of commonly used remote sensing and ground-based technologies to measure plant water stress," *Water SA*, vol. 35, no. 5, 2009.

- [270] Y. Kim, D. M. Glenn, J. Park, H. K. Ngugi, and B. L. Lehman, "Hyperspectral image analysis for water stress detection of apple trees," *Computers and Electronics in Agriculture*, vol. 77, no. 2, pp. 155–160, 2011.
- [271] M. Maimaitiyiming, A. Ghulam, A. Bozzolo, J. L. Wilkins, and M. T. Kwasniewski, "Early detection of plant physiological responses to different levels of water stress using reflectance spectroscopy," *Remote Sensing*, vol. 9, no. 7, p. 745, 2017.
- [272] A. B. González-Fernández, J. R. Rodríguez-Pérez, V. Marcelo, and J. B. Valenciano, "Using field spectrometry and a plant probe accessory to determine leaf water content in commercial vineyards," *Agricultural Water Management*, vol. 156, pp. 43–50, 2015.
- [273] S. Marino, B. Basso, A. Leone, and A. Alvino, "Agronomic traits and vegetation indices of two onion hybrids," *Scientia Horticulturae*, vol. 155, pp. 56–64, 2013.
- [274] W. Wang and C. Li, "A multimodal machine vision system for quality inspection of onions," *Journal of Food Engineering*, vol. 166, pp. 291–301, 2015.
- [275] M. N. Islam, G. Nielsen, S. Stærke, A. Kjær, B. Jørgensen, and M. Edelebos, "Novel non-destructive quality assessment techniques of onion bulbs: A comparative study," *Journal of Food Science and Technology*, pp. 1–11, 2018.
- [276] R. A. Fisher, "The use of multiple measurements in taxonomic problems," *Annals of Eugenics*, vol. 7, no. 2, pp. 179–188, 1936.
- [277] F. Rosenblatt, "The perceptron: A probabilistic model for information storage and organization in the brain.," *Psychological Review*, vol. 65, no. 6, p. 386, 1958.
- [278] M. Minsky and S. Papert, "Perceptrons.," *APA PsycNet*, 1969.
- [279] F. Pedregosa, G. Varoquaux, A. Gramfort, V. Michel, B. Thirion, O. Grisel, M. Blondel, P. Prettenhofer, R. Weiss, V. Dubourg, *et al.*, "Scikit-learn: Machine learning in Python," *Journal of Machine Learning Research*, vol. 12, no. Oct, pp. 2825–2830, 2011.
- [280] R. Rault and D. Trentesaux, "Artificial intelligence, autonomous systems and robotics: Legal innovations," in *Service Orientation in Holonic and Multi-Agent Manufacturing*, pp. 1–9, Springer, 2018.

- [281] R. Oberti, M. Marchi, P. Tirelli, A. Calcante, M. Iriti, E. Tona, M. Hočevár, J. Baur, J. Pfaff, C. Schütz, *et al.*, “Selective spraying of grapevines for disease control using a modular agricultural robot,” *Biosystems Engineering*, vol. 146, pp. 203–215, 2016.
- [282] D. J. Romero, E. Ben-Dor, J. A. Demattê, A. B. e Souza, L. E. Vicente, T. R. Tavares, M. Martello, T. F. Strabeli, P. P. da Silva Barros, P. R. Fiorio, *et al.*, “Internal soil standard method for the Brazilian soil spectral library: Performance and proximate analysis,” *Geoderma*, vol. 312, pp. 95–103, 2018.
- [283] P. Kashyap, “Machine learning algorithms and their relationship with modern technologies,” in *Machine Learning for Decision Makers*, pp. 91–136, Springer, 2017.
- [284] K. Ghaffarzadeh and H. Zervos, “Conductive ink markets 2013-2018: Forecasts, technologies, players,” *IDTechEx Market Report*, 2013.
- [285] W. Pei, Y. Lan, L. Xiwen, Z. Zhiyan, Z. Wang, and Y. Wang, “Integrated sensor system for monitoring rice growth conditions based on unmanned ground vehicle system.,” *International Journal of Agricultural & Biological Engineering*, vol. 7, no. 2, 2014.
- [286] S. Bhandari, A. Raheja, R. L. Green, and D. Do, “Towards collaboration between unmanned aerial and ground vehicles for precision agriculture,” in *Autonomous Air and Ground Sensing Systems for Agricultural Optimization and Phenotyping II*, vol. 10218, p. 1021806, International Society for Optics and Photonics, 2017.
- [287] M. Pierzchała, P. Giguère, and R. Astrup, “Mapping forests using an unmanned ground vehicle with 3D LiDAR and graph-SLAM,” *Computers and Electronics in Agriculture*, vol. 145, pp. 217–225, 2018.
- [288] C. M. Lopes, A. Torres, R. Guzman, J. Graça, M. Reyes, G. Vitorino, R. Braga, A. Monteiro, and A. Barriguinha, “Using an unmanned ground vehicle to scout vineyards for non-intrusive estimation of canopy features and grape yield,” in *GiESCO International Meeting, 20th, Sustainable Viticulture and Wine Making in Climate Change Scenarios, 5-10 November 2017*, GiESCO, 2017.
- [289] C. W. Pirk, U. Strauss, A. A. Yusuf, F. Demares, and H. Human, “Honeybee health in Africa—A review,” *Apidologie*, vol. 47, no. 3, pp. 276–300, 2016.
- [290] D. Makori, A. Fombong, E. Abdel-Rahman, K. Nkoba, J. Ongus, J. Irungu, G. Mosomtai, S. Makau, O. Mutanga, J. Odindi, *et al.*, “Predicting spatial distribution of key honeybee pests in Kenya using remotely sensed and bioclimatic variables: Key honeybee pests distribution models,” *ISPRS International Journal of Geo-Information*, vol. 6, no. 3, p. 66, 2017.

- [291] J. Popp, K. Petó, and J. Nagy, “Pesticide productivity and food security: A review,” *Agronomy for Sustainable Development*, vol. 33, no. 1, pp. 243–255, 2013.
- [292] E. Muli, H. Patch, M. Frazier, J. Frazier, B. Torto, T. Baumgarten, J. Kilonzo, J. N. Kimani, F. Mumoki, D. Masiga, *et al.*, “Evaluation of the distribution and impacts of parasites, pathogens, and pesticides on honey bee (*Apis mellifera*) populations in East Africa,” *PLoS One*, vol. 9, no. 4, p. e94459, 2014.
- [293] F. M. Kelliher, A. D. Noble, S. Dennis, A. Rickerby, and T. Knight, “A graphical method to evaluate irrigation water application uniformity,” *New Zealand Journal of Agricultural Research*, vol. 60, no. 1, pp. 80–92, 2017.
- [294] A. Burkart, V. Hecht, T. Kraska, and U. Rascher, “Phenological analysis of unmanned aerial vehicle based time series of barley imagery with high temporal resolution,” *Precision Agriculture*, vol. 19, no. 1, pp. 134–146, 2018.
- [295] P. Tokekar, J. Vander Hook, D. Mulla, and V. Isler, “Sensor planning for a symbiotic UAV and UGV system for precision agriculture,” *IEEE Transactions on Robotics*, vol. 32, no. 6, pp. 1498–1511, 2016.
- [296] S. Sankaran, A. Mishra, R. Ehsani, and C. Davis, “A review of advanced techniques for detecting plant diseases,” *Computers and Electronics in Agriculture*, vol. 72, no. 1, pp. 1–13, 2010.
- [297] R. Gebbers and V. I. Adamchuk, “Precision agriculture and food security,” *Science*, vol. 327, no. 5967, pp. 828–831, 2010.
- [298] J. E. Taylor, D. Charlton, and A. Yúnez-Naude, “The end of farm labor abundance,” *Applied Economic Perspectives and Policy*, vol. 34, no. 4, pp. 587–598, 2012.
- [299] J. Billingsley, A. Visala, and M. Dunn, “Robotics in agriculture and forestry,” *Springer Handbook of Robotics*, 2008.
- [300] M. Quigley, B. Gerkey, and W. D. Smart, *Programming Robots with ROS: A Practical Introduction to the Robot Operating System*. O’Reilly Media, Inc., 2015.
- [301] L. Feng, L. Gao, and Y.-h. Li, “Research on information processing of intelligent lane-changing behaviors for unmanned ground vehicles,” in *2016 9th International Symposium on Computational Intelligence and Design (IS-CID)*, vol. 2, pp. 38–41, IEEE, 2016.

- [302] M. A. Fields, C. Lennon, M. Martin, and C. Lebiere, “Priming for autonomous cognitive systems,” in *Micro-and Nanotechnology Sensors, Systems, and Applications IX*, vol. 10194, p. 1019421, International Society for Optics and Photonics, 2017.
- [303] S. Hood, K. Benson, P. Hamod, D. Madison, J. M. O’Kane, and I. Rekleitis, “Bird’s eye view: Cooperative exploration by UGV and UAV,” in *2017 International Conference on Unmanned Aircraft Systems (ICUAS)*, pp. 247–255, IEEE, 2017.
- [304] J. Engel, T. Schöps, and D. Cremers, “LSD-SLAM: Large-scale direct monocular SLAM,” in *European Conference on Computer Vision*, pp. 834–849, Springer, 2014.
- [305] M. J. Milford, G. F. Wyeth, and D. Prasser, “RatSLAM: A hippocampal model for simultaneous localization and mapping,” in *IEEE International Conference on Robotics and Automation, 2004. Proceedings. ICRA’04. 2004*, vol. 1, pp. 403–408, IEEE, 2004.
- [306] C. Forster, M. Pizzoli, and D. Scaramuzza, “SVO: Fast semi-direct monocular visual odometry,” in *2014 IEEE International Conference on Robotics and Automation (ICRA)*, pp. 15–22, IEEE, 2014.
- [307] A. Q. Li, A. Coskun, S. M. Doherty, S. Ghasemlou, A. S. Jagtap, M. Modasshir, S. Rahman, A. Singh, M. Xanthidis, J. M. O’Kane, *et al.*, “Experimental comparison of open source vision-based state estimation algorithms,” in *International Symposium on Experimental Robotics*, pp. 775–786, Springer, 2016.
- [308] R. Mur-Artal, J. M. M. Montiel, and J. D. Tardos, “ORB-SLAM: A versatile and accurate monocular SLAM system,” *IEEE Transactions on Robotics*, vol. 31, no. 5, pp. 1147–1163, 2015.
- [309] A. J. Suppé and M. Hebert, “Using deep learning to bridge the gap between perception and intelligence,” in *Unmanned Systems Technology XIX*, vol. 10195, p. 1019503, International Society for Optics and Photonics, 2017.
- [310] N. Kussul, M. Lavreniuk, S. Skakun, and A. Shelestov, “Deep learning classification of land cover and crop types using remote sensing data,” *IEEE Geoscience and Remote Sensing Letters*, vol. 14, no. 5, pp. 778–782, 2017.
- [311] J. D. Foster, “Swarming unmanned aerial vehicles (UAVs): Extending marine aviation ground task force communications using UAVs,” tech. rep., Naval Postgraduate School, Monterey, CA, Graduate School of Business and Public, 2015.

- [312] S. Bonadies, A. Lefcourt, and S. A. Gadsden, “A survey of unmanned ground vehicles with applications to agricultural and environmental sensing,” in *Autonomous Air and Ground Sensing Systems for Agricultural Optimization and Phenotyping*, vol. 9866, p. 98660Q, International Society for Optics and Photonics, 2016.
- [313] G. Danoy, M. R. Brust, and P. Bouvry, “Connectivity stability in autonomous multi-level UAV swarms for wide area monitoring,” in *Proceedings of the 5th ACM Symposium on Development and Analysis of Intelligent Vehicular Networks and Applications*, pp. 1–8, 2015.
- [314] M. Saska, T. Baca, J. Thomas, J. Chudoba, L. Preucil, T. Krajník, J. Faigl, G. Loianno, and V. Kumar, “System for deployment of groups of unmanned micro aerial vehicles in GPS-denied environments using onboard visual relative localization,” *Autonomous Robots*, vol. 41, no. 4, pp. 919–944, 2017.
- [315] H. Yu and R. Beard, “A vision-based collision avoidance technique for micro air vehicles using local-level frame mapping and path planning,” *Autonomous Robots*, vol. 34, no. 1, pp. 93–109, 2013.
- [316] P. Fazli, A. Davoodi, and A. K. Mackworth, “Multi-robot repeated area coverage,” *Autonomous Robots*, vol. 34, no. 4, pp. 251–276, 2013.
- [317] A. F. Winfield, W. Liu, J. Nembrini, and A. Martinoli, “Modelling a wireless connected swarm of mobile robots,” *Swarm Intelligence*, vol. 2, no. 2, pp. 241–266, 2008.
- [318] A. Marjovi and L. Marques, “Optimal spatial formation of swarm robotic gas sensors in odor plume finding,” *Autonomous Robots*, vol. 35, no. 2, pp. 93–109, 2013.
- [319] M. Kloetzer and C. Belta, “Temporal logic planning and control of robotic swarms by hierarchical abstractions,” *IEEE Transactions on Robotics*, vol. 23, no. 2, pp. 320–330, 2007.
- [320] N. Cai, J.-X. Xi, and Y.-S. Zhong, “Swarm stability of high-order linear time-invariant swarm systems,” *IET Control Theory & Applications*, vol. 5, no. 2, pp. 402–408, 2011.
- [321] C. C. Cheah, S. P. Hou, and J. J. E. Slotine, “Region-based shape control for a swarm of robots,” *Automatica*, vol. 45, no. 10, pp. 2406–2411, 2009.
- [322] J. A. Brito, D. W. Dickson, R. Kaur, S. Vau, and J. D. Stanley, *The peach root-knot nematode: Meloidogyne floridensis, and its potential impact for the peach industry in Florida*. Florida Department of Agriculture and Consumer Services, 2015.

- [323] M. V. McKenry, "The replant problem and its management." online: [http://kare.ucanr.edu/programs/Nematodes/The\\_Replant\\_Problem/index.cfm?editon=0](http://kare.ucanr.edu/programs/Nematodes/The_Replant_Problem/index.cfm?editon=0), 1999. (Accessed: 19 March 2020).
- [324] A. Westphal, Z. T. Maung, D. A. Doll, M. A. Yaghmour, J. J. Chitambar, and S. A. Subbotin, *First report of the peach root-knot nematode, meloidogyne floridensis infecting almond on root-knot nematode resistant 'Hansen 536' and 'Bright's hybrid 5' rootstocks in California, USA*. Society of Nematologists, 2019.
- [325] B. Westerdahl, A. Westphal, J. K. Hasey, and M. McKenry, "UC IPM pest management guidelines: Walnut nematodes." Online: <https://www2.ipm.ucanr.edu/agriculture/walnut/Nematodes/>, 2017. (Accessed: 19 March 2020).
- [326] S. Singh, B. Singh, and A. Singh, "Nematodes: A threat to sustainability of agriculture," *Procedia Environmental Sciences*, vol. 29, pp. 215–216, 2015.
- [327] J. D. Eisenback, H. H. Triantaphyllou, *et al.*, "Root-knot nematodes: Meloidogyne species and races," *Manual of Agricultural Nematology*, vol. 1, pp. 191–274, 1991.
- [328] M. McKenry, T. Buzo, S. Kaku, and J. McKenna, "A three-year search for nematode resistance in walnut-final report," *Walnut Research Reports*, vol. 2000, pp. 509–512, 2001.
- [329] G. D. Martins, M. d. L. B. T. Galo, and B. S. Vieira, "Detecting and mapping root-knot nematode infection in coffee crop using remote sensing measurements," *IEEE Journal of Selected Topics in Applied Earth Observations and Remote Sensing*, vol. 10, no. 12, pp. 5395–5403, 2017.
- [330] P. K. Palacharla, S. S. Durbha, R. L. King, B. Gokaraju, and G. W. Lawrence, "A hyperspectral reflectance data based model inversion methodology to detect reniform nematodes in cotton," in *Proceedings of the 6th International Workshop on the Analysis of Multi-temporal Remote Sensing Images (Multi-Temp)*, pp. 249–252, IEEE, 2011.
- [331] G. W. Lawrence, R. King, G. Ellis, R. Doshi, K. Lawrence, J. Caceres, and S. Samson, "Population estimation of the reniform nematode using hyperspectral reflectance data and applications to variable rate nematicide applications," in *Proceedings of the National Beltwide Cotton Conference, National Cotton Council. Memphis TN*, vol. 1, 2007.
- [332] C. Hillnhütter, A.-K. Mahlein, R. A. Sikora, and E.-C. Oerke, "Use of imaging spectroscopy to discriminate symptoms caused by *Heterodera schachtii* and *Rhizoctonia solani* on sugar beet," *Precision Agriculture*, vol. 13, no. 1, pp. 17–32, 2012.

- [333] R. Li, Y. Lu, J. M. Peters, B. Choat, and A. J. Lee, “Non-invasive measurement of leaf water content and pressure–volume curves using terahertz radiation,” *Scientific Reports*, vol. 10, no. 1, pp. 1–14, 2020.
- [334] H. Niu, T. Zhao, A. Westphal, and Y. Chen, “A low-cost proximate sensing method for early detection of nematodes in walnut using Walabot and scikit-learn classification algorithms,” in *Autonomous Air and Ground Sensing Systems for Agricultural Optimization and Phenotyping V*, International Society for Optics and Photonics, 2020.
- [335] Y. Wang, Y. Chen, X. Liao, and L. Dong, “Lithium-ion battery face imaging with contactless Walabot and machine learning,” in *Proceedings of the 2019 IEEE International Conference on Mechatronics and Automation (ICMA)*, pp. 1067–1072, IEEE, 2019.
- [336] Y. Wang, H. Niu, T. Zhao, X. Liao, L. Dong, and Y. Chen, “Contactless Li-Ion battery voltage detection by using Walabot and machine learning,” in *Proceedings of the ASME 2019 International Design Engineering Technical Conferences and Computers and Information in Engineering Conference*, American Society of Mechanical Engineers Digital Collection, 2019.
- [337] C.-C. Chang and C.-J. Lin, “LIBSVM: A library for support vector machines,” *ACM Transactions on Intelligent Systems and Technology (TIST)*, 2011.
- [338] L. Breiman, “Random forests,” *Machine Learning*, vol. 45, no. 1, pp. 5–32, 2001.
- [339] J. Goldberger, G. E. Hinton, S. Roweis, and R. R. Salakhutdinov, “Neighbourhood components analysis,” *Advances in neural information processing systems*, vol. 17, pp. 513–520, 2004.
- [340] W.-Y. Loh, “Classification and regression trees,” *Wiley Interdisciplinary Reviews: Data Mining and Knowledge Discovery*, vol. 1, no. 1, pp. 14–23, 2011.
- [341] P. Boniecki, M. Zaborowicz, A. Pilarska, and H. Piekarska-Boniecka, “Identification process of selected graphic features apple tree pests by neural models type MLP, RBF and DNN,” *Agriculture*, vol. 10, no. 6, p. 218, 2020.
- [342] J. You, W. Liu, and J. Lee, “A DNN-based semantic segmentation for detecting weed and crop,” *Computers and Electronics in Agriculture*, vol. 178, p. 105750, 2020.
- [343] A. J. Izenman, “Linear discriminant analysis,” in *Proceedings of the Modern Multivariate Statistical Techniques*, pp. 237–280, Springer, 2013.

- [344] H. G. Jones and R. A. Vaughan, *Remote Sensing of Vegetation: Principles, Techniques, and Applications*. Oxford University Press, 2010.
- [345] E. San-Blas, G. Paba, N. Cubillán, E. Portillo, A. M. Casassa-Padrón, C. González-González, and M. Guerra, “The use of infrared spectroscopy and machine learning tools for detection of meloidogyne infestations,” *Plant Pathology*, vol. 69, no. 8, pp. 1589–1600, 2020.
- [346] M. Guerra, G. Paba, N. Cubillán, E. Portillo, A. M. Casassa-Padrón, E. Aballay, and E. San-Blas, “Sequential spectral changes of meloidogyne enterolobii-infected plants using two dimensional correlation IR spectroscopy,” *Nematology*, vol. 1, pp. 1–15, 2020.
- [347] C. Riefolo, I. Antelmi, A. Castrignanò, S. Ruggieri, C. Galeone, A. Belmonte, M. R. Muolo, N. A. Ranieri, R. Labarile, G. Gadaleta, *et al.*, “Assessment of the hyperspectral data analysis as a tool to diagnose xylella fastidiosa in the asymptomatic leaves of olive plants,” *Plants*, vol. 10, no. 4, p. 683, 2021.
- [348] W. Verstraeten, F. Veroustraete, and J. Feyen, “Assessment of evapotranspiration and soil moisture content across different scales of observation,” *Sensors*, vol. 8, no. 1, pp. 70–117, 2008.
- [349] J. Wu and D. Wang, “Estimating evaporation coefficient during two-stage evaporation from soil surfaces,” *Soil Sci.*, vol. 170, no. 4, pp. 235–243, 2005.
- [350] S. Kaplan, S. W. Myint, C. Fan, and A. J. Brazel, “Quantifying outdoor water consumption of urban land use/land cover: Sensitivity to drought,” *Environmental Management*, vol. 53, no. 4, pp. 855–864, 2014.
- [351] P. J. Wetzel and J.-T. Chang, “Evapotranspiration from nonuniform surfaces: A first approach for short-term numerical weather prediction,” *Monthly Weather Review*, vol. 116, no. 3, pp. 600–621, 1988.
- [352] R. G. Allen, L. S. Pereira, D. Raes, and M. Smith, “FAO Irrigation and drainage paper No. 56,” *Rome: Food and Agriculture Organization of the United Nations*, vol. 56, no. 97, p. e156, 1998.
- [353] C.-Y. Xu and V. Singh, “Evaluation of three complementary relationship evapotranspiration models by water balance approach to estimate actual regional evapotranspiration in different climatic regions,” *Journal of Hydrology*, vol. 308, no. 1-4, pp. 105–121, 2005.
- [354] Y.-A. Liou and S. Kar, “Evapotranspiration estimation with remote sensing and various surface energy balance algorithms—A review,” *Energies*, vol. 7, no. 5, pp. 2821–2849, 2014.

- [355] R. Allen, A. Irmak, R. Trezza, J. M. Hendrickx, W. Bastiaanssen, and J. Kjaersgaard, "Satellite-based ET estimation in agriculture using SEBAL and METRIC," *Hydrological Processes*, vol. 25, no. 26, pp. 4011–4027, 2011.
- [356] D. Angus and P. Watts, "Evapotranspiration-How good is the Bowen ratio method?," in *Developments in Agricultural and Managed Forest Ecology*, vol. 13, pp. 133–150, Elsevier, 1984.
- [357] L. J. Fritschen, "Accuracy of evapotranspiration determinations by the Bowen ratio method," *Hydrological Sciences Journal*, vol. 10, no. 2, pp. 38–48, 1965.
- [358] P. L. Nagler, R. L. Scott, C. Westenburg, J. R. Cleverly, E. P. Glenn, and A. R. Huete, "Evapotranspiration on western US rivers estimated using the enhanced vegetation index from MODIS and data from Eddy covariance and Bowen ratio flux towers," *Remote Sensing of Environment*, vol. 97, no. 3, pp. 337–351, 2005.
- [359] Z. Su, "The surface energy balance system (SEBS) for estimation of turbulent heat fluxes," *Hydrology and Earth System Sciences*, vol. 6, no. 1, pp. 85–100, 2002.
- [360] W. Kustas and M. Anderson, "Advances in thermal infrared remote sensing for land surface modeling," *Agricultural and Forest Meteorology*, vol. 149, no. 12, pp. 2071–2081, 2009.
- [361] R. G. Allen, M. Tasumi, A. Morse, and R. Trezza, "A Landsat-based energy balance and evapotranspiration model in western US water rights regulation and planning," *Irrigation and Drainage Systems*, vol. 19, no. 3-4, pp. 251–268, 2005.
- [362] W. G. Bastiaanssen, M. Menenti, R. Feddes, and A. Holtslag, "A remote sensing surface energy balance algorithm for land (SEBAL). 1. Formulation," *Journal of Hydrology*, vol. 212, pp. 198–212, 1998.
- [363] W. P. Kustas and J. M. Norman, "A two-source approach for estimating turbulent fluxes using multiple angle thermal infrared observations," *Water Resources Research*, vol. 33, no. 6, pp. 1495–1508, 1997.
- [364] R. R. McShane, K. P. Driscoll, and R. Sando, "A review of surface energy balance models for estimating actual evapotranspiration with remote sensing at high spatio temporal resolution over large extents," *Scientific Investigations Report 2017–5087*. Reston, VA: US Geological Survey. 19 p., 2017.

- [365] R. G. Allen, M. Tasumi, and R. Trezza, "Satellite-based energy balance for mapping evapotranspiration with internalized calibration (METRIC)—Model," *Journal of Irrigation and Drainage Engineering*, vol. 133, no. 4, pp. 380–394, 2007.
- [366] J. M. Norman, W. P. Kustas, and K. S. Humes, "Source approach for estimating soil and vegetation energy fluxes in observations of directional radiometric surface temperature," *Agricultural and Forest Meteorology*, vol. 77, no. 3-4, pp. 263–293, 1995.
- [367] D. A. Quattrochi and J. C. Luvall, "Thermal infrared remote sensing for analysis of landscape ecological processes: Methods and applications," *Landscape Ecology*, vol. 14, no. 6, pp. 577–598, 1999.
- [368] M. S. Moran and R. D. Jackson, "Assessing the spatial distribution of evapotranspiration using remotely sensed inputs," *Journal of Environmental Quality*, vol. 20, no. 4, pp. 725–737, 1991.
- [369] W. Kustas and J. Norman, "Use of remote sensing for evapotranspiration monitoring over land surfaces," *Hydrological Sciences Journal*, vol. 41, no. 4, pp. 495–516, 1996.
- [370] S. C. Zipper and S. P. Loheide II, "Using evapotranspiration to assess drought sensitivity on a subfield scale with HRMET, a high resolution surface energy balance model," *Agricultural and Forest Meteorology*, vol. 197, pp. 91–102, 2014.
- [371] K.-l. Hsu, H. V. Gupta, and S. Sorooshian, "Artificial neural network modeling of the rainfall-runoff process," *Water Resources Research*, vol. 31, no. 10, pp. 2517–2530, 1995.
- [372] R. J. Abrahart, F. Anctil, P. Coulibaly, C. W. Dawson, N. J. Mount, L. M. See, A. Y. Shamseldin, D. P. Solomatine, E. Toth, and R. L. Wilby, "Two decades of anarchy? Emerging themes and outstanding challenges for neural network river forecasting," *Progress in Physical Geography*, vol. 36, no. 4, pp. 480–513, 2012.
- [373] B. Keshtegar, J. Piri, and O. Kisi, "A nonlinear mathematical modeling of daily pan evaporation based on conjugate gradient method," *Computers and Electronics in Agriculture*, vol. 127, pp. 120–130, 2016.
- [374] M. R. Kousari, M. E. Hosseini, H. Ahani, and H. Hakimelahi, "Introducing an operational method to forecast long-term regional drought based on the application of artificial intelligence capabilities," *Theoretical and Applied Climatology*, vol. 127, no. 1-2, pp. 361–380, 2017.

- [375] A. Moghaddamia, M. G. Gousheh, J. Piri, S. Amin, and D. Han, "Evaporation estimation using artificial neural networks and adaptive neuro-fuzzy inference system techniques," *Advances in Water Resources*, vol. 32, no. 1, pp. 88–97, 2009.
- [376] S. Park, J. Im, E. Jang, and J. Rhee, "Drought assessment and monitoring through blending of multi-sensor indices using machine learning approaches for different climate regions," *Agricultural and Forest Meteorology*, vol. 216, pp. 157–169, 2016.
- [377] T. Poblete, S. Ortega-Farías, M. Moreno, and M. Bardeen, "Artificial neural network to predict vine water status spatial variability using multispectral information obtained from an unmanned aerial vehicle (UAV)," *Sensors*, vol. 17, no. 11, p. 2488, 2017.
- [378] J. Norman, W. Kustas, J. Prueger, and G. Diak, "Surface flux estimation using radiometric temperature: A dual-temperature-difference method to minimize measurement errors," *Water Resources Research*, vol. 36, no. 8, pp. 2263–2274, 2000.
- [379] G. Boulet, A. Olioso, E. Ceschia, O. Marloie, B. Coudert, V. Rivalland, J. Chirouze, and G. Chehbouni, "An empirical expression to relate aerodynamic and surface temperatures for use within single-source energy balance models," *Agricultural and Forest Meteorology*, vol. 161, pp. 148–155, 2012.
- [380] J. Kalma and D. Jupp, "Estimating evaporation from pasture using infrared thermometry: Evaluation of a one-layer resistance model," *Agricultural and Forest Meteorology*, vol. 51, no. 3-4, pp. 223–246, 1990.
- [381] W. Massman, "A model study of kBH-1 for vegetated surfaces using localized near-field lagrangian theory," *Journal of Hydrology*, vol. 223, no. 1-2, pp. 27–43, 1999.
- [382] A. Verhoef, H. De Bruin, and B. Van Den Hurk, "Some practical notes on the parameter kb-1 for sparse vegetation," *Journal of Applied Meteorology*, vol. 36, no. 5, pp. 560–572, 1997.
- [383] P. D. Colaizzi, S. R. Evett, T. A. Howell, and J. A. Tolk, "Comparison of aerodynamic and radiometric surface temperature using precision weighing lysimeters," in *Proceedings of the Remote Sensing and Modeling of Ecosystems for Sustainability*, vol. 5544, pp. 215–229, International Society for Optics and Photonics, 2004.
- [384] J. M. Norman and F. Becker, "Terminology in thermal infrared remote sensing of natural surfaces," *Agricultural and Forest Meteorology*, vol. 77, no. 3-4, pp. 153–166, 1995.

- [385] W. P. Kustas and J. M. Norman, "Evaluation of soil and vegetation heat flux predictions using a simple two-source model with radiometric temperatures for partial canopy cover," *Agricultural and Forest Meteorology*, vol. 94, no. 1, pp. 13–29, 1999.
- [386] P. D. Colaizzi, W. P. Kustas, M. C. Anderson, N. Agam, J. A. Tolk, S. R. Evett, T. A. Howell, P. H. Gowda, and S. A. O'Shaughnessy, "Two-source energy balance model estimates of evapotranspiration using component and composite surface temperatures," *Advances in Water Resources*, vol. 50, pp. 134–151, 2012.
- [387] W. J. Timmermans, W. P. Kustas, M. C. Anderson, and A. N. French, "An intercomparison of the surface energy balance algorithm for land (SEBAL) and the two-source energy balance (TSEB) modeling schemes," *Remote Sensing of Environment*, vol. 108, no. 4, pp. 369–384, 2007.
- [388] D. Troufleau, J.-P. Lhomme, B. Monteny, and A. Vidal, "Sensible heat flux and radiometric surface temperature over sparse sahelian vegetation. i. an experimental analysis of the kb-1 parameter," *Journal of Hydrology*, vol. 188, pp. 815–838, 1997.
- [389] D. Matsushima, "Relations between aerodynamic parameters of heat transfer and thermal-infrared thermometry in the bulk surface formulation," *Journal of the Meteorological Society of Japan. Ser. II*, vol. 83, no. 3, pp. 373–389, 2005.
- [390] W. Brutsaert *et al.*, *Hydrology: An Introduction*. Cambridge University Press, 2005.
- [391] W. J. Timmermans, W. P. Kustas, and A. Andreu, "Utility of an automated thermal-based approach for monitoring evapotranspiration," *Acta Geophysica*, vol. 63, no. 6, pp. 1571–1608, 2015.
- [392] G. Roerink, Z. Su, and M. Menenti, "S-sebi: A simple remote sensing algorithm to estimate the surface energy balance," *Physics and Chemistry of the Earth, Part B: Hydrology, Oceans and Atmosphere*, vol. 25, no. 2, pp. 147–157, 2000.
- [393] C. Crisci, B. Ghattas, and G. Perera, "A review of supervised machine learning algorithms and their applications to ecological data," *Ecological Modelling*, vol. 240, pp. 113–122, 2012.
- [394] V. Z. Antonopoulos, S. K. Gianniou, and A. V. Antonopoulos, "Artificial neural networks and empirical equations to estimate daily evaporation: Application to Lake Vegoritis, Greece," *Hydrological Sciences Journal*, vol. 61, no. 14, pp. 2590–2599, 2016.

- [395] M. Gocić, S. Motamedi, S. Shamshirband, D. Petković, S. Ch, R. Hashim, and M. Arif, “Soft computing approaches for forecasting reference evapotranspiration,” *Computers and Electronics in Agriculture*, vol. 113, pp. 164–173, 2015.
- [396] O. Kisi, H. Sanikhani, M. Zounemat-Kermani, and F. Niazi, “Long-term monthly evapotranspiration modeling by several data-driven methods without climatic data,” *Computers and Electronics in Agriculture*, vol. 115, pp. 66–77, 2015.
- [397] S. Mehdizadeh, J. Behmanesh, and K. Khalili, “Using MARS, SVM, GEP and empirical equations for estimation of monthly mean reference evapotranspiration,” *Computers and Electronics in Agriculture*, vol. 139, pp. 103–114, 2017.
- [398] N. Misaghian, S. Shamshirband, D. Petković, M. Gocic, and K. Mohammadi, “Predicting the reference evapotranspiration based on tensor decomposition,” *Theoretical and Applied Climatology*, vol. 130, no. 3-4, pp. 1099–1109, 2017.
- [399] D. Petković, M. Gocic, S. Shamshirband, S. N. Qasem, and S. Trajkovic, “Particle swarm optimization-based radial basis function network for estimation of reference evapotranspiration,” *Theoretical and Applied Climatology*, vol. 125, no. 3-4, pp. 555–563, 2016.
- [400] H. Tabari, C. Martinez, A. Ezani, and P. H. Talaei, “Applicability of support vector machines and adaptive neurofuzzy inference system for modeling potato crop evapotranspiration,” *Irrigation Science*, vol. 31, no. 4, pp. 575–588, 2013.
- [401] M. A. Yassin, A. A. Alazba, and M. A. Mattar, “Comparison between gene expression programming and traditional models for estimating evapotranspiration under hyper arid conditions,” *Water Resources*, vol. 43, no. 2, pp. 412–427, 2016.
- [402] X. Dou and Y. Yang, “Evapotranspiration estimation using four different machine learning approaches in different terrestrial ecosystems,” *Computers and Electronics in Agriculture*, vol. 148, pp. 95–106, 2018.
- [403] M. Gocic, D. Petković, S. Shamshirband, and A. Kamsin, “Comparative analysis of reference evapotranspiration equations modelling by extreme learning machine,” *Computers and Electronics in Agriculture*, vol. 127, pp. 56–63, 2016.

- [404] R. Hashim, C. Roy, S. Motamedi, S. Shamshirband, D. Petković, M. Gocic, and S. C. Lee, "Selection of meteorological parameters affecting rainfall estimation using neuro-fuzzy computing methodology," *Atmospheric Research*, vol. 171, pp. 21–30, 2016.
- [405] D. Petković, M. Gocic, S. Trajkovic, S. Shamshirband, S. Motamedi, R. Hashim, and H. Bonakdari, "Determination of the most influential weather parameters on reference evapotranspiration by adaptive neuro-fuzzy methodology," *Computers and Electronics in Agriculture*, vol. 114, pp. 277–284, 2015.
- [406] M. J. Alizadeh, M. R. Kavianpour, O. Kisi, and V. Nourani, "A new approach for simulating and forecasting the rainfall-runoff process within the next two months," *Journal of Hydrology*, vol. 548, pp. 588–597, 2017.
- [407] S. Shamshirband, M. Amirmojahedi, M. Gocić, S. Akib, D. Petković, J. Piri, and S. Trajkovic, "Estimation of reference evapotranspiration using neural networks and cuckoo search algorithm," *Journal of Irrigation and Drainage Engineering*, vol. 142, no. 2, p. 04015044, 2015.
- [408] A. Pour-Ali Baba, J. Shiri, O. Kisi, A. F. Fard, S. Kim, and R. Amini, "Estimating daily reference evapotranspiration using available and estimated climatic data by adaptive neuro-fuzzy inference system (ANFIS) and artificial neural network (ANN)," *Hydrology Research*, vol. 44, no. 1, pp. 131–146, 2012.
- [409] A. F. Torres-Rua, A. M. Ticlavilca, M. Aboutalebi, H. Nieto, M. M. Alsina, A. White, J. H. Prueger, J. G. Alfieri, L. E. Hipps, L. G. McKee, *et al.*, "Estimation of evapotranspiration and energy fluxes using a deep learning-based high-resolution emissivity model and the two-source energy balance model with sUAS information," in *Proceedings of the Autonomous Air and Ground Sensing Systems for Agricultural Optimization and Phenotyping V*, International Society for Optics and Photonics, 2020.
- [410] W. P. Kustas and J. M. Norman, "A two-source energy balance approach using directional radiometric temperature observations for sparse canopy covered surfaces," *Agronomy Journal*, vol. 92, no. 5, pp. 847–854, 2000.
- [411] C. H. B. Priestley and R. Taylor, "On the assessment of surface heat flux and evaporation using large-scale parameters," *Monthly Weather Review*, vol. 100, no. 2, pp. 81–92, 1972.
- [412] A. N. French, D. J. Hunsaker, and K. R. Thorp, "Remote sensing of evapotranspiration over cotton using the TSEB and METRIC energy balance models," *Remote Sensing of Environment*, vol. 158, pp. 281–294, 2015.

- [413] M. Choi, W. P. Kustas, M. C. Anderson, R. G. Allen, F. Li, and J. H. Kjaersgaard, "An intercomparison of three remote sensing-based surface energy balance algorithms over a corn and soybean production region (Iowa, US) during smacex," *Agricultural and Forest Meteorology*, vol. 149, no. 12, pp. 2082–2097, 2009.
- [414] P. Colaizzi, S. Evett, T. Howell, F. Li, W. Kustas, and M. Anderson, "Radiation model for row crops: I. Geometric view factors and parameter optimization," *Agronomy Journal*, vol. 104, no. 2, pp. 225–240, 2012.
- [415] L. Song, S. Liu, W. P. Kustas, J. Zhou, Z. Xu, T. Xia, and M. Li, "Application of remote sensing-based two-source energy balance model for mapping field surface fluxes with composite and component surface temperatures," *Agricultural and Forest Meteorology*, vol. 230, pp. 8–19, 2016.
- [416] R. Guzinski, M. C. Anderson, W. P. Kustas, H. Nieto, and I. Sandholt, "Using a thermal-based two source energy balance model with time-differencing to estimate surface energy fluxes with day-night MODIS observations," *Hydrology and Earth System Sciences*, vol. 17, no. 7, pp. 2809–2825, 2013.
- [417] J. A. Santanello Jr and M. A. Friedl, "Diurnal covariation in soil heat flux and net radiation," *Journal of Applied Meteorology*, vol. 42, no. 6, pp. 851–862, 2003.
- [418] R. Guzinski, H. Nieto, R. Jensen, and G. Mendiguren, "Remotely sensed land-surface energy fluxes at sub-field scale in heterogeneous agricultural landscape and coniferous plantation," *Biogeosciences*, vol. 11, no. 18, pp. 5021–5046, 2014.
- [419] R. Guzinski, H. Nieto, S. Stisen, and R. Fensholt, "Inter-comparison of energy balance and hydrological models for land surface energy flux estimation over a whole river catchment," *Hydrology and Earth System Sciences*, vol. 19, no. 4, pp. 2017–2036, 2015.
- [420] W. G. M. Bastiaanssen, *Regionalization of Surface Flux Densities and Moisture Indicators in Composite Terrain: A Remote Sensing Approach under Clear Skies in Mediterranean Climates*. SC-DLO, 1995.
- [421] W. G. Bastiaanssen, "SEBAL-based sensible and latent heat fluxes in the irrigated Gediz Basin, Turkey," *Journal of Hydrology*, vol. 229, no. 1-2, pp. 87–100, 2000.
- [422] W. G. Bastiaanssen, M.-u.-D. Ahmad, and Y. Chemin, "Satellite surveillance of evaporative depletion across the Indus Basin," *Water Resources Research*, vol. 38, no. 12, pp. 9–1, 2002.

- [423] A. L. Ruhoff, A. R. Paz, W. Collischonn, L. E. Aragao, H. R. Rocha, and Y. S. Malhi, “A MODIS-based energy balance to estimate evapotranspiration for clear-sky days in Brazilian tropical savannas,” *Remote Sensing*, vol. 4, no. 3, pp. 703–725, 2012.
- [424] Z. Sun, B. Wei, W. Su, W. Shen, C. Wang, D. You, and Z. Liu, “Evapotranspiration estimation based on the SEBAL model in the Nansi Lake Wetland of China,” *Mathematical and Computer Modelling*, vol. 54, no. 3-4, pp. 1086–1092, 2011.
- [425] R. Singh and G. Senay, “Comparison of four different energy balance models for estimating evapotranspiration in the midwestern United States,” *Water*, vol. 8, no. 1, p. 9, 2016.
- [426] W. Bastiaanssen, E. Noordman, H. Pelgrum, G. Davids, B. Thoreson, and R. Allen, “SEBAL model with remotely sensed data to improve water-resources management under actual field conditions,” *Journal of Irrigation and Drainage Engineering*, vol. 131, no. 1, pp. 85–93, 2005.
- [427] P. H. Gowda, J. L. Chavez, P. D. Colaizzi, S. R. Evett, T. A. Howell, and J. A. Tolck, “ET mapping for agricultural water management: Present status and challenges,” *Irrigation Science*, vol. 26, no. 3, pp. 223–237, 2008.
- [428] F. Jacob, A. Olioso, X. F. Gu, Z. Su, and B. Seguin, “Mapping surface fluxes using airborne visible, near infrared, thermal infrared remote sensing data and a spatialized surface energy balance model,” *Agronomie*, vol. 22, no. 6, pp. 669–680, 2002.
- [429] M. Tasumi, R. G. Allen, R. Trezza, and J. L. Wright, “Satellite-based energy balance to assess within-population variance of crop coefficient curves,” *Journal of Irrigation and Drainage Engineering*, vol. 131, no. 1, pp. 94–109, 2005.
- [430] E. R. Hunt, M. Cavigelli, C. S. Daughtry, J. E. McMurtrey, and C. L. Walthall, “Evaluation of digital photography from model aircraft for remote sensing of crop biomass and nitrogen status,” *Precision Agriculture*, vol. 6, no. 4, pp. 359–378, 2005.
- [431] P. Gentine, D. Entekhabi, and B. Heusinkveld, “Systematic errors in ground heat flux estimation and their correction,” *Water Resources Research*, vol. 48, no. 9, 2012.
- [432] F. Li, W. P. Kustas, J. H. Prueger, C. M. Neale, and T. J. Jackson, “Utility of remote sensing-based two-source energy balance model under low-and high-vegetation cover conditions,” *Journal of Hydrometeorology*, vol. 6, no. 6, pp. 878–891, 2005.

- [433] J. Feng and Z. Wang, "A satellite-based energy balance algorithm with reference dry and wet limits," *International Journal of Remote Sensing*, vol. 34, no. 8, pp. 2925–2946, 2013.
- [434] D. Long and V. P. Singh, "Assessing the impact of end-member selection on the accuracy of satellite-based spatial variability models for actual evapotranspiration estimation," *Water Resources Research*, vol. 49, no. 5, pp. 2601–2618, 2013.
- [435] M. Duggin and C. Robinove, "Assumptions implicit in remote sensing data acquisition and analysis," *Remote Sensing*, vol. 11, no. 10, pp. 1669–1694, 1990.
- [436] T. Lillesand, R. W. Kiefer, and J. Chipman, *Remote Sensing and Image Interpretation*. John Wiley & Sons, 2015.
- [437] J. Wang, T. Sammis, V. Gutschick, M. Gebremichael, and D. Miller, "Sensitivity analysis of the surface energy balance algorithm for land (SEBAL)," *Transactions of the ASABE*, vol. 52, no. 3, pp. 801–811, 2009.
- [438] R. Allen, M. Tasumi, R. Trezza, and J. Kjaersgaard, "METRICTM—Mapping evapotranspiration at high resolution—applications manual for Landsat satellite imagery (version 2.0.4)," *University of Idaho*, 2008.
- [439] H. Zhang, D. Wang, J. E. Ayars, and C. J. Phene, "Biophysical response of young pomegranate trees to surface and sub-surface drip irrigation and deficit irrigation," *Irrigation Science*, vol. 35, no. 5, pp. 425–435, 2017.
- [440] D. Wang, J. Ayars, R. Tirado-Corbala, D. Makus, C. Phene, and R. Phene, "Water and nitrogen management of young and maturing pomegranate trees," in *III International Symposium on Pomegranate and Minor Mediterranean Fruits 1089*, pp. 395–401, 2013.
- [441] C. Phene, R. McCormick, K. Davis, J. Pierro, and D. Meek, "A lysimeter feedback system for precise evapotranspiration measurement and irrigation control," *Trans. ASAE*, vol. 32, no. 2, pp. 477–484, 1989.
- [442] J. B. Fisher, F. Melton, E. Middleton, C. Hain, M. Anderson, R. Allen, M. F. McCabe, S. Hook, D. Baldocchi, P. A. Townsend, *et al.*, "The future of evapotranspiration: Global requirements for ecosystem functioning, carbon and climate feedbacks, agricultural management, and water resources," *Water Resources Research*, vol. 53, no. 4, pp. 2618–2626, 2017.
- [443] S. B. Idso, R. D. Jackson, and R. J. Reginato, "Remote-sensing of crop yields," *Science*, vol. 196, no. 4285, pp. 19–25, 1977.

- [444] R. Jackson, R. Reginato, and S. Idso, "Wheat canopy temperature: A practical tool for evaluating water requirements," *Water Resources Research*, vol. 13, no. 3, pp. 651–656, 1977.
- [445] R. D. Jackson, S. Idso, R. Reginato, and P. Pinter Jr, "Canopy temperature as a crop water stress indicator," *Water Resources Research*, vol. 17, no. 4, pp. 1133–1138, 1981.
- [446] H. Zhang and D. Wang, "Management of postharvest deficit irrigation of peach trees using infrared canopy temperature," *Vadose Zone Journal*, vol. 12, no. 3, pp. vzj2012–0093, 2013.
- [447] K. L. Clawson and B. L. Blad, "Infrared thermometry for scheduling irrigation of corn 1," *Agronomy Journal*, vol. 74, no. 2, pp. 311–316, 1982.
- [448] S. Khanal, J. Fulton, and S. Shearer, "An overview of current and potential applications of thermal remote sensing in precision agriculture," *Computers and Electronics in Agriculture*, vol. 139, pp. 22–32, 2017.
- [449] H. Niu, T. Zhao, J. Wei, D. Wang, and Y. Chen, "Reliable tree-level evapotranspiration estimation of pomegranate trees using lysimeter and UAV multispectral imagery," in *2021 IEEE Conference on Technologies for Sustainability (SusTech)*, pp. 1–6, IEEE, 2021.
- [450] M. Raissi, P. Perdikaris, and G. E. Karniadakis, "Physics-informed neural networks: A deep learning framework for solving forward and inverse problems involving nonlinear partial differential equations," *Journal of Computational Physics*, vol. 378, pp. 686–707, 2019.
- [451] U. Simsekli, L. Sagun, and M. Gurbuzbalaban, "A tail-index analysis of stochastic gradient noise in deep neural networks," *arXiv preprint arXiv:1901.06053*, 2019.
- [452] Y. LeCun, Y. Bengio, and G. Hinton, "Deep learning," *Nature*, vol. 521, no. 7553, pp. 436–444, 2015.
- [453] S. Khaki, L. Wang, and S. V. Archontoulis, "A CNN-RNN framework for crop yield prediction," *Frontiers in Plant Science*, vol. 10, p. 1750, 2020.
- [454] N. S. Chandel, S. K. Chakraborty, Y. A. Rajwade, K. Dubey, M. K. Tiwari, and D. Jat, "Identifying crop water stress using deep learning models," *Neural Computing and Applications*, vol. 33, no. 10, pp. 5353–5367, 2021.
- [455] R. Li, R. Wang, J. Zhang, C. Xie, L. Liu, F. Wang, H. Chen, T. Chen, H. Hu, X. Jia, *et al.*, "An effective data augmentation strategy for CNN-based pest localization and recognition in the field," *IEEE Access*, vol. 7, pp. 160274–160283, 2019.

- [456] W. Yang, T. Nigon, Z. Hao, G. D. Paiao, F. G. Fernández, D. Mulla, and C. Yang, “Estimation of corn yield based on hyperspectral imagery and convolutional neural network,” *Computers and Electronics in Agriculture*, vol. 184, p. 106092, 2021.
- [457] C. Ballester, J. Castel, M. Jiménez-Bello, J. Castel, and D. Intrigliolo, “Thermographic measurement of canopy temperature is a useful tool for predicting water deficit effects on fruit weight in citrus trees,” *Agricultural Water Management*, vol. 122, pp. 1–6, 2013.
- [458] D. Holland, K. Hatib, I. Bar-Ya’akov, *et al.*, “2 pomegranate: Botany, horticulture, breeding,” *Horticultural Reviews*, vol. 35, no. 2, pp. 127–191, 2009.
- [459] M. D. Sumner, M. Elliott-Eller, G. Weidner, J. J. Daubenmier, M. H. Chew, R. Marlin, C. J. Raisin, and D. Ornish, “Effects of pomegranate juice consumption on myocardial perfusion in patients with coronary heart disease,” *The American Journal of Cardiology*, vol. 96, no. 6, pp. 810–814, 2005.
- [460] E. P. Lansky and R. A. Newman, “*Punica granatum* (pomegranate) and its potential for prevention and treatment of inflammation and cancer,” *Journal of Ethnopharmacology*, vol. 109, no. 2, pp. 177–206, 2007.
- [461] A. Feng, J. Zhou, E. D. Vories, K. A. Sudduth, and M. Zhang, “Yield estimation in cotton using UAV-based multi-sensor imagery,” *Biosystems Engineering*, vol. 193, pp. 101–114, 2020.
- [462] Q. Zaman, A. Schumann, D. Percival, and R. Gordon, “Estimation of wild blueberry fruit yield using digital color photography,” *Transactions of the ASABE*, vol. 51, no. 5, pp. 1539–1544, 2008.
- [463] Z. Zhang, Y. Jin, B. Chen, and P. Brown, “California almond yield prediction at the orchard level with a machine learning approach,” *Frontiers in Plant Science*, vol. 10, p. 809, 2019.
- [464] Q. Yang, L. Shi, J. Han, Y. Zha, and P. Zhu, “Deep convolutional neural networks for rice grain yield estimation at the ripening stage using UAV-based remotely sensed images,” *Field Crops Research*, vol. 235, pp. 142–153, 2019.
- [465] D. Stateras and D. Kalivas, “Assessment of olive tree canopy characteristics and yield forecast model using high resolution UAV imagery,” *Agriculture*, vol. 10, no. 9, p. 385, 2020.
- [466] X. Zhang, A. Toudeshki, R. Ehsani, H. Li, W. Zhang, and R. Ma, “Yield estimation of citrus fruit using rapid image processing in natural background,” *Smart Agricultural Technology*, p. 100027, 2021.

- [467] A. Feng, M. Zhang, K. A. Sudduth, E. D. Vories, and J. Zhou, "Cotton yield estimation from UAV-based plant height," *Transactions of the ASABE*, vol. 62, no. 2, pp. 393–404, 2019.
- [468] D. Turner, A. Lucieer, Z. Malenovskỳ, D. H. King, and S. A. Robinson, "Spatial co-registration of ultra-high resolution visible, multispectral and thermal images acquired with a micro-UAV over Antarctic moss beds," *Remote Sensing*, vol. 6, no. 5, pp. 4003–4024, 2014.
- [469] N. Dalezios, C. Domenikiotis, A. Loukas, S. Tzortzios, and C. Kalaitzidis, "Cotton yield estimation based on NOAA/AVHRR produced NDVI," *Physics and Chemistry of the Earth, Part B: Hydrology, Oceans and Atmosphere*, vol. 26, no. 3, pp. 247–251, 2001.
- [470] K. Yawata, T. Yamamoto, N. Hashimoto, R. Ishida, and H. Yoshikawa, "Mixed model estimation of rice yield based on NDVI and GNDVI using a satellite image," in *Remote Sensing for Agriculture, Ecosystems, and Hydrology XXI*, vol. 11149, p. 1114918, International Society for Optics and Photonics, 2019.
- [471] R. A. Schwalbert, T. J. Amado, L. Nieto, S. Varela, G. M. Corassa, T. A. Horbe, C. W. Rice, N. R. Peralta, and I. A. Ciampitti, "Forecasting maize yield at field scale based on high-resolution satellite imagery," *Biosystems Engineering*, vol. 171, pp. 179–192, 2018.
- [472] T. S. Magney, J. U. Eitel, and L. A. Vierling, "Mapping wheat nitrogen uptake from RapidEye vegetation indices," *Precision Agriculture*, vol. 18, no. 4, pp. 429–451, 2017.
- [473] M. Din, W. Zheng, M. Rashid, S. Wang, and Z. Shi, "Evaluating hyperspectral vegetation indices for leaf area index estimation of *Oryza sativa* L. at diverse phenological stages," *Frontiers in Plant Science*, vol. 8, p. 820, 2017.
- [474] Y. Gong, B. Duan, S. Fang, R. Zhu, X. Wu, Y. Ma, and Y. Peng, "Remote estimation of rapeseed yield with unmanned aerial vehicle (UAV) imaging and spectral mixture analysis," *Plant Methods*, vol. 14, no. 1, pp. 1–14, 2018.
- [475] J. Ren, Z. Chen, Q. Zhou, and H. Tang, "Regional yield estimation for winter wheat with MODIS-NDVI data in Shandong, China," *International Journal of Applied Earth Observation and Geoinformation*, vol. 10, no. 4, pp. 403–413, 2008.
- [476] O. G. Narin and S. Abdikan, "Monitoring of phenological stage and yield estimation of sunflower plant using Sentinel-2 satellite images," *Geocarto International*, pp. 1–15, 2020.

- [477] I. Khosravi and S. K. Alavipanah, “A random forest-based framework for crop mapping using temporal, spectral, textural and polarimetric observations,” *International Journal of Remote Sensing*, vol. 40, no. 18, pp. 7221–7251, 2019.
- [478] D. Haboudane, J. R. Miller, E. Pattey, P. J. Zarco-Tejada, and I. B. Strachan, “Hyperspectral vegetation indices and novel algorithms for predicting green LAI of crop canopies: Modeling and validation in the context of precision agriculture,” *Remote Sensing of Environment*, vol. 90, no. 3, pp. 337–352, 2004.
- [479] B. Duan, S. Fang, R. Zhu, X. Wu, S. Wang, Y. Gong, and Y. Peng, “Remote estimation of rice yield with unmanned aerial vehicle (UAV) data and spectral mixture analysis,” *Frontiers in Plant Science*, vol. 10, p. 204, 2019.
- [480] B. Duan, S. Fang, Y. Gong, Y. Peng, X. Wu, and R. Zhu, “Remote estimation of grain yield based on UAV data in different rice cultivars under contrasting climatic zone,” *Field Crops Research*, vol. 267, p. 108148, 2021.
- [481] Y. Peng, Y. Li, C. Dai, S. Fang, Y. Gong, X. Wu, R. Zhu, K. Liu, *et al.*, “Remote prediction of yield based on LAI estimation in oilseed rape under different planting methods and nitrogen fertilizer applications,” *Agricultural and Forest Meteorology*, vol. 271, pp. 116–125, 2019.
- [482] A. M. Rovnyak, C. S. Burks, A. J. Gassmann, and T. W. Sappington, “Interrelation of mating, flight, and fecundity in navel orangeworm females,” *Entomologia Experimentalis ET Applicata*, vol. 166, no. 4, pp. 304–315, 2018.
- [483] B. S. Higbee and J. P. Siegel, “Field efficacy and application timing of methoxyfenozide, a reduced-risk treatment for control of navel orangeworm (Lepidoptera: Pyralidae) in almond,” *Journal of Economic Entomology*, vol. 105, no. 5, pp. 1702–1711, 2012.
- [484] D. Lightle, “Navel orangeworm: A costly pest in almonds,” 2018. See also URL <https://www.farmprogress.com/tree-nuts/navel-orangeworm-costly-pest-almonds>.
- [485] L. Kuenen, J. Siegel, *et al.*, “Sticky traps saturate with navel orangeworm in a nonlinear fashion,” *California Agriculture*, vol. 70, no. 1, pp. 32–38, 2016.
- [486] J. P. Siegel, M. M. Strmiska, F. J. Niederholzer, D. K. Giles, and S. S. Walse, “Evaluating insecticide coverage in almond and pistachio for control of navel orangeworm (*Amyelois transitella*)(Lepidoptera: Pyralidae),” *Pest Management Science*, 2018.

- [487] D. Downey, D. Giles, P. Klassen, F. Niederholzer, *et al.*, ““Smart” sprayer technology provides environmental and economic benefits in California orchards,” *California Agriculture*, vol. 65, no. 2, pp. 85–89, 2011.
- [488] J. N. Seiber, B. W. Wilson, and M. M. McChesney, “Air and fog deposition residues of four organophosphate insecticides used on dormant orchards in the San Joaquin Valley, California,” *Environmental Science & Technology*, vol. 27, no. 10, pp. 2236–2243, 1993.
- [489] J. Cross, P. Walklate, R. Murray, and G. Richardson, “Spray deposits and losses in different sized apple trees from an axial fan orchard sprayer: 1. Effects of spray liquid flow rate,” *Crop Protection*, vol. 20, no. 1, pp. 13–30, 2001.
- [490] D. K. Giles, M. Delwiche, and R. Dodd, “Control of orchard spraying based on electronic sensing of target characteristics,” *Transactions of the ASAE*, vol. 30, no. 6, pp. 1624–1636, 1987.
- [491] R. Girshick, “Fast r-cnn,” in *Proceedings of the IEEE International Conference on Computer Vision*, pp. 1440–1448, 2015.
- [492] J. Long, E. Shelhamer, and T. Darrell, “Fully convolutional networks for semantic segmentation,” in *Proceedings of the IEEE Conference on Computer Vision and Pattern Recognition*, pp. 3431–3440, 2015.
- [493] T. Oksanen and A. Visala, “Coverage path planning algorithms for agricultural field machines,” *Journal of Field Robotics*, vol. 26, no. 8, pp. 651–668, 2009.
- [494] C. Alexopoulos and P. M. Griffin, “Path planning for a mobile robot,” *IEEE Transactions on Systems, Man, and Cybernetics*, vol. 22, no. 2, pp. 318–322, 1992.
- [495] C. Niederberger, D. Radovic, and M. Gross, “Generic path planning for real-time applications,” in *Proceedings Computer Graphics International, 2004.*, pp. 299–306, IEEE, 2004.
- [496] M. Freeman, M. Viveros, K. Klonsky, and R. De Moura, “Sample costs to establish an almond orchard and produce almonds: San Joaquin Valley South micro-sprinkler irrigation,” *University of California Cooperative Extension, Davis, CA*, 2008.
- [497] C. D. Allen, A. K. Macalady, H. Chenchouni, D. Bachelet, N. McDowell, M. Vennetier, T. Kitzberger, A. Rigling, D. D. Breshears, E. T. Hogg, *et al.*, “A global overview of drought and heat-induced tree mortality reveals emerging climate change risks for forests,” *Forest Ecology and Management*, vol. 259, no. 4, pp. 660–684, 2010.

- [498] D. Goldhamer, E. Fereres, *et al.*, “Simplified tree water status measurements can aid almond irrigation,” *California Agriculture*, vol. 55, no. 3, pp. 32–37, 2001.
- [499] B. Lampinen, S. Sibbett, W. Olson, and K. Shackel, “The relation of mid-day stem water potential to the growth and physiology of fruit trees under water limited conditions,” in *III International Symposium on Irrigation of Horticultural Crops 537*, pp. 425–430, 1999.
- [500] L. Sack, G. P. John, and T. N. Buckley, “ABA accumulation in dehydrating leaves is associated with decline in cell volume, not turgor pressure,” *Plant Physiology*, vol. 176, no. 1, pp. 489–495, 2018.
- [501] H. Jones, “Plants and microclimate: A quantitative approach to environmental plant physiology. doi: 10.1017,” *CBO9780511845727*, 2013.
- [502] M. Browne, N. T. Yardimci, C. Scoffoni, M. Jarrahi, and L. Sack, “Prediction of leaf water potential and relative water content using terahertz radiation spectroscopy,” *Plant Direct*, vol. 4, no. 4, p. e00197, 2020.
- [503] E. T. Engman, “Applications of microwave remote sensing of soil moisture for water resources and agriculture,” *Remote Sensing of Environment*, vol. 35, no. 2-3, pp. 213–226, 1991.
- [504] D. Entekhabi, J. Nakamura, and E. Njoku, “Retrieval of soil moisture profile by combined remote sensing and modeling,” *JPL Technical Report Server*, 1994.
- [505] J. D. Fast and M. D. McCorcle, “The effect of heterogeneous soil moisture on a summer baroclinic circulation in the central United States,” *Monthly Weather Review*, vol. 119, no. 9, pp. 2140–2167, 1991.
- [506] L. Powell, A. A. Berg, D. Johnson, and J. Warland, “Relationships of pest grasshopper populations in Alberta, Canada to soil moisture and climate variables,” *Agricultural and Forest Meteorology*, vol. 144, no. 1-2, pp. 73–84, 2007.
- [507] L. Wang and J. J. Qu, “Satellite remote sensing applications for surface soil moisture monitoring: A review,” *Frontiers of Earth Science in China*, vol. 3, no. 2, pp. 237–247, 2009.
- [508] E. T. Engman, “Progress in microwave remote sensing of soil moisture,” *Canadian Journal of Remote Sensing*, vol. 16, no. 3, pp. 6–14, 1990.
- [509] L. Wang and J. J. Qu, “NMDI: A normalized multi-band drought index for monitoring soil and vegetation moisture with satellite remote sensing,” *Geophysical Research Letters*, vol. 34, no. 20, 2007.

- [510] M. Friedl and F. Davis, "Sources of variation in radiometric surface temperature over a tallgrass prairie," *Remote Sensing of Environment*, vol. 48, no. 1, pp. 1–17, 1994.
- [511] J. P. Walker, *Estimating soil moisture profile dynamics from near-surface soil moisture measurements and standard meteorological data*. PhD thesis, University of Newcastle, 1999.
- [512] J.-P. Wigneron, J.-C. Calvet, T. Pellarin, A. Van de Griend, M. Berger, and P. Ferrazzoli, "Retrieving near-surface soil moisture from microwave radiometric observations: Current status and future plans," *Remote Sensing of Environment*, vol. 85, no. 4, pp. 489–506, 2003.
- [513] S. Wold, K. Esbensen, and P. Geladi, "Principal component analysis," *Chemometrics and Intelligent Laboratory Systems*, vol. 2, no. 1-3, pp. 37–52, 1987.
- [514] S. Balakrishnama and A. Ganapathiraju, "Linear discriminant analysis: A brief tutorial," *Institute for Signal and Information Processing*, vol. 18, pp. 1–8, 1998.
- [515] J. Tian, H. Niu, P. Wang, and Y. Chen, "Smart and autonomous farm field scouting service robot as an edge device under \$1000: Challenges and opportunities," in *ASME 2019 International Design Engineering Technical Conferences and Computers and Information in Engineering Conference*, American Society of Mechanical Engineers Digital Collection, 2019.